Proceeding of

The 12th Rajamangala University of Technology International Conference (12th RMUTIC)

30 August – 1 September, 2023

Venue: Nongnooch Tradition Center Hall, Nongnooch Pattaya Garden, Chonburi, Thailand

รายงานสืบเนื่องจากการประชุมวิชาการระดับนานาชาติ มหาวิทยาลัยเทคโนโลยีราชมงคล ครั้งที่ 12

Proceeding of The 12th Rajamangala University of Technology International Conference

"9 RMUT Empowering and Promoting of Sustainable Innovation and BCG Model for the Next Normal"

Collaboration with :

- Thai Home Economics Association under the Royal Patronage of Her Majesty the Queen (THEA),
- The Thai Veterinary Medical Association under Royal Patronage (ThaiVMA),
- Council of Engineers Thailand
- and Innovation and Creative Technology Association (ICTA)

30 August – 1 September, 2023

Venue: Nongnooch Tradition Center Hall,
NongnoochPattaya Garden, Chonburi, Thailand

Introduction

Rajamangala University of Technology Tawan-ok has been entrusted as the host for the 13th Rajamangala University of Technology National Conference (13th RMUTNC), the 12th Rajamangala University of Technology International Conference (12th RMUTIC), and the 5th RMUT Innovation Awards (RMUTCON2023), which will take place from August 30th to September 1st, 2023, at Nongnooch Tradition Center Hall, Nongnooch Pattaya Garden, Najomtien, Sattahip, Chonburi, Thailand. This academic event aims to promote and support the exchange of diverse academic works, spanning various disciplines, and represents a significant platform for researchers, academics, professors, and students from within and outside the university to collaborate and create academic networks in various dimensions, leading to sustainable utilization of research outcomes.

The RMUTCON2023 academic conference will feature presentations by researchers from various fields, both nationally and internationally, including lectures and poster sessions. The works presented will include 188 national research projects, 40 international research projects, 80 inventions, innovations, and creative works, and 12 RMUT Start Up Awards projects. The event will host 6 distinguished guest speakers, 1 national-level invited speaker, and 3 international-level invited speakers.

In this regard, the university fervently hopes that the RMUTCON2023 academic conference will provide significant benefits to its participants, fostering continuous development and cooperation among faculty members, educational personnel, and students, both within and beyond the institution. This collaboration extends to involve the private sector and industrial stakeholders, ultimately contributing to the ongoing advancement of higher education and the development of the nation's human resources.

Message from the President

Rajamangala University of Technology Tawan-ok (RMUTTO) is delighted and honored to be the main co-host with 8 Rajamangala University of Technology in the organization of the "13th Rajamangala University of Technology National Conference (13th RMUTNC), the 12th Rajamangala University of Technology International Conference (12th RMUTIC), and the 5th RMUT Innovation Awards" (RMUTCON2023), scheduled to take place from August 30th to September 1st, 2023, at the Nongnooch Tradition Center Hall, Nongnooch Pattaya Garden, Najomtien, Sattahip, Chonburi, Thailand. The primary objective of this event is to enhance and support the exchange of diverse academic knowledge, promote and disseminate technology and innovations, extend research findings to practical applications, and present new perspectives for the development of collaborative networks within various disciplines. This conference serves as a platform for researchers to showcase and promote academic achievements, creative products, inventions, and innovations that contribute to industrial and commercial benefits. The event comprises the 13th Rajamangala University of Technology National Conference, the 12th Rajamangala University of Technology International Conference, and the 5th RMUT Innovation Awards, all guided by the theme "9 RMUT Empowering and Promoting Sustainable Innovation and BCG Model for The Next Normal." The activities include national and international academic conferences, special guest speaker presentations, competitions for inventions and innovations, exhibitions, and the RMUT Start Up Awards competition.

On behalf of all 9 Rajamangala University of Technology, we express our gratitude to the collaborating network organizations that graciously co-host this event, the invited speakers from both domestic and international arenas, the qualified individuals within and outside the university, researchers, conference participants, and the organizing committee. We extend our sincere appreciation to the Governor of Chonburi Province and the Permanent Secretary of the Ministry of Higher Education, Science, Research, and Innovation for their gracious presence as keynote speakers and opening the proceedings of this academic conference.

(Associate Professor Rerkchai Fooprateepasiri, Ph.D.)
President, Rajamangala University of Technology Tawan-ok

List of Contents

List of Contents

Schedule: The 12th Rajamangala University of Technology International Conference (12th RMUTIC)
On: August 30th - September 1st, 2023
Venue: Nongnooch Tradition Center Hall, NongnoochPattaya Garden Chonburi, Thailand

Time	Agenda	Location
Day 1: August 30th, 2023		
8.00 a.m. - 8.30 a.m.	Conference registration	Hall 1
8.30 a.m. - 10.10 a.m.	**Opening ceremony**	
	- Opening remark - Special speech By Ministry of Higher Education, Science, Research and Innovation - Plaque of appreciation organizations that support academic conferences	
10.10 a.m. - 10.40 a.m.	Keynote address title "Innovation and Sustainable for Architecture and Engineering" By Professor Dr. Soontorn Boonyatikarn	
10.40 a.m. - 11.00 a.m.	Break	
11.00 a.m. - 11.30 a.m.	Keynote address title "BCG model-based Organic Livestock for Sustainable Economy" By Department of Livestock Development	
11.30 a.m. - 12.00 a.m.	Visit the exhibition	Hall 2
1.00 p.m. - 1.30 p.m.	Keynote address title "Maximizing Photosynthesis to Regenerate Agriculture, Climate and Biodiversity" By Professor Dr. Andre Leu	2nd floor meeting room A1
	- RMUT Exhibition	
1.30 p.m. - 2.00 p.m.	Keynote address title "Nanomaterials for optical energy harvesting and management" By Professor Dr. Wisanu Pecharapa	2nd floor meeting room A1
2.00 p.m. - 2.40 p.m.	Oral Presentations	
2.40 p.m. - 3.00 p.m.	Break	
3.00 p.m. - 4.30 p.m.	Oral Presentations	
6.00 p.m - 10.00 p.m.	**Welcoming Party** (Theme: Old Fashioned Party Night and Jeans)	LIDO Room
Day 2: August 31st, 2023		
08.30 a.m. - 5.00 p.m.	Oral and Poster presentations	2nd floor meeting room A1-C2
	- Poster Presentations - Exhibition of Inventions and Innovations - RMUT Exhibition	Hall 2
09.00 a.m. - 3.00 p.m.	RMUT Start Up Awards Contest	Hall 1

Time	Agenda	Location
Day 3: September 1st, 2023		
08.30 a.m. - 12.00 a.m.	- Presentation National and International Posters - Exhibition of Inventions and Innovations - Presentation of the Start Up Awards Contests	Hall 2
1.30 p.m. - 16.00 p.m.	**Closing Ceremony**	Hall 1
	- **Outstanding Award Ceremony** in order as follows: • Oral and Posters Presentations • Invention and Innovation Contests • RMUT Start Up Awards • RMUTTO Researchers Award 2023 - **Closing ceremony** by President of Rajamangala University of Technology Tawan-ok	
Remark: The schedule is subject to change as appropriate. Break at 10.40 a.m. - 11.00 a.m., 2.40 p.m. - 3.00 p.m. Lunch Break at 12.00 p.m. - 1.00 p.m.		

Schedule: Oral Presentations

Day 1: August 30th, 2023
Location: 2nd floor meeting room A1

Time	No.	Topics
Session 1: Nanotechnology and Applied Materials		
2.00 p.m. - 2.20 p.m.	**A1-1-1**	Green Synthesis of ZnO/CuO Nanocomposites from Kratom Leaf Extract and Photocatalytic Methylene Blue Dye Degradation Activity [11033] **Nuchita Sukprasil**
2.20 p.m. - 2.40 p.m.	**A1-1-2**	Effect of CMC/SBR binder content on mechanical properties and electrochemical performance for Si/graphite Anode in Lithium-Ion Batteries [11012] **Voranan Piyavarakorn**
Session 2: Innovation and Sustainable for Architecture and Engineering		
3.00 p.m. - 3.20 p.m.	**A1-2-1**	The need of Blockchain in Carbon Neutrality [10965] **Puckpimon Singhapong**
3.20 p.m. - 3.40 p.m.	**A1-2-2**	The Efficiency of Mild Alkaline Pretreatment on Papyrus Fibers for Cellulose Nanofibril Isolation [11003] **Thaneeya Rangseesuriyachai**
3.40 p.m. - 4.00 p.m.	**A1-2-3**	Alternative procedures for Cellulose Production from Cattail (*Typha angustifolia*. L.) [11004] **Thaneeya Rangseesuriyachai**
4.00 p.m. - 4.20 p.m.	**A1-2-4**	Studying of Nut's structure that effects the loosen of Implant Rods Spine Inside Patient's body [11032] **Banpot Meesa and Sanphasit Chonlaphan**
4.20 p.m. - 4.40 p.m.	**A1-2-5**	Optimizing Pick-Place Operations: Leveraging K-means for Visual Object Localization and Decision-Making in Collaborative Robots [11141] **Nattasit Dancholvichit**
4.40 p.m. - 5.00 p.m.	Certificate Acceptance	
Remark: The schedule is can be to changed as appropriate consideration. Break at 2.40 p.m. - 3.00 p.m.		

Day 2: August 31st, 2023
Location: 2nd floor meeting room A1

Time	No.	Topics
Session 3: Creative Food and Technology of Smart Farm		
8.30 a.m. - 8.50 a.m.	**A1-3-1** **Online**	Development of a Mexican homemade sauce, a creative food, using carotenoid pigments (astaxanthins) obtained from shrimp exoskeleton and cephalothorax [11150] **Romero-Olmos, D.**
8.50 a.m. - 9.10 a.m.	**A1-3-2**	Nutritional values and formula development of Samed mushroom (Boletus *griseipurpureus cor*.) crackers [11137] **Chompunooch Somaree**
9.10 a.m. - 9.30 a.m.	**A1-3-3**	AMMI Analysis for Yield Stability of Yardlong Bean (*Vigna unguiculata* (L.) Walp. ssp. sesquipedalis) [10984] **Pramote Pornsuriya**
9.30 a.m. - 9.50 a.m.	**A1-3-4**	Genetic Divergence in 23 Commercial Cultivars of Yard Long Bean (*Vigna unguiculata* (L.) Walp. ssp. sesquipedalis) [10988] **Ruethairat Mangta**
10.10 a.m. - 10.30 a.m.	**A1-3-5**	Development of Chinese Sausage (Kun-Chiang) from Trimmed Crocodile Meat mixed with Chicken Meat [11029] **Grant Thamkaew**
10.30 a.m. - 10.50 a.m.	**A1-3-6**	Boosting Cordycepin Production through Plant-Based Oils for Vegetarian Consumption [11128] **Watcharin Yuttavanichakul**
11.00 a.m. -12.00 a.m.	- Poster Presentation	
12.00 p.m. - 1.00 p.m.	**Lunch Break**	
Session 4: Digital Technology		
1.00 p.m. - 1.20 p.m.	**A1-4-1**	A prototype of an intelligent rice contamination monitoring system on CiRA CORE platform [10929] **Weerayuth Khunrattanasiri and Burasakorn Yoosooka**
1.20 p.m. - 1.40 p.m.	**A1-4-2**	Web-based Cooking Recipe Recommender System based on Stocked Groceries [10967] **Suvil Chomchaiya**

Time	No.	Topics
1.40 p.m. - 2.00 p.m.	**A1-4-3**	Emergency Reporting System via Smartphone The Case Study of The Rajamangala University of Technology Thanyaburi (RMUTT) [10980] **Weena Janratchakool**
2.00 p.m. - 2.20 p.m.	**A1-4-4**	Ongoing Research in Secondary Learner Engagement in Immersive Learning [11007] **Orakarn Laoharutanun**
2.20 p.m. - 2.40 p.m.	**A1-4-5**	Wildlife Guardian: The Development of an Augmented Reality Game-Based Learning Application [11080] **Fian Tohkeng**
Session 5: Business Innovation		
3.00 p.m. - 3.20 p.m.	**A1-5-1**	The Predicting TOEIC Score with Regression Model: A Case Study of Institute of Aviation and Aerospace Technology, RMUTTO [11102] **Boonyawat Aksornkitti**
3.20 p.m. - 3.40 p.m.	**A1-5-2**	Application of Unmanned Aerial Vehicle to Develop Geo-Informatics System of RMUTTO [11097] **Thitinan Wareewanich**
Session 6: Tourism Cultural and Creative Technology		
3.40 p.m. - 4.00 p.m.	**A1-6-1**	The Web Application of Information Presentation with Augmented Reality Technique with Case Study of Temple, Market and Museum [10937] **Uraiwan Inyaem**
4.00 p.m. - 4.20 p.m.	Certificate Acceptance	
Remark: The schedule is can be to changed as appropriate consideration. Break at 9.50 a.m. - 10.10 a.m., 2.40 p.m. - 3.00 p.m.		

Schedule: Poster Presentations

Day 2: August 31st, 2023

Time	Topics
Location: 2nd floor meeting room A1	
10.30 a.m. – 12.00 a.m.	- All presenters are present at the poster. - Sorted by presentation order as follows: No.E1-E8
12.00 a.m. - 1.00 p.m.	**Lunch Break**
1.00 p.m. - 3.30 p.m.	- All presenters are present at the poster. - Sorted by presentation order as follows: No.E9-E19
3.30 p.m. - 4.00 p.m.	Certificate Acceptance
Remark: The schedule is can be to changed as appropriate consideration. Break at 10.40 a.m. - 11.00 a.m., 2.40 p.m. - 3.00 p.m.	

Sorted by presentation order:

Code Poster No.	Topics	Presenter
Session 1: Innovation and Sustainable for Architecture and Engineering		
E1	Fed-Batch Ethanol Fermentation from Pineapple Peel Juice Mixed with Cane Sugar [11111]	Kitti Orasoon
E2	The Process of Creating a Community Identity to Add Product Value Case Study: Klaeng Subdistrict, Krasae Bon District, Rayong Province [11040]	Sirisopa Ongkananuwong
Session 2: Application of Medical Science and Herb		
E3	Investigation of Biological Properties of Raw Wild Mango *(Spondias pinnata)* Fruit Extract for Cosmetic, Food Supplement, and Medicinal Development [10975]	Supawadee Patathananone
E4	Phytochemical Screening and Study of Cholesterol Esterase Inhibitory Activity of Extracts from Stem Wood of Dipterocarpusintricatus Dyer [11048]	Sunan Jaisamut
E5	Fabrication and Characterization of Hydrogels Containing Xanthone Extract from Mangosteen Peel [11107]	Anan Athipornchai
E6	Antioxidation and Anti-Inflammatory Activities of Blended Essential Oil [10991]	Punyanut Amorndoljai
E7	Enhancing Antimicrobial Activity of Garlic Extracts by Kombucha Fermentation and Ethanol Extraction [11047]	Duongruitai Nicomrat
E8	Super Hydrophobic Peptides: Syntheses and Purification [11014]	Nattamon Trirattanaporn

Code Poster No.	Topics	Presenter
Session 3: Nanotechnology and Applied Materials		
E9	Efficiency of Wastewater Treatment from Environmental Laboratory of Science and Technology, RMUTP using Ozonation [10940]	Supachai Hirunsupachote
E10	Characterization and Screening of Anti-phytopathogenic Activity of Termite-associated Actinomycetes [10972]	Khomsan Supong
E11	Ultrafast Production of Reduced Graphene Oxide via Laser-Based Reduction Under Ambient Air Conditions [11120]	Komsak Aranmala
Session 4: Business Innovation		
E12	Effects of Dynamic Environment to Performance of Small and Medium Enterprises in NakonChai Burin [11090]	Araya Uengpaiboonkit
E13	Effects of Market Orientation to Innovation of Small and Medium Enterprises in Surin Province [11133]	Araya Uengpaiboonkit
E14	Brand Image Affecting Brand Awareness of Online Consumers in Thailand [11084]	Voradit Thanapatra
E15	Application of Artificial Intelligence for Airport Runway Pavement Inspection [11063]	Khunanun Sukpascharoen
Session 5: Creative Food and Technology of Smart Farm		
E16	Development of Low-Sodium Salted Egg Yolk Processing with Salt and Maltodextrin [10917]	Supuksorn Masavang
E17	Study on Rumen Digestibility of Calcium Soap and Cackaging by In Vitro Technique [10999]	Onanong Poungchompu
E18	The Study of Sample Preparation for Spectrophotometric Determination of Formaldehyde in Food Samples [11135]	Nutnicha Sakornkhum
Session 6: Routine to Research (R2R)		
E19	Characterization of Attenuated Precocious Line of Eimeria tenella [11036]	Wipaporn Jarujareet

Green Synthesis of ZnO/CuO Nanocomposites from Kratom Leaf Extract and Photocatalytic Methylene Blue Dye Degradation Activity

Nuchita Sukprasit and Voranuch Thongpool*

Division of Physics, Faculty of Science and Technology, Rajamangala University of Technology Thanyaburi, Pathum Thani 12110, Thailand

*Corresponding author. *E-mail address:* voranut_t@rmutt.ac.th

Abstract

In this work, ZnO/CuO nanocomposites were prepared by a green synthesis method using Kratom leaves extract. The as-synthesized ZnO/CuO nanocomposites were characterized using field-emission scanning electron microscopy (FESEM, energy dispersive X-ray spectroscopy (EDS), Fourier transform infrared spectroscopy (FTIR), X-ray diffraction (XRD), and UV-visible spectrophotometer (UV-vis). The results show that, the ZnO/CuO nanocomposites were relatively spherical in shape and some were found to form rods. X-ray diffraction analysis reveals the monoclinic crystal phase for CuO and hexagonal wurtzite for ZnO in ZnO/CuO nanocomposites. The as-synthesized ZnO/CuO nanocomposites have an average crystalline size of 12.5 nm and a maximum absorbance of 360 nm. Furthermore, photocatalytic performances were investigated for methylene blue (MB) degradation. According to the results, the MB degradation efficiency was 80.821% within 60 minutes.

Keywords: green synthesis, methylene blue dye, photocatalytic, Mitragyna Speciosa Korth, plant extract

1. Introduction

Organic dyes are widely present in industrial wastewaters from the paper, textile, and garment industries, resulting in significant environmental damage. Several studies have found that 10-12% of dyes used in textile industries, such as Rhodamine B, Victoria blue, Rose Bengal, Indigo Red, Caramine, Red 120, Eriochrome, Methylene Blue (MB), Black-T (EBT), and Thymol blue, are lost during synthesis and processing operations and end up in wastewater (Rafiq et al., 2021). These dyes are highly toxic, carcinogenic, and non-biodegradable (Khan et al., 2022), which has led researchers to consider treating methylene blue with methods such as Electrochemical therapy (Singh et al., 2013) and the Fenton process (Liu, 2020). However, these processes are inefficient and costly (Bekru et al., 2022). The photocatalytic process is an advanced oxidation process that uses a catalyst in combination with ultraviolet light. Metals commonly used as photocatalysts include titanium dioxide (TiO_2) (Wang et al., 2011), copper oxide (CuO), and zinc oxide (ZnO) (Shubha et al., 2023) (Basit et al., 2023).

ZnO is an N-type semiconductor with a wide energy band gap of about 3.37 eV. However, the fast electron recombination of ZnO limits its dye degradation efficiency (Sakib, 2019). In recent studies, researchers have enhanced the properties of ZnO by incorporating CuO. Unlike ZnO, CuO is a P-type semiconductor with a narrow energy band gap of about 1.4 eV, enabling it to operate within the visible light range and reduce electron-hole pair recombination (Yu et al., 2015). The synthesis of zinc oxide/copper oxide nanoparticles (ZnO/CuO NPs) has been achieved through various processes, including chemical vapor deposition, the sol-gel method, electrospinning, and green chemistry (Das & Srivastava, 2018). Green chemistry is an energy-efficient and environmentally friendly process that utilizes plant extracts, carbohydrates, and proteins (Duan et al., 2015) (Qamar et al., 2020). These extracts function by reducing metal ions to nanoparticles through a redox reaction (Dubey et al., 2009). Literature reviews indicate the utilization of several plants, such as Momordica charantia (Qamar et al., 2020), Eucalyptus Hybrida Safeda Leaf (Dubey et al., 2009), Olive Leaf (Khalil et al., 2014), and Tea Leaf (Sun el al., 2014), for synthesizing metal oxide nanoparticles.

Kratom, also known as Mitragyna Speciosa Korth, is a plant in the Rubiaceae family and is native to Southeast Asia. It possesses pharmaceutical and medical uses (Veltri, 2019). Kratom contains various chemical compounds such as alkaloids, flavonoids, triterpenes, and phenolics. These extracts can serve as both reducing agents and capping agents during the synthesis process of nanoparticles (Iravani, 2011).

In this study, ZnO/CuO nanocomposites were synthesized using a green chemistry approach employing kratom leaf extracts. The morphology of the resulting nanoparticles was examined through scanning electron microscopy (FE-SEM). The elemental composition, chemical functional groups, crystalline structure, and optical absorbance were determined using energy-dispersive X-ray spectroscopy (EDS), Fourier transform infrared spectroscopy (FTIR), X-ray diffraction (XRD), and UV-visible spectrophotometry (UV-vis), respectively. Furthermore,

the efficiency of the as-synthesized ZnO/CuO nanocomposites in degrading methylene blue under ultraviolet light was also studied.

2. Experimental Method

2.1 Chemicals.

Zinc Acetate ($Zn(CH_3COO)2{\cdot}H_2O$) (99.5%, Ajax Finechem™), Cupric Nitrate Trihydrate ($Cu(NO_3)_2{\cdot}3H_2O$) (99.5%, LOBA CHEMIE), Sodium Hydroxide, pellet (NaOH) (QReC), and methylene blue ($C_{16}H_{18}ClN_3S$), leaves of Mitragyna speciosa Korth. and deionized water (DI) was utilized throughout the experiment.

2.2 Preparation of Kratom leaves extract

The Kratom leaves were washed with distilled water, dried at 50 °C for 3 days, and then ground into powder. A mixture of 25 g of kratom leaf powder and 50 ml of distilled water was prepared in a beaker, stirred with a magnetic stirrer at 500 rpm for 30 minutes, and heated to 60 °C. Following this, the mixture was filtered to separate the sediment from the extract. The resulting fresh supernatant was utilized for the synthesis of ZnO/CuO nanocomposites.

2.3 Synthesis of ZnO/CuO Nanocomposites using Kratom leaves extract

The synthesis of ZnO/CuO nanocomposites using Kratom leaves extract in this study involved the utilization of copper nitrate and zinc acetate as substrates. The preparation steps are as follows: Firstly, dissolve zinc acetate and copper nitrate in distilled water, maintaining a molar ratio of $ZnC_4H_6O_4$: $Cu(NO_3)_2$ as 1:0.5:0.5. Next, mix 100 mL of the resulting solution with 50 mL of Kratom leaf extract, followed by sonication for 1 hour. Subsequently, adjust the pH to 8 using a 2 M solution of sodium hydroxide. The mixture is then filtered and washed with distilled water until the pH reaches 7. Finally, dry the filtered material at 105 °C for 24 hours and subsequently subject it to calcination at 400 °C for 2 hours.

2.4 Characterization of the as-synthesized ZnO/CuO nanocomposites

The morphology of the nanoparticles was examined using scanning electron microscopy (FESEM; JEOL JSM7800F, JAPAN) The elemental composition, chemical functional groups, crystalline structure, and optical absorbance were determined through energy-dispersive X-ray spectroscopy (EDS; Oxford X-Max 20, United Kingdom)Fourier transform infrared spectroscopy (FTIR; Thermoscientific nicolet iS5 with a diamond ATR) X-ray diffraction (XRD; Bruker AXS Model D8 Advance, Germany) and UV-visible spectrophotometry (UV-vis; PG Instruments - Model T60), respectively.

2.5 Efficiency in degradation of methylene blue dye under ultraviolet light

25 mg of ZnO/CuO NPs were added to 50 ml of 25 ppm methylene blue solution. The mixture was kept in the dark for 30 minutes to reach equilibrium. After that, the dye was catalyzed by ultraviolet light for 60 min. At 10-minute intervals, 3 ml of the dye solution was aspirated and the precipitate was separated by centrifuge at 6,000 rpm for 10 min. The absorbance at a wavelength of 667 nm was then measured using a UV-visible spectrophotometer (UV-vis). The degradation efficiency of methylene blue dye was calculated from equation (1):

$$\%\,degradation = \frac{|A_0 - A|}{A_0} \times 100 \quad (1)$$

where $A0$ is the absorbance at the initial time.
A is the absorbance at any time.

3. Results and Discussion

Fig. 1 shows the morphology of CuO nanoparticles, ZnO nanoparticles, and ZnO/CuO nanocomposites synthesized by green synthesis method. The results show that CuO nanoparticles are spherical shape and tightly adhered to each other. The elemental composition of copper (Cu) and oxygen (O) were 75.39 and 24.61%wt., respectively. The ZnO nanoparticles were relatively spherical and some rod-like shapes have been found. The elemental composition of zinc (Zn) and oxygen (O) elements were 74.01 and 25.99 %wt., respectively. The ZnO/CuO nanocomposites have the same shape as ZnO nanoparticles. In addition, the elemental compositions of copper (Cu), zinc (Zn), and oxygen (O) were 27.68, 42.45, and 29.87 %wt., respectively, which corresponded to the formation of zinc oxide (ZnO) and copper oxide (CuO) nanoparticles.

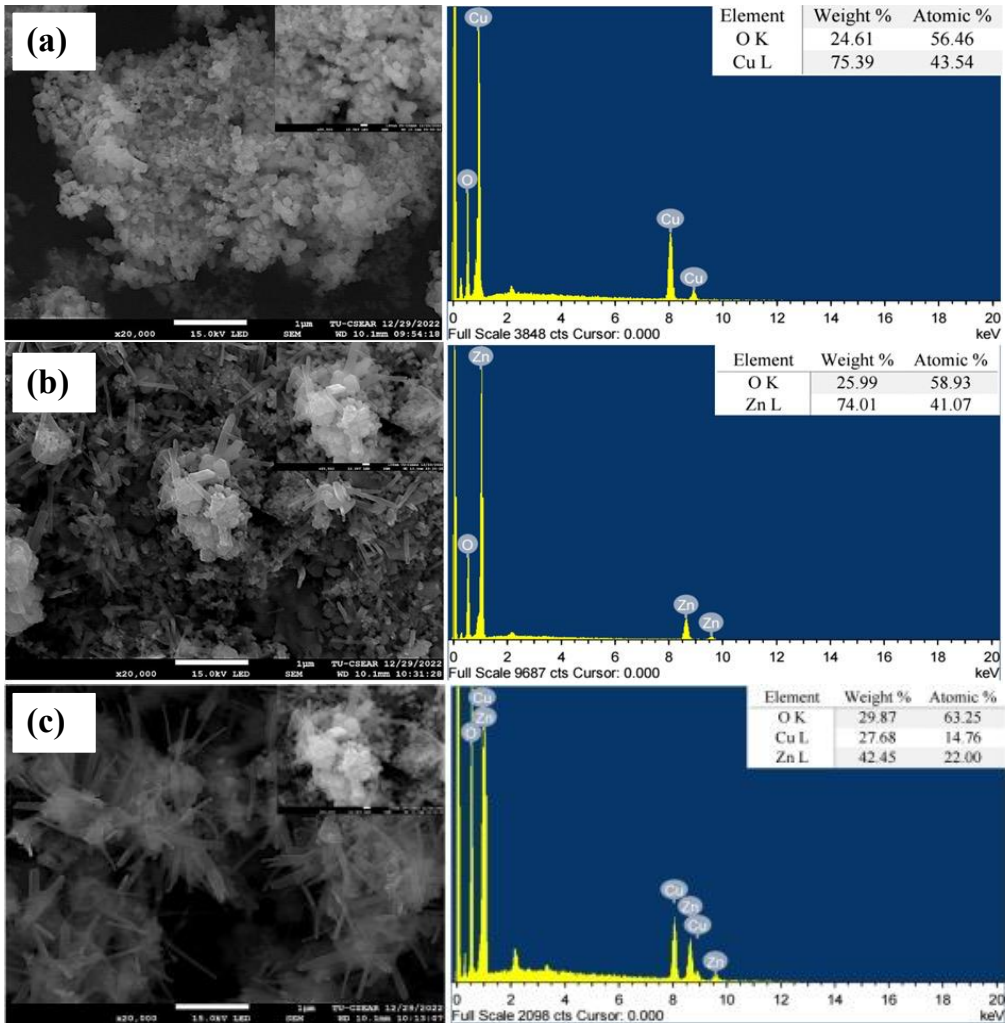

Figure 1. SEM image and confirmation of elemental composition by an elemental analyzer (a) CuO nanoparticles, (b) ZnO nanoparticles and (c) ZnO/CuO nanocomposites.

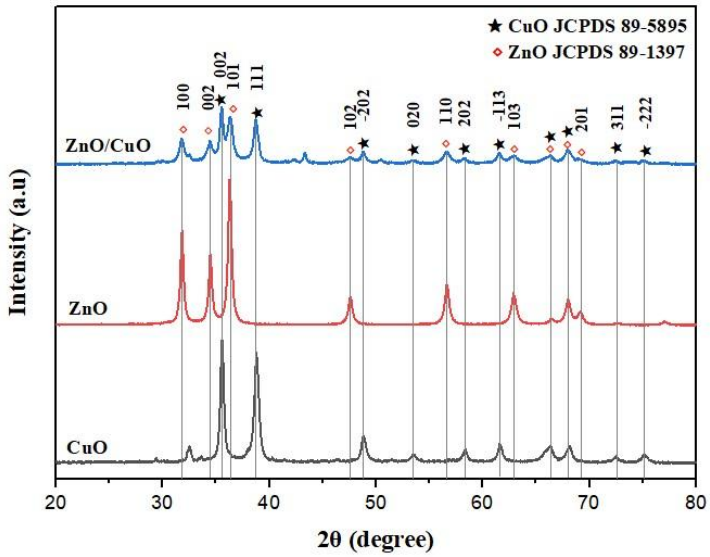

Figure 2. XRD patterns of CuO nanoparticles, ZnO nanoparticles and ZnO/CuO nanocomposites.

Fig. 2 shows the XRD patterns of CuO nanoparticles, ZnO nanoparticles and ZnO/CuO nanocomposites. The CuO nanoparticles exhibited diffraction peaks at 2θ of 35.40°, 38.72°, 48.81°, 53.48°, 58.30°, 61.60°, 66.32°, 68.12°, 72.43° and 75.31° that was related to the (002), (111), (-202), (020), (202), (-113), (-311), (220), (311), and (-222) planes of monoclinic CuO (JCPDS No. 89-5895), respectively. The ZnO nanoparticles showed diffraction peaks at 2θ of 31.73 °, 34.37 °, 36.21°, 47.48 °, 56.53 °, 62.77 °, 66.30 °, 67.86 °, and 69.00 °, which corresponds to the (100), (002), (101), (102), (103), (200), (112), and (201) planes of hexagonal ZnO (JPCDS No. 89-1397), respectively.The XRD patterns of ZnO/CuO nanocompsites showed the presence of ZnO and CuO. According to the XRD results, the other impurities were not present. The average crystallite size was calculated from the equation of Debye-Scherer as equation (2):

$$D = \frac{0.9\lambda}{\beta \cos\theta} \quad (2)$$

where D is the average crystallite size.
λ is the X-ray wavelength (1.54178 Å).
β is the FWHM (Full Width at Half Maximum) of XRD peak.
θ is XRD peak position, one half of 2θ

The average crystallite size of CuO nanoparticles, ZnO nanoparticles and ZnO/CuO nanocomposites were 18.31, 21.14, and 12.52 nm, respectively.

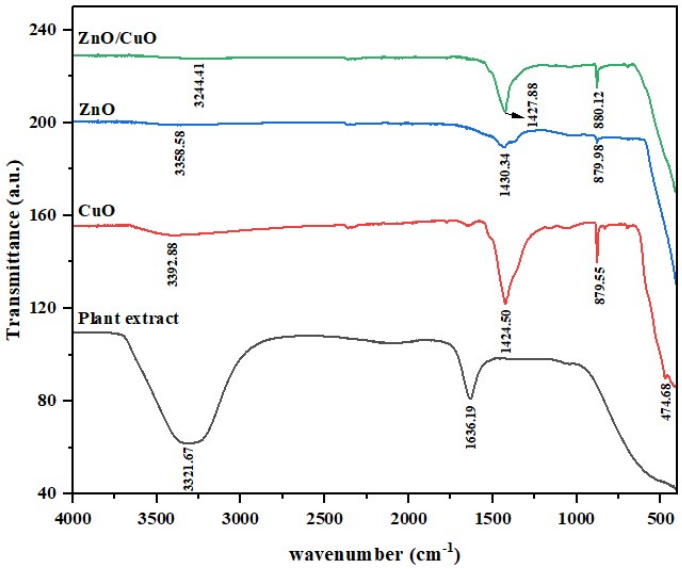

Figure 3 FTIR spectra of plant extract, CuO nanoparticles, ZnO nanoparticles and ZnO/CuO nanocomposites.

Fig. 3 shows FTIR spectra of Kratom leaf extract, CuO nanoparticles, ZnO nanoparticles and ZnO/CuO nanocomposites. Kratom leaf extract shows absorption peaks at positions 3321.67 cm^{-1} and 1636.19 cm^{-1}, which are due to stretching vibrations of the O-H and C=C group, respectively (berra et al., 2018). Metal-oxide absorption bands are located in the fingerprint region, i.e., below 1000 cm^{1}. The strong bands in the range of 400-600 cm1in the current study is attributed to the combined presence of ZnO and CuO (Theivandran et al., 2015) (Petel et al., 2022) (Ghane et al., 2010) (Akkaya et al., 2020).

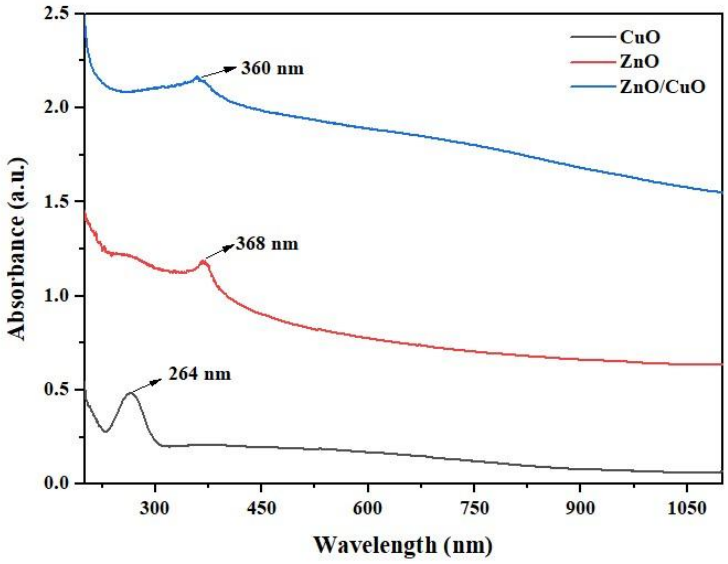

Figure 4 UV-vis spectra of CuO nanoparticles, ZnO nanoparticles and ZnO/CuO nanocomposites.

The UV-Vis spectra of CuO nanoparticles, ZnO nanoparticles and ZnO/CuO nanocomposites were shown in Fig.4. The absorption peaks were at 264, 368 and 360 nm, respectively. These absorption peaks caused by plasmon resonance at the surface of metal oxide.

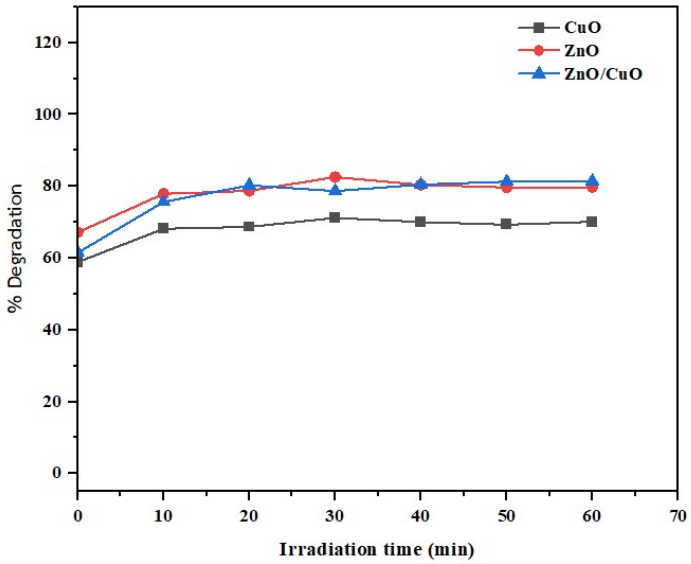

Figure 5 Effect of MB dye degradation on synthesized copper oxide (CuO) nanoparticles, zinc oxide (ZnO) nanoparticles, and zinc oxide (ZnO)-copper oxide (CuO) nanoparticles under ultraviolet light.

Fig. 5 shows the methylene blue dye degradation efficiency of the CuO nanoparticles, ZnO nanoparticles and ZnO/ CuO nanocomposites under ultraviolet light. The results showed that ZnO/CuO nanocomposites had a methylene blue degradation efficiency of 80.821% at 60 min. It was better than CuO and ZnO nanoparticles.

4. Conclusions

In this work, ZnO/CuO nanocomposites at various ratios were synthesized by green synthesis method by using Kratom leaves extract as reducing agent and capping agent. According to the results, the CuO nanoparticles were relatively spherical in shape, while the ZnO nanoparticles were rod-like shape. The ZnO/CuO nanocomposites had a combination of spherical and rod shapes. The crystalline structure of the ZnO/CuO nanocomposites was found to be both CuO and ZnO structures with an average crystallite size of 12.52 nm. The ZnO/CuO nanocomposites exhibited light absorption at a wavelength of 360 nm. When testing the degradation of methylene blue dye under UV light, it was found that the MB dye could degrade 80.821% within 60 min.

5. Acknowledgements

This research was supported by The Science, Research and Innovation Promotion Funding (TSRI) (Grant no. FRB660012/0168). This research block grants was managed under Rajamangala University of Technology Thanyaburi (FRB66E0627).

6. References

Rafiq, A., Ikram, M., Ali, S., Niaz, F., Khan, M., Khan, Q., & Maqbool, M. (2021). Photocatalytic degradation of dyes using semiconductor photocatalysts to clean industrial water pollution. Journal of Industrial and Engineering Chemistry, 97, 111-128.

Khan, I., Saeed, K., Zekker, I., Zhang, B., Hendi, A. H., Ahmad, A., & Khan, I. (2022). Review on methylene blue: its properties, uses, toxicity and photodegradation. Water, 14(2), 242.

Singh, S., Srivastava, V. C., & Mall, I. D. (2013). Mechanism of dye degradation during electrochemical treatment. The Journal of Physical Chemistry C, 117(29), 15229-15240.

Liu, Q. (2020, May). Pollution and treatment of dye waste-water. In IOP Conference Series: Earth and Environmental Science (Vol. 514, No. 5, p. 052001). IOP Publishing.

Bekru, A. G., Tufa, L. T., Zelekew, O. A., Goddati, M., Lee, J., & Sabir, F. K. (2022). Green Synthesis of a CuO–ZnO Nanocomposite for Efficient Photodegradation of Methylene Blue and Reduction of 4-Nitrophenol. ACS omega, 7(35), 30908-30919.

Wang, C., Shi, H., Zhang, P., & Li, Y. (2011). Synthesis and characterization of kaolinite/TiO2 nano-photocatalysts. Applied Clay Science, 53(4), 646-649.

Shubha, J. P., Roopashree, B., Patil, R. C., Khan, M., Shaik, M. R., Alaqarbeh, M., & Adil, S. F. (2023). Facile synthesis of ZnO/CuO/Eu heterostructure photocatalyst for the degradation of industrial effluent. Arabian Journal of Chemistry, 16(3), 104547.

Basit, R. A., Abbasi, Z., Hafeez, M., Ahmad, P., Khan, J., Khandaker, M. U., & Khalid, A. (2023). Successive photocatalytic degradation of methylene blue by ZnO, CuO and ZnO/CuO synthesized from coriandrum sativum plant extract via green synthesis technique. Crystals, 13(2), 281.

Sakib, A. A. M., Masum, S. M., Hoinkis, J., Islam, R., & Molla, M. A. I. (2019). Synthesis of CuO/ZnO nanocomposites and their application in photodegradation of toxic textile dye. Journal of Composites Science, 3(3), 91.

Yu, J., Zhuang, S., Xu, X., Zhu, W., Feng, B., & Hu, J. (2015). Photogenerated electron reservoir in hetero-p–n CuO–ZnO nanocomposite device for visible-light-driven photocatalytic reduction of aqueous Cr (VI). Journal of Materials Chemistry A, 3(3), 1199-1207.

Das, S., & Srivastava, V. C. (2018). An overview of the synthesis of CuO-ZnO nanocomposite for environmental and other applications. Nanotechnology Reviews, 7(3), 267-282.

Duan, H., Wang, D., & Li, Y. (2015). Green chemistry for nanoparticle synthesis. Chemical Society Reviews, 44(16), 5778-5792.

Qamar, H., Rehman, S., Chauhan, D. K., Tiwari, A. K., & Upmanyu, V. (2020). Green synthesis, characterization and antimicrobial activity of copper oxide nanomaterial derived from Momordica charantia. International Journal of Nanomedicine, 2541-2553.

Dubey, M., Bhadauria, S., & Kushwah, B. S. (2009). Green synthesis of nanosilver particles from extract of Eucalyptus hybrida (safeda) leaf. Dig J Nanomater Biostruct, 4(3), 537-543.

Khalil, M. M., Ismail, E. H., El-Baghdady, K. Z., & Mohamed, D. (2014). Green synthesis of silver nanoparticles using olive leaf extract and its antibacterial activity. Arabian Journal of Chemistry, 7(6), 1131-1139.

Sun, Q., Cai, X., Li, J., Zheng, M., Chen, Z., & Yu, C. P. (2014). Green synthesis of silver nanoparticles using tea leaf extract and evaluation of their stability and antibacterial activity. Colloids and surfaces A: Physicochemical and Engineering aspects, 444, 226-231.

Veltri, C., & Grundmann, O. (2019). Current perspectives on the impact of Kratom use. Substance abuse and rehabilitation, 23-31.

Iravani, S. (2011). Green synthesis of metal nanoparticles using plants. Green Chemistry, 13(10), 2638-2650.

Berra, D., Laouini, S. E., Benhaoua, B., Ouahrani, M. R.,Berrani, D., and Rahal, A. (2018). "Green synthesis of copper oxide nanoparticles by Pheonix dactylifera L leaves extract". Digest Journal of Nanomaterials and Biostructures, Vol. 13(4), 1231-1238.

Theivandran, G., Ibrahim, S. M., and Murugan, M. (2015). "Fourier transform infrared (Ft-Ir) spectroscopic analysis of Spirulina fusiformis". Journal of Medicinal Plants Studies, Vol. 3(4), 30-32.

Patel, M., Mishra, S., Verma, R., & Shikha, D. (2022). Synthesis of ZnO and CuO nanoparticles via Sol gel method and Its Characterization by using XRD and FT-IR Analysis.

Ghane, M., Sadeghi, B., Jafari, A. R., & Paknejhad, A. R. (2010). Synthesis and characterization of a Bi-Oxide nanoparticle ZnO/CuO by thermal decomposition of oxalate precursor method.

Akkaya, A., Şahin, B., Aydın, R., Çetin, H., & Ayyıldız, E. (2020). Solution-processed nanostructured ZnO/CuO composite films and improvement its physical properties by lustrous transition metal silver doping. Journal of Materials Science: Materials in Electronics, 31(17), 14400-14410.

Effect of CMC/SBR Binder Content on the Mechanical Properties and Electrochemical Performance of Si/Graphite Anodes in Lithium-Ion Batteries

Voranan Piyavarakorn[a], Komsak Aranmala[a], Jeffrey Nash[a] and Nonglak Meethong[a,b]
[a]*Materials Science and Nanotechnology Program, Department of Physics, Faculty of Science, Khon Kaen University, Muang District 40002, Khon Kaen, Thailand*
[b]*Institute of Nanomaterials Research and Innovation for Energy (IN-RIE), Khon Kaen University, Muang District 40002, Khon Kaen, Thailand*
*Corresponding author's E-mail: nonmee@kku.ac.th

Abstract
Silicon (Si) is a promising active material for anodes in lithium-ion batteries (LIBs). It allows for high capacity that enhances the energy density of LIBs, but high-volume expansion shortens battery life. To avoid this problem, a silicon/graphite composite is a good choice to overcome the volume expansion of silicon. Furthermore, use of a binder is another approach to decrease volume expansion of silicon and enhance battery life. A carboxymethyl cellulose (CMC)/styrene butadiene rubber (SBR) composite is a commercial binder for anodes in water-base systems. Strong covalent bonds of CMC and the flexibility of SBR enhance electrode stability by resisting the volume expansion of silicon. However, excessive amounts of CMC or SBR affect electrode fabrication to produce unfavorable results. In the current work, a pure CMC binder achieved the highest discharge capacity while adding SBR binder reduced discharge capacity. Pure SBR binder had almost no discharge capacity in an Si/graphite anode. Tensile testing show increased flexibility of binder films with higher SBR content. Adding CMC made the binder film more brittle which negatively impacted electrode integrity during rolling tests. We expect that the brittle nature of CMC promotes electrode cracking and peel out from the current collector in sheets. A pure SBR binder demonstrates peeling of the electrode powder from the current collector after a rolling test. CS02 (40% CMC:60% SPR) binder is the most suitable formulation of CMC and SBR. It achieves a balance between flexibility, a medium capacity, and it can be rolled into a cylindrical cell.

Keywords: Lithium-ion battery, Si-graphite anode, Binder, Styrene butadiene rubber, Carboxyl methyl cellulose

1. Introduction
Lithium-ion batteries are widely used for energy storage in electrical devices such as portable electronics, electric vehicles and even in the aerospace field. Their advantages include high specific energy, high working voltage, light weight, long cycle life, small size, and less self-discharge [1-3]. Si is a promising active material for anodes in LIBs due to its high theoretical capacity, 4200 mAh g^{-1}, which is more than ten times that of a conventional active material such as graphite, 372 mAh g^{-1}. However, reactions between Si and Li can form a phase of an $SiLi_x$ alloy, $0 \leq x \leq 4.4$, which results in a large volume expansion of Si during charge-discharge cycling. This causes fracture and pulverization of the Si anode, followed by a loss of contact between active Si materials and conductive additives, bringing about rapid capacity fading and a shortened cycle life [4-6]. A binder plays an important role as a dispersing agent and promoting firm attachment of electrode species to the current collector. Furthermore, an acceptable binder should have good flexibility and strong adhesion to enable electrodes to achieve structural stability and good electrochemical performance [1,7]. Polyvinylidene fluoride (PVDF) is a common binder in LIBs, due to its excellent electrochemical properties, thermal stability, and good adhesion between the electrode species and current collector. However, it is not environmentally friendly. PVDF is dissolved in an organic solvent such as N-methyl-2-pyrrolidone (NMP), N,N-dimethylacetamide (DMAc) and N,N-dimethylformamide (DMF), which are volatile and flammable organic solvents that are harmful to the environment [1,8]. Furthermore, for Si-base anodes, the weak Van der Waals force of PVDF are insufficient to overcome the volume expansion of Si particles during charge-discharge cycling. Thus, there is a sharp initial capacity decline in the first several cycles and corrosion of Si particles due to reactions of the F atoms of the PVDF binder. This results in destruction of the PVDF chain structure leading to poor cycling performance of the Si electrode [9]. Aqueous binders are becoming popular for LIBs due to their low-cost and environmental friendliness. A combination of CMC and SBR can be used in a good aqueous binder due to its excellent chemical and mechanical stability [1,2]. Hochgatterer *et al.* demonstrated outstanding performance of CMC, which can achieve a higher capacity than a commercial PVDF binder in an Si/graphite anode. This is due to an important functional group of the CMC binder, the carboxylic group (-COOH). This group can react with hydroxyl groups (-OH) on the Si particle surfaces to form covalent bonds *via* a condensation mechanism and maintain the long-lasting cycling stability of Si based anodes [10]. Furthermore, a CMC binder enhances distribution and maintenance of structural integrity to a greater degree than a PVDF binder [11,12]. Several researchers investigated the use of SBR, which can serve as an elastomer and dispersing agent providing higher flexibility, stronger binding force, and better heat resistance than PVDF [1,2,13,14]. However, little experimental research has demonstrated the necessity of using SBR, especially to manage stresses that develop during manufacturing processes. Müllner *et al.* showed the role of SBR in terms of cracking and porosity. Increasing the SBR content clearly reduces cracking of an Si-rGO electrode, resulting in a compact and low-porosity coating [15]. However, excessive content of CMC or SBR

can cause electrode brittleness or reduce cohesion of the electrode species, respectively. In this research, we studied the effects of binder content on electrode mechanical properties and electrochemical performance. We found that when using only CMC as a binder, electrode chemical performance is high. However, such electrodes are too brittle, which prevents them from being rolled and packed in a cylindrical battery. Using only SBR as a binder will decrease electrochemical performance of an electrode and also decrease cohesion of the electrode species. From rolling tests, a combination of CMC and SBR is an excellent binder that balances the brittleness of CMC with the flexibility of SBR. It also has strong cohesion to hold the electrode material together and attach to a current collector even after being rolled and packed into a cylindrical battery, while achieving a medium discharge capacity from CMC and SBR composite binder.

2. Methodology

2.1. Binder film preparation

Binder solutions were prepared with various binder contents following Table 1 using DI water as a solvent. Then, the binder solution was poured onto a 1 cm x 2 cm rectangular-shaped mold at a thickness of 0.1-0.2 mm. It was dried at room temperature to obtain binder films for tensile testing.

Formula	Binder (%wt)	
	CMC	SBR
SBR	0	100
CS01	20	80
CS02	40	60
CS03	60	40
CS04	80	20
CMC	100	0

Table 1 Weight ratios of components in binder films.

2.2 Electrode preparation

An electrode slurry was prepared by mixing S420 (active material, BTR, China) and Super P^{TM} (conductive additive, Alfa Aesar) in a microcentrifuge followed by mixing in a horizontal shaker for 30 min. Then, a binder solution was added at the various ratios given in Table 2 and shaking was continued for 30 min to form an electrode slurry. Then, the slurry was cast on copper foil to form electrodes using a doctor blade followed by drying overnight in vacuum at 80 ºC. Coin cell batteries were assembled in an Ar glovebox using Li metal foil as an anode (Alfa Aesar), 1 M LiPF6 dissolved in ethyl carbonate (EC), dimethyl carbonate (DMC) (3:7 in volume), and 10% of fluoroethylene carbonate (FEC) as an electrolyte, and Celgard 2400 as a separator.

Formula	Active material (%wt)	Conductive additive (%wt)	Binder (%wt)	Binder (%wt)	
				CMC	SBR
SBR	80	10	10	0	100
CMC-SBR	80	10	10	40	60
CMC	80	10	10	100	0

Table 2 Weight ratio of components in electrodes.

2.3. Characterization, mechanical property testing, and electrochemical testing

Electrode morphologies were observed using field-emission scanning electron microscopy (FE-SEM, MIRA, TESCAN). Mechanical properties of the binder films were evaluated using a universal testing machine (Zwick/Roell, Z0.5) with a crosshead speed of 100 mm min^{-1}. FT-IR spectra were recorded on a Bruker TENSOR27. Rolling tests were performed to determine the mechanical properties by rolling 1 cm x 4 cm electrodes on a metal rod for 24 hours, then observing crack formation on electrode surfaces. Galvanostatic charge and discharge cycling testing was done on a battery cycler (BST8-MA, MTI) over a voltage range of 0.01−1.50 V at room temperature.

3. Results and Discussion

3.1. Morphological characterization

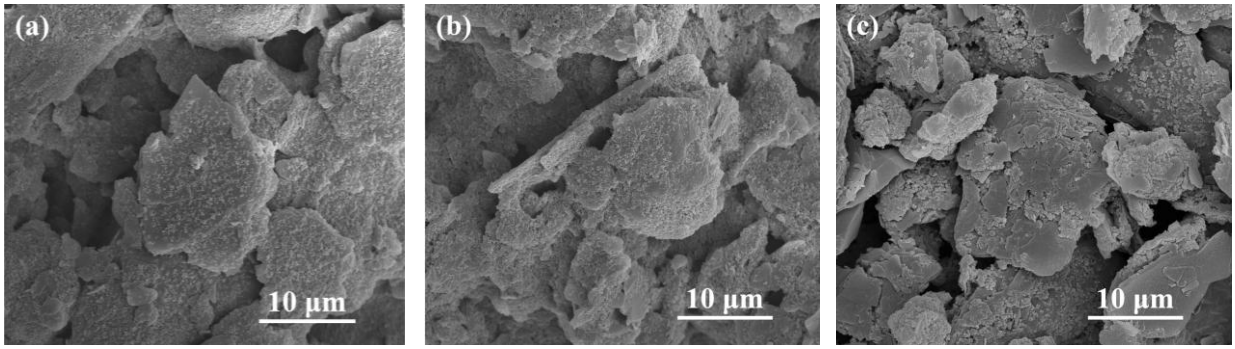

Figure 1. SEM images of Si/graphite electrodes with different binders. (a) CMC, (b) CMC-SBR, and (c) SBR.

The morphology of the Si/graphite electrodes was characterized using SEM and the results are shown in Fig. 1. There is no significant difference in the morphologies of the Si/graphite electrodes with CMC, CMC-SBR, or SBR binders.

3.2 FTIR

Figure 2. FTIR spectra of SBR, CMC and CMC-SBR samples.

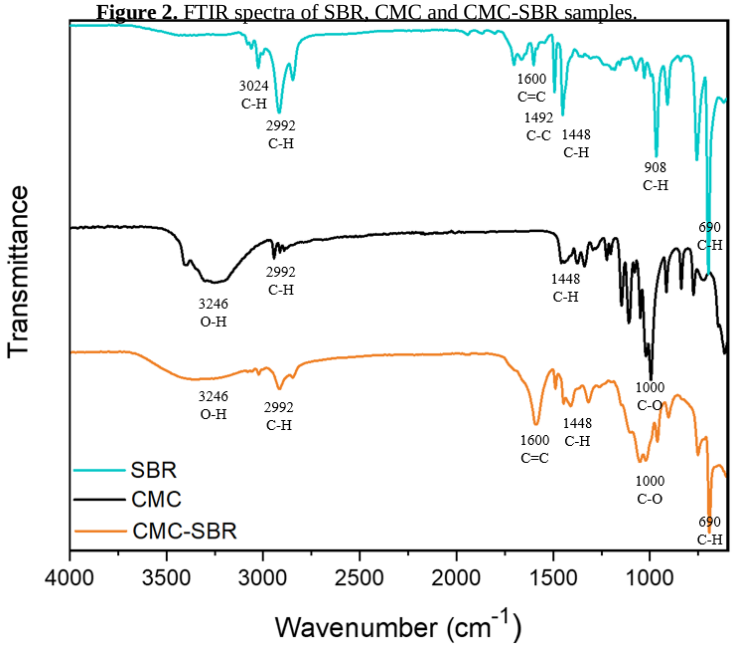

FTIR spectra were used to characterize the CMC, SBR and CMC-SBR samples (Fig. 2). The absorption bands of SBR spectra at 3,024 and 2,992 cm^{-1} correspond to aromatic C–H stretching and alkane C–H stretching, respectively. The peak at 1,600 cm^{-1} is ascribed to C=C stretching vibrations, while the peak at 1,492 cm^{-1} corresponds to aromatic C-C stretching. The peaks at 1,448, 908 and 690 cm^{-1} are ascribed to C–H bending and monosubstituted benzene [16]. For CMC and CMC-SBR samples, the broad peak at 3246 cm^{-1} is due to O-H stretching of CMC, while the peak at 2992 cm^{-1} corresponds to alkane C-H stretching. The peak at 1448 cm^{-1} corresponds to C-H bending, and the peak at 1000 cm^{-1} is ascribed to C-O stretching of CMC. Only CMC-SBR has peaks at 1600 and 690 cm^{-1} corresponding to C=C stretching vibrations, C-H bending and monosubstituted benzene from SBR. This examination confirms the characteristics of CMC and SBR in CMC-SBR binder, but there is no crosslinking between these polymer binders.

3.3 Tensile testing

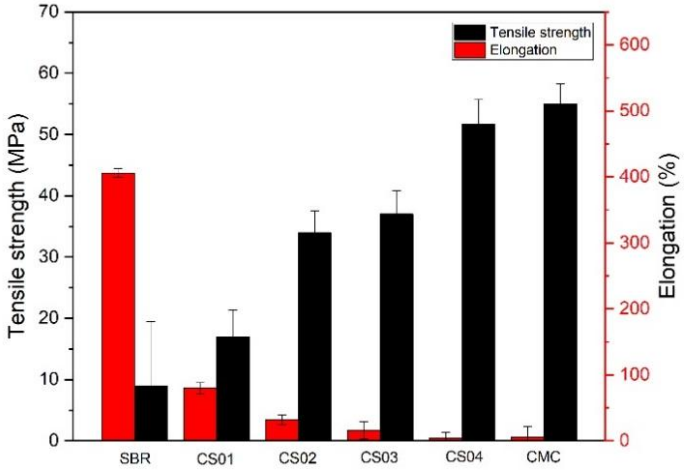

Figure 3. Tensile strength and elongation of binder films with varied ratios of CMC and SBR.

Mechanical properties of binder films are shown in Fig. 3. This figure shows the results of varying binder content on the tensile strength and elongation of binder films. These results demonstrate the brittle property of CMC with its maximal tensile strength of 55 MPa and lowest elongation of 6%. However, the SBR film achieve the lowest tensile strength, 9 MPa and maximal elongation of 406%. Therefore, a combination of CMC and SBR is expected to balance the tensile strength and elongation of binder polymers. Tensile strength of binder films became lower when the CMC content was decreased, while elongation of binder films became higher when the SBR content was increase. Balancing tensile strength and elongation is advantageous for electrodes that are to be used in cylindrical batteries. This is because rolling electrodes for packaging into cylindrical cells can create stresses inside materials resulting in cracking of electrode surfaces and loss of electrical conductivity. CS02 is an optimal formulation to balance the tensile strength and elongation of binder films.

3.4. Rolling testing

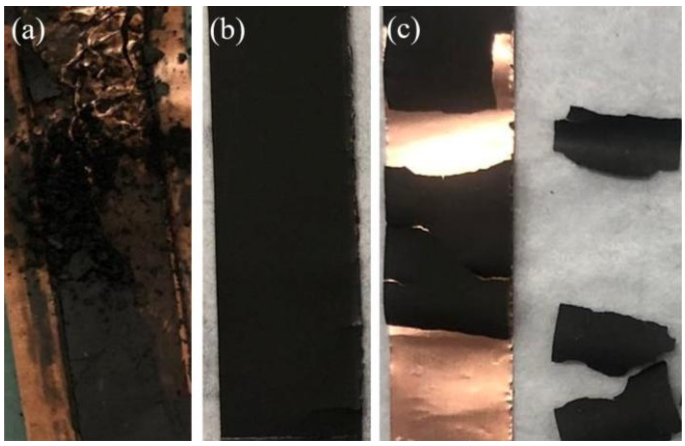

Figure 4. Electrodes with (a) SBR, (b) CMC-SBR, (c) CMC binders 24 hours after rolling.

The effects upon electrodes after being rolled for 24 hours is shown in Fig. 4. Figure 4a demonstrates peeling of some electrode powder due to a lack of CMC that makes electrode materials incohesive with subsequent breakage and separation from the electrode during the rolling test. Figure 4c shows cracking and peeling of electrodes from a current collector. CMC presents strong attachment between electrode components. However, its brittleness did not support electrode rolling due to its cracking and peeling from the current collector. We selected formulation CS02 from Table 1 for the rolling test as it can provide a balance between flexibility and brittleness in the binder film. After a rolling test, Figure 4b shows a smooth electrode that could attach to the current collector with no peeling or cracking. This rolling test achieved its purpose of demonstrating the effect of CMC/SBR content on electrode elasticity when rolling an electrode into a cylindrical battery.

3.5. Electrochemical testing

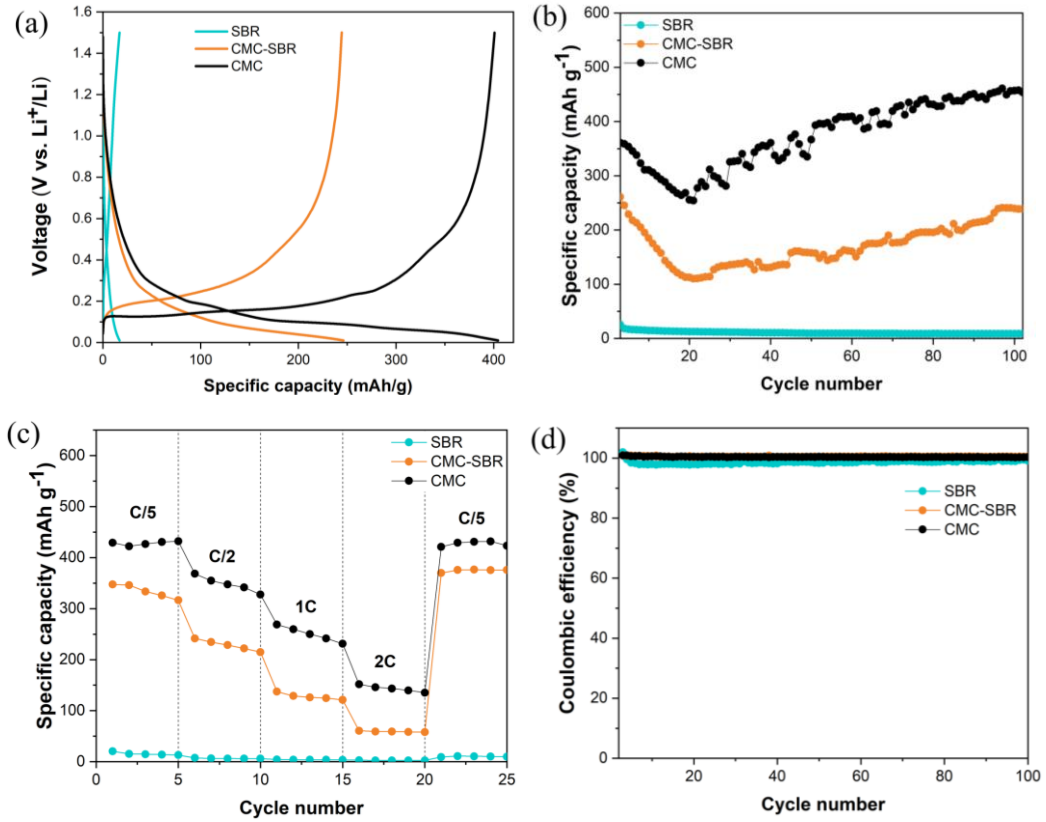

Figure 5. Electrochemical performance of Si/graphite anodes with SBR, CMC-SBR, CMC binders. (a) Initial charge/discharge profiles of electrodes at a rate of C/2. (b) Cycling performance of electrodes at a rate of C/2 for 100 cycles. (c) Rate performance of electrodes ranging from C/5 to 2C. (d) Coulombic efficiencies.

Galvanostatic charge/discharge tests were done over a voltage range of 0.01−1.5 V. Figure 5a shows voltage profiles of electrodes at a C/2 rate with a plateau at ~0.11 V, which may be due to the formation of a solid electrolyte interphase (SEI) film during insertion of Li+ into the Si/graphite anode material [7]. We selected the CS02 formulation from Table 1 to clearly demonstrate the electrochemical effects from CMC and SBR binders. This was to achieve a balance between flexibility and brittleness in the binder film. Figure 5b shows long cycling behaviours of electrodes at C/2. From this graph, SBR shows zero discharge capacity from the first cycle, which means that using only SBR as a binder would give poor electrochemical performance. After 100 cycles, CMC achieved the highest discharge capacity, 457 mAh g^{-1}, caused by strong covalent bonding between -COOH, -OH groups of CMC and other materials. This decreased the volume expansion effect of Si. For a CMC-SBR binder at 100 cycles, a discharge capacity of 393 mAh g^{-1} was observed due to the effects of SBR, which decreased discharge capacity from that of CMC. Figure 5c shows the rate performance of electrodes with various binders. CMC achieved the highest discharge capacity at all rates, while CMC-SBR had a lower discharge capacity. SBR shows zero discharge capacity from the first cycle. In Figure 5d, CMC and CMC-SBR electrodes displayed excellent Coulombic efficiency, 100%, from the first cycle until 100 cycles. SBR shows a Coulombic efficiency of around 98-99% at 100 cycles.

4. Conclusions

We studied the behaviours of CMC-SBR binders for Si/graphite anodes in LIBs with varied proportions of CMC and SBR and evaluated their effects on the mechanical properties and electrochemical performance. A combination of CMC and SBR showed decreased discharge capacity compared to CMC. Tensile testing show that CS02 is an optimal ratio which can balance the tensile strength and elongation of binder film during rolling tests. The brittleness of pure CMC made the electrodes unsuitable for rolling and packing into cylindrical battery cells. So, the flexibility of SBR is necessary for electrode fabrication for LIBs in cylindrical cells. CS02 demonstrated smooth electrodes 24 hours after a rolling test due to its balance between the tensile strength and elongation of the binder.

5. Acknowledgements

This work was supported by the Institute of Nanomaterials Research and Innovation for Energy (IN-RIE), Khon Kaen University, Thailand.

6. References

Wang, R., Feng, L., Yang, W., Zhang, Y., Zhang, Y., Bai, W., ... & Guan, H. (2017). Effect of different binders on the electrochemical performance of metal oxide anode for lithium-ion batteries. *Nanoscale research letters*, *12*, 1-11.

Zhang, R., Yang, X., Zhang, D., Qiu, H., Fu, Q., Na, H., ... & Wei, Y. (2015). Water soluble styrene butadiene rubber and sodium carboxyl methyl cellulose binder for $ZnFe_2O_4$ anode electrodes in lithium ion batteries. *Journal of Power Sources*, 285, 227-234.

Lee, K., Lim, S., Go, N., Kim, J., Mun, J., & Kim, T. H. (2018). Dopamine-grafted heparin as an additive to the commercialized carboxymethyl cellulose/styrene-butadiene rubber binder for practical use of SiO_x/graphite composite anode. *Scientific reports*, *8*(1), 11322.

Hu, S., Cai, Z., Huang, T., Zhang, H., & Yu, A. (2019). A modified natural polysaccharide as a high-performance binder for silicon anodes in lithium-ion batteries. *ACS applied materials & interfaces*, 11(4), 4311-4317.

Liu, J., Zhang, Q., Zhang, T., Li, J. T., Huang, L., & Sun, S. G. (2015). A robust ion- conductive biopolymer as a binder for Si anodes of lithium- ion batteries. *Advanced Functional Materials*, 25(23), 3599-3605.

Yim, C. H., Courtel, F. M., & Abu-Lebdeh, Y. (2013). A high capacity silicon–graphite composite as anode for lithium-ion batteries using low content amorphous silicon and compatible binders. *Journal of Materials Chemistry A*, 1(28), 8234-8243.

Yu, L. M., Luo, Z., Gong, C. R., Zheng, Y. Q., Zhou, Z. X., Zhao, H., & Xu, Y. (2021). Water-based binder with easy reuse characteristics for silicon/graphite anodes in lithium-ion batteries. *Polymer Journal*, 53(8), 923-935.

Pace, G. T., Wang, H., Whitacre, J. F., & Wu, W. (2021). Comparative study of water- processable polymeric binders in $LiMn_2O_4$ cathode for aqueous electrolyte batteries. *Nano Select*, 2(5), 939-947.

Huang, W., Wang, W., Wang, Y., Qu, Q., Jin, C., & Zheng, H. (2021). Overcoming the fundamental challenge of PVDF binder use with silicon anodes with a super-molecular nano-layer. *Journal of Materials Chemistry A*, 9(3), 1541-1551.

Hochgatterer, N. S., Schweiger, M. R., Koller, S., Raimann, P. R., Wöhrle, T., Wurm, C., & Winter, M. (2008). Silicon/graphite composite electrodes for high-capacity anodes: influence of binder chemistry on cycling stability. *Electrochemical and solid-state letters*, 11(5), A76.

Zuo, P., Yang, W., Cheng, X., & Yin, G. (2011). Enhancement of the electrochemical performance of silicon/carbon composite material for lithium ion batteries. *Ionics*, 17, 87-90.

Lim, S., Kim, S., Ahn, K. H., & Lee, S. J. (2015). The effect of binders on the rheological properties and the microstructure formation of lithium-ion battery anode slurries. *Journal of Power Sources*, 299, 221-230.

Yan, X., Zhang, Y., Zhu, K., Gao, Y., Zhang, D., Chen, G., ... & Wei, Y. (2014). Enhanced electrochemical properties of TiO_2 (B) nanoribbons using the styrene butadiene rubber and sodium carboxyl methyl cellulose water binder. *Journal of Power Sources*, 246, 95-102.

Yen, J. P., Lee, C. M., Wu, T. L., Wu, H. C., Su, C. Y., Wu, N. L., & Hong, J. L. (2012). Enhanced high-temperature cycle-life of mesophase graphite anode with styrene–butadiene rubber/carboxymethyl cellulose binder. *ECS Electrochemistry Letters*, 1(6), A80.

Müllner, S., Michlik, T., Reichel, M., Held, T., Moos, R., & Roth, C. (2023). Effect of Water-Soluble CMC/SBR Binder Ratios on Si-rGO Composites Using µm-and nm-Sized Silicon as Anode Materials for Lithium-Ion Batteries. *Batteries*, 9(5), 248.

Zhang, J., Chen, H., Zhou, Y., Ke, C., & Lu, H. (2013). Compatibility of waste rubber powder/polystyrene blends by the addition of styrene grafted styrene butadiene rubber copolymer: effect on morphology and properties. Polymer *Bulletin*, 70, 2829-2841.

The Efficiency of Mild Alkaline Pretreatment on Papyrus Fibers for Cellulose Nanofibril Isolation

Pitiporn Manokhoon[a] and Thaneeya Rangseesuriyachai[b*]

[a]*Engineering Field of Study, Faculty of Engineering, Rajamangala University of Technology Thanyaburi, Pathum Thani 12110, Thailand*
[b]*Faculty of Engineering, Rajamangala University of Technology Thanyaburi, Pathum Thani 12110, Thailand*
*Corresponding author. Tel. (+66)81-733-9150; *E-mail address:* thaneeya.r@en.rmutt.ac.th

Abstract

Papyrus is a wetland plant that stands out as a highly productive source of lignocellulosic materials. This plant has immense potential for generating cellulose fibers to cater to various applications. The conversion of lignocellulosic plants into nanocellulose fibers typically involves multiple processes such as mechanical pretreatment, chemical pretreatment, bleaching, and isolation. The results showed that Ca(OH)2 pretreatment has the ability pretreatment to recovery cellulose. The pretreatment increased the cellulose content by 20% and markedly ruptured the plant cell wall components. SEM images showed the smooth and distinct fiber shapes caused by fractures compared with native papyrus. The result of XRD indicated that fibers are in an amorphous region and crystallinity. Nanocellulose-based materials are utilized in the field of research and development for a range of water and wastewater treatment applications, including but not limited to oil adsorption, heavy metal removal, coating of reverse osmosis membranes, and other relevant applications within the realm of environmental engineering.

Keywords: Mild Alkaline, Papyrus, Cellulose Nanofibril, TEMPO-Oxidation

1. Introduction

Cellulose, the most abundant organic compound on earth, is a naturally occurring polymer found in the cell walls of plants. Its versatile nature makes it a valuable resource in various domains, including materials, advanced technology, medical and personal care, environmental concerns, and the food industry (Gilfillan, Moghaddam, & Doherty, 2014; Rana, Mostafavi, Alsanie, Siwal, & Thakur, 2023; Bhat, Dasan, Khan, & Jawaid, 2017). The structural stability and rigidity of cellulose arise from the formation of beta-1,4 glycosidic bonds that link the linear chains of glucose monomers (Rana et al., 2021). In wetlands, the Papyrus Cyperus plant stands out as a highly productive source of lignocellulosic materials. This plant has immense potential for generating cellulose fibers to cater to various applications. The process involves mild aqueous oxidation mediated by TEMPO (2,2,6,6-tetramethylpiperidine-1-oxyl radical), followed by moderate mechanical treatment (Isogai, Saito, & Fukuzumi, 2011).

The conversion of lignocellulosic plants into nanocellulose fibers typically involves multiple processes such as mechanical pretreatment, chemical pretreatment, bleaching, and isolation. The efficiency of pretreatment plays a crucial role in the successful synthesis of nanocellulose. Among the various pretreatment methods, chemical pretreatment is highly preferred as it effectively breaks down the strong bonds present in lignocellulosic materials. Alkaline solutions are particularly favored for their gentler nature compared to acidic solutions. Sodium hydroxide (NaOH) is commonly employed as a reagent for the pretreatment process to remove lignin from cellulose fibers. It efficiently breaks down and dissolves lignin, leaving behind cellulose. However, the use of NaOH has environmental drawbacks (J. S. Kim, Lee, & Kim, 2016). As an alternative reagent, calcium hydroxide $Ca(OH)_2$ has gained attention due to its low energy requirements (Riadi, Hansen, Pratiwi, & Purwanto, 2020), simplicity, low cost (T. H. Kim, 2013), and effectiveness in treating various lignocellulosic materials such as sugarcane bagasse (Riadi, Hansen, Pratiwi, & Purwanto, 2020), giant reed (Jiang et al., 2017), maize straw, grass (from landscape, extensive management), and sprout stem (Brassica oleracea convar. oleracea var. gemmifera) (Khor, Rabaey, & Vervaeren, 2015).

This study aims to investigate the potential of chemically pretreating papyrus to enable its synthesis into nanofibers. The use of $Ca(OH)_2$ as a pretreatment agent is chosen due to its simplicity, cost-effectiveness, and environmentally friendly nature. The resulting product holds promise for various applications in environmental engineering, including water and wastewater treatment, as well as other potential uses. The properties of nanocellulose are subject to influence from a range of factors, including the type of fiber, ecological circumstances, methods employed in manufacturing, and any modifications made to the surface of the fiber. Nanocellulose-based materials find application in the research and development of various technologies, including solar cells, transistors,

touchscreens, supercapacitors, skin electronics, photodetectors, biomedical applications, and water treatment (Khalid M. Y., et al., 2021).

2. Materials and Methods

This study was to investigate the feasibility of pretreatment with a mild alkaline solution to produce nanocellulose from Egyptian papyrus and to synthesize it with TEMPO-oxidation. Research materials and methodology were described as follows:

2.1. Materials

Papyrus (Cyperus papyrus L.) was harvested after 3 months of planting, separated into culm and umbel. Papyrus was dried at 60 °C for 24 hr, milled and sieved through mesh no. 60-100 and keep in plastic bags. Reagents in this research were purchased from Sigma-Aldrich as 2,2,6,6-tetramethylpiperidine-1-oxyl (TEMPO), hydrogen peroxide, sodium hypochlorite (6% w/v) and sodium borohydride from LOBA.

2.2. Methods

2.2.1 Isolation of cellulose nanofibers (CNFs): this procedure consists of three-step processes as shown below:

- First step: alkaline pretreatment

Alkaline pretreatment was conducted with $Ca(OH)_2$ 5% (w/v) concentration as mild alkaline chemicals. The papyrus sample 20 g was mixed with alkali dilution at a 1:30 (solid to liquid ratio), then stirred at 200 rpm at 70 ± 2 °C for 2 hr. Finally, the solid fraction was rinsed with DI water until it reached a neutral pH.

- Second step: pulping and bleaching

In this step, 10 g dry weight of papyrus was suspended in 4% (w/w) NaOH 200 ml (1:20 solid to liquid ratio) and slowly add 200 ml 7% (w/w) H_2O_2. Stirred at 500 rpm and heated at 70 ± 2 °C for 1 hr. After that filtrated and rinsed with DI water until neutral pH. Finally, biomass was dried at 60 °C for 24 hr, milled, and kept in a plastic bag.

- Third step: CNFs isolation

TEMPO-Oxidation was prepared with 5 g dry weight of papyrus soaked in DI water for 24 hr to obtain the CNFs a grinder in a high-speed blender was used at 24,000 rpm for 10 min (divided into two steps of 5 min interspersed with 5 min intervals) (see fig. 1) add 0.08 g TEMPO, 0.5 g NaBr and 50 mmol of 6% NaClO and adjusted pH about 10.5 by NaOH or HCl (Pinto, Bernardes, & Rezende, 2019). Stirred at 200 rpm at room temperature was finally rinsed with DI water and was centrifuged at 5000 rpm until constant conductivity and kept in the refrigerator.

2.2.2 Chemical Composition

The chemical composition of cellulose fibers for raw papyrus, after pretreatment and pulping, and bleaching was determined by using the standard Technical Association of the Pulp and Paper Associations (TAPPI). The TAPPI standard procedures T222 om-88 were used for the lignin test method and standard procedures T203 om-88 were the cellulose and hemicellulose test methods (Ben Arfi, Karoui, Mougin, & Ghorbal, 2017).

2.2.3 Characterization

The crystalline index of raw papyrus, after pretreatment and after pulping and bleaching processes was observed by XRD analysis (Empyrean, Mavern Panalytical, Malvern, UK). The measurements were carried out with CuKα radiation at 40 kV. The analysis was performed with a 2θ diffraction angle of 10°-45° 2θ. From the intensity of the peaks, the crystalline index (CrI) was estimated using the peak height method that has been widely used for the study of the crystallinity of native cellulose, followed by Eq. (1) (Terinte, Ibbett, & Schuster, 2011):

$$CrI(\%) = \frac{I_{(002)} - I_{(101)}}{I_{(002)}} \times 100 \quad (1)$$

Where $I_{(002)}$ is the maximum intensity of the peak corresponding to the plane in the sample at a diffraction angle of 25°-30° 2θ and $I_{(101)}$ is the intensity of the peak at a diffraction angle of 18°-22° 2θ.

The surface morphology of untreated, after pretreatment and after pulping and bleaching was observed using SEM (Scanning Electron Microscope), JEOL JSM-5410LV (Tokyo, Japan). Cellulose nanofiber isolation was observed

by TEM (Transmission Electron Microscopy): JEOL (JEM-2010, Japan) is a high-resolution electron microscope operating at 200 kV.

3. Results and Discussion

3.1. Chemical Composition

A comparative analysis of the chemical composition highlights notable variations among raw papyrus, post $Ca(OH)_2$ pretreatment, and following the pulping and bleaching processes, as demonstrated in Table 1. The findings revealed a notable increase in cellulose content during the pretreatment process, contributing to the enhancement of fiber physical properties in the subsequent pulping and bleaching stages. Furthermore, compared to raw papyrus, the process exhibited high efficiency in the removal of hemicellulose and lignin. Alkali pretreatment, facilitated by hydroxyl ions, induces cellulose swelling, which disrupts intermolecular hydrogen bonds between cellulose and hemicellulose. This, in turn, leads to substantial hemicellulose solubilization in the aqueous solution, leaving behind a solid residue enriched with cellulose (Bian et al., 2012). Mild alkali treatment using $Ca(OH)_2$ has been reported to cause a significant 20-40% hemicellulose dissolution, 60-80% delignification, and de-acetylation (J. S. Kim et al., 2016). This simple and cost-effective process makes it an appealing option for pretreatment (T. H. Kim, 2013).

Table 1 Composition percentages of cellulose, hemicellulose, lignin, and other components in papyrus, both after the pretreatment process and subsequent pulping and bleaching processes.

Parameter (%)	Raw Papyrus	after the pretreatment process	after the pulping and bleaching processes
Cellulose	31.12 ± 0.54	38.87 ± 0.54	41.24 ± 0.27
Hemicellulose	13.14 ± 0.71	4.08 ± 0.42	1.57 ± 0.12
Lignin	19.21 ± 0.59	10.56 ± 0.24	8.40 ± 0.47
Other	36.53 ± 1.89	46.48 ± 0.16	48.80 ± 0.71

3.2 Characterization

3.2.1 Surface Morphology and Structural Analysis

In this study, the morphology of raw papyrus was examined at different stages, including pretreatment, pulping, and bleaching, as depicted in Figure 1. Scanning electron microscopy (SEM) images provided valuable insights into the surface morphology of raw papyrus. The images revealed that the fibers had a globular appearance, accompanied by noticeable impurity deposits on the surface (Fig 1A). Upon pretreatment, the surface of the papyrus exhibited increased rigidity and enhanced structural integrity compared to the hydrolyzed and bleached biomass. Fig 1B and 1C depict the surfaces of pretreated papyrus and papyrus subjected to the pulping and bleaching processes, utilizing a 5% calcium hydroxide chemical treatment. It is expected that these treatments would further enhance the rigidity and structural integrity of the papyrus surface compared to the hydrolyzed and bleached biomass. The pretreatment process is typically employed to modify the properties of papyrus fibers or eliminate impurities. This can involve various methods, including mechanical refining, chemical treatments, or enzymatic processes. Following that, appropriate raw materials were utilized for the synthesis of cellulose nanofibrils (CNFs). Fig. 2 showcases the morphology of CNFs derived from papyrus through TEMPO-oxidation, as observed through TEM analysis. Notably, in terms of nanofibril production, the source of cellulose's anatomical origin proves to be crucial during TEMPO-mediated oxidation and blending. The impact of TEMPO-oxidation on cellulose fibers involves subjecting them to selective oxidation of primary alcohol groups, resulting in the formation of carboxyl groups. This oxidation reaction takes place under mild conditions and is typically conducted in the presence of sodium hypochlorite (NaClO) and sodium bromide (NaBr) as co-reactants (Isogai et al., 2011).

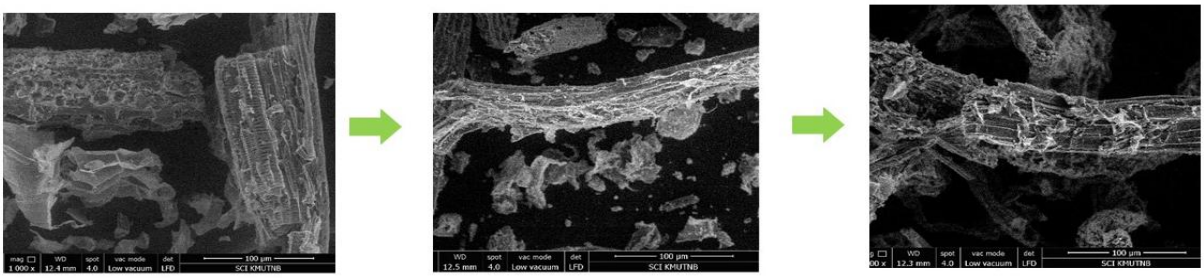

(A) Raw Papyrus (B) Pretreatment (C) Pulping and bleaching

Figure. 1 SEM image of raw material preparation process for nanocellulose synthesis from papyrus (A) raw papyrus, (B) pretreatment and (C) pulping and bleaching.

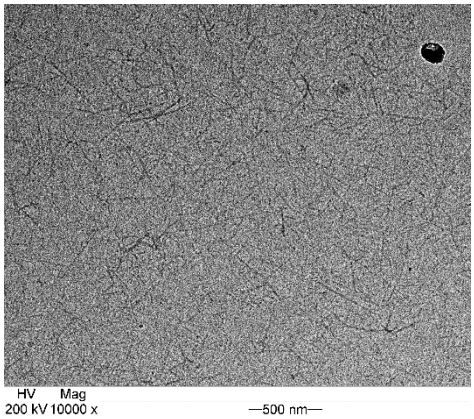

Figure. 2 TEM image of papyrus after TEMPO-oxidation synthesis process.

3.2.2 Crystallinity of Papyrus

Figure 3 displays the XRD patterns of both raw papyrus and CNFs papyrus. The spectra exhibited prominent peaks at approximately 2θ diffraction angles of 15°, 22°, and 34°, corresponding to the 101, 002, and 040 lattice planes, respectively (El Oudiani, Chaabouni, Msahli, & Sakli, 2011). Specifically, the peak at 22° 2θ indicated the presence of the crystalline phase of cellulose, while the peaks at 15° and 34° 2θ represented the amorphous phases of cellulose (Galiwango, Abdel Rahman, Al-Marzouqi, Abu-Omar, & Khaleel, 2019), encompassing substances such as lignin, hemicellulose, pectins, and amorphous cellulose. These peaks, along with their associated lattice planes, provide valuable insights into the crystal structure of the investigated material. Both raw papyrus and CNFs papyrus predominantly exhibited the cellulose I polymorph, as evidenced by the major peaks at 15° and 22° 2θ for the 101 and 002 lattice planes, respectively, unlike cellulose II, where the major peak occurs at 20° and 22° 2θ (El Oudiani et al., 2011). The diffraction pattern of cellulose typically displays peaks at various angles, and the specific peaks and their intensities can vary based on factors such as sample crystallinity, cellulose source, and any modifications or treatments applied to the cellulose. The crystallinity index (CI) was calculated for the cellulose samples using the formula given in Eq. (1). In this case, the reported crystallinity index of 59.16% indicates that the CNFs obtained from papyrus exhibit a relatively high level of crystallinity compared to raw papyrus, which has a crystallinity index of 39.68%. This suggests the presence of a significant amount of organized and ordered cellulose structure within the nanofibers.

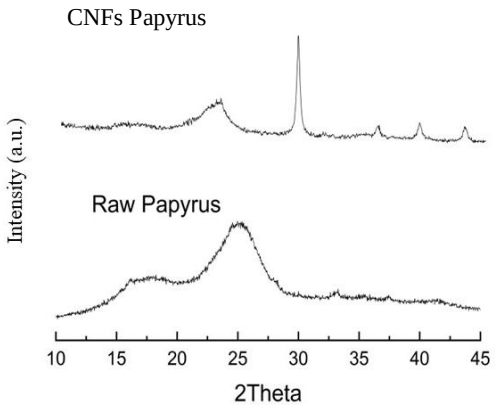

Figure 3. The XRD spectra of raw papyrus and CNFs papyrus.

4. Conclusions

In this study, nanocellulose fibers were synthesized from papyrus. By evaluating the feasibility of using $Ca(OH)_2$ as a pretreatment before synthesis with TEMPO-oxidation. The results show the successfully environmental process for nanomaterial isolation. The pretreatment increased the cellulose content by 20% and markedly ruptured the plant cell wall components. The crystallinity of the obtained nanofibrils was 59%. This research reduces the use of harsh chemicals in the production of nanocellulose. This substance has the potential to be utilized as a biomaterial for the purpose of bio-absorption in future environmental remediation efforts.

5. Acknowledgements

The authors express their gratitude to the Faculty of Engineering at Rajamangala University of Technology Thanyaburi and the Faculty of Engineering and Architecture at Rajamangala University of Technology Suvanabhumi, located in Thailand, for their generous financial assistance and provision of experimental resources in relation to this research.

6. References

Ben Arfi, R., Karoui, S., Mougin, K., & Ghorbal, A. (2017). Adsorptive removal of cationic and anionic dyes from aqueous solution by utilizing almond shell as bioadsorbent. Euro-mediterranean journal for environmental integration, 2, 1-13.

Bhat, A., Dasan, Y., Khan, I., & Jawaid, M. (2017). Cellulosic biocomposites: Potential materials for future. Green Biocomposites: Design and Applications, 69-100.

Bian, J., Peng, F., Peng, X.-P., Peng, P., Xu, F., & Sun, R.-C. (2012). Acetic acid enhanced purification of crude cellulose from sugarcane bagasse: structural and morphological characterization. BioResources, 7(4).

de Morais Teixeira, E., Bondancia, T. J., Teodoro, K. B. R., Corrêa, A. C., Marconcini, J. M., & Mattoso, L. H. C. (2011). Sugarcane bagasse whiskers: extraction and characterizations. Industrial crops and products, 33(1), 63-66.

El Oudiani, A., Chaabouni, Y., Msahli, S., & Sakli, F. (2011). Crystal transition from cellulose I to cellulose II in NaOH treated Agave americana L. fibre. Carbohydrate Polymers, 86(3), 1221-1229.

Galiwango, E., Abdel Rahman, N. S., Al-Marzouqi, A. H., Abu-Omar, M. M., & Khaleel, A. A. (2019). Isolation and characterization of cellulose and α-cellulose from date palm biomass waste. Heliyon, 5(12), e02937. doi:https://doi.org/10.1016/j.heliyon.2019.e02937

Gilfillan, W. N., Moghaddam, L., & Doherty, W. O. (2014). Preparation and characterization of composites from starch with sugarcane bagasse nanofibres. Cellulose, 21, 2695-2712.

Isogai, A., Saito, T., & Fukuzumi, H. (2011). TEMPO-oxidized cellulose nanofibers. nanoscale, 3(1), 71-85.

Jiang, D., Ge, X., Zhang, Q., Zhou, X., Chen, Z., Keener, H., & Li, Y. (2017). Comparison of sodium hydroxide and calcium hydroxide pretreatments of giant reed for enhanced enzymatic digestibility and methane production. Bioresource technology, 244, 1150-1157.

Khalid, M. Y., Rashid, A. Al, Arif, Z. U., Ahmed, W., and Arshad H. (2021). Recent advances in nanocellulose-based different biomaterials: types, properties, and emerging applications. Journal of Materials Research and Technology. 14, 2601-2623.

Khor, W. C., Rabaey, K., & Vervaeren, H. (2015). Low temperature calcium hydroxide treatment enhances anaerobic methane production from (extruded) biomass. Bioresource technology, 176, 181-188.

Kim, J. S., Lee, Y., & Kim, T. H. (2016). A review on alkaline pretreatment technology for bioconversion of lignocellulosic biomass. Bioresource technology, 199, 42-48.

Kim, T. H. (2013). Pretreatment of lignocellulosic biomass. Bioprocessing technologies in biorefinery for sustainable production of fuels, chemicals, and polymers, 91-110.

Nicu, R., Ciolacu, F., & Ciolacu, D. E. (2021). Advanced functional materials based on nanocellulose for pharmaceutical/medical applications. Pharmaceutics, 13(8), 1125.

Pinto, L. O., Bernardes, J. S., & Rezende, C. A. (2019). Low-energy preparation of cellulose nanofibers from sugarcane bagasse by modulating the surface charge density. Carbohydrate Polymers, 218, 145-153.

Rana, A. K., Gupta, V. K., Saini, A. K., Voicu, S. I., Abdellattifaand, M. H., & Thakur, V. K. (2021). Water desalination using nanocelluloses/cellulose derivatives based membranes for sustainable future. Desalination, 520, 115359. doi:https://doi.org/10.1016/j.desal.2021.115359

Rana, A. K., Mostafavi, E., Alsanie, W. F., Siwal, S. S., & Thakur, V. K. (2023). Cellulose-based materials for air purification: A review. Industrial crops and products, 194, 116331. doi:https://doi.org/10.1016/j.indcrop.2023.116331

Riadi, L., Hansen, Y., Pratiwi, J., & Purwanto, M. G. M. (2020). Mild alkaline pretreatment on sugarcane bagasse: effects of pretreatment time and lime to dry bagasse ratio. Proceedings of the Pakistan Academy of Sciences: Pakistan Academy of Sciences B. Life and Environmental Sciences, 57(1), 43-50.

Terinte, N., Ibbett, R., & Schuster, K. C. (2011). Overview on native cellulose and microcrystalline cellulose I structure studied by X-ray diffraction (WAXD): Comparison between measurement techniques. Lenzinger Berichte, 89(1), 118-131.

Alternative Procedures for Cellulose Production from Cattail (*Typha angustifolia* L.)

Phattharamat Thiamngoen[a] and Thaneeya Rangseesuriyachai[*b]

[a]*Engineering Field of Study, Faculty of Engineering, Rajamangala University of Technology Thanyaburi, Pathum Thani 12110, Thailand*
[b] *Profoessor, Faculty of Engineering, Rajamangala University of Technology Thanyaburi, Pathumthani, 12110, Thailand*
*Corresponding author. Tel: 08-1733-9150 e-mail: thaneeya.r@en.rmutt.ac.th

Abstract

The production of cellulose for various applications includes a wide range of pretreatment methods specific to the type of biomass material. Choosing the right method can increase the yield of cellulose. Pretreatment process, bleaching of fibers are all important to study. The objective of this study is to investigate appropriate cellulose production procedures for Cattail. Three procedures of cellulose production were used in this study: 1) one-stage pretreatment of sodium hydroxide (NaOH) + 3.5% NaOH bleaching + 80 °C deep eutectic solvents (DES): C1, 2) one-stage pretreatment of calcium hydroxide ($Ca(OH)_2$)) + 3.5% NaOH bleaching + 80 °C DES: C2, and 3) two-stage pretreatment of the combination between hydrothermal pretreatment (HTP) and NaOH + 3.5% H_2O_2 and 3% NaOH bleaching + 70 °C DES: C3. The results show an efficiency in cellulose production from the native cattail at 68% up to a maximum of 90% in C3. It was found that this method had higher cellulose content and Crystallinity Index (CrI) than untreated samples. Removal of hemicellulose and lignin is also best achieved by this method. This study promotes in the production of weed-based cellulose materials and could develop more environmentally friendly methods in the future.

Keywords: Cattail, Cellulose production, Crystallinity Index

1. Introduction

The current discourse is dominated by the concept of a circular economy, an approach that encourages resource efficiency and has seen these ideas coalesce into national policy directives. Central to this approach is the utilization of lignocellulosic biomass, a naturally abundant source of renewable energy. This type of biomass has been gaining considerable attention as an alternative to synthetic materials, especially for environmental remediation. Its appeal primarily lies in its renewable and biodegradable nature, along with its minimal impact on the environment, making it a preferred choice in striving towards a sustainable future (Van-Hai et al., 2015). Cattail, or *Typha angustifolia* L., is a type of lignocellulosic biomass from the Typhaceae family, which is native to Europe and America. This herbaceous weed typically reaches maturity around two years, growing to heights of 1.5 to 2 meters. With holocellulose content ranging between 53-65% and lignin at 11-17% (Pimchan, 2020), cattails are recognized for their high cellulose content compared to other plant species. It is suitable to be used in various applications. Cellulose, a high molecular mass, linear homopolymer, is comprised of ring-shaped glucose units. These units are linked together in a flat, ribbon-like structure through β-1,4 glycosidic bonds, thus forming the complex structure of cellulose (Muddasar et al., 2022). In recent years, a wide range of pre-treatment methods aimed at enhancing the value of lignocellulose-based materials have been extensively investigated (Qaseem et al., 2021). The production process of cellulose from lignocellulose plants is the pretreatment of raw materials to obtain pure cellulose. There are several methods of pretreatment: 1. Physical pretreatment; it is generally used to reduce the particle size of biomass. The most common physical pretreatment methods are mechanical methods such as milling. grinding, screwing, ultrasound, ultraviolet radiation and microwave. 2. Chemical pretreatment; such as the use of acids, alkalis, bleaching, oxidation, 2,2,6,6-Tetramethylpiperidine-1-oxylradical (TEMPO), Ionic Liquid Solvent (ILS), Deep Eutectic Solvent (DES) ect. 3. Physico-chemical pretreatment; for example, physical pretreatment can be performed in parallel with alkali pretreatment to enhance the conditioning efficiency. 4. Enzyme pretreatment; although enzymatic pretreatment is an inexpensive and environmentally friendly method that has enormous potential for commercial scale-up, the reaction rate may be slower than chemical treatment, and it is necessary to determine the ratio for each cellulose raw material. (Dhali et al., 2021)

The pretreatment process of lignocellulose-based materials is an important step in separating cellulose from other constituents. The chemical pretreatment process has been widely used to remove hemicellulose and lignin for biomass. It also helps to break bonds between cellulose, hemicellulose, and lignin. Alkali chemicals that have been used, consist of sodium hydroxide (NaOH), potassium hydroxide (KOH), calcium hydroxide ($Ca(OH)_2$), hydrazine and ammonium hydroxide. Calcium hydroxide is the most economical alkalinity compared to ammonia, sodium hydroxide and potassium hydroxide (Cheah et al., 2020). However, the major disadvantages of the alkali pretreatment process include the high post-alkali pretreatment costs used to neutralize the solution and the use of longer duration (Kumar et al., 2020).6

The Hydrothermal pretreatment (HTP) method employs hot water or steam as a pre-treatment technique prior to initiating chemical processes. HTP is used in the pretreatment of many raw materials, including agricultural biomass such as bagasse and wheat straw (Ma et al., 2022), energy crops such as oil palm (Abu-Bakar et al., 2022), and

forest biomass such as eucalyptus and beech (Nitsos et al., 2016). HTP offers several advantages, such as moderate energy demands, industrial feasibility, no requirement for chemicals or corrosion-resistant equipment, minimal degradation of products, increased particle sizes, and a low environmental impact (Scapini et al., 2021).

Deep eutectic solvents (DES) are a special combination of two components: Hydrogen bond donor (HBD) and hydrogen bond acceptor (HBA)(Dhali et al., 2021) DES is easy to prepare, low cost, low toxicity and high biodegradability. (Chen and Mu, 2019) DES has the ability to selectively remove lignin from complex lignocellulose biomass. Thus, a new environmentally-friendly and novel approach was established for the pretreatment of lignocellulose biomass under mild reaction conditions(Mankar et al., 2021). Based on the processes mentioned above, a combination of at least two pretreatment processes is used to optimize the timely removal of lignin and hemicellulose. There must be a balance between improving efficiency and costs and increasing operating costs(Mankar et al., 2021). To provide a guideline for high-yield cellulose production, the main objective of this study was to evaluate the best method among one-stage pretreatment of NaOH/ $Ca(OH)_2$ with one chemical bleaching and higher temperature of DES and two-stage pretreatment of HTP with NaOH for cellulose pretreatment with two chemicals bleaching and lower temperature of DES. The development of the cellulose production process will increase the value of weed crops and renewable crops that can replace the use of commercial cellulose.

2. Methodology

2.1 Raw Material

Cattail samples were obtained from a wetland in Nonthaburi Province, Thailand. Initially, the samples were rinsed with tap water to eliminate water-soluble impurities. Following this, they were oven-dried at 60 °C for 24 h. until a constant weight was achieved and then mechanically crushed. The resulting material was sieved to a granularity between 60-100 mesh. For this experiment, NaOH, $Ca(OH)_2$, Choline chloride (ChCl), and oxalic acid dihydrate (OA) were procured from Applichem Panreac, Loba Chemie PVT.LTD., and Kemaus, respectively. All experimental procedures were conducted using deionized water.

2.2 Experimental conditions of cattail for cellulose production

This research consisted of three cellulose pretreatment options with the different pretreatment, bleaching, and temperature of DES methods. Design of different pretreatment processes with and without and hydrothermal pretreatment in combination with NaOH in two-stage pretreatment and the use of two alkaline solutions, $Ca(OH)_2$ and NaOH for one-stage pretreatment. Bleaching process was applied with the different chemicals. Finally, the cellulose was performed with DES at the different operating temperature. In each process the sample was washed with DI water until the neutral pH of the filtrated and ground before drying at 60 °C for 24 h for further step. Each cellulose production procedures were processed under the conditions shown in the Table 1.

Table 1 Conditions of Pre-treatment Cattail

Conditions	**C1**	**C2**	**C3**
Hydrothermal at 180 °C for 20 min	-	-	✓
Mild Alkaline	3% NaOH	3% $Ca(OH)_2$	3% NaOH
solid: liquid ratio	1:20		
Temperature of reaction (°C)	90		
Time at temperature (h)	3		2
Bleaching	3.5% H_2O_2		3.5% H_2O_2 + 3% NaOH
Temperature and time of bleaching (°C)	70°C for 3 h		70°C for 2 h
solid: liquid ratio	1:20		
DES, Choline Chloride (ChCl):Oxalic acid			
DES (mole)	1:1		
Cattial:DES ratio	1:10		
Temperature of reaction (°C)	80		70
Time at temperature (h)	4		2

2.3 Chemical composition analysis

The chemical composition of native and cellulose extraction of a cattail was determined using the standard Technical Association of the Pulp and Paper Associations (TAPPI) methods for different components. Cellulose and

hemicellulose were according to the TAPPI standard (TAPPI T203 om-88). Lignin was determined by the TAPPI T222 om-88 test method.

2.4 Cattail morphology

The morphology of the sample was analyzed before and after pre-treatment by Scanning Electron Microscopy (SEM) model QUANTA 450, US.

2.5 XRD Analysis

X-ray diffraction patterns of the different cellulose samples were obtained by Rigaku TTRAX III, Japan. The crystallinity index (CrI) was used to calculate the relative amount of crystalline material in the cellulose by the Segal method (Segal et al.,1959). as shown in Eq. (1):

$$\text{CrI (\%)} = \frac{I_{(cry)} - I_{(am)}}{I_{(cry)}} \text{ x } 100\% \quad (1)$$

Where $I_{(cry)}$ = the intensity of crystalline region ($2\Theta = 22°$)
$I_{(am)}$ = the intensity of the amorphous region ($2\Theta = 18°$)

3. Results and Discussion

3.1. Chemical composition analysis

The experimental cellulose content ranged from 80% to 90%, whereas the initial cattail's cellulose content, determined after the acclimatization process, was found to be 68%. The cellulose amounts obtained from C1 and C2 were comparable. In contrast, C3 exhibited the highest cellulose content at 90%, accompanied by a decrease in hemicellulose content to 9.93%. These findings are presented in Table 2.

The experimental findings revealed that the addition of hydrothermal pretreatment in C3 led to a remarkable 69% reduction in hemicellulose content compared to its initial level. This hydrothermal process effectively promotes the breakdown of cellulose and disrupts the hemicellulose structure, as supported by Scapini et al. (2021). When the biomass is heated, water undergoes auto-ionization, and hydronium ions catalyze the deacetylation of xylan. Consequently, the dissociation of acetic acid produces a proton that facilitates the partial hydrolysis of hemicellulose, as explained by Martín et al. (2022). The outcome of the hydrothermal treatment, which alters the chemical composition, is influenced by various factors, including reaction temperature, duration, material size, and more, as highlighted by Sun et al. (2022).

Table 2 Chemical compositions of Cattail

Component	Cellulose (%)	Hemicelluloses (%)	Lignin (%)
Raw cattail	68.13	31.87	30.17
C1	82.47	17.53	27.67
C2	80.75	19.25	28.48
C3	90.07	9.93	22.23

The bleaching process conducted on C3 utilizing a combination of 3% NaOH and 3.5% H_2O_2 resulted in the lowest lignin content. DES exhibits selective lignin removal capability from complex lignocellulosic biomass, as demonstrated by Cheah et al. (2020), even when the reaction time was shortened to 2 h. The bleaching procedure aims to eliminate residual lignin, thereby obtaining pure cellulose and significantly enhancing the surface appearance of cellulose fibers. This conditioning step holds great importance, as emphasized by Ng et al. (2015).

3.2 Morphology of Cattail

The structure of the treated cattail as shown in Figure 1(a-d). C1 and C2 were treated with alkali without hydrothermal treatment. Alkali removes amorphous components and smooth surfaces. C3 was pretreated with HTP resulting in more structure fragmentation. It is then treated with alkali to remove amorphous components in the structure.

The hydrothermal samples (fig. 1, d) showed more structural disintegration than other samples and suitable for biomass with high hemicellulose content. It also helps the breakdown of cellulose as well as a slight dissociation of lignin (Martín et al., 2022).

3.3 Crystallinity Index

This study focused on examining the impact of each alternative procedure (C1, C2, and C3) of cellulose production on the crystallinity of cattail. The XRD analysis results of native cattail and the best option are presented in Figure 2, and the calculation of CrI (crystallinity index) is calculated following by Eq. 1. Notably, C3 exhibited the highest CrI value. The hydrothermal pretreatment process was found to disrupt the crystal structure of cellulose by breaking both intramolecular and intermolecular hydrogen bonds within the cellulose chains. X-ray measurements of CrI are

widely recognized as the most reliable method for evaluating biomass crystallinity, as emphasized by Yu et al. (2020). The hydrothermal process had a significant impact on the CrI of cattail, increasing it from 50% to 71%.

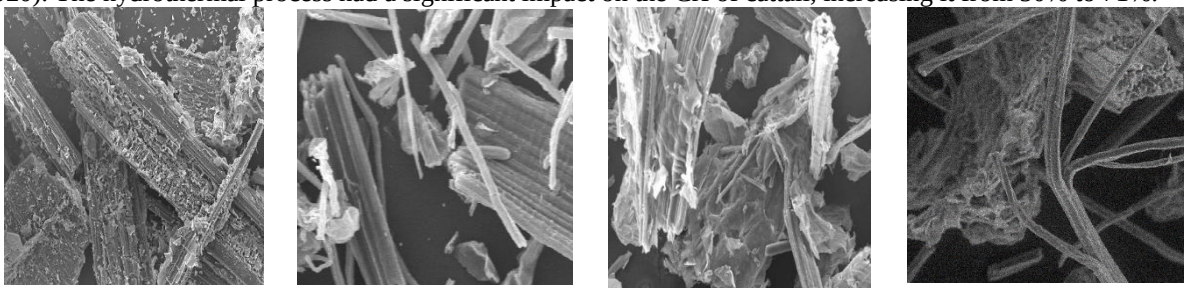

(a) (b) (c) (d)

Figure 1 SEM image of Cattail in the process of pretreatment (a) native (b) pretreatment in C1 (c) pretreatment in C2, and (d) pretreatment in C3

This increase can be attributed, in part, to the formation of new hydrogen bonds between the cellulose chains, facilitated by the partial removal of hemicellulose and lignin. This phenomenon tends to separate the cellulose chains, while also leading to rearrangements within the crystalline regions, as discussed by Reddy et al. (2014). It is worth noting that CrI serves as an indirect measure of hemicellulose removal following treatment, specifically representing the intact crystalline fraction of cellulose within the autohydrolyzed residues, as indicated by da-Silva-Morais et al. (2016). Consistent with the findings of Kumar et al. (2020), pretreatment with NaOH resulted in an 84.8% removal of lignin. Furthermore, the treated sample exhibited an increased crystallinity index of 71.5% compared to the untreated sample, which had a lower crystallinity index of 45.1%. These results provide additional evidence confirming the successful removal of lignin during the treatment process.

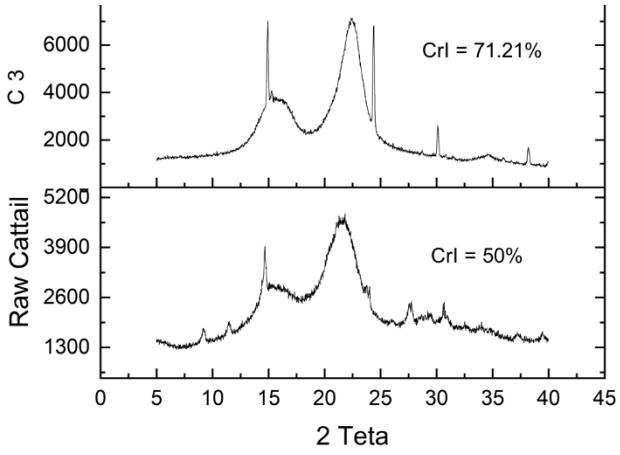

Figure 2 XRD analysis and crystallinity index of raw cattail and the best procedure of cellulose production

All the experimental results show that the process for producing the highest amount of cellulose and the lowest hemicellulose and lignin content is C3. The results show that each step of cellulose production is important. Pretreatment using a combination of physico-chemical methods enhances cellulose yield enhancement. Good pretreatment will make the fibers fragment well, make the production easier and reduce the pretreatment temperature In future studies, this process could be used to develop nanoscale cellulose.

4. Conclusions

The best process for cellulose production of cattail was C3 which enhanced the highest cellulose content at 90.07%, the hemicellulose content at 9.93%, and the lignin content at 22.23%. Pretreatment by the combination of hydrothermal and chemical processes in C3 showed the most fractured morphology compared to C2 and C3 which are treated by chemical processes. The highest CrI was 71.21% at C3 method.

5.Acknowledgements

The authors express their gratitude to the Faculty of Engineering at Rajamangala University of Technology Thanyaburi and the Faculty of Engineering and Architecture at Rajamangala University of Technology Suvanabhumi, Thailand, for their financial support and provision of experimental facilities for this study. Special thanks are extended to Dr. Samunya Sanguanpak from the National Metal and Materials Technology Center for providing valuable support with the analytical tools utilized in this research.

6. References

Abu-Bakar, N. F., Abd-Rahman, N., Mahadi, M. B., Mohd-Zuki, S. A., Mohd-Amin, K. N., Wahab, M. Z., and Wuled-Lenggoro, I. (2022). Nanocellulose from oil palm mesocarp fiber using hydrothermal treatment with low concentration of oxalic acid. *Materials Today: Proceedings*, 48, 1899-1904. https://doi.org/https://doi.org/10.1016/j.matpr.2021.09.357

Cheah, W. Y., Sankaran, R., Show, P. L., Tg. Ibrahim, T. N. B., Chew, K. W., Culaba, A., and Chang, J.-S. (2020). Pretreatment methods for lignocellulosic biofuels production: current advances, challenges and future prospects. *Biofuel Research Journal*, *7*(1), 1115-1127. https://doi.org/10.18331/BRJ2020.7.1.4

Chen, Y., and Mu, T. (2019). Application of deep eutectic solvents in biomass pretreatment and conversion. *Green Energy & Environment*, *4*(2), 95-115. https://doi.org/https://doi.org/10.1016/j.gee.2019.01.012.

da-Silva-Morais, A. P., Sansígolo, C. A., and de-Oliveira-Neto, M. (2016). Effects of autohydrolysis of Eucalyptus urograndis and Eucalyptus grandis on influence of chemical components and crystallinity index. *Bioresource Technology*, 214, 623-628. https://doi.org/https://doi.org/10.1016/j.biortech.2016.04.124

Dhali, K., Ghasemlou, M., Daver, F., Cass, P., and Adhikari, B. (2021). A review of nanocellulose as a new material towards environmental sustainability. *Sci Total Environ*, *775*, 145871. https://doi.org/10.1016/j.scitotenv.2021.145871

dos-Santos-Rocha, M. S. R., Pratto, B., de-Sousa, R., Almeida, R. M. R. G., and Cruz, A. J. G. d. (2017). A kinetic model for hydrothermal pretreatment of sugarcane straw. *Bioresource Technology*, 228, 176-185. https://doi.org/https://doi.org/10.1016/j.biortech.2016.12.087

Kumar, B., Bhardwaj, N., Agrawal, K., Chaturvedi, V., and Verma, P. (2020). Current perspective on pretreatment technologies using lignocellulosic biomass: An emerging biorefinery concept. *Fuel Processing Technology*, *199*, 106244.

Ma, H., Fu, P., Zhao, J., Lin, X., Wu, W., Yu, Z., Xia, C., Wang, Q., Gao, M., and Zhou, J. (2022). Pretreatment of Wheat Straw Lignocelluloses by Deep Eutectic Solvent for Lignin Extraction. *Molecules*, 27(22), 7955. https://www.mdpi.com/1420-3049/27/22/7955

Mankar, A. R., Pandey, A., Modak, A., and Pant, K. K. (2021). Pretreatment of lignocellulosic biomass: A review on recent advances. *Bioresource Technology*, *334*, 125235. https://doi.org/https://doi.org/10.1016/j.biortech.2021.125235

Martín, C., Dixit, P., Momayez, F., and Jönsson, L. J. (2022). Hydrothermal Pretreatment of Lignocellulosic Feedstocks to Facilitate Biochemical Conversion [Review]. *Frontiers in Bioengineering and Biotechnology*, 10. https://doi.org/10.3389/fbioe.2022.846592

Muddasar, M., Beaucamp, A., Culebras, M., and Collins, M. N. (2022). Cellulose: Characteristics and applications for rechargeable batteries. *International Journal of Biological Macromolecules*, 219, 788-803. https://doi.org/https://doi.org/10.1016/j.ijbiomac.2022.08.026

Ng, H.-M., Sin, L. T., Tee, T.-T., Bee, S.-T., Hui, D., Low, C.-Y., and Rahmat, A. R. (2015). Extraction of cellulose nanocrystals from plant sources for application as reinforcing agent in polymers. *Composites Part B: Engineering*, *75*, 176-200. https://doi.org/https://doi.org/10.1016/j.compositesb.2015.01.008

Nitsos, C. K., Choli-Papadopoulou, T., Matis, K. A., and Triantafyllidis, K. S. (2016). Optimization of Hydrothermal Pretreatment of Hardwood and Softwood Lignocellulosic Residues for Selective Hemicellulose Recovery and Improved Cellulose Enzymatic Hydrolysis. *ACS Sustainable Chemistry & Engineering*, 4(9), 4529-4544. https://doi.org/10.1021/acssuschemeng.6b00535

Pimchan, S. U., Sangravee Bidon, Sirikan Duangde and A-roonrat Utaiku. (2020). Studyonchemical compositionof Typha angustifalia L. and extracted cellulose from *Typha angustifalia* L. for food applications [Research Article]. *The Journal of Applied Science*, 19, 116-128. https://doi.org/10.14416/j.appsci.2020.02.010

Qaseem, M. F., Shaheen, H., & Wu, A.-M. (2021). Cell wall hemicellulose for sustainable industrial utilization. *Renewable and Sustainable Energy Reviews*, 144, 110996. https://doi.org/https://doi.org/10.1016/j.rser.2021.110996

Reddy, K. O., Ashok, B., Reddy, K. R. N., Feng, Y. E., Zhang, J., and Rajulu, A. V. (2014). Extraction and Characterization of Novel Lignocellulosic Fibers from Thespesia Lampas Plant [Article]. *International Journal of Polymer Analysis and Characterization*, 19(1), 48-61. https://doi.org/10.1080/1023666X.2014.854520

Scapini, T., dos-Santos, M. S. N., Bonatto, C., Wancura, J. H. C., Mulinari, J., Camargo, A. F., Klanovicz, N., Zabot, G. L., Tres, M. V., Fongaro, G., and Treichel, H. (2021). Hydrothermal pretreatment of lignocellulosic biomass for hemicellulose recovery. Bioresource Technology, 342, 126033. https://doi.org/https://doi.org/10.1016/j.biortech.2021.126033

Segal, L., Creely, J. J., Martin-Jr, A. E., Conrad, C. M. (1959). An empirical method for estimating the degree of crystallinity of native cellulose using the X-ray diffractometer. *Textile Research Journal*. 1959;29(10):786-794. doi:10.1177/004051755902901003

Sun, D., Lv, Z.-W., Rao, J., Tian, R., Sun, S.-N., and Peng, F. (2022). Effects of hydrothermal pretreatment on the dissolution and structural evolution of hemicelluloses and lignin: A review. *Carbohydrate Polymers*, 281, 119050. https://doi.org/https://doi.org/10.1016/j.carbpol.2021.119050

Van-Hai, L., Son, H. N., & Seo, Y. B. (2015). Physical and bio-composite properties of nanocrystalline cellulose from wood, cotton linters, cattail, and red algae. *Cellulose*, 22, 1789-1798.

Yu, W., Wang, C., Yi, Y., Wang, H., Zeng, L., Li, M., Yang, Y., and Tan, Z. (2020). Comparison of Deep Eutectic Solvents on Pretreatment of Raw Ramie Fibers for Cellulose Nanofibril Production. *ACS Omega*, 5(10), 5580-5588. https://doi.org/10.1021/acsomega.0c00506

Studying of Nut's Structure that Effects the Loosen of Implant Rods Spine Inside Patient's body

Sanphasit Chonlaphan[a], Nattapat Kanchanaruanrong[b], Prayuth Inban[c], Weerapol Taptimdee[d] and Banpot Meesa[e]

[a]Automated Manufacturing Engineering, Industrial Technology, Rajabhat Rajanagarindra University, Thailand.
[b]Industrial Management Engineering, Industrial Technology, Rajabhat Rajanagarindra University, Thailand.
[c]Electrical Engineering, Industrial Technology, Rajabhat Rajanagarindra University, Thailand.
[d]Automated Manufacturing Engineering, Industrial Technology, Rajabhat Rajanagarindra University, Thailand.
[e]Industrial Management Engineering, Industrial Technology, Rajabhat Rajanagarindra University, Thailand.
*Corresponding author. Tel 089-5587782; *E-mail address:* banpotmeesa@gmail.com

Abstract

Spinal surgery is required to treat the spine with screws for a spinal injury, an accident. One of the most common problems in spinal surgery is "Nut loosening condition" which will cause the titanium rod that holds the screw together fall off. This case must be corrected with surgery to replace the screw with a new piece only. To prevent further loosening of the screws in patients. Researcher has created a screw head model that used with sloping thread and zigzag thread type of nut. An experimental sample and analyzed with Solidworks program for analyzed the stress by Solidworks simulation. The results found that a screw head of sloping thread has Von mises stress lower than a screw head of zigzag thread which are 336 - 480 MPa and 356 – 508 MPa for sloping thread and zigzag thread respectively. The analysis result has shown the max stress spot is in edge of thread at screw head.

Keywords: Spine surgery, Solidworks, Finite element analysis, spine screw, Simulation

1. Introduction

The human spine is a very important part. The spine has both nerves. cervical pillow and is connected to several vital organs that are essential to human life. When spine got injury or bone disease then requires immediate treatment. There are cases where spinal surgery is required to treat the spine with screws for a spinal injury, an accident, entering old age. Treatment with this method requires spine surgery by fixing the bone with spinal screws and connecting each screw with titanium rod. This allows the patient to live a normal life in daily life. The size and number of screws used in each case depends on the size of the patient's spine and the level of damage.

The structure of spine that is attached to the screw consists of 3 elements, pedicle, cortical and spongy bone as shown in figure 1. [1] Spinal screw surgery is performed by drilling down to the level of spongy bone. When the screws are attached to the spine is complete. A titanium rod is loaded into the area of the screw head and covered with a nut to hold both the screw and the titanium rod in place as shown in figure 2. Due to the thread characteristics of nuts in the market have different characteristics. Chomphuphan Medical CO., LTD. is interested in studying the thread characteristics of each type of nut. When nut is pressed by internal loads in the patient. In order to use the information for decision the use of equipment in spinal surgery. And to prevent loosening of the nuts in patients.

One of the most common problems in spinal surgery is "Nut loosening condition" which will cause the titanium rod that holds the screw together fall off. Must be corrected with surgery to replace the screw with a new piece only. Therefore, KJ Chomphuphan Medical CO., LTD. want to study about the effect of nut's tread with screw head inside a patient. This research will test the stress that occurs around the screw head that changes according to the force which comes from the weight of the patient. Therefore, to analyze the problem. researcher has created a screw head model which was an experimental sample and analyzed with Solidworks program for analyzed the stress by Solidworks simulation. The data and knowledge from this research will adapt to the treatment of patients who require spinal surgery and to prevent further loosening of the screws in patients.

2. Methodology

2.1 Model

The 3D model of the experimental sample was created by Solidworks. The model in this research is a nut that is attached to the screw head with the titanium bar. The characteristics of nut, screw and rod shown in figure 3. [2] From the joint research topic with KJ Chomphuphan Medical CO., LTD. There are two widely used nuts analyzed in this study, as shown in Fig. 4a and 4b. Therefore, the 3D model produces a screw head which is held by the nut as shown in Fig. 6. The material of nut is titanium. (Ti-6Al-4V treated and aged) [3] That is medical grade for a surgery operation implant and instrument. The material properties were show in Table 1 [4, 5]

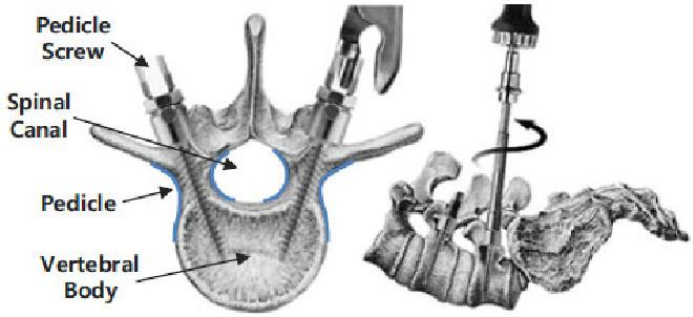

Figure 1 spine bone composition (Jongwon Lee, 2011)

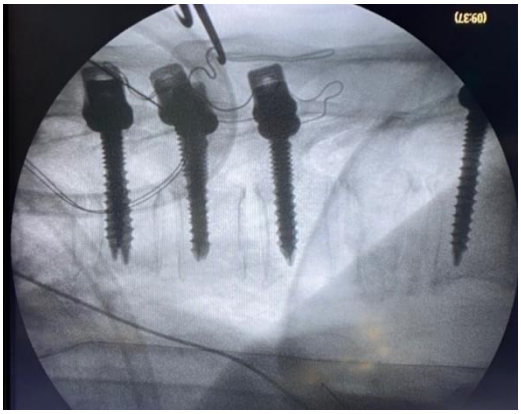

Figure 2 Screw position in surgical spine (Jongwon Lee, 2011)

Figure 3 surgery set up with screw, rod and nut

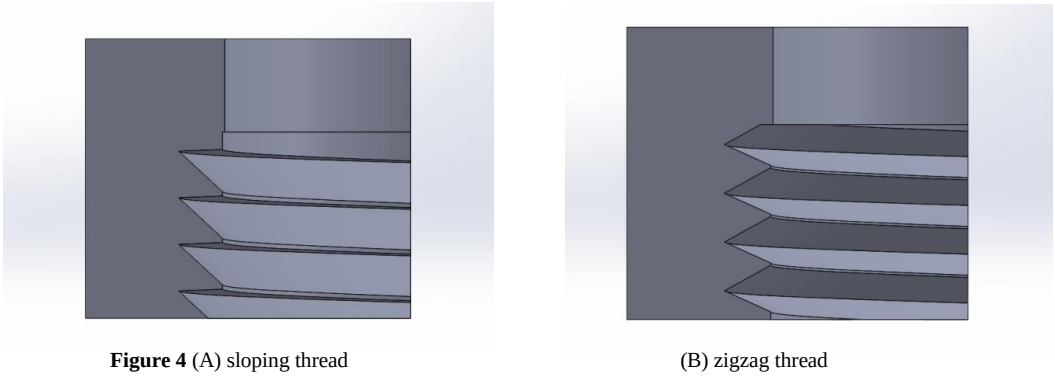

Figure 4 (A) sloping thread (B) zigzag thread

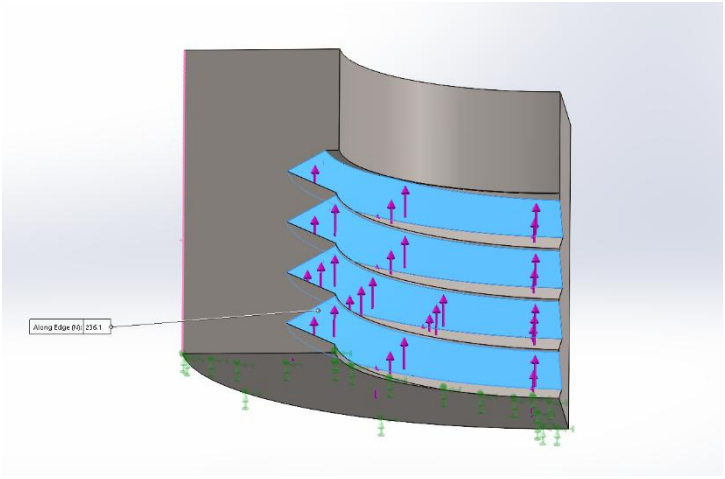

Figure 5 Preprocessing model

Table 1 Material properties of Ti-6Al-4V treated and aged

Properties	Value	Unit
Elastic Modulus	1.048×10^{11}	N/m^2
Poisson's ratio	0.31	-
Shear Modulus	4.102×10^{10}	N/m^2
Mass Density	4428.784	Kg/m^3
Tensiles Strength	1050000000	N/m^2
Yield Strength	827370880	N/m^2
Thermal Expansion Coefficient	9×10^{6}	K^{-1}
Thermal Conductivity	6.7	W/ (m.K)

2.2 Experimental set up

The 3D models from Fig. 6a and 6b were analyzed by finite element analysis using Solidworks simulation [6]. The weight acting on the nut is the weight acting on the spine which differs according to the posture that have ranges from 25% - 275% of body weight. [7] According to information from KJ Chomphuphan Medical CO., LTD., it was found that patients who experience loosening of the nut tend to be in the weight range of 70 - 100 kg. Such weight considering the case of maximum load. The range of forces studied is shown in Table 2.

Table 2 Calculation of load for case study

Weight (kg)	Weight press spine (kg)	Load (N)	Max Load (2.75 multiplier) (N)	Load pull nut (N)
70	35	343.35	944.21	236.10
80	40	392.40	1079.10	269.78
90	45	441.45	1213.99	303.50
100	50	490.50	1348.86	337.22

This research has studied 2 kinds of nuts. That includes zigzag thread and sloping thread as shown in figure 4. From data in table 2 can created an analysis condition for this research as shown in table 3. The 3D model after preprocessing until created mesh is shown in figure 6.

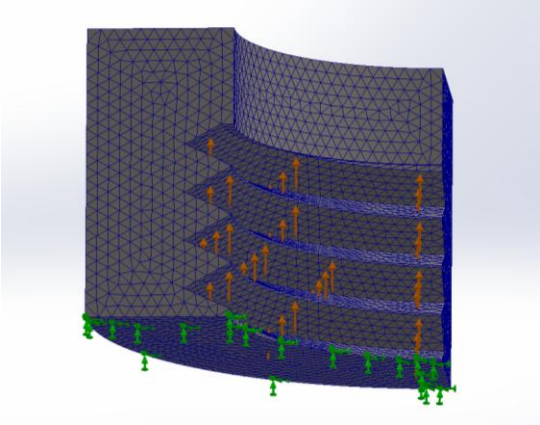

Figure 6 Meshing model

Table 3 Experimental condition

Zigzag thread load (N)	Sloping thread load (N)
236.10	236.10
269.78	269.78
303.50	303.50
337.22	337.22

3. Results and Discussion

3.1. Result

From the experimental results, it was found that the screw head of the inclined thread had a stress of 336 - 480 MPa. The screw head of the zigzag thread A stress of 356 – 508 MPa occurred, causing the screw head of the inclined thread to have a lower stress than the screw head of the zigzag thread, respectively. The analysis results showed that the highest stress point was at the thread edge of the screw head. As shown in Figures 7 and 8.

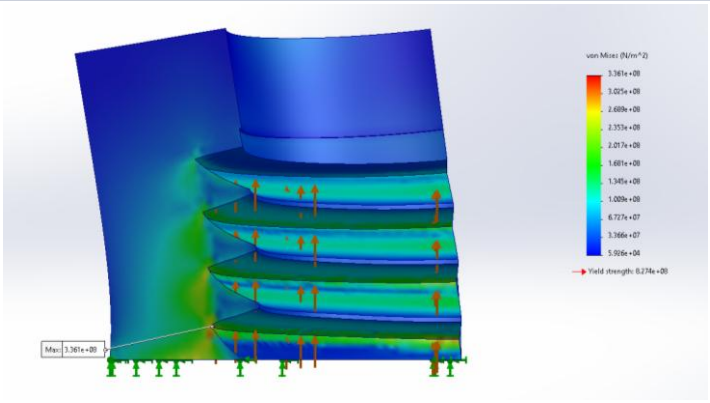

(A) Sloping thread 236.1 N

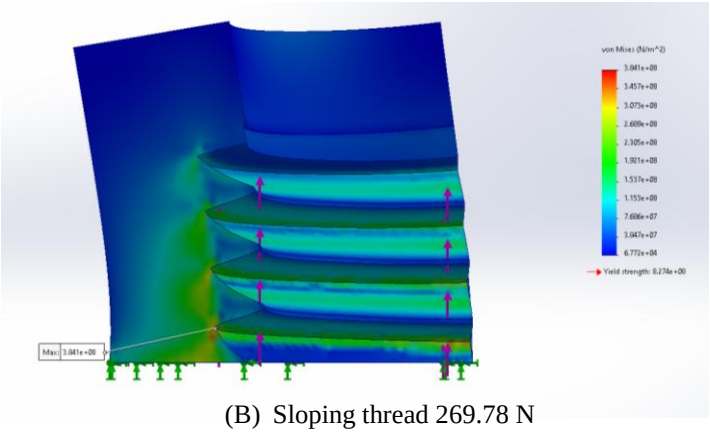

(B) Sloping thread 269.78 N

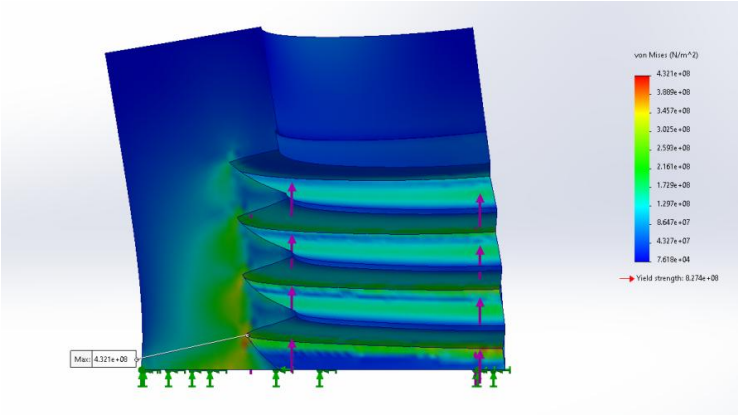

(C) Sloping thread 303.5 N

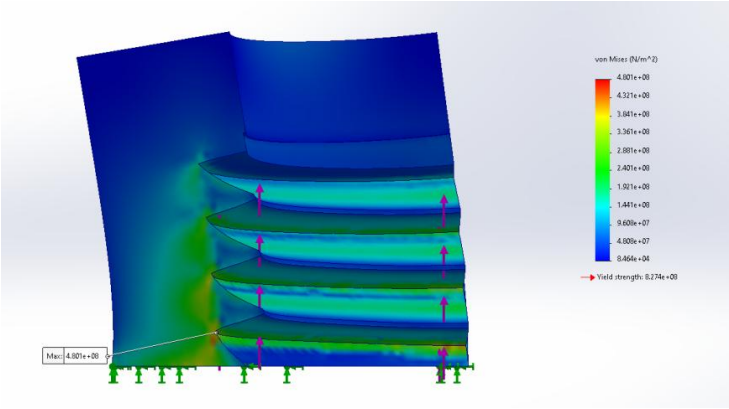

(D) Sloping thread 337.22 N

Figure 7 Von Mises stress result of sloping thread nut effect

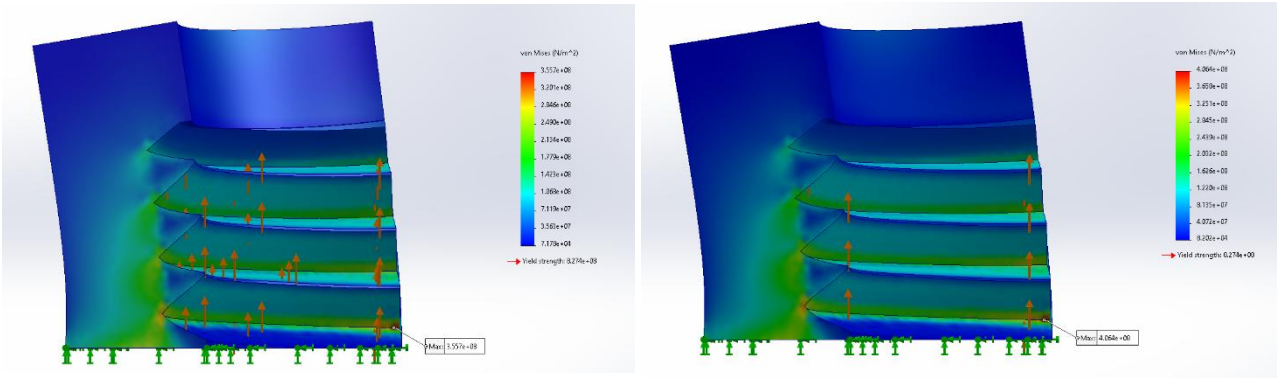

(A) Zigzag thread 236.1 N (B) Zigzag thread 269.78 N

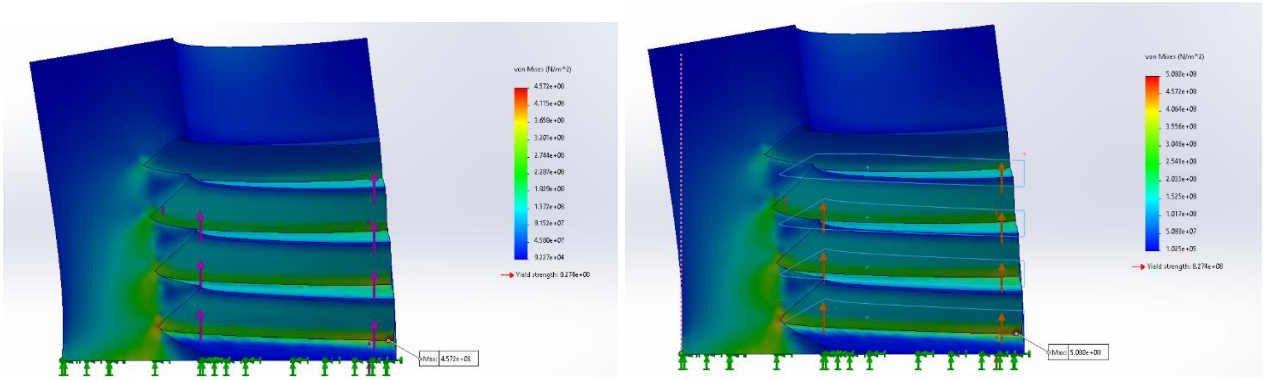

(C)Zigzag thread 303.5 N (D) Zigzag thread 337.22 N

Figure 8 Von Mises stress result of zigzag thread nut effect

3.2 Discussion

Von Mises stress is based on the Von Mises – Henky theory. This theory also known as the Shear – energy theory or maximum distortion energy theory. Von Mises stress has a formula as show in equation 1. [8]

$$\sigma_{vonMises} = \{[(\sigma_1 - \sigma_2)^2 + (\sigma_2 - \sigma_3)^2 + (\sigma_1 - \sigma_3)^2] / 2\}^{1/2} \quad (1)$$

where σ_1 is principal stress in x axis.
σ_2 is principal stress in y axis.
σ_3 is principal stress in z axis.

Von Mises stress has calculated the stress that can affect material to plastic deformation. If compare Von Mises stress with yield strength and has found it over yield strength value. These mean the material has a plastic deformation and this force is over the limit that can accept. According to experimental results. A Von Mises stress in material in both design is not reaching the yield strengths. From the yield strength divided by a maximum stress in each case. These mean both design is safety because the safety factor is over 2.

According to experimental results, sloping thread will create stress lower than zigzag thread in same condition of preprocessing. The max stress will happen in the edge inside the screw head close to the lowest position as shown in figure 7 and 8. Von Mises stress from sloping thread nut is lower than zigzag thread nut, 19.6, 22.3, 25.1 and 27.9 MPa for load 236.1, 269.78, 303.5 and 337.22 N respectively. This difference in value is about 5.5%. as shown in figure 9. The lower stress in screw head can reduces a chance of loosen nut in patients after have surgery case. Therefore, from analysis results the sloping thread has more durability than zigzag thread in the same load condition.

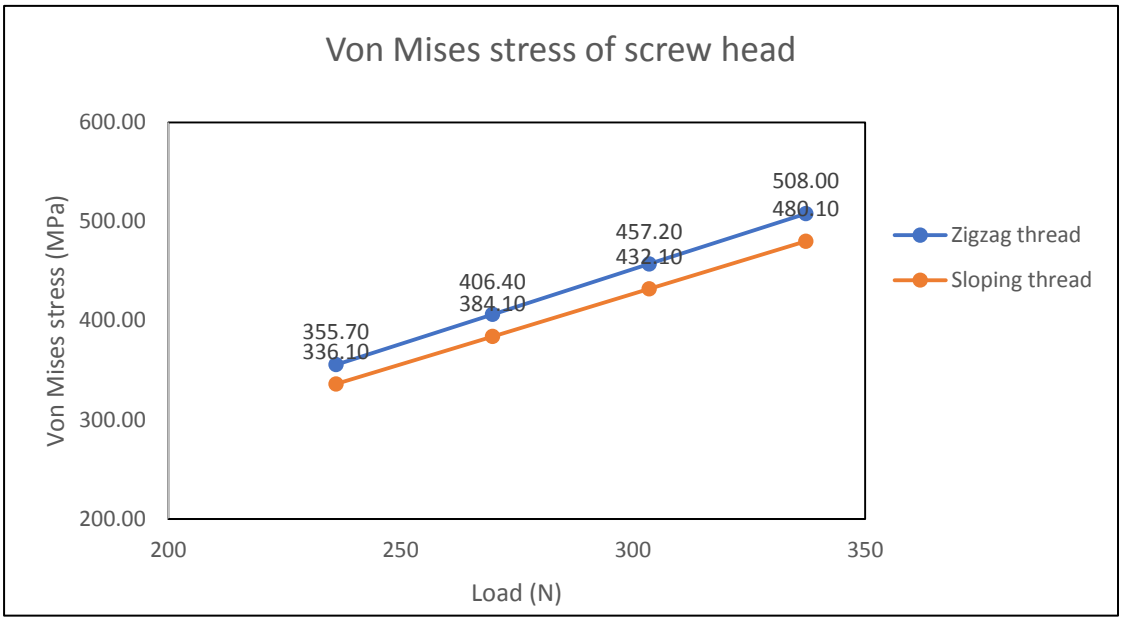

Figure 9 Comparison of Von Mises stress from sloping thread and zigzag thread

4. Conclusions

The experimental results revealed that the analysis of screw head for sloping thread and zigzag thread by using finite element analysis found that a sloping thread will create Von Mises stress to screw head lower than a zigzag thread. Mises stress from sloping thread nut is lower than zigzag thread nut, 19.6, 22.3, 25.1 and 27.9 MPa for load 236.1, 269.78, 303.5 and 337.22 N respectively. This difference in value is about 5.5%.

Therefore, under the limitation and condition of KJ Chomphuphan Medical CO., LTD., from analysis results the sloping thread has more durability than zigzag thread in the same load condition.

5.Acknowledgements

The authors would like to express our sincere gratitude to all the individuals and organizations that have contributed to the publication of this research paper. We would like to thank KJ Chomphuphan Medical CO., LTD for giving us data, an instrument and a chance to complete this research paper that can help a patient. The authors are also like to thank Radjaphat Rajanagarindra university for their feedback and support throughout the research process. The authors would like to thank all the participants in this research for their time and willingness to complete this research. And finally, the authors would also like to express our appreciation to this journal for considering our work and providing the opportunity to publish our findings

6. References

Jongwon, L., Sungmin, K., and Young, S. K, 2011, Automated Surgical Planning System for Spinal Fusion Surgery with Three-Dimensional Pedicle Model. Retrieve from https://www.researchgate.net/figure/A-vertebra-fused-using-pedicle-screws_fig1_221064176.

Globus, M, 2023, ANTERIOR CERVICAL DISCECTOMY AND FUSION, Retrieved from https://www.catablog.com/post/depuy-synthes-expedium-spine-system-catalog-179702000

Andrew, W, Steven, J. Girdler., Christopher, M., M, Amy, A and Samuel, K., C, 2020, Biomaterials in Spinal Implants: A Review, Neurospine 2020; 17, 101 – 110.

Solidworks2021, 2021, Solidworks properties material.

Globus, M, 2023, ANTERIOR CERVICAL DISCECTOMY AND FUSION, Retrieved from https://www.globusmedical.com/patient-education-musculoskeletal-system-conditions/procedures/anterior-cervical-fusion-procedure/

Pramote, D, 2013, Application of Fininte Element by Solidworks Simulation, Bangkok. Technology Promotion Association (Thailand-Japan).

kdms hospital, 2023, Supporting the weight of the spine in various postures. Retrieved from https://kdmshospital.com/article/backache/

Development of a Mexican Homemade Sauce, a Creative Food, Using Carotenoids (Astaxanthins) Obtained from Shrimp Exoskeleton and Cephalothorax

Romero-Olmos, D.[a], García-Gómez, R.S.[b] and Durán-Domínguez-de-Bazúa, M.d.C.[c]*

a, b, c Laboratories of Environmental Chemical Engineering and Chemistry (LECEC), Faculty of Chemistry, National Autonomous University of Mexico, UNAM, Mexico City, 04510 Mexico

* Corresponding author. Tel. +52 55 5622 5300; fax:. +52 55 5622 5303; *E-mail address:* mcduran@quimica.unam.mx

Abstract

The capture of crustaceans in Mexico, especially shrimp (*Litopenaeus vannamei*) has shown constant growth over the years due to its national and international demand. By separating the cephalothorax and exoskeletons from the rest of the crustacean body, by-products are generated that, when not reused and properly disposed of create a source of contamination. Valuable by-products of these crustaceans include protein, chitin, and carotenoid pigments. In particular, the latter are of great interest due to the worldwide trend in the use of natural pigments especially when these are considered nutraceuticals. In this investigation, carotenoids (astaxanthins) were extracted from the cephalothorax and exoskeletons of shrimp using a vegetable oil (soybean, *Glycine max*) so that after the unit operations of washing, drying, grinding, and sifting, it was possible to obtain an integral powder. This powder, after a demineralization process with 8% v/v acetic acid, was dried and placed in amber glass jars for safekeeping. As carotenoids are oil soluble, the oil extraction experimental design was multifactorial, having three factors: a) two type of powders (integral and demineralized), b) three extraction temperatures (room temperature, 60, and 80°C), and c) two powder:soybean oil ratios (1:10 and 1:30). The carotenoid compounds present in shrimp powders were identified by thin layer chromatography (identifying lutein, free astaxanthin, canthaxanthin, astaxanthin monoester, and β-carotene). Finally, using the pigmented soybean oil, two samples of a creative food: Mexican chilli and peanuts sauce was prepared. "*Chile de árbol*" (tree chilli, *Capsicum annuum* Árbol) and "*chile morita*" (*morita* chilli, *Capsicum annuum* Morita) with peanuts (*Arachis hypogaea*) sauce were prepared to determine, through a sensory evaluation with untrained judges, the existence of sensory differences between the two types of sauces, using the soybean oil with and without shrimp pigments and, evaluating its level of acceptability. Of the 101 sensory tests carried out, it was found that, when evaluating the attributes of color, smell, texture, and flavor, there were no significant differences at a $p \geq \alpha$ of 0.05 between these attributes, with the level of liking for these attributes being practically the same in the two samples (with and without the addition of pigmented soybean oil). When evaluating the probability of purchase, between one sauce and another, it also turned out that there was no significant difference, so it is feasible to add shrimp pigments to foods of this type to increase their nutraceutical value, giving consumers purchase options to improve their health.

***Keywords*:** Carotenoid pigments (nutraceutical astaxanthins), carotene-protein, shrimp cephalothorax and exoskeletons, solid-liquid extraction, creative food: Mexican chilli-peanut sauce

1. Introduction

Mexico is located as the seventh country in the world in terms of shrimp production (SAGARPA, 2018). The inedible fraction of the shrimp is not used by consumers and is frequently thrown into the high seas, ports, and municipal dumps, generating pollution problems due to the large amount of organic matter deposited in those sites. However, shrimp cephalothorax and exoskeletons are useful by-products due to its high content of proteins, chitin, and carotenoid pigments (Higuera-Ciapara et al., 2006). There is a large market for those consumers who prefer to avoid products with synthetic food additives, preferring instead, food made with natural additives. Food, from the beginning of its production to its consumption, is exposed to various conditions that can generate changes in its properties. Among them, their smell, color, and flavor, as well as nutritional and functional changes, that might produce certain diseases due to the accumulation of harmful compounds. In this study, it was proposed to take advantage of the inedible portions of shrimp, with the aim of extracting carotenoids (mainly astaxanthins) using an edible vegetable oil (soybean oil, *Glycine max*) to proceed with their incorporation into some food for human consumption. A popular Mexican chilli sauce from two varieties of chilli known in Mexico as "*chile de árbol*", tree chilli (*Capsicum annuum* Árbol), and "*chile morita*", morita chilli (*Capsicum annuum* Morita), adding peanut paste (*Arachis hypogaea*) may be an appropriate creative food when the oil used to prepare it has been pigmented with shrimp's byproduct pigments to take advantage of its antioxidant characteristics, increasing its nutritional value. In this way, the following **general objective** was raised: Obtain carotenoids (mainly astaxanthins) from shrimp waste by means of a solid-liquid extraction with edible soybean oil as a vehicle to be added to this creative food. **Particular objectives**: 1) Obtain powders from shrimp cephalothorax and exoskeletons of *Litopenaeus vannamei* shrimp species. 2) Identify some of the pigments present carotenoids by thin layer chromatography. 4) Prepare a functional food with pigmented soybean oil (a typical Mexican sauce, as a creative food) carrying out a sensory evaluation by untrained judges to determine its acceptability.

2. Methodology

2.1. Obtaining and conditioning the sample

The cephalothorax and exoskeletons of shrimp (*Litopenaeus vannamei*) were obtained in the Mexico City market known as *"Central de Abastos La Nueva Viga"*. Upon arrival to the laboratories, the byproducts were washed and dried using a Felisa model F-293D oven, at 60±5°C/24 hours until completely dry. Subsequently, they were ground in a home-type Hamilton Beach blender model 50242R-MX at maximum power (1500 rpm) until a powder was obtained. It was sieved with 40 and 80 mesh sieves (0.420 and 0.177 mm, respectively) with the objective of homogenizing particle size (granulometry). Bromatological analyses were performed (ashes, Kjeldhal Nitrogen (protein), fat, fiber, moisture content (AOAC, 2001). Part of the previously obtained powder was subjected to a demineralization operation using glacial acetic acid as demineralizing agent (Ameh et al., 2014) at 8% v/v in a 1:9 (m/v) powder:demineralizing agent ratio under constant stirring for 1 hour. Subsequently, powder was washed with distilled water until a neutral pH was obtained and filtered with Whatman No.1 filter paper, to proceed to its drying at 60±5°C for 3-4 hours until reaching an absolute humidity of 4-7%. For the carotenoids extraction, edible soybean oil (Nutrioli brand) was used for both whole (integral) and demineralized powders, using three extraction temperatures with constant stirring for 20 minutes (Luna-Rodríguez et al., 2008): a) T_1, Room temperature (22±2°C), b) T_2, Heating to 60°C, and c) T_3, Heating to 80°C. Two powder:oil ratios were used: a)1:10 and b)1:30. Subsequently, each sample was centrifuged at 4,000 rpm in an Eppendorf model 5810-R centrifuge for 15 minutes at a temperature of 4°C, recovering the oily extract. Finally, the quantification of the carotenoids was carried out in a UV-Visible Rayleigh spectrophotometer UV-2601 (λ_{max}=488 nm), after previously carrying out the calibration curve with astaxanthin standards (Sigma-Aldrich).

2.2. Identification of the carotenoids

To identify the carotenoids present in shrimp waste powders (whole and demineralized), the methodology established by Grung et al. (1992), using a vortex (at 3000 rpm), 10-15 mg (approx.) of the samples were dissolved with approximately 7 mL of acetone. Subsequently, the excess acetone was dried and the sample was resuspended with 0.2mL (approx.) of ethyl ether. The above was repeated for the astaxanthin standard. From the upper part of the suspension, the spots of each sample were placed on a 10x5cm silica gel chromatoplate. Immediately afterwards, they were placed at each point on the chromatoplate. It was introduced into an eluting solution of 25% acetone in hexane, previously prepared. Finally, at the end of the elution, each one of the points was identified with the help of UV light and an iodine chamber. The identification of carotenoids present in shrimp waste powder (whole or integral and demineralized) was carried out through thin layer chromatography, TLC, following the methodology established by Grung et al. (1992) in which the retardation factor (Rf) of each pigment was calculated and compared with respect to the commercial astaxanthin standard of the Sigma-Aldrich brand.

2.3. Preparation of a creative food: Mexican chilli-peanut sauce

To evaluate the acceptability of the carotenoids obtained from shrimp cephalothorax in a food, two samples of the creative food Mexican sauce (chilli sauce with peanuts) were prepared, using the following ingredients: For the sample 1 soybean oil with carotenoids (mainly astaxanthins), peanuts, *chile de árbol* (Figure 1), *chile morita* (Figure 2), vinegar, lemon juice, oregano (*Origanum vulgare*), and salt. Sample 2 was made with the same ingredients but without the addition of carotenoids, only soybean oil was used as a basis.

Figure 1. *Chile de árbol* (*Capsicum annuum* Árbol) dried chilli [pungency medium to high, 15000- 23000 SHU, Scoville heat units]

Figure 2. *Chile morita* (*Capsicum annuum* Morita) dried and smoked chilli [pungency medium to high, 15000- 23000 SHU, Scoville heat units]

2.4. Sensory evaluation of Mexican sauce

Sensory evaluations were performed through scalar tests (verbal hedonic scale and preference level). Untrained judges (101) were considered for the sensory tests. From the data obtained from the sensory evaluations, analysis of variance (ANOVA) of one factor was performed for each of the sensory attributes (color, smell, texture, and flavor), and for the probability of purchase a commercial sauce based on the samples. Data were evaluated using Excel (with a confidence level of 95%) for the existence of significant differences between the two elaborated sauce samples.

3. Results and Discussion

3.1. Granulometry and percentage of ashes by particle size of the whole powder of shrimp residues

The results of Table 1 show that the distribution by particle size of the shrimp cephalothorax powder were uniform with respect to each other, since there was practically the same percentage of particle size between the 40 and 80 meshes and the "basis ” (which is what is not retained by the last mesh No. 80).

Table 1. Granulometry of shrimp powder

No. of mesh	Particle size (mm)	Amount retained (g)	Percentage (%)	Ashes (%)
40	>0.420	165.2	31.9	$13.77^{\pm 0.07}$
80	0.420-0.177	191.4	37.0	$16.22^{\pm 0.04}$
Basis	<0.177	161.3	31.1	$14.48^{\pm 0.03}$
Total		**517.9**	**100.0**	
Average				**$14.82^{\pm 0.02}$**

*Results shown are the average of 2 determinations

Regarding the determination of the ash content (Table 2), it was carried out in order to know if there was any variation between the particle sizes, determining which fraction of the shrimp powder would be the most suitable for demineralization. However, the data showed a minimal variation between them and, therefore, it was decided to pool all the fractions and carry out the demineralization to the corresponding part of the set of them.

Table 2. Analysis of the ash content of whole and demineralized shrimp residue powder

Component (%)	**Whole powder (*Litopenaeus vannamei*)**	**Demineralized powder (*Litopenaeus vannamei*)**	**Whole flour or powder (*Litopenaeus vannamei*) (Mendes et al., 2013)**	**Whole powder (Simpson and Haard 1985)******
Ashes*	$14.75^{\pm 0.31}$	$6.32^{\pm 0.09}$	$19.77^{\pm 1.20}$	26.00

*The reported results are the average of 3 experimental measurements

3.2. Carotenoids extraction and identification

According to Ameh et al. (2014), during the acid demineralization of the shrimp exoskeleton and cephalothorax, the calcium present in the form of salt (calcium carbonate) is dissolved by the acid. In this work, the demineralization process of shrimp powder was carried out with 8% v/v glacial acetic acid, in a powder:demineralizing agent ratio of 1:9 m/v, for which it was observed that the treatment served its purpose; which consisted of considerably reducing the mineral content. From the above, it can be assumed that the vast majority of the shrimp ashes present in it correspond to calcium, since after demineralization the ash content decreased more than double. Table 3 shows that the maximum concentration of carotenoids in soybean oil was obtained with demineralized powders in a 1:10 powder:oil ratio and by heating at 80°C for 20 minutes. When comparing the extraction between the two types of powders analyzed (whole and demineralized powders) it was observed that, for the three extraction temperatures (T_{amb}, 60, 80°C) and the two powder:oil ratios (1:10 and 1:30), a higher concentration of carotenoids was always obtained in the demineralized powders, because this process concentrates fat in the sample. On the other hand, the increase in temperature improves the extraction of carotenoids.

Table 3. Concentration of carotenoids (mg/100 mL of oil) in shrimp powder samples under different treatments

Type of powder							
Whole powder				Demineralized powder			
Powder:oil ratio				Powder:oil ratio			
1:10		**1:30**		**1:10**		**1:30**	
Extraction type (mg carotenoids/100 mL oil)		Extraction type (mg carotenoids/100 mL oil)		Extraction type (mg carotenoids/100 mL oil)		Extraction type (mg carotenoids/100 mL oil)	
T_1	$45.475^{\pm 1.557}$	**T_1**	$21.541^{\pm 1.775}$	**T_1**	$50.417^{\pm 1.475}$	**T_1**	$31.923^{\pm 1.884}$
T_2	$58.481^{\pm 2.148}$	**T_2**	$39.182^{\pm 2.215}$	**T_2**	$78.532^{\pm 2.254}$	**T_2**	$63.048^{\pm 2.141}$
T_3	$67.913^{\pm 2.565}$	**T_3**	$51.833^{\pm 2.679}$	**T_3**	**$83.724^{\pm 2.452}$**	**T_3**	$70.446^{\pm 2.741}$

The reported results are the average of 3 experimental measurements where: T1=Constant stirring at room temperature (22±2°C) for 20 minutes, T2= Constant stirring at 60°C for 20 minutes, and T3= Constant stirring at 80°C for 20 minutes

The analysis of variance used was performed using Excel with a significance level of α=0.05 (95% confidence level).The results of this analysis are shown in Table 4. These results show that among the three variables (A: Type of powder, B: Powder:oil ratio and C: Extraction temperature) and among their interactions (AC, BC and ABC) there were significant differences in terms of the concentration of the carotenoids. The yield expressed in grams of carotenoids (astaxanthins)/kg of powder (Table 5) used was to find the most efficient separation. The highest concentrations were 12.941g and 16.647g of carotenoids (astaxanthin)/kg desmineralized powder of carotenoids pigments/kg desmineralized powder with the second value being the best but using three times more oil. It is worth mentioning that the reported values in Table 5 is the total content of carotenoids of the demineralized powder at the time of each extraction in each condition. However, these are reported as caroteoids (mainly astaxanthin)/kg of demineralized powder because the standard purchased was Sigma-Aldrich commercial astaxanthin at 99.9% purity.

Table 4. Analysis of variance of 3 factors with interaction for the concentration of carotenoids in different samples of shrimp powder

Source	Sum of squares	DF	Mean square	Cf	Tf	Conclusion
A: Type of powder	19.02	1.00	19.02	9.45	4.26	H_1
B: Powder:oil ratio	27.77	1.00	27.77	13.80	4.26	H_1
C: Extraction temperatura	6.82	2.00	7.26	4.61	3.40	H_1
AB	10.43	1.00	10.43	5.18	4.26	H_1
AC	20.93	2.00	10.47	5.20	3.40	H_1
BC	23.47	2.00	11.74	5.83	3.40	H_1
ABC	17.14	2.00	8.57	4.26	3.40	H_1
Total error	48.31	24.00	2.01			
Total (correction)	276.94	35.00				

Where: DF= Degrees of freedom, H_1= Significant difference, Cf-Calculated Factor, Tf-Table factor

Table 5. Yield obtained from carotenoids (astaxanthin) (g/kg sample)

Whole powder				Whole powder			
Powder:oil ratio				Powder:oil ratio			
1:10		**1:30**		**1:10**		**1:30**	
(g carotenoids/kg desmineralized powder)		(g carotenoids/kg desmineralized powder)		(g carotenoids/kg desmineralized powder)		(g carotenoids/kg desmineralized powder)	
T_1	4.450	T_1	8.725	T_1	4.970	T_1	9.587
T_2	5.643	T_2	7.578	T_2	7.578	T_2	13.385
T_3	6.647	T_3	8.195	T_3	**12.941**	T_3	**16.647**

Where: T1=Constant stirring at room temperature (22±2°C) for 20 minutes, T2= Constant stirring at 60°C for 20 minutes and T3= Constant stirring at 80°C for 20 minutes

The identification of carotenoids present in shrimp waste powder (whole or integral and demineralized) was carried out through thin layer chromatography, TLC, as mentioned in the methodology. Table 6 shows the results obtained when performing the TLC, both for the whole shrimp waste fluor sample and for the demineralized one. In it, the following compounds were identified: Lutein, free astaxanthin, canthaxanthin, astaxanthin monoesters and β-carotene. Figures 3 and 4 present the TLC results with ***Rf***.

Table 6. Identification of carotenoids by thin layer chromatography, TLC

A		B		C	
Rf	Rf Carotenoid identified	***Rf***	Carotenoid identified	***Rf***	Carotenoid identified
		0.23	*Lutein/Zeaxanthin	0.23	*Lutein/Zeaxanthin
0.32	Free astaxanthin	0.32	Free astaxanthin	0.32	Free astaxanthin
		0.39	Canthaxanthin	0.39	Canthaxanthin
0.97	*β-carotene	0.49	Astaxanthin monoester	0.47	Astaxanthin monoester
		0.95	*β-carotene	0.95	*β-carotene

A: Astaxanthin standard, B: Demineralized shrimp powder, C: Whole shrimp powder
*Both β-carotene and lutein were developed using an iodine chamber

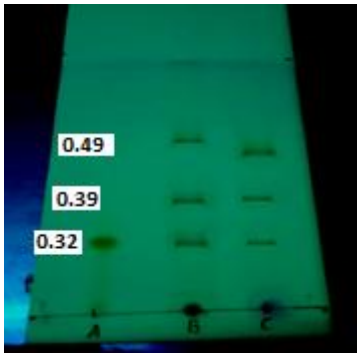

Figure 3. Chromatoplate obtained under UV light. A) Sigma astaxanthin standard. B) Pigments obtained from previously demineralized shrimp cephalothorax and exoskeleton powder. C) Pigments obtained from whole shrimp cephalothorax and exoskeleton powder

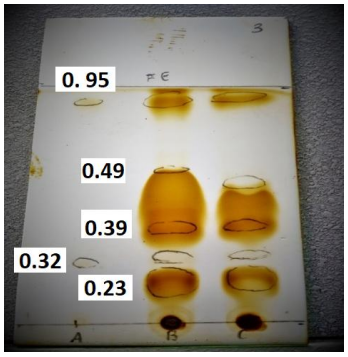

Figure 4. Chromatoplate obtained by developing with an iodine chamber. A) Sigma astaxanthin standard.
B) Pigments obtained from previously demineralized shrimp cephalothorax and exoskeleton powder. C) Pigments obtained from whole shrimp cephalothorax and exoskeleton powder

When placing the chromatoplate under UV light only 3 carotenoids could be seen for both shrimp powder samples (points B and C), while for the astaxanthin standard (point A) only the band was seen corresponding to free astaxanthin (Figure 3). Subsequently, the same chromatoplate was introduced into an iodine chamber and it was possible to identify two additional carotenoids for points B and C, which corresponded to lutein and β-carotene; while for point A, β-carotene was identified (Figure 4). In the studies carried out by Takeungwongtrakul et al. (2013) and by Gulzar and Benjakul (2018), the same carotenoids (with the exception of lutein) were identified through TLC from shrimp cephalothorax samples of the same species (*Litopenaeus vannamei*).

3.3. Preparation and sensory evaluation

According to the methodology (2.3 and 2.4), Table 7 shows the final formulation used for the preparation of two samples of a creative Mexican chilli-peanut sauce.

Table 7. Formulation of the creative food: Mexican chilli-peanut sauce

Ingredient	Amount (g)	Percentage (%)
*** Soybean oil (*Glycine max*)**	200.00	65.60
Peanuts (*Arachis hypogaea*)	50.00	16.40
Chile de árbol (*Capsicum annuum* Árbol)	15.32	5.02
Chili morita (*Capsicum annuum* Morita)	8.40	2.76
Vinegar	9.22	3.02
Lemon juice	7.00	2.30
Oregano (*Origanum vulgare*)	1.56	0.51
Salt	13.40	4.39
Total	304.90	100.00

* M1: Soybean oil without carotenoids, M2: Soybean oil with carotenoids

The sample 1 (M1) was made with normal soybean oil (without the addition of carotenoids), while sample 2 (M2) was made with soybean oil in which shrimp carotenoids were extracted (Figure 5). The results obtained from the affective tests always allow the evaluators to know the acceptance, rejection, preference or level of liking of one or several products. Specifically, affective-type scalar tests are those used for the purpose of knowing the level of liking or disliking a product. These tests have great practical application, are easy to interpret and the results obtained from them allow important actions to be taken based on the sale of the product, possible changes in its formulation, etc. (Espinosa-Manfugás, 2007).

Figure 5. Shrimp seasoned with **the creative food: Mexican chilli-peanut sauce**

According to the analysis of variance carried out for each of the four sensory attributes evaluated (color, smell, texture and taste) (Table 8), no significant differences were found between the samples. This indicates that the application of pigmented soybean oil in the sauce was not different from unpigmented soybean oil; since the formulation for each sauce was exactly the same, modifying only the type of oil. The average score obtained in the samples for each attribute was very similar. Observing an average level of liking of 7 ("I like it moderately") in all sensory attributes.

Table 8. Average satisfaction levels obtained for each sensory attribute in the two prepared sauce samples

Sample	**M1**				**M2**			
Sensory attribute	**Color**	**Odor**	**Texture**	**Taste**	**Color**	**Odor**	**Texture**	**Taste**
Average score	7.01	7.45	6.70	6.92	7.31	7.52	6.94	7.07

* **M1: Sauce without carotenoids, M2: Sauce with carotenoids**

It was observed that the average purchase probability for sample 2 (sauce with carotenoids) had slightly higher than that of sample 1 (sauce without carotenoids); observing an average purchase probability of 2 ("I would probably buy it") (Tables 9 and 10).

Table 9. Scale used to determine the probability of purchase

Score	Possibility of purchase
1	Definitely buy it
2	I would probably buy it
3	I'm not sure
4	I Probably Wouldn't Buy It
5	I definitely wouldn't buy it

Table 10. Average purchase probability for each sauce sample (M1: Sauce without carotenoid, M2: Sauce with carotenoids)

Sample	Possibility of purchase (Average)	Scale
M1	2.24	I would probably buy it
M2	2.45	I would probably buy it

However, the analysis of variance showed that there was no significant difference in the probability of purchase. This means that the potential consumer would buy indistinctly either one sauce or the other.

4. Conclusions

According to the objectives of this research, the following conclusions can be drawn: The acid demineralization process of shrimp powder achieved a considerable reduction in the ash content, allowing the fat to be concentrated and thus facilitating the extraction of carotenoids. Thanks to the demineralization process, the highest concentration of carotenoids in soybean oil (oil extract) was achieved using demineralized powder in a proportion of 1:10 by heating to 80°C; obtaining a concentration of 83,724 mg of carotenoids/100 mL of soybean oil. Additionally, the highest concentration of carotenoids per kilogram of powder was achieved using demineralized powder in a ratio of 1:30 by heating to 80°C; obtaining a concentration of 16.647 g/kg. When performing the analysis of variance of three factors (type of powder, powder:oil ratio and extraction temperature) with a significance level of 0.05, significant differences were obtained in the concentration of carotenoids for each factor and between their interactions. Once the carotenoids were extracted, it was possible to identify the presence of five of them using thin layer chromatography in the shrimp powder samples (lutein, free astaxanthin, canthaxanthin, astaxanthin monoesters, and β-carotene). It was found that the prepared creative food Mexican chilli sauce with nutraceutical carotenoids presented a good level of satisfaction and that the probability of purchasing both samples was high. Finally, it was determined that for the four sensory attributes evaluated (color, smell, texture, and flavor) there were no significant differences. As a recommendation, for the carotenoids extraction, a comparison between different types of edible oils might be the subject of another research (vegetable origin oils: olive, sesame, soybean, sunflower, etc., and animal origin: cod liver, herring, mackerel, etc.) (Luna-Rodríguez et al., 2008; Torres-Aguirre, 2007). Therefore, consumers may benefit with the addition of carotenoids from byproducts of shrimps and other crustacean improving their ingestion of nutraceutical compounds at a very low cost.

5. Acknowledgments

The authors acknowledge the financial support to acquire the materials and reagents used in this research from the Research and Postgraduate Support Program (*PAIP* in Spanish) Number 50009067 of the Faculty of Chemistry of the National Autonomous University of Mexico through the last author.

6. References

Ameh, A.O., Abutu, D., Isa, M.T., and Rabiu, U., 2014, Kinetics of demineralization of shrimp shell using lactic acid. Electronic Journal of Practices and Technologies, 24, 13-22.

AOAC, 2001, Official Methods of Analysis of the Association of Official Analytical Chemistry, Vol. 2, Parte 2, 17th Ed., AOAC, 1417 pp., Washington, D.C., U.S.

Espinosa-Manfugás, J., 2007, Sensory evaluation (*Evaluación sensorial* in Spanish), Editorial Universitaria, La Habana, Cuba.

Grung, M., D'Souza, F.M.L., Borowitzka, M., and Liaaen-Jensen, S., 1992, Algal carotenoids 51. Secondary carotenoids 2. *Haematococcus pluvialis* aplanospores as a source of (3S, 3'S)-astaxanthin esters, Journal of Applied Phycology, 4, 165-171.

Gulzar, S. and Benjakul, S., 2018, Ultrasound waves increase the yield and carotenoid content of lipid extracted from cephalothorax of Pacific white shrimp (*Litopenaeus vannamei*), Wiley Online Library, 120(5), 1700495. https://onlinelibrary.wiley.com/doi/abs/10.1002/ejlt.201700495

Higuera-Ciapara, I., Félix-Valenzuela, L., and Goycoolea, F.M., 2006, Astaxanthin: A review of its chemistry and applications, Critical Reviews in Food Science, 46, 185-196. DOI: 10.1080/10408690590957188

Luna-Rodríguez, A., Medina-Reyna, C. E., Pedroza-Islas, R., and Durán-de-Bazúa, C., 2008, Oleous extraction of carotenoids from shrimp cephalothorax and its effect on a microencapsulated diet with Nauplii larvae, Journal of Aquatic Food Production Technology, 17(4), 367-386. https://doi.org/10.1080/10498850802392072

Mendes, T., Andrade, J., Andrade, A.H., Oliveira, J.M., da-Conceição, M.L., 2013, Flour production from shrimp by-products and sensory evaluation of flour based products, Scientific Electronic Library Online, 48(8), 962-967.

SAGARPA, 2018, Blog SAGARPA, Shrimp, growth production, Secretary (Ministry) of Agriculture, Rural Development, Fisheries, and Food (*Camarón, producción en crecimiento, Secretaría de Agricultura Desarrollo Rural Pesca y Alimentación, SAGARPA*, in Spanish). https://www.inforural.com.mx/camaron-produccion-en-crecimiento/

Simpson, B.K. and Haard, N.F., 1985, The use of proteolytic enzymes to extract carotenoproteins from shrimp wastes, Journal of Applied Biochemistry, 7(3), 212-222.

Takeungwongtrakul, S., Benjakul S., Santoso, J., Trilaksani, W., Nurilmala, M., 2013, Extraction and stability of carotenoid-containing lipids from hepatopancreas of Pacific white shrimp (*Litopenaeus vannamei*), Journal of Food Processing and Preservation, 39(1), 10-18. https://doi.org/10.1111/jfpp.12203

Torres-Aguirre, L., 2007, Extraction of carotene-proteins from shrimp cephalothorax with edible oils (*Extracción de caroteno-proteínas de cefalotórax de camarón con aceites comestibles*, in Spanish), Professional thesis, Faculty of Chemistry, National Autonomous University of Mexico (*UNAM*, in Spanish), Mexico City, Mexico.

AMMI Analysis for Yield Stability of Yardlong Bean (*Vigna unguiculata (L.) Walp. ssp. sesquipedalis*)

Pramote Pornsuriya [a*], Apisit Chittawanij [a], Supansa Chinaworn [a] and Arak Tira-umphon [b]

a, Division of Plant Production Technology, Faculty of Agriculture and Natural Resources, Rajamangala University of Technology Tawan-ok, Chonburi, 20110, Thailand.
b, School of Crop Production Technology, Institute of Agricultural Technology, Suranaree University of Technology, Nakhon Ratchasima, 30000, Thailand
*Corresponding author. Tel.: +668-6845-3795 ; *E-mail address:* : *pramote_po@rmutto.ac.th*

Abstract

The objective of this study was to determine genotype-environment interaction and yield stability of yardlong bean genotypes. Field experiments were conducted with 10 yardlong bean lines and cultivars under nine different environments in a randomized complete block design with three replications in each environment. Combined analysis of variance showed highly significant for genotypes (G), environments (E), and genotype-environment interaction (GEI). The results of AMMI (additive main effect and multiplicative interaction) analysis indicated that the first three multiplicative components of the interaction (IPCA1, IPCA2 and IPCA3) were all significant and could explain 91.40 percent of the total GEI variance. The first genotype in stability rank according to AMMI analysis was Number 1 (G5), with the lowest AMMI stability value (ASV = 1.271), ASV rank first and the yield of 14.368 t/ha, which was higher than grand mean (14.135 t/ha). The second and third stability ranks were Number 33 (G10) and Number 30 (G9), with ASV rank of 2 and 3, respectively and the yield of 14.353 and 15.079 t/ha, respectively. These three lines were not different in yield. Bangpra2 (G2) and No.25 (G8) gave high yield (16.249 and 15.548 t/ha, respectively) but they had high values of AMMI stability value (ASV = 4.595 and 3.374, respectively), implied that they were highly affected from GEI and might be suitable for favorable environments. In conclusion, productivity and yield stability should be considered together in the selection of outstanding genotypes.

Keywords: yardlong bean, yield stability, GEI, AMMI model

1. Introduction

Yardlong bean (*Vigna unguiculata* (L.) Walp. subsp. *sesquipedalis* (L.) Verdc.) is a member of the Fabaceae family. It is primarily cultivated for their crisp, supple green pods, which can be consumed both raw and cooked. According to Ano and Ubochi (2008), it is a particularly nutrient-dense vegetable that has a good quantity of digestible protein in both the pods and the leaves. It is cultivated year-round and is one of the most significant vegetables in Thailand. Yardlong bean had around 6,437.5 hectares of plantation nationwide, and it generated about 61,104 tons of crop during the 2021 planting season, according to Department of Agricultural Extension (2022).

Both genes and environment have a role in determining a plant phenotypic. The genotype-environment interaction weakens the relationship between phenotypic and genotypic values, biases estimate of gene effects, and impairs the capacity to combine different features sensitive to environmental changes. Genotype-environment interaction (GEI) makes it difficult to identify superior genotypes for a variety of circumstances and necessitates the study of genotypes across multiple conditions to ascertain their actual genetic potential (Yaghotipour and Farshadfar, 2007). In practically all-important crops, including yardlong bean genotypes, the significance of GxE interactions has been proven in national cultivar evaluation and breeding programs (Pornsuriya et al., 2017; Pornsuriya et al., 2021). Numerous statistical techniques, both parametric and non-parametric, have been suggested to investigate the interactions between genotype and environment (Lin et al., 1986; Becker and Léon, 1988; Crossa, 1990; Lin and Binns, 1994; Hussein et al., 2000; Mohammadi and Amri, 2008; Mohammadi et al., 2010).

To assess the effect of GEI, it can be done in both univariate analysis and multivariate analysis. The most commonly used univariate methods are the Finlay and Wilkinson (1963) model and the Eberhart and Russell (1966) model, neither of which takes into account the majority of GEI effects. Both models use regression analysis, which is univariate, while GEI results are multivariate (Akpan and Udoh, 2017). Therefore, the most reliable method for analyzing cultivar stability should be the multivariate analysis method (multivariate model) (Badu-Apraku et al., 2012).

AMMI (additive main effects and multiplicative interaction) analysis is a multivariate method that combines analysis of variance (ANOVA) and Principal Component Analysis (PCA). It is therefore a highly effective method to explain most of the effects of GEI (Ebdon and Gauch, 2002). AMMI biplots also allow visualization and classification of both genotypes and environments on the same graph (Gauch, 2006), enabling accurate analysis of crop yield tests in multiple environments (Zobel et al., 1988; Crossa et al., 1990; Gauch and Zobel, 1996).

Testing the yield of plant cultivars in many areas is often costly. However, if different environments are created by planting experimental material at various sowing dates, using various spacings and doses of fertilizer, and using various irrigation levels, etc., unilocational trials can also serve the purpose. (Ottai et al., 2006). Pornsuriya et al. (2017) also reported the study on nitrogen fertilizer dose-dependent yield stability of yardlong bean lines/cultivars exposed to 6 modified environments.
The purpose of this study was to determine yield stability of 10 yardlong bean genotypes by using AMMI analysis.

2. Methodology

Ten yardlong bean cultivars and lines, including 6 new superior lines, 2 parental lines, and 2 commercial cultivars, were planted for a yield trial in nine different conditions. They were set up in a randomized complete block design with three replications for each environment. There were 24 plants per plot (2 plants per hill) in each experimental unit (plot size) of 1 × 3 sqm, 2 rows, and 50 x 75-cm spacing (hill x row). Plants were cultivated in beds covered with plastic mulch under a bamboo stake-supported trellising system. According to locations, seasons, and fertilizer treatments, the nine environments were set up for different conditions as described in Table 1.

Table 1. The nine modified growing environments were set for the stability study of 10 yardlong bean genotypes.

Growing Environments[1/]	Planting Seasons	Planting Dates	Places	Fertilizer applications[2/]
1	1	Jan 13, 2020	RMUTTO, Chonburi	Chemical fertilizers
2	1	Jan 13, 2020	RMUTTO, Chonburi	Cow manure
3	2	Apr 30, 2020	RMUTTO, Chonburi	Chemical fertilizers
4	2	Apr 30, 2020	RMUTTO, Chonburi	Cow manure
5	3	Jul 30, 2020	RMUTTO, Chonburi	Chemical fertilizers
6	3	Jul 30, 2020	RMUTTO, Chonburi	Non-fertilizer
7	4	Nov 23, 2020	RMUTTO, Chonburi	Chemical fertilizers
8	5	Nov 28, 2020	Chanthaburi Land Development Station, Chanthaburi	Chemical fertilizers + Cow manure + spraying bio-extract from durian flowers
9	6	Dec 19, 2020	Uthaithani College of Agriculture and Technology, Uthaithani	Chemical fertilizers

[1/] Chemical fertilizers and cow manure or non-feritlizer were applied to modify the growing environments conducted in the same place and planting date.
[2/] Chemical fertilizers: - 15-15-15 (N-P-K) 500 kg/ha and 46-0-0 (N-P-K) 125 kg/ha; cow manure 11.13 t/ha; bio-extract from durian flowers 225 ml/l, sprayed weekly, once a week.

The yield data (t/ha) were subjected to combined analysis of variance (International Rice Research Institute, 2014) and AMMI analysis which is a combination of analysis of variance and multiplication effect analysis, was performed according to the method described by Gauch and Zobel (1996). The AMMI stability value (ASV) was calculated as described by Purchase (2000). A more stable genotype across environments is indicated by lower ASV scores. The stability index (SI) was calculated from the sum of ASV rank and yield rank (Oliveira et al., 2014). Smaller stability index (SI) indicates a more stable genotype across environments.

3. Results and Discussion

3.1 Genotype by Environment Interactions (GEI)

The combined analysis of variance (ANOVA) for yield of yardlong bean genotypes in nine environments is displayed in Table 2. The contributions of genotypes (G), environments (E), and their interactions (GEI) on yardlong bean yields were 4.30%, 77.68%, and 8.58%, respectively, which were all highly significant ($P < 0.01$). The environment effects provided the highest contribution to the yield variation, implied that there were diverse variations of the nine environments, as shown in Figure 1. Similar findings were discovered for peanuts, where 93% of the variation was attributed to environmental factors and the GxE interaction, highlighting the difficulty of choosing the best genotypes (Oliveira and Godoy, 2006). The high proportion of variance among the environments resulted in significant difference among the environment means. The significance of the GEI indicated that the genotypes varied from environment to environment, thus further analysis for the stability of the genotypes according to the AMMI method could be performed (Farshadfar and Sutka, 2006).

3.2 AMMI analysis for GEI

From the results of AMMI analysis in yield characteristic, IPCA1, IPCA2 and IPCA3 were all significant and could explain 58.4, 20.0 and 13.0 percent of the GEI variance, respectively. The first 2 IPCA (IPCA1 and IPCA2), totally accounted for 78.40% of the overall GEI variance in this study, were generally used for explaining GEI in AMMI analysis. Gauch and Zobel (1996) showed that AMMI1 with IPCA1 and mean yield, and AMMI2 with IPCA1 and IPCA2 are usually selected, and the graphical representation of axes are generally informative.

When considering the cultivar stability in terms of yield, from the biplot between IPCA1 and mean yield (AMMI1), it was found that Number 1 (G5) was the most stable variety, because it was in the position close to position 0 of IPCA1 (Figure 2), and also yielded (14.368 t/ha) more than the grand mean (14.135 t/ha) axis. The AMMI1 biplot was constructed from the first interaction principal component value and mean grain yield, indicated that genotype and environments found at the right side of the perpendicular line passing though the origin, gave a mean yield greater than the grand mean (14.135 t/ha). The graphical results corresponded to the IPCA1 and yield values shown in Table 3, and also corresponded to the AMMI stability value (ASV = 1.271), of which Number 1 (G5) had the lowest ASV, therefore it was ranked in the first position of stability rank (Table 3). The second and third stability rank according to AMMI analysis were Number 33 (G10) and Number 30 (G9), with ASV rank of 2 and 3, respectively and the yield of 14.353 and 15.079 t/ha, respectively (Table 3). It corresponded to AMMI1 Biplot (Figure 2), which its position was close to zero of PC1 axis and yielded more than average of the yield (horizontal axis).

Bangpra2 (G2) and No.25 (G8) gave high yield (16.249 and 15.548 t/ha, respectively) but they had high values of AMMI stability value (ASV = 4.595 and 3.374, respectively), implied that they were highly affected from GEI and might be suitable for specific environment. These results corresponded to the research of Pornsuriya et al. (2021), studied on yield stability of ten genotypes of yardlong bean following Eberhart and Russell (1966) method and reported that Bangpra2 (G2) and No.25 (G8) had highly positive phenotypic index (yielded more than average) and regression coefficient around 1, but the deviation from regression values were significantly different from zero, signified that there was high sensitivity to environmental changes, thus these 2 lines quite gave high yield performance when environmental conditions were conductive (Arshad et al., 2003).

Lamnamch (G3) and Tarntong (G4) genotypes, which were commercial cultivars, were the less stable cultivars according to AMMI stability values (ASV = 5.318 and 4.792, respectively), and yielded (12.951 and 12.487 t/ha, respectively) lower than average (Table 3). The results of these two cultivars were in line with the report of Pornsuriya et al. (2021).

The effect of environment on yield characteristic, considering Figure 3, it was discovered that environments 7 (E7) and 2 (E2) had the most effects on cultivar stability, because it is located closest to the center of both axes. On the other hand, environment 3, 4, 9 and 1 (E3, E4, E9 and E1) contributed the most to the significance of GEI because they were positioned far from the central intercept of the AMMI2 biplot.

The AMMI technique has three primary applications. The first is model diagnoses, in the initial statistical analysis of yield experiments, AMMI is more suited, because it offers a diagnostic tool for identifying alternative models as sub instances when these are more appropriate for specific data sets (Gauch, 1988). Second, AMMI highlights patterns and connections between genotypes and environments and clarifies the G-E interaction. The third application is to increase the precision of yield estimates (Zobel et al., 1988; Crossa et al., 1990). Similar studies were performed using AMMI analysis to determine yield stability in legumes, including faba bean, cowpea and snap beans (Afeta et al., 2019; Tadesse et al., 2021; Tola et al., 2021; Araméndiz-Tatis et al., 2021; Tryphone and Bilaro, 2022).

Table 2 Analysis of variance for yield (t/ha) of 10 yardlong bean lines/cultivars under 9 environments, including the G×E interaction partition according to the AMMI analysis.

		Yield (t/ha)		
Source	df	MS	% Explained	% Accumulated
Environments (E)	8	872.9736**		
Block/Environments	18	6.0430 ns		
Genotypes (G)	9	42.9128**		
G x E	72	10.7190**		
IPCA1	16	28.1540**	58.40	58.40
IPCA2	14	11.0410**	20.00	78.40
IPCA3	12	8.3392*	13.00	91.40
IPCA4	10	3.4670ns	4.50	95.90
IPCA5	8	2.4038 ns	2.50	98.40
IPCA6	6	1.1529 ns	0.90	99.30
IPCA7	4	1.2093 ns	0.60	99.90
IPCA8	2	0.5014 ns	0.10	100.00
Pooled Error	162	4.5648		
Total	269			

IPCA = Interaction Principal Component Axis
ns Not significant
*, ** Significant at P < 0.05 and 0.01, respectively.

Table 3 The first and second Interaction Principal Component Axis (IPCA), yield (t/ha), AMMI stability value (ASV), stability index (SI) and stability rank of 10 yardlong bean lines/cultivars.

Cultivars	IPCA1	IPCA2	Yield (t/ha)	ASV	ASV rank	Yield rank	Stability Index	Stability rank
BP Purple (G1)	0.874	-1.164	12.708 c	2.800	5	9	14	5
Bangpra2 (G2)	-1.575	0.231	16.249 a	4.595	8	1	9	3
Lamnamch (G3)	1.774	1.250	12.951 c	5.318	10	8	18	6
Tarntong (G4)	1.628	0.684	12.487 c	4.792	9	10	19	7
Number 1 (G5)	0.315	-0.880	14.368 abc	1.271	1	4	5	1
Number 17 (G6)	-0.544	-0.186	14.286 abc	1.597	3	6	9	3
Number 18 (G7)	0.224	-1.461	13.318 bc	1.600	4	7	11	4
Number 25 (G8)	-1.140	0.593	15.548 a	3.374	7	2	9	3
Number 30 (G9)	-1.139	0.529	15.079 ab	3.361	6	3	9	3
Number 33 (G10)	-0.416	0.406	14.353 abc	1.278	2	5	7	2
Grand mean (t/ha)			14.135					
CV. (%)			15.12					

Means with the same letter in a column are not significantly different at $DMRT_{0.05}$

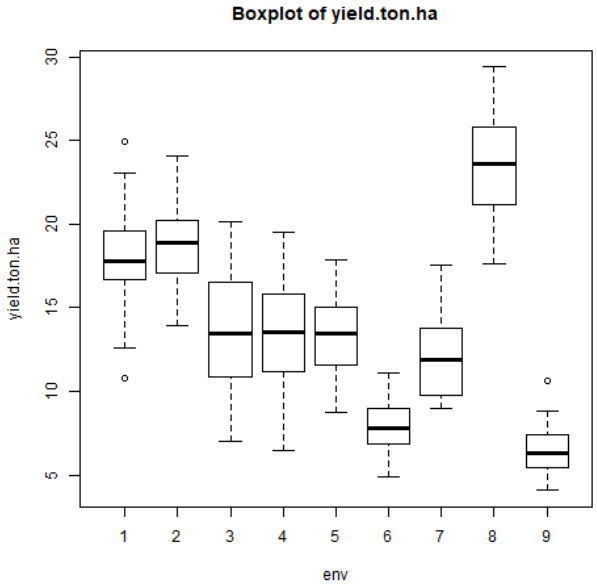

Figure 1 Boxplot showing variations for yield (t/ha) of 10 yardlong bean lines/cultivars in 9 environments.

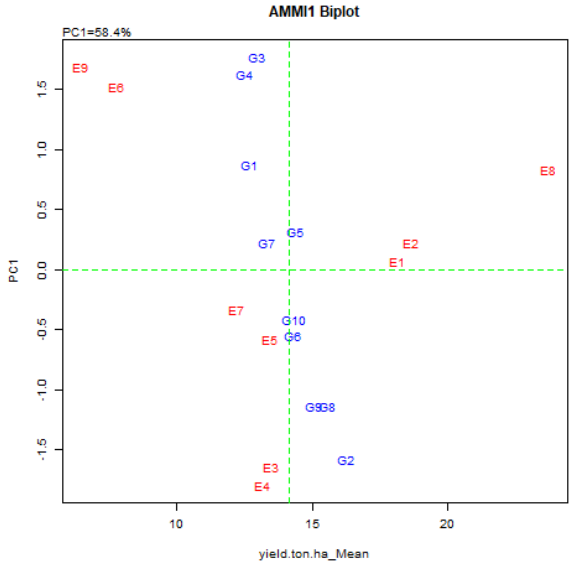

Figure 2 AMMI1 biplot showing the IPCA1 vs. means for yield (t/ha) of 10 yardlong bean lines/cultivars evaluated in 9 environments.

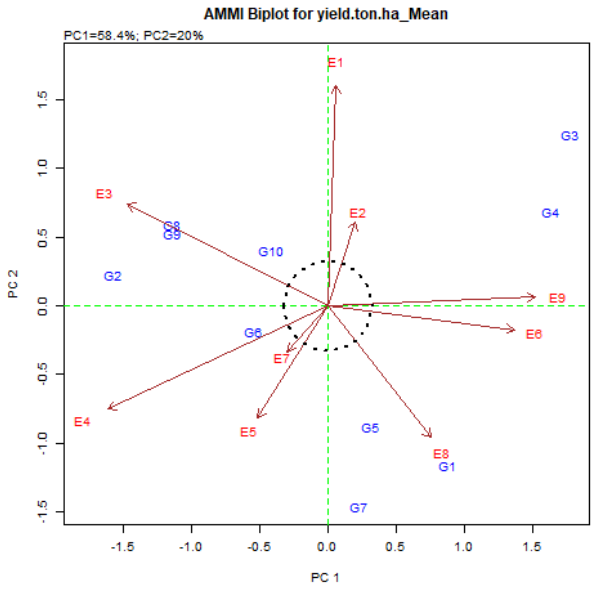

Figure 3 AMMI2 biplot showing the first two principal axes of interaction (IPCA1 vs. IPCA2) for yield (t/ha) of 10 yardlong bean lines/cultivars evaluated in 9 environments.

4. Conclusions

Genotype-by-environment interaction (GEI) has been a significant and difficult obstacle to plant breeders accomplishing performance testing. GEI lowers the relationship between phenotypic and genotypic values and biases estimates of the effects of genes for traits that are susceptible to environmental changes. The results of this investigation revealed that yardlong bean line No. 1 (G5) was the most stable in yield performance according to AMMI analysis, indicating that it had wide adaptability. The second and third stability ranks were Number 33 (G10) and Number 30 (G9). Bangpra2 (G2) and No.25 (G8) had high yields but might be highly affected by GEI, so they should be suitable for favorable environments. In conclusion, to lessen the impact of GE interaction and to increase the precision and perfection of genotype selection, yield and stability of performance should be taken consideration simultaneously.

5. Acknowledgements

This research project is funded by the Agricultural Research Development Agency (Public Organization) (ARDA) under Grant Agreement No. PRP6305030250. The Department of Plant Production Technology's field workers and research assistants deserve appreciation from the authors for their cooperation and assistance.

6. References

Afeta, T., Tesso, B., and Lule, D., 2019, Interaction effects of genotype by environment and AMMI stability analysis of seed yield and agronomic performance of Faba Bean genotypes in the highlands of Oromia Region, Ethiopia. Int. J. Res. Agric. Forestry, 6, 22-31.

Akpan, E.A. and Udoh, V.S, 2017, Evaluation of cassava (*Manihot esculenta* crantz) genotype for yield and yield component, tuber bulking, early maturity in cross river basin flood plains. Canadian Journal of Agriculture and Crops, 2(2), 68-73.

Ano, A.O., and Ubochi, C.I., 2008, Nutrient composition of climbing and prostrate vegetable cowpea accessions. African Journal of Biotechnology, 7(20), 3795-3798.Department of Agricultural Extension. 2022. Report on agricultural statistics (Ror Tor. 01), vegetables group, country level. Department of Agricultural Extension. Available from: https://production.doae.go.th/site/login. [accessed on 27 Mar 2022].

Araméndiz-Tatis, H., Cardona-Ayala, C., and Espitia-Camacho, M., 2021, Stability and phenotypic adaptability by AMMI analysis in cowpea beans (*Vigna unguiculata* (L.) Walp.). Revista Ciência Agronômica, v. 52, n. 3, e20207304.

Arshad, M., Bakhsh, A. Haqqani, M. and Bashir, M., 2003, Genotype-environment interaction for grain yield in chickpea (*Cicer arietinum* L.) Pakistan Journal of Botany 35: 181-186.

Badu-Apraku, B., Oyekunle, M., Obeng-Antwi, K., Osuman, A.S., Ado, S.G., Coulibay, N., Yallou, C.G., Abdulai, M., Boakyewaa, G.A. and Didjeira, A., 2012, Performance of extra-early maize cultivars based on GGE biplots and AMMI analysis. Journal Agricultural Sciences, 150, 473-483.

Becker, H.C. and Leon, J., 1988, Stability analysis in Plant Breeding. Plant Breeding, 101, 1-23.

Crossa J., 1990, Statistical analysis of multilocation trials. Advances in Agronomy, 44, 55-85.

Crossa J, Gauch, H.G, and Zobel, R.W., 1990, Additive main effect and multiplicative interaction analysis of two international maize cultivar trials. Crop Sci, 30, 493–500.

Ebdon, J.S. and Gauch, H.G., 2002, Additive main effects and multiplicative interaction analysis of national turfgrass performance trials. Crop Science, 42, 497-506.

Eberhart, S.A. and Russell, W.A., 1966, Stability parameters for comparing varieties. Crop Science, 6, 36-40.

Farshadfar, E., and Sutka, J., 2006, Biplot analysis of genotype-environment interaction in durum wheat using the AMMI model. Acta Agron Hung, 54(4), 459–467.

Gauch, H.G., 1988, Model selection and validation for yield trials with interaction. Biometrics, 44, 705-715.

Gauch, H.G., 2006, Statistical analysis of yield trials by AMMI and GGE. Crop Science, 46, 1488-1500.

Gauch, H.G. and Zobel, R.W., 1996, AMMI analysis of yield trials. pp. 85-122. In Kang, M.S. and H.G. Gauch (eds.). Genotype by environment interaction. CRC Press, Boca Raton, FL, USA.

Hussein, M.A., Bjornstad, A. and Aastveit, A.H., 2000. SASG 3 ESTAB: A SAS program for computing genotype 3 environment stability statistics. Agron J., 92, 454–459.

International Rice Research Institute, 2014, Statistical Tool for Agricultural Research, User's Manual. Plant Breeding, Genetics and Biotechnology Division, International Rice Research Institute, Los Baños, Philippines.

Lin, C.S. and Binns, M.R., 1994, Concepts and methods for analyzing regional trial data for cultivar and location selection. Plant Breed Rev, 12, 271–297.

Lin, CS, Binns M.R. and Lefkovitch, L.P., 1986, Stability analysis: Where do we stand?. Crop Sci 26: 894- 900.

Mohammadi, R. and Amri, A., 2008. Comparison of parametric and non-parametric methods for selecting stable and adapted durum wheat genotypes in variable environments. Euphytica, 159, 419–432.

Mohammadi, R., Mozaffar Roostaei, M., Yousef, A., Mostafa, A. and Amri, A., 2010, Relationships of phenotypic stability measures for genotypes of three cereal crops. Can J Plant Sci, 90, 819-830.

Oliveira, E.J.D., Freitas, J.P.X.D. and Jesus, O.N.D., 2014, AMMI analysis of the adaptability and yield stability of yellow passion fruit varieties. Scientia Agricola 71: 139-145.

Oliveira, E.J., Godoy, I.J., 2006, Pod yield stability analysis of runner peanut lines using AMMI. Crop Breeding and Applied Biotechnology, 6, 311-317.

Ottai, M.E.S., Aboud, K.A., Mahmoud, I.M. and El-Hariri, D.M., 2006, Stability analysis of roselle cultivars (*Hibiscus sabdariffa* L.) under different nitrogen fertilizer environments. World Journal of Agricultural Science 2(3): 333-339.

Pornsuriya, P., Pornsuriya, P. and Kwun-on, P., 2017, Stability analysis of yardlong bean under different nitrogen fertilizer environments. The research report (completed). Rajamangala University of Technology Tawan-ok, Chonburi.

Pornsuriya, P., Pornsuriya, P., Kwun-on, P. and Chittawanij, A., 2021, Yield stability of new elite lines of yardlong bean (Vigna *unguiculata* (L.) Walp. subsp. *sesquipedalis* Verdc.). International Journal of Agricultural Technology, 17(6), 2251-2264.

Purchase, J.L., Hatting, H. and Vandeventer, C.S., 2000, Genotype × environment interaction of winter wheat (*Triticum aestivum* L.) in South Africa. II. Stability analysis of yield performance. South African Journal of Plant and Soil 17: 101-107.

Tadesse, T., Tekalign, A., Sefera, G., and Asmare, B., 2021, AMMI Analysis for Grain Yield Stability in Faba Bean Genotypes Evaluated in the Highlands of Bale, Southeastern Ethiopia. Research & Development, 2(2), 27-31.

Tola, M., Arega, A., Debela, C., Bekele, S., and Dhabessa, A., 2021, Genotype× Environment Interaction and Yield Stability of Large Speckled Common Bean (Phaseolus vulgaris L.) Genotypes in Ethiopia Using AMMI Analysis. Environment, 12(9), 12-17.

Tryphone, G. M., and Bilaro, A. L., 2022, AMMI Analysis for Stability and Genotype by Environment Interaction on Common Bean (Phaseolus vulgaris L.) Genotypes in Mbeya Region, Tanzania. Current Journal of Applied Science and Technology, 41(29), 8-15.

United States Department of Agriculture, 2012, *Vigna unguiculata* (L.) Walp. subsp. *sesquipedalis* (L.). Verdc. Available from: http://www.ars-grin.gov/cgibin/npgs/html/taxon. pl?41646. [accessed on 19 April 2023].

Yaghotipoor, A. and Farshadfar, E., 2007, Non-parametric estimation and component analysis of phenotypic stability in chickpea (*Cicer arietinum* L.). Pak J Biol Sci, 10, 2646-2646.

Zobel, R.W., Wright, M.J. and Gauch, H.G., 1988, Statistical analysis of a yield trial. Agronomy Journal, 80, 388-393.

Genetic Divergence in 23 Commercial Cultivars of Yard Long Bean (*Vigna unguiculata* (L.) Walp. ssp. *sesquipedalis*)

Ruethairat Mangta [a*], Pramote Pornsuriya [a], Supaporn Ieamkheng [a] and Rusama Marubodee [a]

a, Division of Plant Production Technology, Faculty of Agriculture and Natural Resources, Rajamangala University of Technology Tawan-ok, Chonburi, 20110, Thailand.

*Corresponding author. Tel.: 064-4265256 ; *E-mail address:* : *Ruethairat.man@rmutto.ac.th*

Abstract

The success of phenotypic selection depends upon the range of genetic diversity available in the population. The objectives of this research are to compare the horticultural characteristics of 23-yard-long bean genotypes and to identify the desired genotypes that would be in the breeding program. Therefore, 20 commercial cultivars of yard long bean, namely Naka, Greenarrow 692, Saifon, Nuethong 9, Saitara, Tarnthong, Lamnamphong 2, Suvarnabhum, Saisawan, Petkajee, Sornsawan 5, Moneygreen, Rangsit 888, Lamnamchee,Yodpetkasem, Airgreen 99, Munggornyok 9, Choiphiphop, Chiataisen, and Nigrodok, and 3 improved lines namely Green 33, Bangpra 2, and Purple 33, were laid out in a randomized complete block design with 3 blocks. The values of 12 morphological characteristics were multivariate analyzed using Mahalanobis distance to assess genetic divergence, and then cluster analysis was performed to group 23 yard long bean genotypes using Tocher's method. The results revealed that most characteristics of yard long bean genotypes were significantly different. According to the Mahalanobis genetic distance, the genotypes fall into six clusters. Cluster 2 had the maximum (13) and cluster 4, 5, 6 had the minimum (1) number of genotypes. Cluster 2 had highest intra-cluster distance (18.92) and the lowest in cluster 4, 5 and 6 (0). The inter-cluster D^2 values of six cluster revealed that the highest inter-cluster generalized distance (122.82) was between cluster 5 and cluster 4, while the lowest (22.25) was between cluster 2 and cluster 1. The percent contribution of each character towards divergence was as followings; pod length with the maximum contribution of 25.69%, followed by yield per plant (25.30%), leaf length (10.28%), plant length (8.30%), pod width (7.51%) and pod weight (5.53%), respectively.

Keywords: Genetic divergence, cultivars, Mahalanobis distance, yard long bean

1. Introduction

Yard long bean is a leguminous plant belonging to the fabaceae family, which its scientific name is *Vigna unguiculata* (L.) Walp. ssp. *sesquipedalis* Verdc. (2n=22). It is a climbing plant that originated in India and China. Generally, yard long bean is easily grown in all types of soil. It is self-pollinating the flowers are either purple or white. Typically, flower are bigger than cowpeas. Black, brown and a variety of spotted colours and has possible seed colours. It is known as a vegetable and herb that is popular for cooking and consuming. It is rich in minerals and vitamins that are important and essential to humans. Young pods consumed as vegetables and the pods are used in a nature similar to that of conventional field beans (Saidaiah et al., 2019). It is also found that yard long bean enriches the soil by fixing atmospheric nitrogen in nodules on its roots. With the help of nitrogen fixing bacteria, the plant can make its own food (United States Department of Agriculture, 2012). It can be planted in every region, every season, throughout the year of Thailand, and is an economically important plant with high nutritional values.

The success of a breeding program primarily depends on the diversity of plant germplasm presented. Plant genetic diversity is an important factor in plant breeding programs to achieve desired traits. Multivariate analysis is useful in identifying plant germplasm and is also an important method for measuring genetic distance by using the data from the phenotypic characteristics of plants. Better knowledge on genetic diversity or genetic similarity could help to get long term selection gain in plants (Chowdhury *et al.*, 2015). Evaluation of genetic diversity is important to know the source of genes for a particular character within the available germplasms (Tomooka, 2019). The Mahalanobis distance analysis method is the one method that has been used to estimate genetic differences in many plant species and also in yard long bean (Asoontha and Abraham, 2017; Bhagavati *et al*., 2018)

Therefore, this experiment aimed to compare the horticultural characteristics of 23-yard-long bean genotypes and to assess genetic divergence by analyzing Mahalanobis distance for classifying the genetic groups of 23-yard long bean genotypes.

2. Methodology

Yard long bean genotypes used in the experiment were 20 commercial cultivars, namely Naka, Greenarrow 692, Saifon, Nuethong 9, Saitara, Tarnthong, Lamnamphong 2, Suvarnabhum, Saisawan, Petkajee, Sornsawan 5, Moneygreen, Rangsit 888, Lamnamchee,Yodpetkasem, Airgreen 99, Munggornyok 9, Choiphiphop, Chiataisen, and Nigrodok, and 3 improved lines namely Green 33, Bangpra 2, and Purple 33, totally 23 genotypes (Table 1). The experiment was carried out at the agricultural experimental greenhouse, Department of Plant Production Technology, Faculty of Agriculture and Natural Resources, Rajamangala University of Technology Tawan-ok, Bangpra Campus, Chonburi Province. The experimental design was a Randomized Complete Block Design with 3 replications (blocks). Each experimental unit contained 4 plants (2 planting hills and 2 plants/hill). Planting spacings

were 50 cm between hills and 75 cm between rows. Data of horticultural characteristics were collected as follows; plant length (cm), number of branches per plant, leaf length (cm), leaf width (cm), leaf greenness (SPAD unit, using SPAD-502 chlorophyll meter), day to first flowering, pod length (cm), pod width (mm), pod weight (g), number of seeds per pod, number of pods per plant and yield per plant (g). The grouping of genotypes into different cluster was done using Tocher's method according to the D^2 Mahalanobis values. All data were analysed using STAR (International Rice Research Institute, 2014) and TNAUSTAT (Manivannan, 2014) statistical packages.

Table 1 List of 23 genotypes of yard long bean.

Genotype No.	Genotype Name	Sources
1	Naka	Ratchaburi Province
2	Greenarrow 692	Ratchaburi Province
3	Saifon	Ratchaburi Province
4	Nuethong 9	Ratchaburi Province
5	Saitara	Ratchaburi Province
6	Tarnthong	Ratchaburi Province
7	Lamnamphong 2	Nakhonratchasima Province
8	Suvarnabhum	Ratchaburi Province
9	Saisawan	Ratchaburi Province
10	Petkajee	Ratchaburi Province
11	Sornsawan 5	Ratchaburi Province
12	Moneygreen	Ratchaburi Province
13	Rangsit 888	Ratchaburi Province
14	Lamnamchee	Nakhonratchasima Province
15	Yodpetkasem	Ratchaburi Province
16	Airgreen 99	Ratchaburi Province
17	Munggornyok 9	Nakhonratchasima Province
18	Choiphiphop	Ratchaburi Province
19	Chiataisen	Ratchaburi Province
20	Nigrodok	Ratchaburi Province
21	Green 33	Improved line (RMUTTO)
22	Bangpra 2	Improved line (RMUTTO)
23	Purple 33	Improved line (RMUTTO)

3. Results and Discussion

3.1 Comparison of horticultural characteristics

Mean comparisons of 12 characteristics of 23 genotypes were depicted in Table 2 and 3. Coefficient of variation (CV), calculated as a percentage, standard error of the mean (SE) and ANOVA (F-test) of 23 genotypes for the 12 characters are also presented (Table 2 and 3). Therefore, from Table 2 and 3, the top three characteristics with the maximum CV were number of branches per plant, number of pods per plant, yield per plant (31.70, 22.11 and 18.01%, respectively), which implied the high variation of these traits. The results from ANOVA found that plant length, leaf length and leaf width (Table 2) were highly significant different ($p<0.01$) among genotypes. Cultivars ranking in top three for plant length were Chiataisen, choiphiphop, Naka (468.50, 462.50 and 458.17 cm, respectively). The leaf length showed that Lamnamphong 2, Suvarnabhum and Nuethong 9 were the first 3 cultivars on the top (18.50, 18.23 and 18.10 branches/plant, respectively). The first top three cultivars for leaf width were Suvarnabhum, Petkajee and Rangsit 888 (12.83, 12.67 and 12.60 cm, respectively). Table 2 also depicted that there were not significant differences ($p>0.05$) in number of branches per plant, leaf greenness and days to first flowering. Green 33, Airgreen 99 and Nuethong 9 were the first top three for number of branches per plant (3.67, 3.33 and 3.00 branches/plant, respectively). Leaf greenness showed that Naka, Lamnamchee and Airgreen 99 were the first top three (65.57, 65.43 and 62.63 SPAD unit, respectively). Airgreen 99, Nigrodok and Purple 33 were the first top three in days to first flowering (44.00, 42.33 and 42.00 days, respectively). Table 3 depicted that there were significant differences ($p<0.01$) in pod length, number of pods per plant, yield per plant and pod weight ($p<0.05$), and no difference ($p>0.05$) in pod width and number of seeds per pod. Cultivars possessing the top three for pod length were Sornsawan 5, Munggornyok 9 and Saisawan the first top three (71.60, 64.47 and 62.90 cm, respectively). Pod width described that Petkajee, Naka and Airgreen 99 were the first top three (9.18, 8.37 and 8.25 mm, respectively. Whereas Sornsawan 5, Saitara and Saifon were the first top three for pod weight (38.41, 36.78 and 35.79 g, respectively). For number of seeds per pod, Chiataisen, Munggornyok 9 and Saifon were the first top three (17.30, 17.27 and 17.07 seeds/pod, respectively. Number of pods per plant revealed that Airgreen 99, Naka and Yodpetkasem were the first 3 cultivars on the top (14.97, 13.83 and 11.58 pods/plant, respectively). For yield per plant, Airgreen 99, Naka and Yodpetkasem were the first top three (327.78, 275.00 and 258.33 g/plant, respectively.

Table 2 Mean values for horticultural characteristics of 23 yardlong bean cultivars.

Genotype No.	Genotype Name	Horticultural traits					
		PL	NB	LL	LW	LG	DFF
1	Naka	458.17 a	1.83	17.78 a	11.80 ab	65.57	39.33
2	Greenarrow 692	408.00 a-e	2.17	17.83 a	11.67 ab	61.37	39.33
3	Saifon	381.83 b-f	2.17	14.43 cd	9.13 de	52.20	41.33
4	Nuethong 9	436.83 a-c	3.00	18.10 a	12.43 ab	59.17	40.33
5	Saitara	432.83 a-d	1.83	18.00 a	11.13 a-c	55.07	41.00
6	Tarnthong	381.17 b-f	2.33	16.77 ab	12.13 ab	57.77	39.67
7	Lamnamphong 2	345.50 ef	1.83	18.50 a	12.50 ab	52.87	41.33
8	Suvarnabhum	396.50 a-e	2.00	18.23 a	12.83 a	54.10	41.67
9	Saisawan	404.67 a-e	1.83	18.00 a	11.70 ab	60.90	40.67
10	Petkajee	414.67 a-e	2.17	17.97 a	12.67 a	51.30	39.00
11	Sornsawan 5	379.33 b-f	2.00	18.00 a	12.23 ab	56.83	38.33
12	Moneygreen	382.50 b-f	2.33	16.47 a-c	11.27 a-c	60.30	38.33
13	Rangsit 888	365.67 c-f	2.17	17.40 a	12.60 ab	56.37	39.67
14	Lamnamchee	362.67 d-f	2.00	17.80 a	12.10 ab	65.43	39.67
15	Yodpetkasem	434.33 a-d	2.33	17.60 a	12.40 ab	60.30	41.33
16	Airgreen 99	433.83 a-d	3.33	17.43 a	11.70 ab	62.63	44.00
17	Munggornyok 9	383.17 b-f	2.67	16.73 ab	11.13 a-c	55.67	40.67
18	Choiphiphop	462.50 a	1.67	17.53 a	12.23 ab	53.40	40.00
19	Chiataisen	468.50 a	2.17	17.40 a	11.63 ab	59.83	41.00
20	Nigrodok	362.50 d-f	2.17	14.63 b-d	9.53 c-e	51.80	42.33
21	Green 33	440.00 ab	3.67	17.90 a	11.70 ab	54.70	41.33
22	Bangpra 2	321.00 f	1.17	12.97 d	8.40 e	52.87	41.67
23	Purple 33	379.50 b-f	2.00	16.33 a-c	10.70 b-d	60.47	42.00
F-test		**	ns	**	**	ns	ns
Mean		401.55	2.21	17.12	11.55	57.43	40.61
SE		5.92	0.10	0.20	0.17	0.86	0.30
CV (%)		9.21	31.70	7.16	8.38	12.47	5.20

Where, PL= Plant length (cm), NB= Number of branches, LL= Leaf length (cm), LW= leaf width (cm), LG = Leaf greenness (SPAD unit), DFF= Days to first flowering,

Note: ns and ** = non-significant and significant at p< 0.01 respectively, Standard error (SE) values were calculated from 69 experimental units (23 genotypes x 3 replications). Means in a column followed by the different letter are significantly different at $DMRT_{0.05}$.

Table 3 Mean values for horticultural characteristics and yield of 23 yardlong bean cultivars.

Genotype No.	Genotype Name	Horticultural traits and yield per plant					
		POL	POWD	POWT	NSP	NPP	YP
1	Naka	56.87 c-h	8.37	35.72 a-c	16.97	13.83 ab	275.00 ab
2	Greenarrow 692	58.87 b-f	7.38	33.79 a-d	16.03	7.17 de	145.00 f-h
3	Saifon	60.23 b-e	7.76	35.79 a-c	17.07	9.64 c-e	198.33 c-f
4	Nuethong 9	49.13 i	7.41	27.75 cd	15.17	8.00 c-e	159.17 e-h
5	Saitara	59.43 b-e	7.65	36.78 ab	15.87	5.75 e	117.50 h
6	Tarnthong	50.37 hi	7.64	28.83 b-d	12.80	8.83 c-e	179.17 d-h
7	Lamnamphong 2	55.87 c-i	7.61	31.20 a-d	15.67	9.25 c-e	191.67 d-g
8	Suvarnabhum	51.13 g-i	7.45	28.46 cd	15.03	8.08 c-e	169.17 d-h
9	Saisawan	62.90 bc	7.20	31.86 a-d	15.40	6.83 de	165.83 d-h
10	Petkajee	51.70 f-i	9.18	29.88 b-d	15.27	8.33 c-e	173.33 d-h
11	Sornsawan 5	71.60 a	7.52	38.41 a	15.63	7.17 de	161.67 d-h
12	Moneygreen	51.90 f-i	8.01	29.89 b-d	14.97	8.44 c-e	184.44 d-h
13	Rangsit 888	50.60 g-i	7.11	26.63 d	14.67	8.92 c-e	184.17 d-h
14	Lamnamchee	49.37 hi	7.30	29.12 b-d	14.67	10.58 b-d	214.17 c-e
15	Yodpetkasem	49.43 hi	7.99	27.88 cd	16.03	11.58 a-c	258.33 bc
16	Airgreen 99	54.93 d-i	8.25	35.34 a-c	16.10	14.97 a	327.78 a
17	Munggornyok 9	64.47 b	7.22	31.44 a-d	17.27	9.83 cd	227.22 b-d
18	Choiphiphop	51.77 f-i	7.24	29.04 b-d	14.60	8.75 c-e	171.67 d-h
19	Chiataisen	56.50 c-i	7.33	29.93 b-d	17.30	10.50 b-d	190.83 d-g
20	Nigrodok	53.87 e-i	6.47	26.43 d	13.63	8.83 c-e	125.83 gh
21	Green 33	57.97 b-g	7.09	31.71 a-d	14.73	9.67 c-e	180.83 d-h
22	Bangpra 2	61.90 b-d	6.13	28.14 c-d	17.00	8.06 c-e	167.50 d-h
23	Purple 33	61.40 b-d	7.55	29.73 b-d	16.20	7.69 c-e	159.17 e-h
F-test		**	ns	*	ns	**	**
Mean		56.18	7.52	31.03	15.57	9.16	188.16
SE		0.79	0.11	0.56	0.21	0.32	6.56
CV (%)		6.89	11.07	13.06	9.83	22.11	18.01

Where, POL= Pod length (cm), POWD = Pod width (mm), POWT= Pod weight (g), NSP= Number of seeds per pod, NPP= Number of pods per plant, YP = Yield/plant (g)

Note: ns, * and ** = non-significant, significant at p< 0.05 and p< 0.01 respectively, Standard error (SE) values were calculated from 69 experimental units (23 genotypes x 3 replications). Means in a column followed by the different letter are significantly different at $DMRT_{0.05}$.

3.2 Grouping of 23 genotypes into different clusters (D^2 analysis)

The D^2 values between any two genotypes were calculated as the sum of squares of the differences between the mean values of all the 12 characters and were used for the final grouping of the genotypes. Based on D^2 values the 23 genotypes were grouped into six highly distinct cluster (Table 4). Among six clusters, cluster 2 was the largest consisting of 13 (*viz.* Greenarrow 692, Saifon, Nuethong 9, Saitara, Tarnthong, Lamnamphong 2, Suvanabhum,

Saisawan, Petkajee, Moneygreen, Rangsit 888, Green 33, Purple 33) genotypes, followed by cluster 1, 3, 5, 4 and 6 with 5 (*viz.* Naka, Lamnamchee , Yodpetkasem, Choiphiphop, Chiataisen), 2 (*viz.* Sornsawaan 5, Munggornyok 9), 1 (Airgreen 99), 1 (Nigrodok) and 1 (Bangpra 2) genotype/genotypes, respectively.

Table 4 Clustering pattern of 23 genotypes of yard long bean (Tocher's method)

Cluster	No. of genotype	Genotypes	Name of the Genotypes
1	5	1, 14, 15, 18, 19	Naka, Lamnamchee , Yodpetkasem, Choiphiphop, Chiataisen
2	13	2, 3, 4, 5, 6, 7, 8, 9, 10, 12, 13, 21, 23	Greenarrow 692, Saifon, Nuethong 9, Saitara, Tarnthong, Lamnamphong 2, Suvanabhum, Saisawan, Petkajee, Moneygreen, Rangsit 888, Green 33, Purple 33
3	2	11, 17	Sornsawaan 5, Munggornyok 9
4	1	16	Airgreen 99
5	1	20	Nigrodok
6	1	22	Bangpra 2

3.3 Mean values of cluster of 23 genotypes

Mean values of each cluster are illustrated in Table 5 and the highest mean values of each characteristic were in bold letters. Cluster 1 was recorded the highest mean values for plant length (437.23 cm), leaf length (17.62 cm) and leaf width (12.03 cm). Cluster 3 was recorded the highest mean value for pod length (68.03 cm). Cluster 4 was recorded the highest mean values for number of branches per plant (3.33 branches), leaf greenness (62.63 SPAD unit), day to first flowering (44.00 days), pod width (8.25 mm), pod weight (35.34 g), number of pods per plant (14.97 pod/plant) and yield per plant (327.78 g/plant). Cluster 6 was recorded the highest mean value for number of seeds per pod (17.00 seeds/pod).

Table 5 Mean values of cluster for 12 characters in 23 yardlong bean genotypes (Tocher's method)

Characters	Cluster 1	Cluster 2	Cluster 3	Cluster 4	Cluster 5	Cluster 6
Plant length (cm)	**437.23**	397.67	381.25	433.83	362.50	321.00
Number of branches/plant	2.00	2.27	2.33	**3.33**	2.17	1.17
Leaf length (cm)	**17.62**	17.38	17.37	17.43	14.63	12.97
Leaf width (cm)	**12.03**	11.73	11.68	11.70	9.53	8.40
Leaf greenness (SPAD unit)	60.91	56.66	56.25	**62.63**	51.80	52.87
Day to first flowering (days)	40.27	40.44	39.50	**44.00**	42.33	41.67
Pod length (cm)	52.79	55.50	**68.03**	54.93	53.87	61.90
Pod width (mm)	7.65	7.62	7.37	**8.25**	6.47	6.13
Pod weight (g)	30.34	30.95	34.92	**35.34**	26.43	28.14
Number of seeds per pod	15.91	15.30	16.45	16.10	13.63	**17.00**
Number of pods per plant	11.05	8.20	8.50	**14.97**	8.83	8.06
Yield per plant (g/plant)	222.00	169.83	194.45	**327.78**	125.83	167.50

3.4 Average intra and inter cluster values of 23 yardlong bean genotypes

The mean intra and inter cluster D^2values are given in Table 6. The intra cluster D^2 values ranged from 0 (cluster 4, 5 and 6) to 18.92 (cluster 2). Clusters 4, 5 and 6 had no intra cluster D^2 because each cluster had only a single genotype. The cluster 2 had the maximum D^2 values (18.92) followed by cluster 3 (18.73) and cluster 1 (17.40). The inter cluster D^2 values of 6 cluster revealed that highest inter cluster generalized distance (122.82) was between cluster 5 and cluster 4, while the lowest (22.25) was between cluster 2 and cluster 1. The inter cluster distance was minimum between cluster 2 and cluster 1 indicating narrow genetic diversity and maximum between cluster 5 and cluster 4 indicating wider genetic diversity among the genotypes included in these groups. Table 6 provides the useful information of intra and inter cluster genetic distances to select the predominant genotypes in the groups which had the highest inter cluster values (which are different groups) for crossing to obtain offspring with the positive transgressive segregations that can be used for selection. It implied that parents possessing high genetic divergence were highly different from each other according to D^2measurement.

Table 6 Average intra and inter cluster D^2 values for 7 cluster in 23 genotypes of yard long bean (Tocher's method)

Cluster	Cluster 1	Cluster 2	Cluster 3	Cluster 4	Cluster 5	Cluster 6
Cluster 1	**17.40**	22.25	50.21	34.37	62.61	73.04
Cluster 2		**18.92**	37.44	49.74	43.44	51.16
Cluster 3			**18.73**	60.44	75.40	36.41
Cluster 4				**0**	122.82	103.57
Cluster 5					**0**	42.74
Cluster 6						**0**

3.5 Percent contribution of characters towards diversity

The percent contribution of each character towards divergence is presented in Table 7. Pod length ranked first (65 times) with the maximum contribution of 25.69%, followed by yield per plant (25.30%) ranked first (64 times), leaf length (10.28%) ranked first (26 times), plant length (8.30%) ranked first (21 times), pod width (7.51%) ranked first (19 times), pod weight (5.53%) ranked first (14 times), number of pods per plant (4.74%) ranked first (12 times), leaf width (3.56%) ranked first (9 times), number of seeds per pod (3.16%) ranked first (8 times) and number of branches per plant (2.77%) ranked first (7 times). Therefore, the pod length, yield per plant, leaf length, pod width and pod weight were expected to be significant traits producing genetic variation. Similar diversity studies were carried by Rambabu *et.al.,* (2016) in yard long bean, Ushakumari *et al.* (2015) also reported the highest contribution of plant height (22.69%) toward divergence followed by seeds per pod (17.63%), number of branches (16.82%), number of pod per cluster (15.27%) and pod length (13.47%) in Cowpea. Valarmathi *et al.* (2018) reported that the maximum contribution of 40.91% was recorded by days to maturity followed by hundred seed weight (30.55%) and seed yield per plant (10.67%) in Cowpea and Yard long bean.

Table 7 Relative contribution of 12 characters towards divergence in 23 yardlong bean genotypes

No.	Character	% Contribution	Times ranked first
1	Plant length (cm)	8.30%	21
2	Number of branches per plant	2.77%	7
3	Leaf length (cm)	10.28%	26
4	Leaf width (cm)	3.56%	9
5	Leaf greenness	1.58%	4
6	Day to first flowering	1.58%	4
7	Pod length (cm)	25.69%	65
8	Pod width (cm)	7.51%	19
9	Pod weight (g)	5.53%	14
10	Number of seeds per pod	3.16%	8
11	Number of pods per plant	4.74%	12
12	Yield per plant	25.30%	64

4. Conclusions

The comparison of 23 yard long bean genotypes disclosed that most characteristics were significantly different. The genetic divergence experiment assessed using Mahalanobis D^2 statistic revealed that the 23 genotypes of yard long bean were grouped into 6 clusters. Among the 12 characters studied, pod length contributed maximum towards divergence. The inter cluster distance was maximum between cluster 5 and cluster 4 indicating wider genetic diversity among the genotypes included between these 2 groups.

5. Acknowledgements

The authors thank for the Rajamangala University of Technology Tawan-ok Bangpra Campus for permitting to conduct this research study. Also, many thanks were given to field workers of the Department of Plant Production Technology, RMUTTO, for their support in the experiment.

6. References

Asoontha and Mareen Abraham., 2017, Variability and Genetic Diversity in Yard Long Bean (Vigna unguiculata subsp. sesquipedalis.). *Int.J.Curr.Microbiol.App.Sci*., 6(9): 3646-3654. doi: http://dx.doi.org/10.20546/ijcmas.2017.608.448 .

Bhagavati, P.P., Kiran Patro, T.S.K.K, Lakshmi Narayana Reddy, M., Emmanuel, N., Salomi Suneetha, D.R. & Vara Prasad, N., 2018. Studies on genetic divergence in yardlong bean (*Vigna ungiculata* (L.) walp. ssp. *sesquipedalis* Verdc.). *International Journal of Chemical Studies*, 6(4), 1139-1142.

Chowdhury, M.A, Vandenbreg, V. and Warkentin, T, 2015, Cultivar identification and genetic relationship among selected breeding lines and cultivars in chick pea (*Cicer arietinum* L.). *Euphytica*. 127:317-325.

International Rice Research Institute, 2014, Statistical Tool for Agricultural Research. Plant Breeding, Genetics and Biotechnology Division, International Rice Research Institute, Los Baños, Philippines.

Manivannan,N., 2014, TNAUSTAT-Statistical package. Available from: https://sites.google.com/site/tnaustat. [accessed on 23 June 2022].

Rambabu, E., Reddy, K. R., Kamala, V., Saidaiah, P., & Pandravada, S. R., 2016, Genetic variability and heritability for quality, yield and yield components in yard long bean *(Vigna unguiculata* (L.) Walp. ssp. *sesquipedalis* Verdc.). *Green Farming*, 7: 63-67.

Saidaiah P, Munnam SB, Nimmarajula S, Gonela N, 2019, Assessment of genetic diversity in yardlong bean (*Vigna unguiculata* (L.) Walp subsp. *sesquipedalis* Verdc.) germplasm from India using RAPD markers. Art- Genetic Resources and Crop Evolution. 2019;66(6):1231-1242.

Tomooka. N, 2019, Genetic diversity and landrace differentiation of Mungbean (*Vigna radiate* L.) Wilczek and evaluation of its wild relatives (The subgenus *ceratotropics*) as breeding material. *Technical Bulletin on Tropical Research*. 28: 1-4.

United States Department of Agriculture, 2012, *Vigna unguiculata* (L.) Walp. subsp. *sesquipedalis* (L.). Verdc. Available from: http://www.ars-grin.gov/cgibin/npgs/html/taxon. pl?41646. [accessed on 19 April 2023].

Ushakumari, R., Backiyarani, S. and Dhanakodi, 2015, Character contribution to diversity in cowpea. *Legume Res.*, 23:1223125.

Valarmathi, V, Surendran, C. and Muthiah, A.R, 2018, Genetic divergence analysis in subspecies of Cowpea (*Vigna unguiculata* ssp. *unguiculat*a and *Vigna unguiculata* ssp. *sesquipedalis*). *Legume Research*. 30: 192-1966.

Development of Chinese Sausage (Kun-Chiang) from Trimmed Crocodile Meat mixed with Chicken Meat

Saijai Chariyaeggapas [a], Dhoungsiri Sayompark [a], Supattra Poonpaerdchon [a] and Grant Thamkaew [*a]

[a]*Division of Food Technology, Faculty of Science and Technology, Rajamangala University of Technology Tawan-ok, Chonburi, 20110, Thailand*

*Corresponding author. Tel.: (+66)64-793-2122; *E-mail address: Grant_th@rmutto.ac.th*

Abstract

The aim of this study was to develop Kun Chiang, a traditional Chinese sausage, using leftover crocodile meat and chicken as ingredients. The main raw material, crocodile meat scraps, had a moisture content, protein content, fat content, ash content, fiber content, and carbohydrate content of 71.05%, 19.62%, 1.50%, 0%, 7.25%, and 0%, respectively. The study consisted of five formulations with different ratios of chicken to crocodile meat: 100:0, 75:25, 50:50, 25:75, and 0:100. Physical analysis revealed that the cutting force increased significantly ($p<0.05$) as the proportion of crocodile meat increased. The 0:100 ratio showed the highest cutting force value at 60.55 N. The L*, a*, and b* color values decreased significantly ($p<0.05$) with the addition of crocodile meat proportion. Sensory evaluations indicated no statistically significant differences ($p>0.05$) in color preference. However, flavour , taste, texture, and overall liking scores decreased significantly ($p<0.05$) with the addition of crocodile meat scraps. When comparing the ratios of 100:0, 75:25, and 50:50, no statistically significant differences ($p>0.05$) were found in the overall sensory parameters. Therefore, the 50:50 ratio of chicken to crocodile meat was selected as the optimal formulation. The final product had a moisture content, protein content, fat content, ash content, fiber content, and carbohydrate content of 26.72%, 25.74%, 21.97%, 3.20%, 0%, and 22.37%, respectively. Consumer acceptance evaluation revealed that 79% of participants expressed satisfaction with the Kun-Chiang product.

Keywords: Chinese sausage, trimmed crocodile meat, By-products utilization

1. Introduction

Crocodile meat has been consumed in Asia for a long time and is currently gaining popularity, especially among Chinese people. In Chinese culture, crocodile meat is considered as natural remedy and believed to improve the body's functioning and create immunity against disease. It is also used as an ingredient in herbal remedies to treat allergies and high blood pressure. In addition to being sold as fresh meat, crocodile meat can be processed in various ways, such as being frozen or cooked. Thailand has a large number of crocodile farms, up to thousands of them (www.bbc.com/thai/international-40461789, 2013). Crocodile meat sold in markets ranges in price from 250 to 450 baht per kilogram (www.crocodilebagme.com, 2013). Products made from crocodile meat that are already available in Thailand include canned crocodile meat, crocodile soup in bottles, and dried crocodile meat. In addition, Chinese restaurants in some countries have used crocodile meat to create various dishes, such as burgers and steaks, such in fast food restaurants in Queens Land and Northern Australia, which are said to be soft and taste like a mix of fish and chicken (Sinee, 2001). In the process of preparing crocodile carcasses, the skin is used in the leather industry, while the remaining meat, including the red meat, fat, scraps, legs, organs, rib bones, and spinal bones, can be used to make soup stock, seasonings, and snacks.

Crocodile meat shares similarities with chicken, as it is a white meat that is rich in protein and low in fat when compared to red meat (Lawrie, 1998). However, during the trimming process of crocodile meat, there are leftover pieces (Figure 1) that possess a tough texture, high fat content, and strong odor, resulting in their sale at a discounted price. These parts of white meat from crocodiles are typically priced at around 80-90 baht per kilogram. Chicken meat (Figure 2) is considered a soft and mild odor white meat, which has a similar color to crocodile meat. Incorporating chicken meat as an ingredient in the processing of crocodile meat products can aid in reducing toughness. The aim of this research is to create meat product that enhance the value of the remaining crocodile meat by developing "Kun-Chiang Crocodile," utilizing chicken meat as a component. The study explores the suitable proportions of crocodile and chicken meat to produce Kun-Chiang Crocodile, while also examining the quality of the raw crocodile meat and evaluating the physical and sensory properties of Kun-Chiang Crocodile. Furthermore, the research investigates the chemical composition of Kun-Chiang Crocodile and its acceptance by consumers, both domestically and internationally, as a premium product suitable for industrial production.

Figure 1 Crocodile meat

Figure 2 Chicken meat

2. Methodology

Ingredients

The ingredients used in the formula include chicken meat and crocodile meat (63%), solid fat (16.00%), granulated sugar (13.00%), soy sauce (1.50%), praque powder ® (salt with sodium nitrite) (0.50%), phosphate (0.10%), five-spice powder (0.50%), and chilled water (5.40%).

Methods

Begin by grinding the crocodile meat, chicken meat, and firm fat using a 7.5 mm sieve (beehive shape) grinder. Combine the ground meats in a mixing bowl. Add all the seasonings and knead the mixture for approximately 2 minutes until it reaches a desire consistency. Next, add the solid fat and knead for an additional 3 minutes until thoroughly incorporated.

Proceed to pack the blended mixture into 19-sized collagen casings using a sausage stuffer. Tie the sausages into 5 inches links. Hang the sausages within a curing chamber set at a temperature of 60°C for a duration of 18 hours. Subsequently, allow the sausages to cool down before packing them into polyethylene plastic bags. Store the packed sausages at room temperature (28±2°C) until they are ready for quality control testing.

Prior to conducting the physical and sensory evaluation, heat the sausages in a frying pan at 120°C for 3 minutes, and then proceed to slice them into 2 mm thick pieces.

2.1. Approximate analysis of crocodile meat scraps

The moisture, protein, fat, fibre, ash, and carbohydrate content were analysed according to AOAC (2000) method.

2.2. Study of suitable proportion of chicken meat and crocodile meat scraps for the crocodile Kun-Chiang product

The study was divided into 5 experiments using different ratios of chicken meat and crocodile meat scraps as follows:

Formula 1: Chicken meat: Crocodile meat scraps = 100:0
Formula 2: Chicken meat: Crocodile meat scraps = 75:25
Formula 3: Chicken meat: Crocodile meat scraps = 50:50
Formula 4: Chicken meat: Crocodile meat scraps = 25:75
Formula 5: Chicken meat: Crocodile meat scraps = 0:100

2.2.1 Analysis of physical characteristics:

2.2.1.1 Colour measurement

Colour measurement was performed using a spectrophotometer (Konica Minolta; CM-3500d) according to CIE system, and each sample was tested in triplicate.

2.2.1.2 Texture analysis

Texture analysis was performed using a Texture Analyzer (TA.XT. Plus) and each sample was tested in triplicate.

2.2.1.3 Water activity (aw)

Water activity (a_w) measurement was performed using an Aqualab Series 3TE water activity meter and each sample was tested in triplicate.

2.2.2 Sensory evaluation

Sensory evaluation of colour, flavour, taste, texture, and overall liking was performed using a 9-point hedonic scale with 30 panellists who were food science and technology students and staff. The scores ranged from 1 (dislike extremely) to 9 (like extremely), and the average score for the highest consumer acceptance was determined.

2.3. Study the quality of the selected crocodile Kun-Chiang from study 2.2

Chemical components including moisture, protein, fat, ash, fibre, and carbohydrates were analysed according to A.O.A.C. (2000) method.

2.4. General consumer acceptance

Study the general consumer acceptance by conducting a Central Location Test (CLT) using Kun-Chiang selected from the study 2.2, to test the acceptance of 100 consumers in a public location. The measurement method used is 9-point hedonic scaling, along with a questionnaire. The obtained results will be reported to assess the level of acceptance and possible sales trends for industrial production of crocodile Kun-Chiang.

2.5. Statistical analysis

Analyse the results statistically using the Completely Randomized Design (CRD) for physical analysis and Randomized Complete Block Design (RCBD) for sensory evaluation. Use Duncan's new multiple rang test (DMRT) to compare the means of the experiments. Data analysis was conducted using the SPSS v.14 software.

3. Results and Discussion

3.1. Analysis of the Chemical Components of Crocodile Meat Scraps

Chemical components of crocodile meat scraps were analysed, including moisture, protein, fat, ash, fibre, and carbohydrate, as shown in Table 1. When compared to major crocodile meat parts, which contains 21.1% protein and 1.9% fat (Mitchell *et al*., 1995), crocodile meat scraps were found to have lower protein and higher fat content.

Table 1 Chemical components of crocodile meat scraps

Chemical components	Contents (%)
Moisture	71.05
Protein	19.62
Fat	7.25
Ash	0.50
Fibre	0
Carbohydrate	1.50

3.2. Physical properties of the crocodile Kun-Chiang

Table 2 Colours, cutting force, and water activity crocodile Kun-Chiang from 5 formulas.

Samples (Chicken: Crocodile)	Colours coordinates			Cutting force* (N)	a_w ns
	L*	a*	b*		
Formula 1 (100:0)	42.19 ± 2.36^{a}	4.57 ± 0.30^{a}	11.15 ± 0.34^{a}	23.35 ± 1.23^{c}	0.66 ± 0.00
Formula 2 (75:25)	40.29 ± 1.33^{ab}	4.51 ± 0.26^{a}	10.47 ± 1.25^{ab}	30.12 ± 3.25^{d}	0.65 ± 0.00
Formula 3 (50:50)	40.15 ± 1.46^{ab}	3.47 ± 0.19^{b}	9.39 ± 0.63^{b}	40.40 ± 0.79^{c}	0.69 ± 0.00
Formula 4 (25:75)	38.92 ± 0.69^{bc}	3.08 ± 0.25^{b}	9.09 ± 0.41^{b}	49.45 ± 1.25^{b}	0.66 ± 0.00
Formula 5 (0:100)	37.14 ± 1.32^{c}	3.69 ± 0.41^{b}	9.07 ± 0.64^{b}	60.55 ± 2.70^{a}	0.69 ± 0.00
C.V. (%)	3.54	8.35	7.88	5.36	3.75

ns remarks data with no statistically difference *(p>0.05)*

The asterisk (*) remarks the value with a statistically significant difference of the data within the column *(p<0.05)*

The colour values were found to have statistically significant differences in the average L*, a*, and b* values ($p<0.05$). The L* value of formula 1 was the highest, but when compared to formulas 2 and 3, there was no statistically significant difference ($p>0.05$). Formula 1 used all chicken meat as a control formula, which is a white meat which has high protein and water holding capacity. Crocodile meat, on the other hand, contained higher amounts of connective tissues and fat, resulting in a cloudier white appearance. As the quantity of crocodile meat used increased, there was a noticeable decline in the brightness value of the product. When comparing all experiments, it was found that formula 5 had the lowest brightness value of 37.14. The positive a* value indicates a red colour. Formula 1 had the highest average a* value of 4.57 and when compared to formula 2, there was no statistically significant difference ($p>0.05$). The red colour in the Kun-Chiang product is caused by the formation of a new compound that is created when nitrite in the praque powder reacts with myoglobin in red meat muscle. This ultimately forms nitrosohemochrome, which is a pink-red colour pigment (Von Elbe and Schwartz, 1996). Increasing the proportion of crocodile meat in Kun-Chiang resulted in a decrease in a* value, as crocodile meat contains higher percentage of connective tissues and fat than that of chicken meat. Therefore, formulas with higher amount of chicken meat will contain higher amount of myoglobin which is a main reactant of nitrosohemochrome reaction (Kritsana and Saiyan, 2550). When Kun-Chiang products from formulas 1, 2, and 3 were subjected to heat during the baking process, they exhibited a significantly darker red colour compared to formulas 4 and 5. Regarding the b* value, which represents the degree of yellow colour, formula 1 had the highest value of 11.15. However, when comparing it to formula 2, it was found that there was no statistically significant difference in the values obtained ($p>0.05$). When chicken meat was replaced with an increased amount of crocodile meat, the b* value decreased. This is because chicken meat naturally has a pale-yellow colour, while crocodile meat contains fat and browning components. With a higher amount of crocodile meat used as a substitution, the b* value decreased sequentially, with formula 5 having a value of 9.07.

The cutting force values were found to have a statistically significant difference among the formulas ($p<0.05$). Formula 5, which utilized 100% crocodile meat, had the highest average value of 60.55 N. This is because the crocodile meat scraps contain a significant amount of connective tissues, as shown in Figure 1. Consequently, Kun-Chiang products made from these scraps had a tougher texture when dried. When measuring the cutting force, formulas with a higher proportions of crocodile meat scraps exhibited higher cutting forces values compared to formulas with a lower amount of the substitution.

The water activity (aw) values were found to have no significant statistical difference ($p \geq 0.05$) with an average range of 0.65-0.69 for all 5 formulas. This range of a_w values inhibit bacterial growth, making the crocodile Kun-Chiang product shelf-stable (Phimphan and Nithiya, 2013).

3.3. Sensory evaluation of crocodile Kun-Chiang products

The results of the sensory evaluation of Kun-Chiang products made from crocodile meat scraps are presented in Table 3.

Table 3: Sensory evaluation of Kun-Chiang Products from Crocodile Meat Scraps (5 samples)

Samples (Chicken: Crocodile)	***Colour***	**Flavour**	**Taste**	***Texture***	**Overall**
Formula 1 (100:0)	7.07±1.57	7.50±1.43^{a}	7.27±1.11^{a}	7.43±1.04^{a}	7.13±1.07^{ab}
Formula 2 (75:25)	6.70±1.51	6.80±1.56^{ab}	7.20±1.27^{ab}	7.37±1.13^{a}	7.40±1.13^{a}
Formula 3 (50:50)	6.40±1.33	6.90±1.21^{ab}	6.87±1.61^{ab}	7.13±1.07^{a}	6.67±1.15^{ab}
Formula 4 (25:75)	6.60±1.43	6.60±1.43^{b}	6.73±1.55^{ab}	6.17±1.37^{b}	6.30±1.29^{c}
Formula 5 (0:100)	6.57±1.28	6.57±1.28^{b}	6.47±1.31^{b}	6.13±1.28^{b}	6.23±1.38^{c}
C.V.(%)	19.88	19.86	20.04	16.60	17.48

ns remarks data with no statistically difference *(p>0.05)*

The asterisk (*) remarks the value with a statistically significant difference of the data within the column *(p<0.05)*

Colour

It was found that there was no statistically significant difference in the average values among all formulas (p>0.05). In this experiment, the same amount of meat and seasonings were used in each formula, including the colour of both crocodile meat scraps and chicken meat, which did not differ when the products underwent the baking process. The resulting colours were observed to be very similar, as indicated by the panellist's scores (Figure 3).

Flavour

It was found that there was a statistically significant difference (p<0.05) in the average scores for odour when crocodile meat scraps were substituted in higher quantities. The evaluators gave lower scores for flavour acceptability. However, when comparing the average scores, there was no statistically significant difference among formulas 1, 2, and 3 (p>0.05). It should be noted that crocodile meat scraps contain a significant amount of connective tissues and fat which contributes strong odour and rancidity. When used it as a substitute for chicken meat in larger quantities, the evaluators perceived a strong odour, resulting in a decrease in the scores for flavour acceptability.

Taste

It was found that the average liking scores differed significantly (p<0.05) However, when comparing formulas 1, 2, 3, and 4, there were no statistically significant differences in the average scores among these formulas (p>0.05). Formula 5 had the lowest taste preference score, scoring at 6.47. It can be observed that the average scores decreased when using crocodile meat as a substitute for chicken meat. This is because crocodile meat contains a significant amount of connective tissue. When used as the main ingredient in making Kun-Chiang, it results in a lower proportion of meat, which affects the protein content and taste of the product. Additionally, the taste of crocodile meat is unfamiliar to the testers, resulting in lower preference scores for formula 5, which utilizes 100% crocodile meat as a substitute, compared to the other formulas.

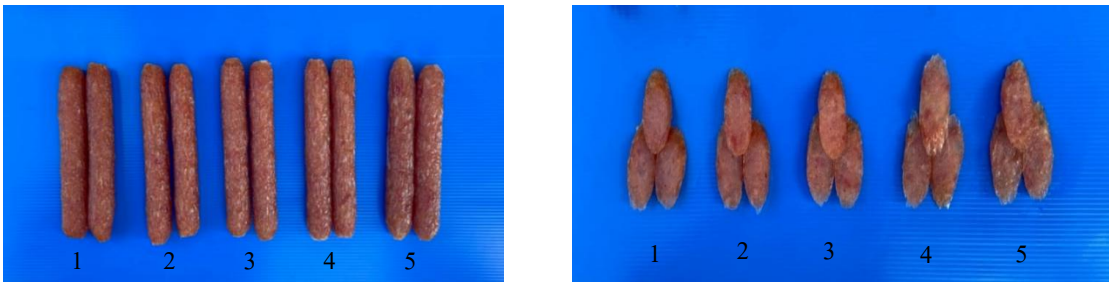

(Chicken Meat: Crocodile Meat ratio; 1 = 100:0, 2 = 75:25, 3 = 50:50, 4 = 25:75, 5 = 0:100)

Figure 3 Kun-Chiang products made from crocodile meat scraps with varying proportions of chicken meat in all 5 formulas.

Texture

The average scores were found to differ significantly (p<0.05). However, when comparing formulas 1, 2, and 3, the average scores did not differ significantly among these formulas (p>0.05). Formulas 4 and 5, which contained 75% and 100% crocodile meat as substitutes, respectively, had the lowest taste preference scores. Kun-Chiang is a semi-dry food product, and the inclusion of crocodile meat as an ingredient introduces connective tissues which contributes to its increased toughness (Phimpan and Nitiya, 2013). The testers perceived this increase in toughness with a decrease in acceptance scores when consuming formulas with a higher proportion of crocodile meat, which is conforming with the increased cutting force values (Table 2).

Overall

It was found that the average scores of overall preferences differed significantly (p<0.05). Formula 2 had the highest average preference score, which was 7.40. However, when comparing the average scores of formulas 1 and 3, no statistically significant differences were observed (p>0.05). The overall preference scores were obtained through testing the quality aspects in various characteristics and evaluating the acceptance of the Kun-Chiang product.

Formulas 1, 2, and 3 received similar scores in terms of colour, aroma, taste, and texture. As the objective of this research is to utilize the crocodile meat scraps, formula 3, with a ratio of 50% chicken meat and 50% crocodile meat scraps, was selected as the suitable formula. This formula will be studied for its chemical components further in this paper.

3.4. Study of the quality of Kun-Chiang products made from selected formula

Table 4 shows the chemical composition analysis of the final Kun-Chiang product made from crocodile meat scraps, using formula 3 with a ratio of 50:50 between chicken meat and crocodile meat scraps. The analysis includes the following components: moisture content, protein, fat, ash, fibre, and carbohydrates.

Table 1 Chemical components of Kun-Chiang products made from crocodile meat scraps with formula 3

Chemical components	Contents (%)
Moisture	16.72
Protein	30.74
Fat	28.97
Ash	3.20
Fibre	0
Carbohydrate	20.37

3.5 Study of consumer acceptance through the Central Location Test (CLT) method

Based on a general consumer acceptance test conducted on 100 individuals, the attitudes and preferences of consumers towards Kun-Chiang crocodile meat scrap products, specifically formula 3, were examined. The test group consisted of 37 females and 63 males, all aged 15 years and above. It was found that 97% of the participants had previously consumed Kun-Chiang products, with a frequency of 1 to 2 times per month. The main reason for consumption was the delicious taste. When the developed Kun-Chiang crocodile meat scrap product was tested, it received a consumer acceptance rate of 79% and was rated as moderately satisfying. If the products is commercially available, the factors that would motivate consumers to purchase it were its novelty and the acceptable taste.

4. Conclusions

The development of Kun-Chiang products using crocodile meat scraps with chicken meat as an ingredient was analysed for its chemical composition. The analysis revealed the following percentages of moisture, protein, fat, ash, fibre, and carbohydrates in the crocodile meat scraps used as raw materials: 71.05%, 19.62%, 1.50%, 0.58%, 0%, and 7.25%, respectively. A physical analysis was conducted to determine the suitable proportions of crocodile meat scraps and chicken meat for the production of Kun-Chiang products. It was found that increasing the amount of crocodile meat scraps resulted in higher cutting force values. Among the tested formulas, formula 5 had the highest cutting force value of 60.55 N (p<0.05), while formula 1 had the lowest value at 22.35 N. Regarding colour analysis, the L* value decreased when the proportion of crocodile meat scraps in the mixture increased. Formulas 1, 2, and 3 showed no statistically significant difference in L* values (p>0.05). The a* value was highest for formulas 1 and 2, and it decreased with an increase in crocodile meat scrap content. The b* value showed a similar trend as L* and a*, decreasing when the amount of crocodile meat scraps increased. In terms of sensory evaluation, the acceptance scores for colour did not show a statistically significant difference among the testers (p>0.05). However, the flavour acceptance scores decreased when more crocodile meat scraps were added (p<0.05). Formulas 1, 2, and 3 had no statistically significant difference in acceptance scores (p>0.05). Regarding taste, the scores decreased with an increase in the amount of crocodile meat scraps. However, there was no statistically significant difference in acceptance scores among formulas 1, 2, 3, and 4 (p>0.05). Overall preference scores followed a similar trend to other quality aspects. When the amount of crocodile meat scraps increased, the testers gave lower acceptance scores. Formula 1 had the highest preference score at 7.13. There was no statistically significant difference in acceptance scores between formulas 2 and 3 (p>0.05). Therefore, formula 3 was selected as the suitable formula for producing Kun-Chiang products for commercialization. When analysing the chemical composition of formula 3, it had the following percentages of moisture, protein, fat, ash, fibre, and carbohydrates: 26.72%, 25.74%, 21.97%, 3.20%, 0%, and 22.37%, respectively. A consumer acceptance study conducted on the general population revealed that Kun-Chiang crocodile meat scrap products were accepted by 79% of the consumers, with moderate satisfaction. The reasons for purchase were the novelty of the product and the acceptance of its taste.

5. Acknowledgements

This research project received funding support from Rajamangala University of Technology Tawan-ok and acknowledges the Department of Food Science and Technology, Faculty of Science and Technology, Bang Phra Campus, Chonburi Province, for providing research equipment and facilities.

6. References

Phonchan, K and Taksin, S. 2007. A Quantitative Analysis of Nitrite and Phosphate in Meat Product from One Tambon One Product. Research project of the Faculty of Science and Technology, Mahasarakham University.

Panyawatthanakul, E. 2007. Integrative Medicine in Allergy Patient Care. Conference Proceedings on Alternative Medicine, 2-4 May 2007, Asia Airport Hotel, Pathum Thani.

Nongtaodam, S. 2001. Development of Seasoned Crocodile Meat Products and Preservation Techniques. Master's Thesis, Faculty of Fisheries, Department of Fisheries Products, Kasetsart University.

Siranawinet, J. 1994. Research on Crocodile towards Innovation and Commercial Utilization. Faculty of Science, Department of Animal Science, Kasetsart University.

A.O.A.C. 2000. Official Methods of Analysis. 17th ed. The Association of Official Analytical Chemists, Maryland.

Lawrie, R. A. 1998. Lawrie's Meat Science. Woodhead Publishing Limited, Cambridge, England

Mitchell, G.E., A.W. Reed and D.B. Houlihan. 1995. Composition of crocodile meat (Crocodylus porosus and C. johnstoni). Food Australia 47:321-325.

Von Elbe, J. H. and Schwartz, S. J. 1996. Colorants. In Food Chemistry. 3 rd ed. Fennema, O. R., Ed. New York: Marcel Dekker: 1051 pp.

Wisaraphan, P. 2023. Crocodile Meat: High Protein, Low Fat, Soaring Sales. Source: https://www.technologychaoban.com/livestock-technology/article_219492

Phetchalerngpongs, P. and Ratthanapannont, N. 2023. Structure and Components of Animal Meat. Source: https://www.foodnet worksolution.com/wiki/word/3351

Phetchalerngpongs, P. and Ratthanapannont, N. 2023. Chicken Chinese sausage. Source: https://www.foodnetworksolution.com/wiki/word/ /3248

BBC News. 2023. Crocodiles: An Economic Animal Facing Declining Exports. Source: https://www.bbc.com/thai/international-40461789

Jomkondee Line ID. 2023. Frozen crocodile meat. Source: www.crocodilebagme.com

A Prototype of an Intelligent Rice Contamination Monitoring System on CiRA CORE Platform

Weerayuth Khunrattanasiri[a], Burasakorn Yoosooka[*a], Suvil Chomchaiya[b]
Khwankaeo Kamonsan[a] and Thanisa Thapolnusit[a]

[a]*Division of Computer Engineering, Faculty of Engineering, Rajamangala University of Technology Phra Nakhon, Bangkok, 10800, Thailand*
[b]*Department of Mathematics, Faculty of Science, King Mongkut's University of Technology Thonburi, Bangkok, 10140, Thailand*
*Corresponding author. Tel.:092-629-6388; *E-mail address:* burasakorn.y@rmutp.ac.th

Abstract
This research is CiRA CORE's technical feasibility study as a domestic industrial application. CiRA CORE can be adopted as the main platform for supporting system for manufacturing process. As the case study of rice milling plant, pertaining to the consequent from post milling process, the impurities separation process is also required, demanding technologies to facilitate such process for the more convenience and the better rice quality. Such technical concept has encouraged and lead to this research project which aims to develop the rice impurities inspection system with deep data analysis via CiRA CORE. Beginning with the image processing of rice grain via webcam in concurrent with the inspection process, the images will be screen captured and send to LINE mobile application to display the inspection results. Therefore, the developed system has been tested based on the actual working condition which is based on the most affectable factor, the light intensity. The user satisfaction is also in GOOD level. In conclusion, the outcome of this research can not only be a CiRA CORE application prototype but also be another development guideline and further domestic industrial applications. The extensive research of this paper can be beneficial to many Thailand's argo-industries, especially the production of grains, which would be beneficial to the national economy as a whole.

Keywords: CiRA CORE, image processing, separation of contaminants

1. Introduction
Domestic rice milling industry has adopted imported technologies to enhance the better overall milling processes. Hence, the higher initial investment is unavoidable which leads to the higher process costs. To promote the better rice quality, impurities, such as dirt, sand, gravel, and straw, must be removed. With this condition and requirement, the adoption of domestic Artificial Intelligence (AI) technologies can be greatly economically useful.

CiRA CORE is an AI platform, developed under the cooperation between the King Mongkut's Institution of Technology Latkrabang (KMITL), the Khon Kaen University (KU), and the King Mongkut's University of Technology North Bangkok (KMUTNB), which is the extensive development of Deep Learning Technology. Core Service that included in CiRA CORE can enable the extensive application development. Currently, not only on smartphone application developments, CiRA CORE is becoming popular among manufacturing industries. Since CiRA CORE is domestically developed in Thailand, which can be ensured regarding the national technological securities promoting the less reliance on costly imported technologies which could lead to the national economical disadvantages.

With such rationales and conditions, this study was conducted with prototyping and development to facilitate the domestic rice milling entrepreneurs. This is to lower the difficulties and complications in rice's impurities inspection process with the application of CiRA CORE. The inspection results will be sent to the LINE application. The outcome of this study can thus be the guideline for industrial CiRA CORE applications in the future.

2. Assumptions and Theories
2.1 Assumptions
The rice grain impurities inspection system with CiRA CORE can effectively inspect the grain quality of the post milling process. This includes the removal of dirt, organic debris, and so on in which the accuracy is 80% or higher with the user satisfaction is in GOOD or better leve l.

2.2 Related Theories
CiRA CORE is the AI platform under the cooperation between the King Mongkut's Institution of Technology Latkrabang (KMITL), the Khon Kaen University (KU), and the King Mongkut's University of Technology North Bangkok (KMUTNB). Since 2010, the Deep Learning is a sub division of AI which is supremely popular in term of application development. CiRA CORE has been domestically developed in Thailand with the basis of Deep Learning which was previously depended on the worldwide popular platforms, such as TensorFlow (by Google) and PyTorch (by Facebook). Such stated platforms are the Deep Learning software developed by global-scale developers in which the technological disadvantages might be unavoidable for our country if still relying on them.

CiRA CORE is recently applied in diversify industries. For example, the manufacturing of medical face mask of the Charoen Pokphand (CP) group of companies which have employed AI to automate the quality inspection of face mask manufacturing process, replacing of 3-4 quality inspection staffs. Nevertheless, such process is human error

prone and time consumed. Another example is the application of CiRA CORE in the large scale cement powder industry in which AI is applied to locate the cement filling position of cement carrier trucks to promote the better accuracy for the truck drivers.

CiRA CORE is also adopted to detect the mutation of COVID-19 viruses. CiRA CORE can support the physician and researcher teams in virus genetically analysis by decoding the more than 30,000 characters in length of genetic code into images to compare and define the variations. This can be performed in seconds with 99% in accuracy.

Figure 1. The Various Industrial Applications of CiRA CORE

The Deep Learning algorithm is developed with the joining of multilayer Neural Network, from the first Data Input to the final Output layers, with multiple in-between hidden layers. Any models with Deep Learning yield high accuracy in diversified problems ranging from the Object Detection to Speech Recognition without any pre-instructed knowledge. Model can learn from the sample input data and automatically synthesize the knowledge. For example, in gaming industry, models require not only no initial playing instructions but also can learn from several expert players and can automatically synthesize and acknowledge the playing instruction.

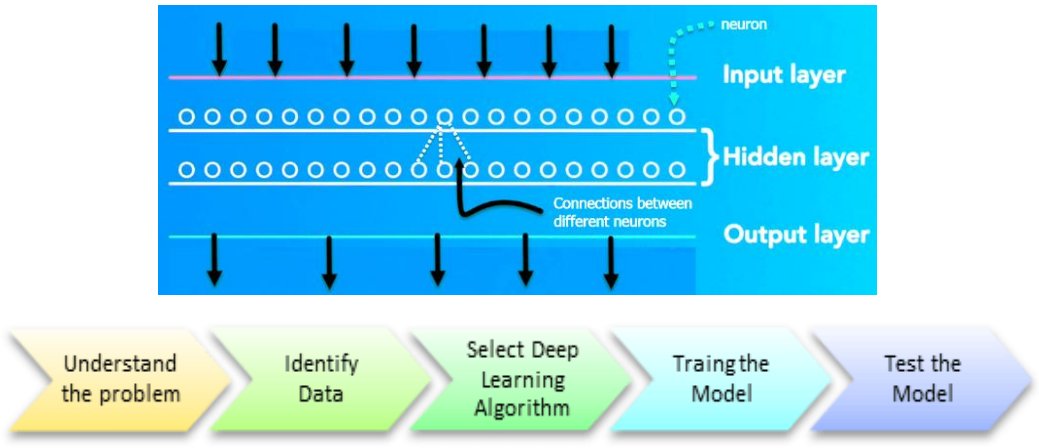

Figure 2. The Deep Learning Model and Process

3. Methodology

3.1 Research Framework

Beginning with conceptual framework and system algorithm, the prototype is consequently developed, pretested, and field tested. This is under the assumption that the developed CiRA CORE base system can inspect the milled rice grain in term of the separation of impurities such as dirt, organic debris, and so on with 80% or better in accuracy and with GOOD or better level of user satisfaction. The scope is that the system can separation impurities via the image processing thru webcams with the Deep Learning analytical concept. Such system is developed with CiRA CORE platform and can capture and send the captured images via LINE Notify.

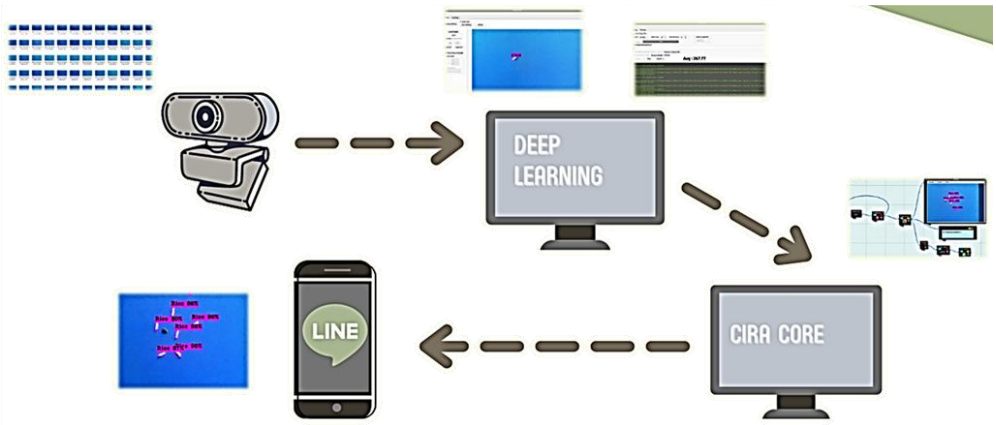

Figure 3. The Research Framework

3.2 System Training with Deep Learning Concept

In this step, the object to be memorized must be well sorted in which the several rice grains with similar size and color is needed to measure the system accuracy. The rice images with actual environment and surroundings are preferable for the better accuracy and correctness. The image capturing module is included in CiRA CORE platform. This step consists of two sub-steps: the preparation of images for system memory training and system training with the following procedures.

Place the Deep Train block into the "Main" and click the gear-shape icon at the bottom right. Then, click the "Load Image" to select the folder of images to be used for system training.

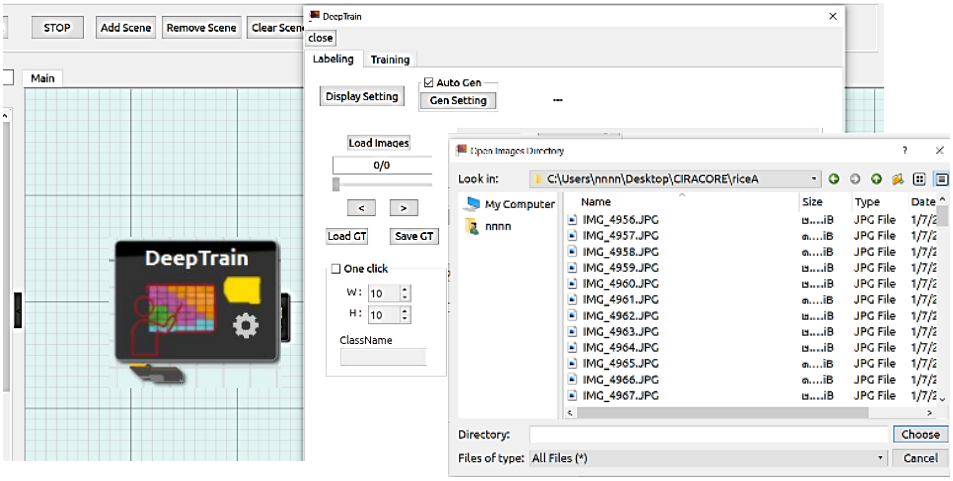

Figure 4. The loading of Images Folder for System Training

Once the folder is selected, the stored images will be displayed. Then, hold and drag the mouse follow to the rice grain sizes and define label names. Therefore, all selected images can be under the same label name and consequently frame all objects.

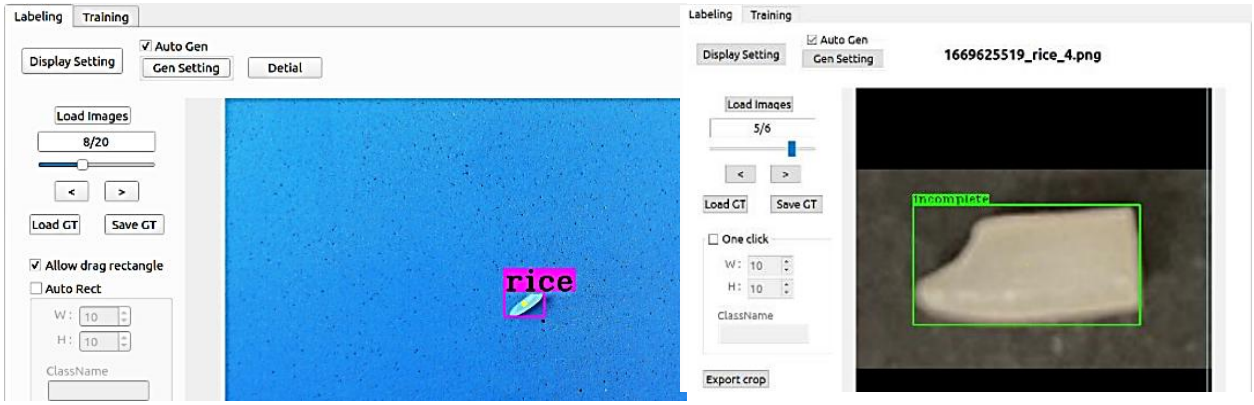

Figure 5. The Label Naming and Object Framing

Once finish all object framing, select Gen Setting and adjust Noise and Blur to the maximum level to enhance the training effectiveness. Then, close and click "Training" tab and select "Generate" and consequently select the folder to save generate.

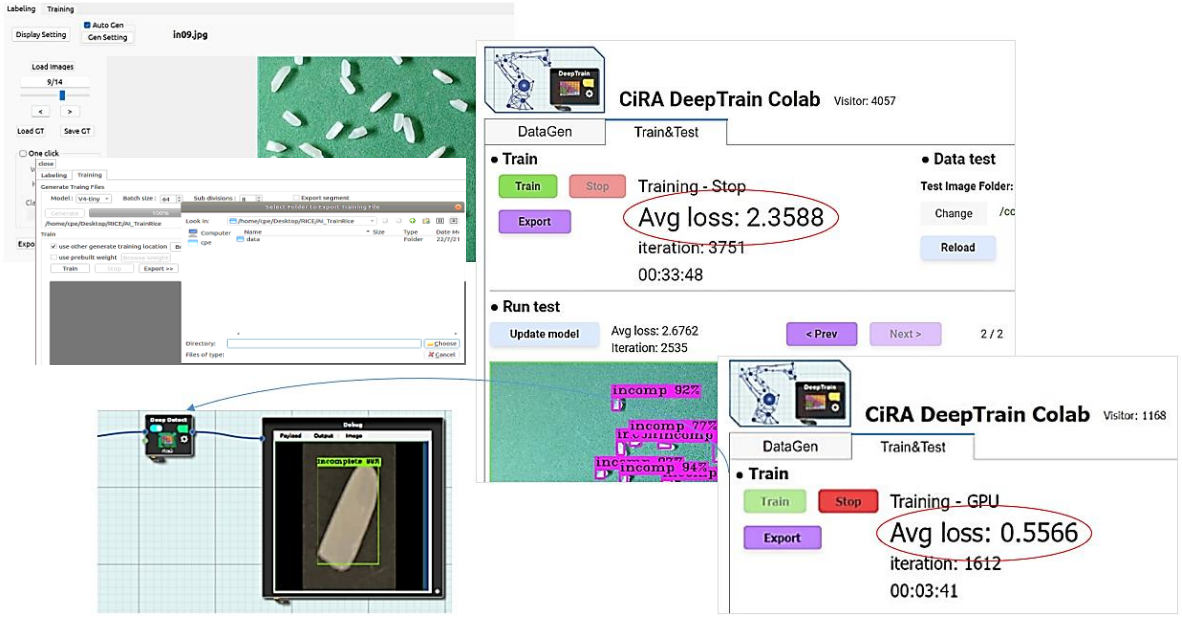

Figure 6. Training and Testing on Google Colab

Once complete 100% generate, select "Use Other Generate Training Location" and click "Browse Training File". Then, select the folder which stores Generate files, named "Data". Click "Choose" when select the folder to store the "Training" file and click "Train" button.

Consequently, the data processing will begin and remain until the average value will be around 0.5 which is considered as the most accurate and effective range. Once the average value has reached this range, click "Stop" and thus click "Export" the training files which stored in the folder. These files are named as obj.names, test.cfg, and train.weights.

Factors to be considered when perform accuracy testing are camera focus, light intensity, and number of objects, by arranging all blocks which consist of Button run, Webcam, Deep Detect, and Debug as illustrated in Figure 7. Then, open the Deep Detect window for Config loading by selecting the prepared folders containing training data. Select the Webcam block to select the webcam to be used. Finally, click the "Button Run" and the outcome will be displayed as illustrated in Figure 7.

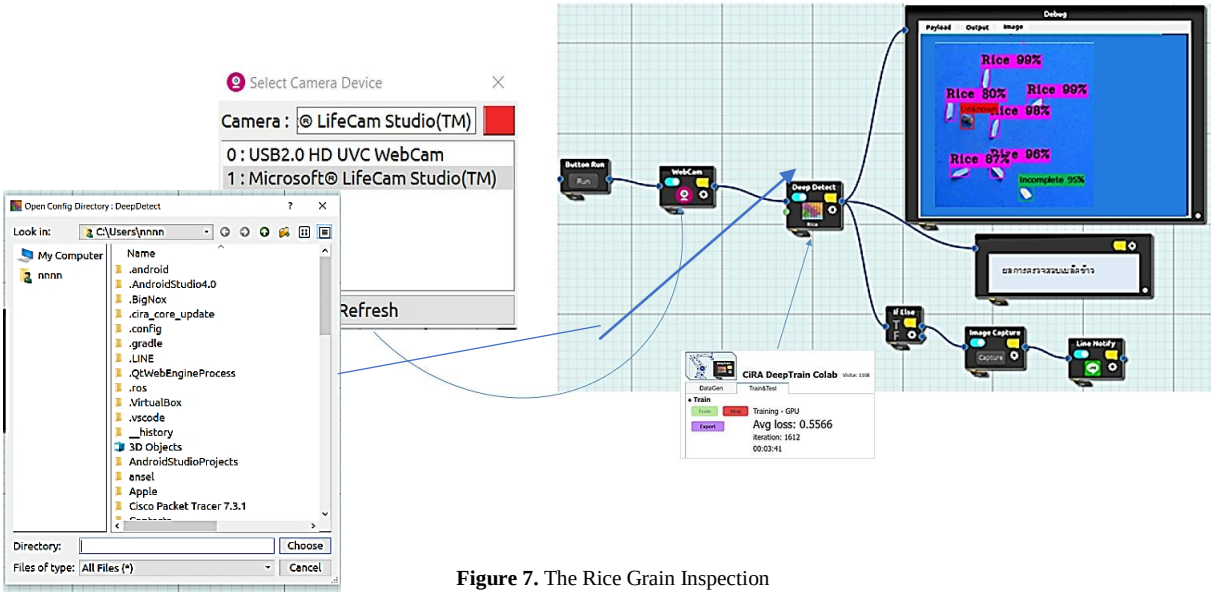

Figure 7. The Rice Grain Inspection

3.3 The Connecting of All Blocks to Initiate the System

In Deep Detect block, the trained date files will be loaded and configured. Concurrently, the Webcam block will perform the image processing and display via the Debug block, pertaining to the accuracy test menu. The Label block will display the message if any rice grain is detected. If the Deep Detect block detected some rice grain, there is the program coding to display message. The IF ELSE code block will be in action if any rice grain(s) is detected while the Image Capture block will also be activated to capture the images on Debug block. The LINE notify block is the interconnection of software and network which will be activated via Image Capture block. Once all blocks are completely linked with the Button Run is clicked, the captured imaged with rice grain inspection percentage will be sent to LINE notify.

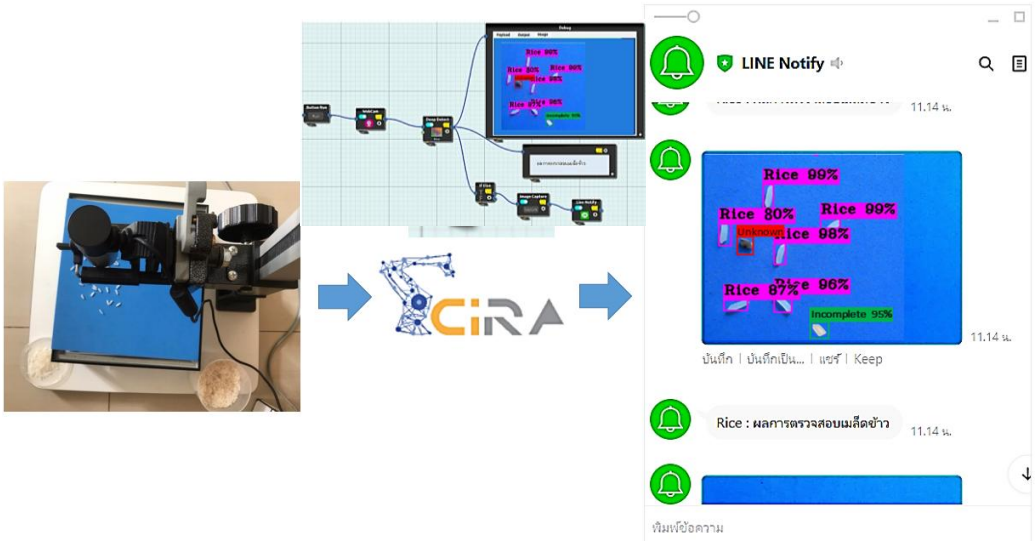

Figure 8. CiRA CORE Tool Blocks and Results

4. Discussion and Conclusion

The research team had experimented and recorded the system effective under the different conditions regarding the environment and light intensity. The developed system had been experimented and field-tested base on the actual working situation in which the variation of light intensity (that is assumed to be the factor that's affecting the system effectiveness), is the mostly considerable. Pertaining to this assumption, the testing has been performed and the results are as exhibited in the Table 1. below.

Table 1. The System Testing Effectiveness

No.	Environment	Total Effectiveness
1	Exactly similar light intensity and timing to the memorized images	90% or better
2	Closely similar light intensity and timing to the memorized images	85% or better
3	Slightly different light intensity and timing to the memorized images	80% or better
4	Completely different light intensity and timing to the memorized images	70% or better

From table above, operational environment and surroundings affect the system effectiveness regarding the inspection of rice grain contaminations. This can be concluded that system should be used within the environment and surroundings that are closely similar to the sample images to enhance the better accuracy. Thus, there should have training images that extensively covered diversified environment and surroundings. This is to enable the system to learn at as extensive as possible for the best effectiveness.

Conclusively, once being tested with the actual rice, the effectiveness is satisfied pertaining to the predefined scope (80% or higher) which was compliant to the actual effectiveness. Regarding the image screen capturing and sending to the LINE notification, this was also compliant to the objectives in that the linkage between the CiRA CORE and LINE notification was successful.

Pertaining to the user satisfaction evaluation, this has been based on the user expectations and user's technical backgrounds. This is partially based on the system usability scale (SUS) but has been adapted for the better fit to the context. The system user satisfaction is evaluated with 5-Likert Scale. The evaluation outcome yielded the GOOD level with 4.42 in total average, as illustrated in the Table 2. below.

Table 2. User Satisfaction Levels from the 30 Questionnaire Respondents

Evaluation Aspects	Mean	Standard Deviation	Satisfaction Level
1.Convenience of Use	4.34	0.51	GOOD
2.Output Accuracy	4.25	0.50	GOOD
3.Responsiveness	4.60	0.52	GOOD
4.System Utilities	4.50	0.51	GOOD
Total Average	4.42	0.51	GOOD

Conclusion

Pertaining to the research beginning from the system design and development until the testing, many aspects regarding the efficiency and effectiveness of the developed system had been discovered and can be concluded as the follows.

- The operation environment and surroundings affect the system effectiveness
- The environment and surroundings that are closely similar to the sample images to enhance the accuracy, is preferable.
- The training images should be extensively covered diversified environment and surroundings for the best effectiveness.
- System effectiveness is satisfied pertaining to the predefined scope (80% or higher) which was compliant to the actual effectiveness.
- Regarding LINE notification, this was also compliant to the objectives in that the linkage between the CiRA CORE and LINE notification was successful.

Base on the stated limitation of the result, the extensive improvement in impurities detecting with 3D camera via color and dimensions should be the interesting further work.

5. Recommendation for Future Application

Since Thailand is one of the world producers of grains, the research regarding this discipline and its applications would be extensively beneficial. The result of this research is the evidence the domestic affordable technologies can be applied in conformance to the Thailand's agricultural contexts. The grain sorting and grading process can be more effective and less resource consumed which would result in the lower manufacturing cost and higher productivity. However, the constant supports and research endeavors should be maintained that could elevate such agriculture-related applications of AI based technologies. This would be beneficial to the national economy, food securities, and technological independencies as a whole.

6. Acknowledgements

It is the deep appreciation to the research project sponsorship via the annual revenue budget of the Faculty of Engineering, Rajamangala University of Technology Phra Nakorn (RMUTP), 2023 fiscal year. The RMUTP executive supports are also deeply appreciated pertaining to the accomplishment of this research project.

7. References

CiRA ROBOTICS, (2022), CiRA CORE. Retrieved 14 May 2022, from: https://www.cira-ai.com/en/features.

Mark Zamoyta, (2022), JavaScript Fundamentals. Retrieved 2 July 2022, from: https://www.pluralsight.com/courses/javascript-fundamentals.

Microsoft, (2022), LifeCam Studio. Retrieved 8 August 2022, from: https://www.microsoft.com/th-th/accessories/products/webcams /lifecam-studio?activetab=overview:primaryr2

Microsoft, (2022). Microsoft LifeCam Studio. Retrieved 8 August 2022, from: https://shop.thaiware.com/1648-Microsoft-LifeCam-Studio.html.

The Predicting TOEIC Score with Regression Model: A Case Study of Institute of Aviation and Aerospace Technology, RMUTTO

Watsamon Santisiri[a] and *Boonyawat Aksornkitti[b]
[a,b] *Institute of Aviation and Aerospace Technology, Rajamangala University of Technology Tawan-ok, Chon Buri, Zip Code: 20110, Thailand*
*Corresponding author. *E-mail address:* boonyawat_ak@rmutto.ac.th

Abstract
This research aims to find correlation between grade average point (GPA) of English language and TOEIC score also predict TOEIC score from grade average point (GPA) of English language. Population is students from Institute of Aviation and Aerospace Technology, Rajamangala University of Technology Tawan-OK (RMUTTO) who have taken TOEIC exam, totaling 110 students by using Correlation coefficient, Linear regression, and Mean absolute percentage error to answer objectives. Result found that correlation between grade average point (GPA) of English language and TOEIC score are moderate correlation at 0.6930 in same direction and equation of TOEIC score prediction model is y = 45.9180 + 85.9564x with MAPE = 16.4623%.

Keywords: Aviation / Correlation / English / Regression / TOEIC

1. Introduction
1.1 Background
Working in the aviation industry always use English as a medium of communication, in order to communicate with completeness and standard in aviation industry commonly used TOEIC (Test of English for International Communication) score. The job in aviation industry required different TOEIC score such as Pilot require 650 – 750, Cabin crew require 600 – 650, Air traffic controller require 600 – 700, Passenger service require 450 – 550. (JobBD, 2023).

Institute of Aviation and Aerospace Technology, Rajamangala University of Technology Tawan-OK produces bachelor degree students to meet Thailand's need for aviation personal. Students who study here will learn in business administration, aviation management, and English language such as English for communication, English for business communication, Aviation Technical English, and Aviation Technical English 2.

However, to prove successful in learning English language of students. We need to find correlation between grade average point (GPA) of English language and TOEIC score to be a guideline for developing in teaching technique and to predict TOEIC score for students to know themselves and preparing before taking TOEIC exam.

1.2 Objective
1.2.1 To find correlation between grade average point (GPA) of English language and TOEIC score
1.2.2 To predict TOEIC score from grade average point (GPA) of English language

1.3 Assumption
1.3.1 English language GPA has very high correlation in same direction with TOEIC scores
1.3.2 Mean absolute percentage error (MAPE) of prediction will less than 20%

1.4 Benefit
1.4.1 A guideline for developing teaching technique
1.4.2 A preparing for student before taking TOEIC exam

1.5 Conceptual framework

Figure 1 Conceptual framework

2. Literature review

Chanchusakun, S., Et al. (2017) have done topic: A Comparison of quality of equating English scores between equipercentile, linear and regression methods with objective to equating English scores between SEPT and TOEIC among equipercentile, linear and regression methods and to comparison of quality of equating among metioned methods. Population was 40 students from bachelor of business administration in hotel management, Silpakorn university international college, Thailand. Linear and regression methods were tool for data analysis. Result found he linear equation is TOEIC score = -176.976 +13.08SEPT.

Ephrem, B. G., Et al. (2017) have done topic Projection of students' exam marks using predictive data analytics with objective to predicting students' grade using the following attributes such as quiz-1, quiz-2, class assignment, class activity, coursework, mid and final exam marks. Population was students' marks from Department of Information Technology, Higher College of Technology, Sultanate of Oman. Boosted trees regression (BRT), Decision trees regression, Random forest regression, Linear regression were tool for data analysis, result found Linear regression had the lowest root mean square error (RMSE).

Ju, Y. J. and Li, C. H (2020) have done topic: TOEIC score prediction according to student's learning performance on university English course with objective to ensure their student's workplace English communication ability meets the needs of the industry and strengthen the student's employment ability. Population was students of the Department of Applied English from the University of Technology, Taiwan. Multiple linear regression (MLR), and support vector regression (SVR) were a tool for data analysis. Result found root mean square error (RMSE) of SVR is better than MLR.

Kusmartini, S. E. and Simanjuntak, T. (2015) have done topic: Predicting English performance of Polytechnic students by using TOEIC score and student perception about academic motivation with objective to predicting English performance of Polytechnic students by using TOEIC score. Population was 60 students of English Department State Polytechnic of Sriwijaya, Indonesia. Pearson's product moment correlation coefficient and Multiple linear regression (MLR) were tool for data analysis. Result found correlation was 0.668.

Sirikanjanawong, N. and Wasanasomsithi, P. (2018) have done topic: Relationship between The ICAO Language Proficiency Requirements (LPRs) and Test of English for International Communication (TOEIC) Scores of Flight Attendants in Thailand with objective to explored the relationship between the ICAO Language Proficiency Requirements (LPRs) and TOEIC scores. Population was 100 Thai Airways international flight attendants Pearson's product moment correlation coefficient and four-point Likertscale were tool for data analysis. Result found correlation between ICAO Language Proficiency Requirements and TOEIC scores was 0.384.

3. Methodology

3.1. Population

Population in this research is students from Institute of Aviation and Aerospace Technology, Rajamangala University of Technology Tawan-OK (RMUTTO) who have taken TOEIC exam, totaling 110 students.

3.2 Statistic

Correlation coefficient (Investopedia, 2023)

$$r = \frac{n\sum xy - \sum x \sum y}{\sqrt{[n\sum x^2 - (\sum x)^2][n\sum y^2 - (\sum y)^2]}} \quad (1)$$

Where r = Correlation coefficient
n = Number of populations
x = English language GPA
y = TOEIC scores
$\sum$ = Summation

Correlation coefficient (r) always has value between -1.0 to +1.0 if r value is between 0.00 and 0.03 (0.00 and -0.03), it means there is a slight correlation in same direction (opposite direction). if r value is between 0.31 and 0.50 (-0.31 and -0.50), it means there is a low correlation in same direction (opposite direction). if r value is between 0.51 and 0.70 (-0.51 and -0.70), it means there is a moderate correlation in same direction (opposite direction). if r value is between 0.71 and 0.90 (-0.71 and -0.90), it means there is a high correlation in same direction (opposite direction). if r value is between 0.91 and 1.00 (-0.91 and -1.00), it means there is a very high correlation in same direction (opposite direction). (Statistics How To, 2023)

Linear regression

$$y = a + bx \qquad (2)$$

Where y = TOEIC scores
a = Intercept of y
b = Slope
x = English language GPA

Linear regression is used to predict the value on the value of another variable. The variable that want to predict is called the dependent variable (TOEIC scores). The variable that using to predict the other variable's value is called the independent variable (English language GPA). (IBM, 2023)

Mean absolute percentage error

$$MAPE = \frac{\sum \frac{|A-P|}{A} \times 100}{N} \qquad (3)$$

Where MAPE = Mean absolute percentage error
A = Actual TOEIC scores
P = Predict TOEIC scores
N = Number of populations
$\sum$ = Summation

Mean absolute percentage error (MAPE) represents the average of the absolute percentage errors of each dataset to calculate how accurate the predicted quantities (Predicted TOEIC scores) were in comparison with the actual quantities (Actual TOEIC scores). (Indeed, 2023). If MAPE value less than 10%, it means very good prediction. If MAPE value between 10% - 20%, it means good prediction. If MAPE value between 21% - 50%, it means moderate prediction. If MAPE value more than 50%, it means poor prediction. (Allwright, S.,2023)

3.3 Data analysis

This research uses secondary data from 110 students from Institute of Aviation and Aerospace Technology, Rajamangala University of Technology Tawan-OK (RMUTTO) who have taken TOEIC exam. English language GPA came from their average GPA of 4 English subjects (English for communication, English for business communication, Aviation Technical English, and Aviation Technical English 2). After we got English language GPA and TOEIC score we used equation (1) to find correlation between English language GPA and TOEIC score to answer first objective and first assumption, equation (2) to predict TOEIC score from English language GPA to answer second objective, and finally equation (3) to answer second assumption.

4. Results and Discussion

4.1. Result

Table 1 Individual English language GPA and TOEIC score

Student	English language GPA	TOEIC score	Student	English language GPA	TOEIC score
1	2.67	290	18	2.67	225
2	2.75	315	19	2.42	225
3	3.08	310	20	2.5	390
4	3.83	375	21	3.00	280
5	3.00	320	22	2.00	285
6	1.83	205	23	1.92	290
7	2.20	205	24	2.00	275
8	2.92	265	25	2.17	250
9	3.08	360	26	3.50	330
10	3.50	345	27	2.00	270
11	2.42	270	28	1.92	230
12	3.75	390	29	2.42	295
13	2.33	265	30	3.58	290
14	2.50	340	31	1.58	195
15	2.33	190	32	2.08	205
16	1.83	265	33	2.00	250
17	2.83	365	34	3.67	265

Table 1 Each student English language GPA and TOEIC score **(Continued)**

Student	English language GPA	TOEIC score	Student	English language GPA	TOEIC score
35	2.17	160	73	3.50	425
36	3.75	395	74	1.67	160
37	2.83	270	75	3.00	230
38	2.67	270	76	2.00	200
39	4.00	490	77	3.00	235
40	2.33	265	78	4.00	610
41	2.75	200	79	2.92	335
42	2.25	225	80	1.42	190
43	2.08	265	81	2.17	245
44	2.58	225	82	2.00	245
45	1.92	250	83	3.58	345
46	2.33	290	84	2.25	200
47	3.75	400	85	3.42	275
48	3.83	275	86	3.08	315
49	3.67	335	87	2.17	200
50	2.25	235	88	1.92	190
51	2.25	235	89	3.25	265
52	3.75	480	90	2.42	230
53	3.25	310	91	3.92	465
54	3.67	255	92	3.33	365
55	3.75	335	93	3.42	275
56	2.25	265	94	3.83	315
57	2.00	200	95	4.00	610
58	3.17	310	96	4.00	470
59	3.25	260	97	3.08	300
60	3.25	255	98	3.75	415
61	2.67	215	99	3.50	295
62	2.92	380	100	3.25	210
63	1.67	190	101	2.08	340
64	3.92	470	102	3.08	215
65	2.00	205	103	2.92	275
66	2.67	255	104	2.75	220
67	2.58	280	105	2.33	185
68	3.92	315	106	3.50	335
69	2.58	220	107	3.00	260
70	2.42	260	108	2.25	250
71	2.58	220	109	2.50	180
72	3.00	215	110	2.25	300

From table 1 minimum and maximum English language GPA is 1.42 from 80th student and 4.00 from 39th, 78th, 95th, 96th student, respectively. Minimum and maximum TOEIC score is 160 from 35th, 74th student and 610 from 78th, 95th student, respectively.

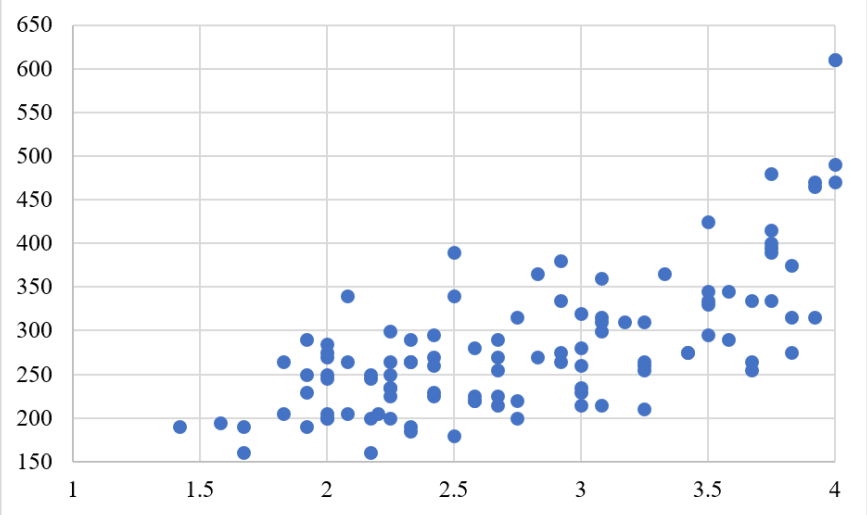

Figure 2 Relationship between English language GPA (x-axis) and TOEIC score (y-axis)

Table 2 Regression statistics

Regression statistics	
Multiple R	0.693395515
R Square	0.48079734
Adjusted R Square	0.475989908
Standard Error	61.3785519
Observations	110

From table 2 Multiple R is approximately 0.6930, R Square is approximately 0.4808, Adjusted R Square is approximately 0.4760, Standard Error is approximately 61.3790, and Observations (Population) equal to 110.

Table 3 Hypothesis testing

	df	SS	MS	F	Significance F
Regression	1	376775.0872	376775.0872	100.011261	4.64803E-17
Residual	108	406871.2764	3767.326633		
Total	109	783646.3636			

From table 3, Null hypothesis (H_0) is English language GPA and TOEIC score have no relationship, Alternative hypothesis (H_1) is English language GPA and TOEIC score have relationship. When look at Significance F value (4.64803E-17 or 0.00000000000000000464803) is less than 0.05, so we reject H_0 and conclude that English language GPA and TOEIC score have relationship at level of significance 0.05, since H_0 is rejected so we can crate prediction model.

Table 4 Crate prediction model

	Coefficients	Standard Error	t Stat	P-value
Intercept	45.91796693	24.72752732	1.856957485	0.066042171
English language GPA	85.95643034	8.595159097	10.00056303	4.64803E-17

From table 4 we can crate predication model y = 45.9180 + 85.9564x, table 5 will show value of actual TOEIC scores, predicted TOEIC scores with measuring prediction performance by using MAPE.

Table 5 Prediction TOEIC scores and measuring prediction performance

Student	Actual TOEIC scores	Predict TOEIC scores	MAPE (%)	Student	Actual TOEIC scores	Predict TOEIC scores	MAPE (%)
1	290	275	5.1724	32	205	225	9.7561
2	315	282	10.4762	33	250	218	12.8000
3	310	311	0.3226	34	265	361	36.2264
4	375	375	0.0000	35	160	232	45.0000
5	320	304	5.0000	36	395	368	6.8354
6	205	203	0.9756	37	270	289	7.0370
7	205	235	14.6341	38	270	275	1.8519
8	265	297	12.0755	39	490	390	20.4082
9	360	311	13.6111	40	265	246	7.1698
10	345	347	0.5797	41	200	282	41.0000
11	270	254	5.9259	42	225	239	6.2222
12	390	368	5.6410	43	265	225	15.0943
13	265	246	7.1698	44	225	268	19.1111
14	340	261	23.2353	45	250	211	15.6000
15	190	246	29.4737	46	290	246	15.1724
16	265	203	23.3962	47	400	368	8.0000
17	365	289	20.8219	48	275	375	36.3636
18	225	275	22.2222	49	335	361	7.7612
19	225	254	12.8889	50	235	239	1.7021
20	390	261	33.0769	51	235	239	1.7021
21	280	304	8.5714	52	480	368	23.3333
22	285	218	23.5088	53	310	325	4.8387
23	290	211	27.2414	54	255	361	41.5686
24	275	218	20.7273	55	335	368	9.8507
25	250	232	7.2000	56	265	239	9.8113
26	330	347	5.1515	57	200	218	9.0000
27	270	218	19.2593	58	310	318	2.5806
28	230	211	8.2609	59	260	325	25.0000
29	295	254	13.8983	60	255	325	27.4510
30	290	354	22.0690	61	215	275	27.9070
31	195	182	6.6667	62	380	297	21.8421

Table 5 Prediction TOEIC scores and measuring prediction performance (Continued)

Student	Actual TOEIC scores	Predict TOEIC scores	MAPE (%)	Student	Actual TOEIC scores	Predict TOEIC scores	MAPE (%)
63	190	189	0.5263	87	200	232	16.0000
64	470	383	18.5106	88	190	211	11.0526
65	205	218	6.3415	89	265	325	22.6415
66	255	275	7.8431	90	230	254	10.4348
67	280	268	4.2857	91	465	383	17.6344
68	315	383	21.5873	92	365	332	9.0411
69	220	268	21.8182	93	275	340	23.6364
70	260	254	2.3077	94	315	375	19.0476
71	220	268	21.8182	95	610	390	36.0656
72	215	304	41.3953	96	470	390	17.0213
73	425	347	18.3529	97	300	311	3.6667
74	160	189	18.1250	98	415	368	11.3253
75	230	304	32.1739	99	295	347	17.6271
76	200	218	9.0000	100	210	325	54.7619
77	235	304	29.3617	101	340	225	33.8235
78	610	390	36.0656	102	215	311	44.6512
79	335	297	11.3433	103	275	297	8.0000
80	190	168	11.5789	104	220	282	28.1818
81	245	232	5.3061	105	185	246	32.9730
82	245	218	11.0204	106	335	347	3.5821
83	345	354	2.6087	107	260	304	16.9231
84	200	239	19.5000	108	250	239	4.4000
85	275	340	23.6364	109	180	261	45.0000
86	315	311	1.2698	110	300	239	20.3333
Average MAPE = 16.4623%							

From table 5 minimum MAPE is 0.000% from 4th student Actual and Predict TOEIC scores is 375, maximum MAPE is 54.7619% from 100th student Actual TOEIC scores is 210 and Predict TOEIC scores is 325. Average MAPE = 16.4623%

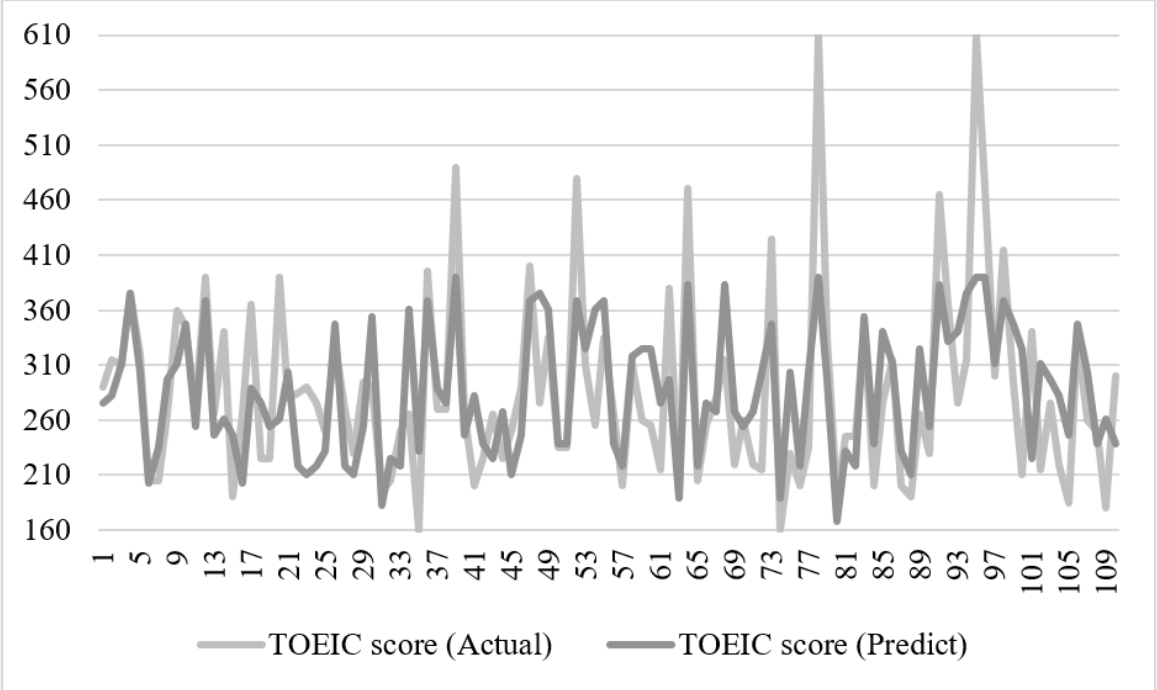

Figure 3 Comparison of TOEIC score (Actual) and TOEIC score (Predict)

5. Conclusions

The first objective to find correlation between grade average point (GPA) of English language and TOEIC score, when look at table 2 we can find that English language GPA and TOEIC score is 0.6930, it means there are moderate correlation in same direction.

Second objective to predict TOEIC score from grade average point (GPA) of English language, when look at table 4 we can find equation of prediction model y = 45.9180 + 85.9564x with Average MAPE = 16.4623%.

The first assumption English language GPA has very high correlation in same direction with TOEIC scores, when we look at table 2 can conclude that it wrong, truly is English language GPA has moderate correlation in same direction with TOEIC scores.

Second assumption MAPE of prediction will less than 20%, when we look at table 5 we can find that MAPE = 16.4623% which is true with good prediction performance.

For above assumption we can prove that teaching technique has effect in TOEIC score and If we improve teaching technique to increase GPA, TOEIC score will be increase and if we use equation of predict TOEIC score from GPA the error will be +- 16% from predict score this means students will know their score and can prepare themselves if they need more score.

Future research there will be create prediction model by using multiple regression from each English language subject (English for communication, English for business communication, Aviation Technical English, and Aviation Technical English 2) with assumption all variable will have high correlation in same direction and MAPE of prediction will less than 10%.

6. Acknowledgements

The authors thank you for Institute of Aviation and Aerospace Technology, RMUTTO for research funding and RMUTIC to give a chance to public our research.

7. References

Allwright, S.,2023, What is a good MAPE score? (Online) From https://stephenallwright.com/good-mape-score/

Chanchusakun, S., Paiwithayasiritham, C., Polpanthin, Y., Supannopaph, P, 2017, A Comparison of quality of equating English scores between equipercentile, linear and regression methods, Veridian E-Journal, Vol10(2),p.2,444 - 2,455.

Ephrem, B. G., Balasupramanian, N., Shuaily, H, 2017, Projection of students' exam marks using predictive data analytics, The Free and Open Source Software Conference, p. 61 – 66.

JobBD, 2023, TOEIC score in aviation industry. (Online) From https://th.jobsdb.com/th/search-jobs/toeic-score-700/1

Ju, Y. J. and Li, C. H, 2020, TOEIC score prediction according to student's learning performance on university English course, Education and New Developments, DOI: 10.36315/2020end034

Kusmartini, S. E. and Simanjuntak, T, 2015. Predicting English performance of Polytechnic students by using TOEIC score and student perception about academic motivation. The 62th TEFLIN International Conference, p. 664 – 654.

IBM, 2023, What is linear regression? (Online) From https://www.ibm.com/topics/linear-regression

Indeed, 2023, What Is MAPE? A Guide to Mean Absolute Percentage Error. (Online) From https://www.indeed.com/career-advice/career-development/what-is-mape

Investopedia, 2023, The Correlation Coefficient: What It Is. (Online) From https://www.investopedia.com/terms/c/correlationcoefficient.asp

Statistics How To, 2023, Correlation Coefficient: Simple Definition, Formula, Easy Steps. (Online) From https://www.statisticshowto.com/probability-and-statistics/correlation-coefficient-formula/

Sirikanjanawong, N. and Wasanasomsithi, P, 2018, Relationship between The ICAO Language Proficiency Requirements (LPRs) and Test of English for International Communication (TOEIC) Scores of Flight Attendants in Thailand, Language Education and Acquisition Research Network Journal, Vol11(1), p. 64 – 86.

The Web Application of Information Presentation with Augmented Reality Technology with Case Studies of Temple, Market and Museum

Uraiwan Inyaem[a*], Kittikhun Sangyoo[b], Teerawut Rukkachat[c]
[a,b,c]*Division of Mathematics and Computer Science, Faculty of Science and Technology, Rajamangala University of Technology Thanyaburi, Pathumthani, 12110, Thailand*
*Corresponding author. 0898944631; 025494195; *E-mail address:* uraiwan.inyaem@rmutt.ac.th

Abstract
Nowadays, after the coronavirus disease (COVID-19), the tourism industry is recovering. There are more Thai and foreign tourists traveling. There are many groups of cultural tourists who like to visit temples or museums. The tourist's problem is that when visiting a tourist attraction, they receive little information about the attraction. The virtual reality technology is widely known and used to present information. The web application for presenting data using virtual reality techniques is proposed and to promote cultural tourism by providing historical information in case studies around the Klong 1 area, Khlong Luang district, Pathum Thani province in Thailand. The findings were prepared as a guidebook in the form of pamphlets by case locations such as Wat Thawi Kara Anan, Talaad Thai market, and Agricultural Museum in Honor of His Majesty the King. According to the assessment of the quality of the proposed system by 100 general users, the evaluation is carried out in 2 aspects, namely, the average design of the web application is 3.77, which is very high. The standard deviation in web application design is 0.65, which is very high. The average function access is 4.06, which is very high, and the standard flat deflection for function access is 0.82, which is very high. The conclusion is shown that the proposed website application for presenting information with virtual reality techniques with case study of temple, market and museum can be put into practice.

Keywords: Guidebook , Temples, Markets, Museums, Augmented Reality Technology

1. Introduction
TAT Review from the website of tatreviewmagazine.com discusses the situation of tourism in Thailand 2022, update as of January 30, 2023. The overall tourism situation of Thai visitors in 2022 is increasing after the COVID-19 pandemic decreased. Tourists start traveling during the holidays. Number of Thai visitors and tourism revenue in Thailand in particular, Bangkok and its vicinity recorded a growth rate of 141% compared to 2021. Tourism revenue is estimated at 142277 million baths. This represents a percentage of recovery from 2019 to 37%. The tourism industry, which consists of many types of businesses, both directly related and supporting the purchase of services by foreign tourists, is considered an invisible export. The production of goods is a service that tourists buy, thus allowing investment which will benefit the country, will help create many jobs and will be economic circulation. In addition, on the social side, tourism is a way to relax and learn about different cultures. Pathum Thani is regarded as a province with a lot of tourism as a city that attracts tourists, the cost of living is not high, making it easy for tourists to decide to visit. Pathum Thani has many attractions, historical aspects, traditions and ancient sites. Historic sites refer to man-made structures that are more than 100 years old with a history that is useful in art, history and archaeology. In addition, ancient sites also include places of historical significance or traces of human activity, it is evident that human wisdom can be learned from ancient sites, antiquities and archaeological sites of various types. We can also learn how to struggle and adapt human beings to survive in order to sustain society. Therefore, it is accepted that the ancient site, antiques and archaeological sites are like containers of many achievements. Which people nowadays can apply to use it for infinite benefits. For this reason, antiquities, archaeological sites, and archaeological sites are classified as cultural resources, cultural property or cultural heritage of each nation. Augmented reality (AR) is the combination of a real environment and a virtual object at the same time. The virtual object may be an image, videos, sounds, data processed from computers and mobile phones, tablets or other small wearables and allow us to respond to the simulation. An example of AR usage is Pokémon Go, which is a major phenomenon for gamers around the world. The core foundations of AR need to include the principles of Motion Detection, Beat Detection, Voice Recognition and Image Processing. In addition to motion detection via motion detect, some of the system's responses through the media require user voice detection and beat detection to create rhythm to create alternative systems such as voice to trigger interactive media. Voice command is classified as AR. The image processing section is complementary to the research, which is a subset of AR because it focuses on the work of artificial intelligent to convey emotions to users through color and images.

Based on literature reviews and research studies related to virtual reality technology we found that follows as: Sricharoen (2019) presented the research on application to promote tourism must to visit tourist 8 destinations in Phetchabun province with virtual reality technology. It was found that the application developed from the Unity program. It can be used to apply the application conveniently. Limpinan (2019) proposed the promotion of tourist attractions in Mahasarakham province using virtual reality technology. It was found that the application has 3 functionalities: 1) Marker in the form of a commemorative postcard to publicize tourist information of 5 tourist attractions in Mahasarakham province such as Phra That Na Dun, Ku Santarat, Ku Ban Khwao, Phra Yuen

Kantaravichai (Buddha Mongkol) and Kaeda wooden bridge. 2) Model in the form of 3D animation with movement of tourist attractions in Mahasarakham province. 3) Application with Android operating system under the name AR Mahasarakham. Klinchan (2020) presented development of information system for presenting mural painting animation in topic of Thotsachart and Phra Sri Ariya in conservation ancient sites in the form of virtual reality technology. In order to inherit local cultural traditions in Khao Samor Khon Subdistrict, Tha Wung District, Lop Buri Province, it was found that the developed system presents ancient paintings and animations. Lawen (2017) researches on the redesigning a mobile application based on Bloom's concept. The mobile application is used in the classroom promotes the expression of various learning behaviors. Boonsomthop (2020) proffers designing travel guides using augmented reality technology adds value and promotes information. Historical tourism in Kanchanaburi city area display in digital tourism. From this article, we found that 1) design of a guide to historical attractions in Kanchanaburi city area is designed to support augmented reality technology. 2) to evaluate historical travel guides that support augmented reality technology, and 3) to assess tourists' satisfaction with the use of historical travel guides. Kluangkhaew (2017) presents the publication design id created for new era Yaowarat tourism. The paper is to make travel publications interesting and attractive to tourists. They use travel publications that they make. it possible to travel as fully as possible in all places. Next article is development of english media to promote tourism of temples in Phitsanulok province by Jumphot Onsuang. It presents travel media in english to be up to date. This medium is available to international travelers and increase the comfort of tourists. The next presents by Ploy-ngam and Jarusen (2018) are the advertising materials on 3D virtual pamphlets via smartphones for exhibition. The article presents making the folding raft that tourists read interesting by using 3D techniques that can be viewed via smartphones for an enjoyable viewing of places. Nowadays, smartphones are a device that everyone has with them. It will make traveling more interesting. Later paper is proposed by Khumraksanichathorn & Montpanthong (2021). The paper is the museum tourism behavior of generation Y tourists. This article presents an exhibition with a format of presentation of information through video, sound, and post-tour behavior. Research has shown that most travelers feel unsure about coming back to visit museums, so they need to review our place from many others in order to come back again in the future. The last article is influence of digital marketing tools dual QR codes and AR technology in applications affecting customer satisfaction in quality for toy museums in Thailand. As well, Tangkuptanon & Saowmuang (2021) presents the use of QR codes and ARs in marketing business. Using this technology makes work faster and more convenient. From the above, the research organizer came up with the idea of developing a web application to present information in case study of temple, market, and museum. The system has been made more interesting by leveraging virtual reality technology in conjunction with tourism maps. The case study with temples, markets and museums are presented in the form of three-dimensional technology. This will promote cultural tourism in line with current modern technology for major attractions in case study of the Klong Nung, Khlong Luang District, Pathum Thani Province.

2. Methodology

Users or tourists can access the application via smartphone. Start by using the smartphone camera feature scan QR codes from brochures. Then the application will display a menu. Users can choose the operation menu according to their needs. Functionality includes video tracking, 3D processing, 3D rendering and animation, and superimpose that can view 3D. In the section of display in AR both model and audio format such as temple, market and museum as shown in below figure 1.

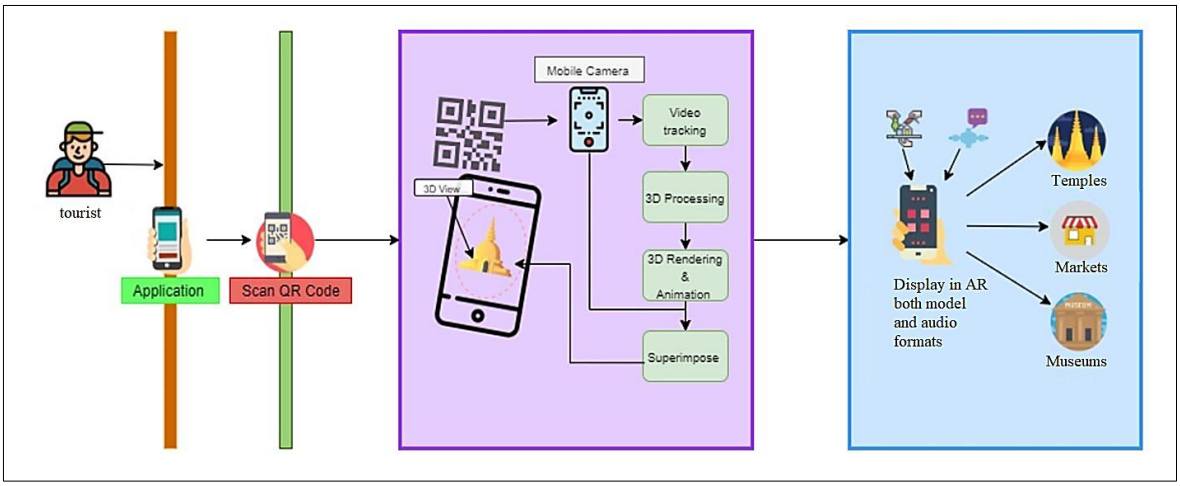

Figure 1 System framework

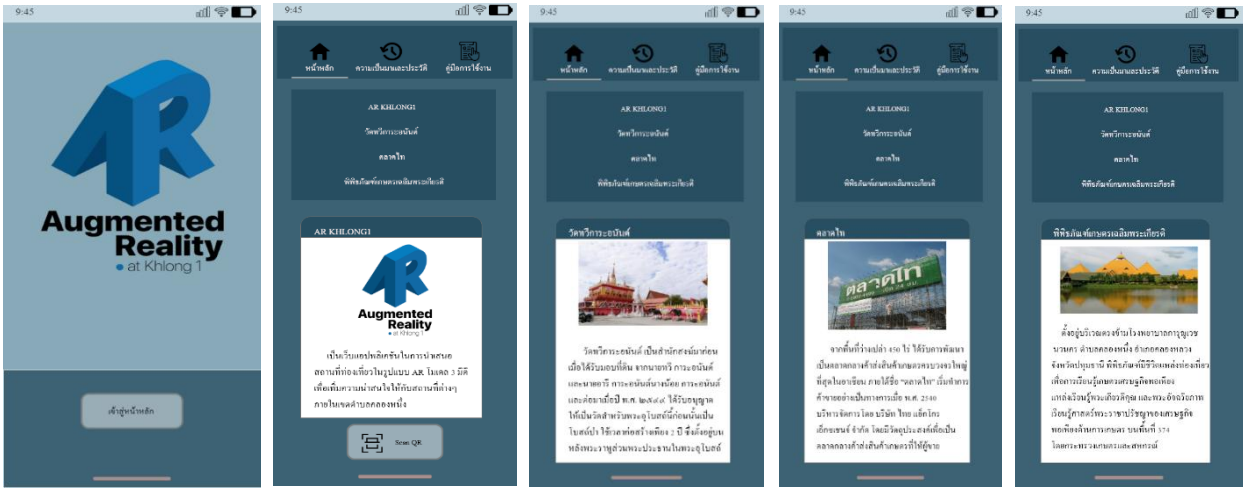

Figure 2 The history of the temple, market and museum

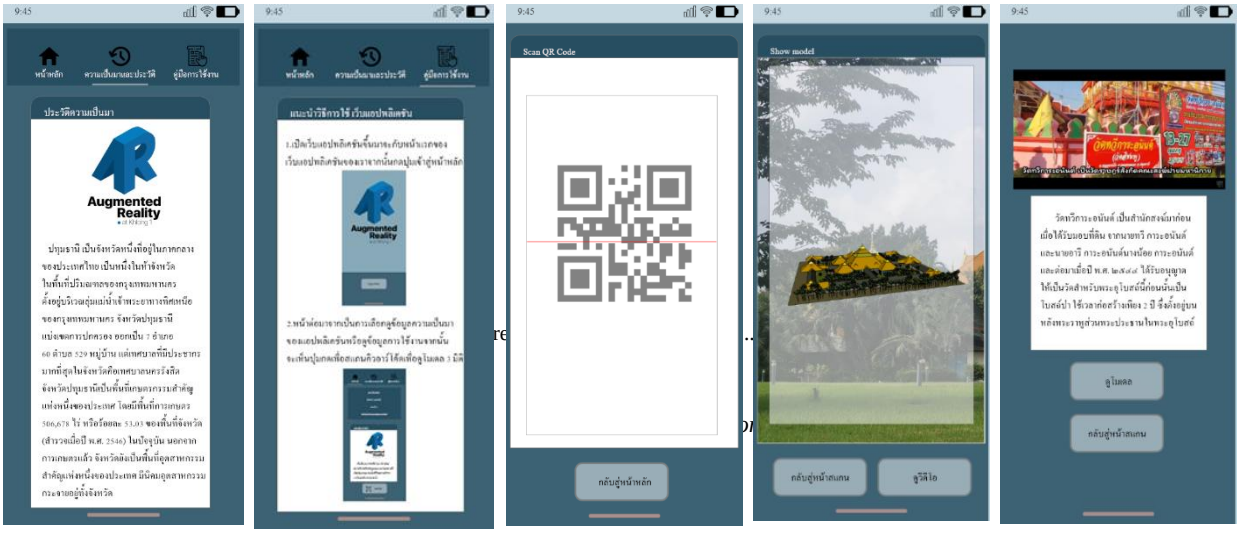

Figure 3 Main functions in application

According to history in figure 2, Wat Thawi Kara Anan used to be a place for a monastery. Mr. Thawee Karaanan, Mr. Aree Karaanan and Mrs. Noi Karaanan gave the land for the construction of the temple. In the temple area, there is a chapel built on the back of Rahu. As for the principal Buddha image in the ubot, it is a Buddha image of Luang Por Sothon in the posture of meditation. In most cases, the main Buddha image in the ordination hall is Phra Phuttha Chinnarat, the posture of dung Mara and the meditation posture. Those who have overlaid faith have come to pay homage to the main Buddha image in the ordination hall continuously. The basement of the ordination hall is a statue of Rahu. There will be relatives who bring things to offer to Rahu before surviving under the ubosot for prosperity. Talaad Thai is the centre of complete agricultural products in the area of around 500 rai. Started trading in 1995, market was officially opened in 1997 with the objective of creating a marketplace for sellers and buyers to trade directly with each other freely at fair prices. Market open daily 24 hours. the objectives of creating a marketplace are for sellers and buyers to trade directly with each other freely at fair prices. The market is located on Phaholyothin Road. Km. 42, Khlong Luang District, Pathum Thani Province. The market has major products such as vegetables, fruits, meat, fish, seafood, rice, grains, flowers, processed foods, consumer products, pet supplies and plants. The market has a suitable geographical location and development to facilitate the business of trading and distributing agricultural products as a leading marketplace for agricultural products and service providers in the ASEAN Economic Community (AEC). The agricultural museum in honor of His Majesty the King was established on the occasion of His Majesty the King's 50th Birthday in 1996 by the ministry of agriculture and cooperatives to disseminate the work of the Thai monarchy and agricultural development and gather knowledge, achievements in agricultural technology development in both public and private sectors. The contents within the buildings consist of land development, land reform and promotion of cooperatives, the story of the forest and the management of forest resources, including the conservation of wildlife and national parks, royal initiative of His Majesty the King with agricultural work, projects due to royal initiatives, irrigation activities, insect activity, crop protection and

agricultural promotion evolution, crops, rice, field crops, horticulture and agro-industry, Huai Hong Khrai development study centre - Phu Phan, Phikunthong-Khao Hin Sorn royal development study centre, Ao Kung Kraben - Huay Sai development study centre, saltwater, freshwater and underwater ecosystems, coastal agriculture a fishing village and stories of livestock and farming communities. Building exterior organized as an outdoor activity including performances, demonstrations, research experiments and recreational activities such as greenhouses demonstration and simulating the living conditions of farmers in all regions of Thailand. In figure 3, a menu of history is displayed, where users can click on how to introduce the web application, scan QR code, show model, and select the video from this menu. Figure 4-6 show a brochure the information of temples, markets, and agricultural museums. The information in the brochure contains history and origin, atmosphere, travel and scan QR code.

Figure 4 The information of Wat Thawi Kara Anan with a scanned QR code

Figure 5 The information of Talaad Thai with a scanned QR code

Figure 6 The information of agricultural museum in honor of His Majesty the King with a scanned QR code

3. Results and Discussion

3.1. Study Results

The developed web application system operates the process with the adaptive waterfall model. According to Chatkaew and their team (2021) suggests the development application starts by researching the data and analyzing the obtained data, and then making a design. Then, the prototype is created and then the prototype is tested and collected data. The application keeps improving until the developed application get a complete piece that meets the target. The application is developed by using the program of visual studio code for web application development, using the program of Sketch Up Pro to create 3D models, using the program of Adobe Photoshop version 23.5.5 to trim the image that will display the model, and using the program of Sony Vegas pro for video editing. Once the system has been developed, the operation of the system will be tested. the system is installed to test the actual use. The installation is divided into two parts: the first part is the software for interacting with real users. The second part is the back end for storing the database. The deployment diagram shows the system architecture in terms of physical architecture, resource utilization structure, hardware and software, as well as showing the relationship of equipment in the system as shown in figure 7 below.

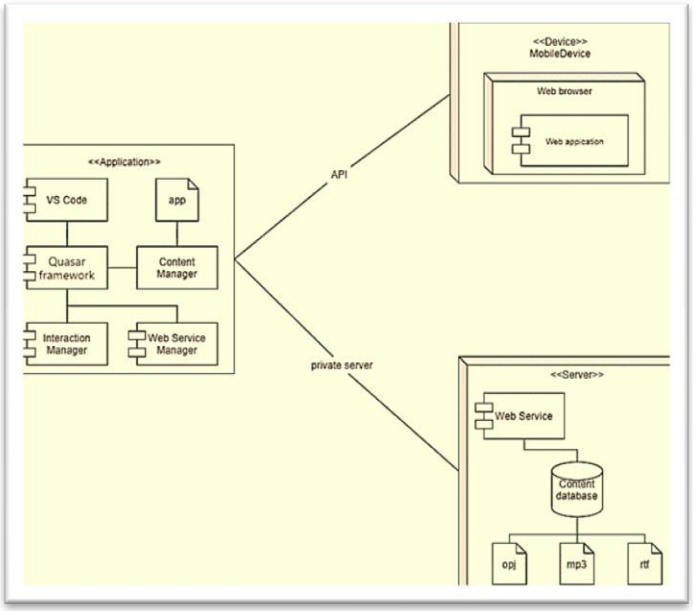

Figure 7 Deployment diagram of the developed application

The diagram shows an application section that contains several objects: programs, application content manager, interaction manager, and web service manager. The device part refers to the mobile phone, consists of a web browser and a web application used to interact with the user through the application program interface. For the server, there is a web service with content database for storing many objects, including RTF, MP3, OPJ.

The results of web application development are consisting of 1) information function, 2) QR code scan, 3) 3D-AR model, 4) view video. They are exported in the following format, shown in figure 8-10;

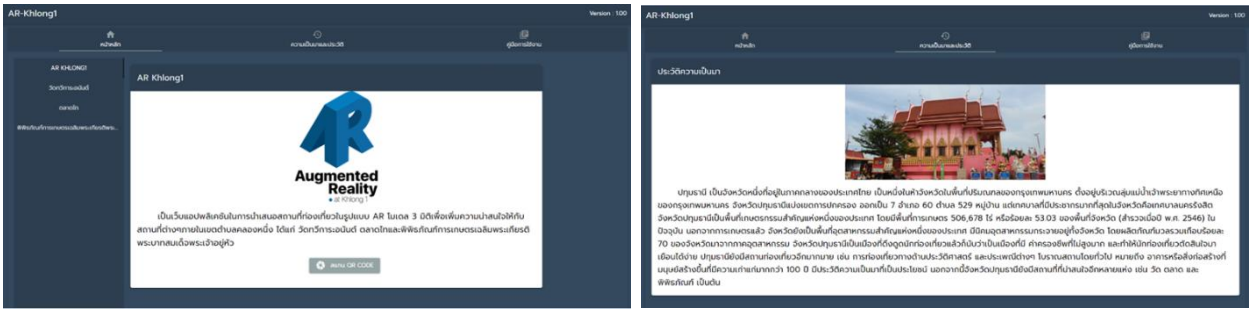

Figure 8 Web application home page (left) and history data of model (right)

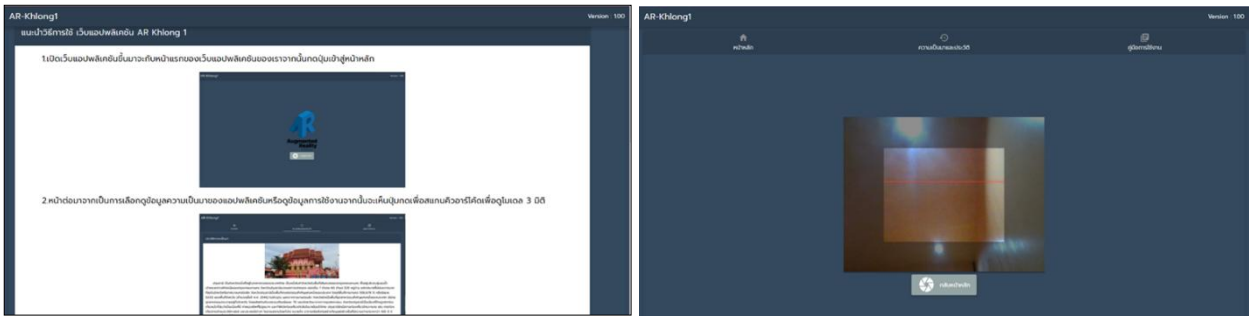

Figure 9 Page scans the QR code used in viewing details of the attractions (left) and the 3D model page (right)

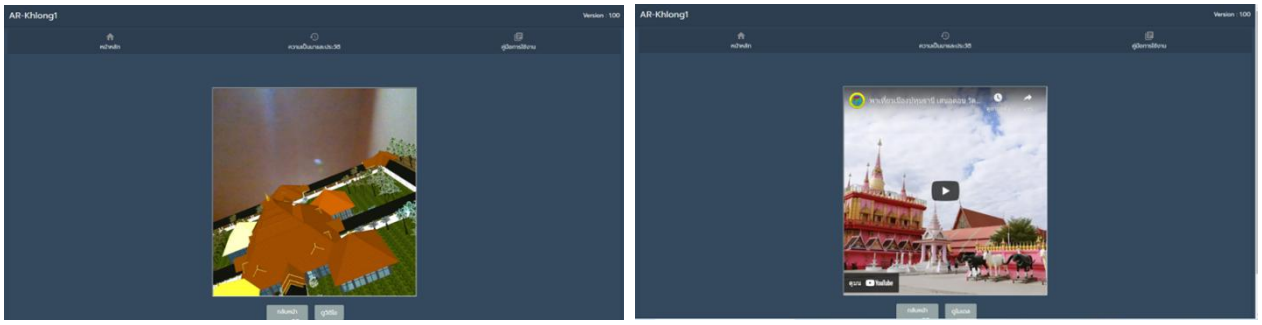

Figure 10 3D model (left) and the video page (right)

3.2. Assessment Results

According to tourism Kumpala and Srisamram (2019) suggests that web application performance testing has two parts: function and web application design. The developed application is assessed by experts and general users. The assessment results are shown in the table below.

Table 1 Display application evaluation results for functionality

No.	Evaluation criteria	N=100		
		Mean	Standard Deviation	Meaning
1	Public Relations Functions	4.00	0.76	Very good
2	QR code scanning function	4.11	0.90	Very good
3	AR model display function	4.11	0.83	Very good
4	Video display page function	4.05	0.80	Very good
Average total score		4.06	0.82	Very good

Table 2 Display application design assessments

No.	Evaluation criteria	N=100		
		Mean	Standard Deviation	Meaning
1	Web application formatting is easy to read and understand.	3.83	0.38	Very good
2	Suitability for choosing the color and font size of the lettering	3.83	0.38	Very good
3	Appropriateness in the use of text and images to describe meaning	3.83	0.38	Very good
4	Uniformity in design	3.72	0.75	Very good
5	Suitability for user interaction	3.77	0.87	Very good
6	Positioning suitability of components	3.94	0.87	Very good
7	The vocabulary used is familiar and easy to understand.	3.88	0.67	Very good
8	Overall image of web application design	3.61	0.91	Very good
Average total score		3.77	0.65	Very good

From allowing ordinary users to evaluate the quality of web applications. It was found that the average web application design was 3.77, the quality was very good. The standard deviation in web application design is 0.65. The average function access is 4.06, the quality is very good, and the standard deviation for function access is 0.82, which is very good quality. The result assess were shown that the data is slightly or similarly different. Therefore, it can be concluded that the web application for presenting data with virtual reality techniques, case studies measure markets and museums are practical

4. Conclusions

The aim of web application development with case studies of temple, market and museum to develop applications for presenting information with virtual reality techniques. To promote cultural tourism by providing information on the history of temples, markets and museums in Klong Nueng area, Khlong Luang District, Pathum Thani Province. The research was conducted as a guidebook in the form of pamphlets with case studies:1) Wat Thawi Kara Anan, 2) Talaad Thai, and 3) The agricultural museum in honour of His Majesty the King. The results showed that tourists could use a web application to present information about the history of the place. Users can scan the QR code via virtual reality technique to view information of tourist attractions in the form of videos describing the history of tourist attractions. Users can view 3D models of tourist attractions. The developed system has two aspects of quality assessment from users: 1) web application design has an average of 3.77, high quality and standard deviation of 0.65, the quality is at a high level. 2) The average access to the function is 4.06, the quality is very high, and the standard deviation is 0.82, which is very high. It shows that there is little or similar difference in the data. Therefore, it concludes that the proposed application for presenting data with virtual reality techniques with case studies of temple, markets and museums which can be applied to the actual work.

5.Acknowledgements

The authors would like to thank everyone who provided helpful comments, suggestions. In particular, the authors would like to thank Faculty of Science and Technology, financial budget RMUTT (Rajamangala University of Technology Thanyaburi) for supporting funding for this research.

6. References

Tourism Authority of Thailand. (2022). The situation of tourism in Thailand 2022. 1 January 2023, Website https://www.tatreviewmagazine.com

Sricharoen, J. (2019). Application to promote tourism 8 must-visit tourist destinations in Phetchabun province with virtual reality technology. Phetchabun Rajabhat University.

Limpinan, P. (2019). Promotion of tourist attractions in Maha Sarakham Province using virtual reality technology. (1). Maha Sarakham Rajabhat University.

Klinchan, C. (2020). Development of information system for presenting mural painting animation. The story of Thotsachart and Phra Sri Ariya in conservation ancient sites in the form of virtual reality technology to inherit local cultural traditions in Khao Samor Khon Subdistrict, Tha Wung District, Lop Buri Province. (2). Maha Sarakham Rajabhat University.

Lawen, S. (2017). Mobile application design based on Bloom's concept. Redesigned. (1). Brupa University.

Boonsomthop, P. (2020). Travel guide design using augmented reality technology to add value and promote historical tourism information in Kanchanaburi as digital tourism. (1). Chiang Rai Rajabhat University.

Kluangkhaew, M. (2017). Design of print media for tourism in Chinatown in the new era. (1). Suan Sunandha Rajabhat University. Jumphot O, 2020, Development of English language media to promote temple tourism in Phitsanulok Province. (1). Mahachulalongkornrajavidyalaya University.

Vongdeuan, P, and Suppak, J. (2018). Advertising media on 3D virtual leaflets via smartphones for display in the exhibition. (1). Mahanakorn University of Technology.

Khumraksanichathorn, S. and Montpanthong, P. (2021). Museum Tourism Behavior of Generation Y Tourists. (5). Loei Rajabhat University.

Information Technology subdivision. (2021). Information on temples and monks across the country. Retrieved 9 January 2022, from National Office of Buddhism: https://www.onab.go.th/th/page/item/

Tangkuptanon, N. and Saowmuang, S. (2020). The influence of digital marketing tools using dual QR code and AR technology in the application that affects customer satisfaction in terms of quality for the Toy Museum in Thailand. (1). King Mongkut's Institute of Technology Ladkrabang.

Chatkaew, M., Butchot, W, Wongtha, P. and Ariya, A. (2021). Develop a Cultural Tourism Promote Website, Case Study if Temples of Muang District, Lamphum Province. Science and Technology Journal of Sisaket Rajabhat University, 1(1), 39-47.

Kumpala, I. and Srisamram, W. (2019). Development of websites in the 360-environment temple tourism in the old city of Nakhon Ratchasima. Journal of Information Science and Technology, 9(1), 71-80.

Jullasikkee, M. (2019). The Approaches to Manage Buddhist Tourism: Temples in the Thonburi Area. Journal of Management Science Review, 21(2), 203-210.

TOUR WAT THAI. (2022). Wat Thawi Kara Anan. Retrieved from 1 January 2023, Website https://tourwatthai.com

TALAADHAI. (2022). Talaad Thai market. Retrieved from 15 January 2023, Website https://www.talaadthai.com

WIKIPEDIA. (2022). The agricultural museum in honor of His Majesty the King. 25 January 2023, Website https://th.wikipedia.org/

Optimization of Fed-Batch Ethanol Fermentation from Pineapple Peel Juice mixed with Cane Sugar

Kitti Orasoon[a], Thapariat Kanhanont[a], Vishnu Punpan[a] and Suthkamol Suthikul[a]
[a]*Expert Centre of Innovative Clean Energy and Environment, Thailand Institution of Scientific and Technology Research, Pathum Thani, 12120 Thailand*
*Corresponding author. Tel. 02-5779510 ; fax: 02-577951; *E-mail address:* kitti_o@tistr.or.th

Abstract
Canned pineapple. factories will have by-products such as pineapple peel. which has sugar content and that suitable for ethanol production raw material. The batch ethanol fermentation from pineapple peel juice was 1 - 8% (v/v) because the sugar content of pineapple peel juice was only 10 - 14 Brix which was not cost-effective for distillation. This research aims to determine the optimum concentration of fed-batch ethanol fermentation from pineapple peel juice mixed with cane sugar at different dissolved solid was 20, 25, 30, 35, and 40 Brix. The results showed that ethanol concentration obtained fed-batch at different dissolved solids 20, 25, 30, 35, and 40 Brix were 10.43 ± 0.36, 11.86 ± 0.08, 13.50±0.05, 13.05±0.41 and 12.11±0.72 %v/v, respectively at 72 h. that higher than batch fermentation of pineapple peel juice found ethanol production only 3.82 ±0.34% at 24 h.

Keywords: pineapple peel juice / fed-batch fermentation / Ethanol Production

1. Introduction
Factory pineapple is an important economic crop of Thailand and Thailand is expected to produce 1.65 million tons of pineapple in 2023. About 72 percent of the output is likely to be processed into various products for exports, while the remaining 28 percent will be consumed domestically. Statistics show that Thailand exported pineapple in the form of products worth 23,869 million baht in 2022. Major importers of Thai canned pineapple include the United States, the Russian Federation, and Germany. Which Thailand is the world's leading exporter. It now holds a 32 percent market share of the global canned pineapple market. (The Government Public Relations Department, 2023) At present, Thailand has 38 large pineapple processing factories, 27 factories were canned pineapple and concentrated pineapple and others were small and medium enterprises. Factories will have by-products such as pineapple peel. which has sugar content and that suitable for ethanol production raw material. (Bio-Innovation Linkage, 2020)

The previous research found ethanol concentration from fermented pineapple peel juice was 1 - 8% (v/v) (J.N. Nigam, 2000; Hajar et al., 2012; Pornpunyapat et al., 2014; Orji et al., 2015) because the sugar content of pineapple peel juice was only 10 - 14 Brix which was not cost-effective for distillation. There have been applied cellulosic ethanol technology that uses enzymes to degradable cellulose molecules before fermentation but fermented concentration broth was not different. (Tropea et al., 2014; Soontornchaiboon et al., 2016; Casabar et al., 2019)

Therefore, fed-batch fermentation was the solution to improve ethanol broth concentration by using cane sugar as fed-batch raw material because of world sugar price was on a long-term downward trend from healthcare megatrend and lawfare in many countries. This research aims to determine the optimum concentration of fed-batch ethanol fermentation from pineapple peel juice mixed with cane sugar.

2. Methodology
2.1. Raw Material
Pineapple peels (Pattawia spp.) were obtained from local market in Pathum Thani, Thailand. The peel was separate residue and juice with hydraulic press machine. The juice was sterilized by using heating at 70 ^{o}C for 3 hr.
Active dry yeast (*Sacchromyces cerevisiae*), Angle alcohol active dry yeast (Hubei, China). Dosing 2 g of yeast was rehydrated in 1.5 L pineapple peel juice to start fermentation.

Cane sugar was Sada® natural cane sugar (Wang Muang, Saraburi). The cane sugar was used to increase the sugar content in pineapple peel juice by diluting it in pineapple peel juice at 70 ^{o}C until the dissolved solid was 20, 25, 30, 35, and 40 Brix for use as a fed-batch substrate.

2.2. Fed-Batch Fermentation
The experiments were carried out in 5 L fermenter, containing sterilized pineapple peel juice 1.5 L added active dry yeast. Fermentation was operated at 32 ^{o}C, 80 rpm agitation speed, without aeration for 12 hr and then added fed-batch substrate 1.5 L at different dissolved solid was 20, 25, 30, 35, and 40 Brix. The samples were periodically withdrawn every 12 h and used for the analysis of reducing sugar, cell number, and ethanol concentration.

2.3 Analytical methods
Reducing Sugar was determined using Dinitrosalicylic acid reagent method (Scherz, H. and Bonn, G.1998). The cell number was determined using a hemacytometer. Ethanol concentration was analysed using gas chromatography, Agilent 6890 series (Agilent GC system, USA) with 19091N-133 Innowax column and flame ionization detector

3. Results and Discussion

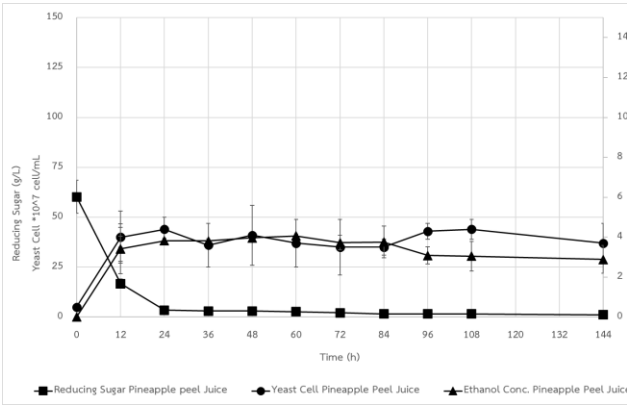

(a) Pineapple Peel Juice Fermentation

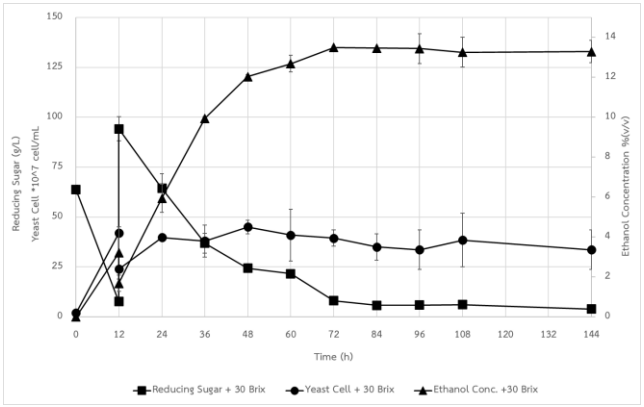

(d) Fed-Batch 30 Brix Fermentation

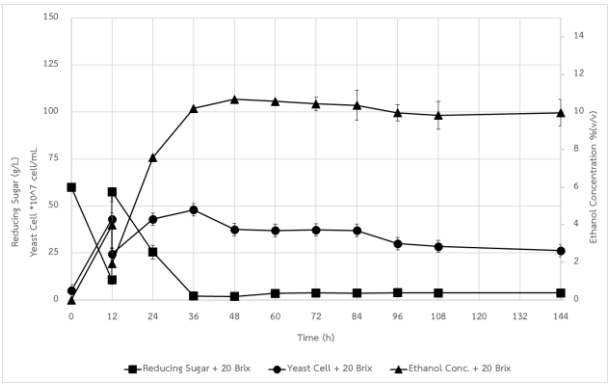

(b) Fed-Batch 20 Brix Fermentation

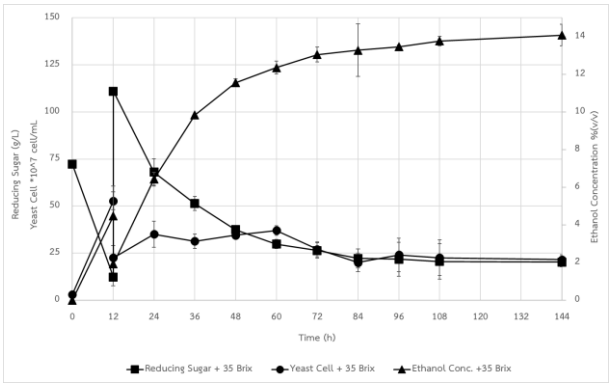

(e) Fed-Batch 35 Brix Fermentation

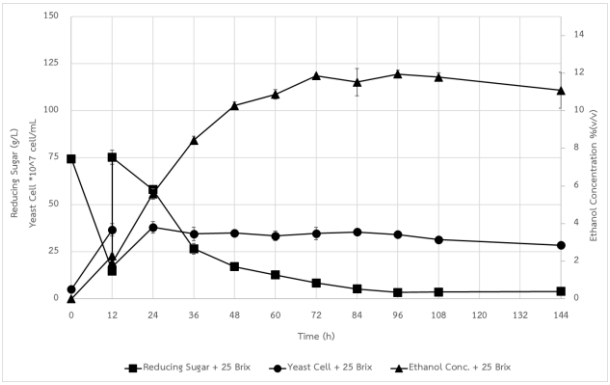

(c) Fed-Batch 25 Brix Fermentation

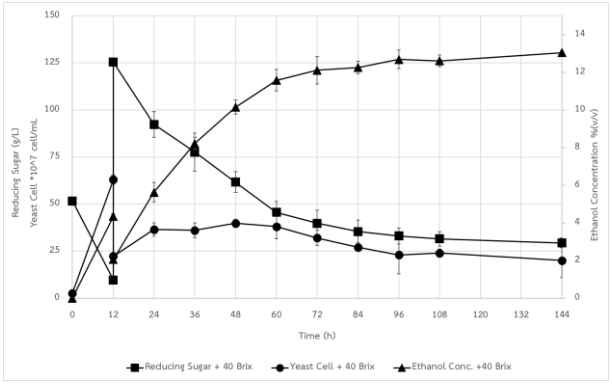

(f) Fed-Batch 40 Brix Fermentation

Figure 1 Time course of Ethanol Production on Different Fed-Batch condition

Table 1 Effect of Fed-Batch Concentration on Ethanol and Reducing Sugar Concentration

Condition	Ethanol Concentration (%v/v) Fermentation Time (h)			Reducing Sugar Concentration (g/L) Fermentation Time (h)		
	24	48	72	24	48	72
Pineapple Peel Juice	3.82 ±0.34	3.97 ± 0.64	3.73 ± 0.68	3.53±0.32	3.04±0.11	2.18±0.17
+ 20 Brix	7.58 ± 0.12	10.68 ± 0.01	10.43 ± 0.36	25.51±3.65	3.93±1.93	3.79±0.13
+ 25 Brix	5.58 ± 0.28	10.27±0.20	11.86 ± 0.08	58.12 ± 1.15	17.13±0.76	8.50±0.56
+ 30 Brix	5.95±0.70	12.03±0.11	13.50±0.05	64.36±7.26	24.43±2.11	8.10±0.41
+ 35 Brix	6.42±0.35	11.55±0.20	13.05±0.41	68.03±3.10	37.43±1.80	26.38±1.55
+ 40 Brix	5.63±0.52	10.15±0.38	12.11±0.72	92.33±6.80	61.63±5.50	39.37±7.00

The results showed initial reducing sugar concentration of pineapple juice was 63.70±7.72 g/L and the initial yeast cell concentration of 2.77±0.28 x 10^7 cells/mL. When passed 12 h yeast cell concentration grew up to 4.62±0.89 x 10^8 cells/mL, reducing sugar remaining 11.99±3.06 g/L and producing ethanol concentration 3.61±0.74%v/v. Immediately, fed-batch at different dissolved solids 20, 25, 30, 35, and 40 Brix found reducing sugar increase to 57.59±2.03, 75.20±3.69, 94.23±6.10, 111.00±6.68 and 125.39±1.96 g/L, respectively. Ethanol production at different dissolved solids were 10.43 ± 0.36, 11.86 ± 0.08, 13.50±0.05, 13.05±0.41 and 12.11±0.72 %v/v, respectively at 72 h. That higher than batch fermentation of pineapple peel juice found ethanol production only 3.82 ±0.34% at 24 h. When focusing on reducing sugar concentration at different dissolved solids were 3.79±0.13, 8.50±0.56, 8.10±0.41, 26.38±1.55 and 39.37±7.00 g/L which observed at 35 and 40 Brix found residue reducing sugar from fermentation because of product inhibition at high ethanol concentration. Thus, the optimum fed-batch fermentation was 30 Brix, which gave a maximum ethanol concentration of 13.50±0.05%v/v at 72 h fermentation time. The fed-batch technology resulted in a higher ethanol production (10-14%, v/v) compared with the 1-5%, v/v from batch fermentation.

4. Conclusions

The optimum fed-batch fermentation was 30 Brix, which gave a maximum ethanol concentration of 13.50±0.05%v/v at 72 h fermentation time and residue reducing sugar was 8.10±0.41 g/L. The fed-batch technology resulted in a higher ethanol production (10-14%, v/v) compared with batch fermentation (1-8%, v/v).

5.Acknowledgements

The authors thank for Thailand Science Research and Innovation (TSRI) for Budget in this research.

6. References

Bio-Innovation Linkage, Office of Industrial Economics, Ministry of Industry, Thailand, Pineapple Value Chain [Online], Available: https://www.oie.go.th/assets/portals/1/fileups/2/files/action%20plan/bio_plan.pdf [27 Aug 2023]

Casabar, J.T., Unpaprom, Y. and Ramaraj, R., 2019, Fermentation of pineapple fruit peel wastes for bioethanol production, Biomass Conversion and Biorefinery, Vol. 9, pp. 761 - 765.

Foreign Office, The Government Public Relations Department, Office of the Prime Minister, Thailand, Thailand Drives to Retain Its Status as the World's Largest Canned Pineapple Exporter [Online], Available: http://thailand.prd.go.th/en/content/category/detail/id/48/iid/174194 [27 Aug 2023]

Hajar, N., Zainal, S., Atikah, O. and Tengku Elida, T. Z. M., 2012, Optimization of Ethanol Fermentation from Pineapple Peel Extract Using Response Surface Methodology (RSM), International Scholarly and Scientific Research & Innovation, Vol. 6 (12), pp. 1102 - 1108.

Nadya Hajar, Zainal, S., Atikah, O. and Tengku Elida, T. Z. M., 2012, Optimization of Ethanol Fermentation from Pineapple Peel Extract Using Response Surface Methodology (RSM), World Academy of Science, Engineering and Technology International Journal of Nutrition and Food Engineering, Vol:6, No:12, pp. 1102 – 1108.

Nigam, J.N., 2000, Continuous ethanol production from pineapple cannery waste using immobilized yeast cells, Journal of Biotechnology, Vol. 80, pp. 189–193.

Orji, J.O., Nworie, O., Ekuma, U.O., Okoli, C.S. and Onwere, C.C., 2015, Production of Ethanol from Pineapple Juice Using Zymomonas mobilis Isolated from Raphia Wine (2015) World Applied Sciences Journal Vol.33 (11), pp. 1773 – 1778.

Pornpunyapat, J., Chotigeat, W. and Chetpattananondh, P., 2014, Bioethanol Production from Pineapple Peel Juice using Saccharomyces Cerevisiae, Advanced Materials Research, Vol. 875-877, p. 242-245.

Scherz, H. and Bonn, G.1998. Analytical chemistry of carbohydrates. Stuttgart: Thieme. Germany.

Soontornchaiboon, W., Chunhachart, O., Pawongrat, R., 2016, Ethanol Production from Pineapple Waste by Co-culture of Saccharomyces cerevisiae TISTR 5339 and Candida shehatae KCCM 11422, KKU Research Journal, Vol. 21, No.2, pp. 347 - 355.

Tropea, A., Wilson, D., La Torre, L.G., Lo Curto, R.B., Saugman, P., Troy-Davies, P., Dugo, G. and Waldron, K.W., 2014, Bioethanol Production from Pineapple Wastes, Journal of Food Research, Vol. 3, No.4, pp. 60 - 70.

Fabrication and Characterization of Hydrogels Containing Xanthone Extract from Mangosteen Peel

Nannapat Trakulsujaritchok[a], Kamonwan Kanphai[b] and Anan Athipornchai[*b]
[a]*Piboonbumpen Demonstration School, Burapha University, Chonburi, 20131, Thailand*
[b]*Department of Chemistry and Center of Excellence for Innovation in Chemistry, Faculty of Science, Burapha University, Chonburi, 20131, Thailand*
*Corresponding author. Tel. 08-1723 4246 ; *E-mail address:* anana@buu.ac.th

Abstract
Polymeric network hydrogels containing xanthone extract from mangosteen peel were fabricated from different blend ratios of poly(vinyl alcohol) (PVOH) and carrageenan (CG) by a solution casting technique. The aqueous PVOH/CG solutions were prepared and mixed with ionic crosslinking agent and xanthone extracted from mangosteen peel. The developed hydrogels were characterized by swelling test, loss of moisture content, compression test, attenuated total reflectance Fourier transform infrared spectroscopy (ATR-FTIR), scanning electron microscopy (SEM) and energy dispersive X-ray spectroscopy (EDX). The PVOH/CG semi-IPNs (semi-interpenetrating polymer networks) hydrogel containing xanthone extract was also examined by cytotoxicity test. It was found that the semi-IPNs hydrogel possessed good dimensional stability and mechanical property, high moisture adsorption capacity, biocompatibility and other characteristics necessary for a biomedical material and applications.

Keywords: Mangosteen Peel, Xanthone, Hydrogel, Carrageenan, Natural extract

1. Introduction
Hydrogels have been widely investigated and employed in pharmaceutical and biomedical applications mainly due to their high water adsorption capacity and biocompatibility. Hydrogels comprise the hydrophilic polymer molecules in network structure. The wide variety of polymeric constituents and synthesis methods enable desirable performances with tunable chemical and physical properties of the hydrogels (Catoira, *et al*., 2019).

Kappa-carrageenan (CG) is a naturally occurring high molecular weight polysaccharide obtained from red seaweed. This biopolymer possesses desirable characters of water solubility, ability to form thermo-reversible gel, non-toxicity and biocompatibility (Mokhtari, *et al*., 2021). However, kappa-carrageenan exhibits dissolution behavior and poor stability in aqueous solution. Crosslinking and blending kappa-carrageenan with other polymers are generally used to enhance its water resistance and mechanical properties (Croitoru, *et al*., 2020; Thomas, *et al*., 2020). Poly(vinyl alcohol), PVOH, is one of the intensively used hydrophilic polymers due to its good chemical stability, processability, and biocompatibility.

Mangosteen, a delicious and healthy fruit, is known as the queen of Thai fruits. Its peel waste has been reported abundant with beneficial xanthone extracts. Mangosteen peel has been used in Thai local wisdom treatment for stomach upset, skin inflammation, and wound healing. Investigations have been performed to utilize mangosteen peel extracts to various medicines and products such as facial masks, hydrogels, and wound dressing pads (Ansori *et al*., 2020; Milan, *et al*., 2022).

In this study, the development of hydrogels containing xanthone extract from mangosteen peel from the blend of poly(vinyl alcohol) and kappa-carrageenan was investigated. The obtained PVOH/CG hydrogels were characterized by Fourier transform infrared (FTIR) spectroscopy and scanning electron microscopy equipped with energy dispersive X-ray spectrometry (SEM-EDX), swelling behavior, moisture holding ability and mechanical strength. Finally, the *in vitro* cytotoxicity of the mangosteen peel extract loaded hydrogels was examined to assess if the materials possessed the potential use for biomedical applications.

2. Methodology
2.1. Chemical and reagents
Kappa-carrageenan and poly(vinyl alcohol) was supplied by Tokyo Chemical Industry. All chemicals and reagents used in this study were analytical grade. Xanthone extract from mangosteen peel waste were prepared in our laboratory (Thai petty patent, application number 2203000643).

2.2. Preparation of the PVOH/CG hydrogels
A blend solution of PVOH and CG was prepared by mixing and dissolving PVOH and CG powders in distilled water with magnetic stirring at 80 ^{o}C for 3 h. After that, a required amount of calcium hydroxide in distilled water or calcium hydroxide solution containing mangosteen peel extract was added into the polymer solution and mixed for uniform dissolution for 30 min. The viscous solution was transferred into silicone molds and allowed to cool down to room temperature. The obtained hydrogels were taken out of the mold and kept in a zipped lock bag. The compositions of hydrogel samples were varied according to the data given in Table 1.

Table 1 Compositions for preparation of PVOH/CG hydrogels

Samples	PVOH (g)	CG (g)	H_2O (mL)	$Ca(OH)_2$* (mL)	M** (g)
75PVOH/25CG	1.1250	0.3750	30	-	-
70PVOH/30CG	1.0500	0.4500	30	-	-
65PVOH/35CG	0.9750	0.5250	30	-	-
65PVOH/35CG-8Ca	0.9750	0.5250	19.5	10.5	-
65PVOH/35CG-8Ca-4M	0.9750	0.5250	19.5	10.5	0.0060
65PVOH/35CG-8Ca-6M	0.9750	0.5250	19.5	10.5	0.0090
65PVOH/35CG-8Ca-8M	0.9750	0.5250	19.5	10.5	0.0120

*$Ca(OH)_2$ 0.23% w/v
**M: Mangosteen peel extract

2.3. Characterization of the PVOH/CG hydrogels

2.3.1 Fourier transform infrared spectroscopy (FTIR)

Dry hydrogels were analysed by FTIR using ATR (attenuated total reflection, PerkinElmer-Frontier) mode. The spectra were obtained in the wavenumber range from 4000 to 400 cm^{-1}.

2.3.2 Morphology observation

The microstructure of hydrogel samples was investigated using scanning electron microscope (SEM, LEO 1450VP) at 250x magnification equipped with an energy dispersive X-ray spectrophotometer (EDX). Prior to characterization, the dried samples were attached on aluminium stubs with adhesive carbon tapes and coated with a thin conductive layer of gold by sputtering.

2.3.3 Swelling ratio

The hydrogels were cut into square-shaped specimens (3 cm × 3 cm), weighed and immersed in 200 mL of distilled water and pH 7.4 buffer solution at room temperature for pre-determined intervals. The hydrogels were taken out from water, wiped off the excess of liquid and weighed by an analytical balance. The %swelling ratio was calculated using the following formula.

$$\% \text{ Swelling ratio} = [(W_t - W_o)/W_o] \times 100 \quad (1)$$

where W_t and W_o represent the weights of the swollen hydrogel and the dry hydrogel, respectively.

2.3.4 Evaluation of compressive strength

Mechanical property of the developed hydrogels was investigated by a compression test. The study was performed on a texture analyzer with a crosshead speed of 1 mm/min and 10 kN load cell. The scaffolds of equal size (10 mm × 40 mm) were compressed to 90 % deformation. The corresponding stress-deformation results were obtained from the test of 5 different specimens at 25 ^oC to ensure reproducibility.

2.3.5 Evaluation of cell viability

The effects mangosteen peel extract and hydrogel composition on cytotoxicity of the fabricated hydrogel were investigated using immortal keratinocyte cell line from adult human skin (HaCat). The hydrogel samples (n = 3) were immersed in a sterile bottle containing Dulbecco's Modified Eagle's Medium and 5% FBS at the concentration of 1 mg scaffold/1 mL medium. After 24 h, the medium was filtrated and used for the test. The cells were cultured, plated into a 24 well plate (1×10^5 cells/mL) and incubated at 37 ^oC for 24 h. The prepared medium (100 µL) was added into the well and kept for 24 h. The cells in culture medium without hydrogel sample were used as a control (Ma *et al*., 2010).

3. Results and Discussion

3.1. Physicochemical characterization of the PVOH/CG hydrogel

The PVOH/CG hydrogels were prepared at three different blend ratios, 65PVOH/35CG, 70PVOH/30CG and 75PVOH/25CG. A digital photograph of the soft and transparent hydrogel placed on a piece of paper with a black letter word can be seen in Figure 1(a). The functionality of hydrogel specimens was confirmed by ATR-FTIR spectroscopy. In the spectra of PVOH/CG hydrogels (Figure 1(b), the broad band around 3294 cm^{-1} and the peak at 2908 cm^{-1} were attributed to the O-H and C-H stretching vibration of both polymers. The characteristic peaks at 1235 and 1066 cm^{-1} were due to the sulfate ester and the 3,6-anhydride-galactose of kappa-carrageenan, respectively (Simona, et. al., 2021).

The potential use of hydrogels significantly depends on their physicochemical properties. In general, the materials should possess an ability to absorb large amount of fluid without losing their dimensional stability. Figure 2(a) demonstrates the mechanical strength of the hydrogels under compression force. The specimens fabricated with the higher content of kappa-carrageenan exhibited an increase in compressive strength and modulus, indicating that they were stronger under applied force. It can be seen that an alteration of the PVOH/CG blend ratio resulted in a tunable strength of the specimens which could be beneficial for different applications. %Swelling ratio of the hydrogels in pH 7.4 buffer solution was evaluated and the results are displayed in Figure 2(b). The PVOH/CG composition comprising hydrogel affected the swelling behavior in which the higher content of poly(vinyl alcohol) brought about and increase in swelling rate and swelling ratio. The hydrogels were also tested for their swelling in distilled water. It was observed that they quickly swelled and absorbed great extent of water, however, the entanglement between linear polymeric molecules was not sufficiently strong to hold the swollen hydrogel matrix together. As a result, disintegration and dissolution of the specimens were observed after 45 min of the test. Considering the finding obtained from the swelling test and the high compressive strength, the optimization on 65PVOH/35CG sample was carried out by ionic-crosslinking of kappa-carrageen using an aqueous solution of calcium ion.

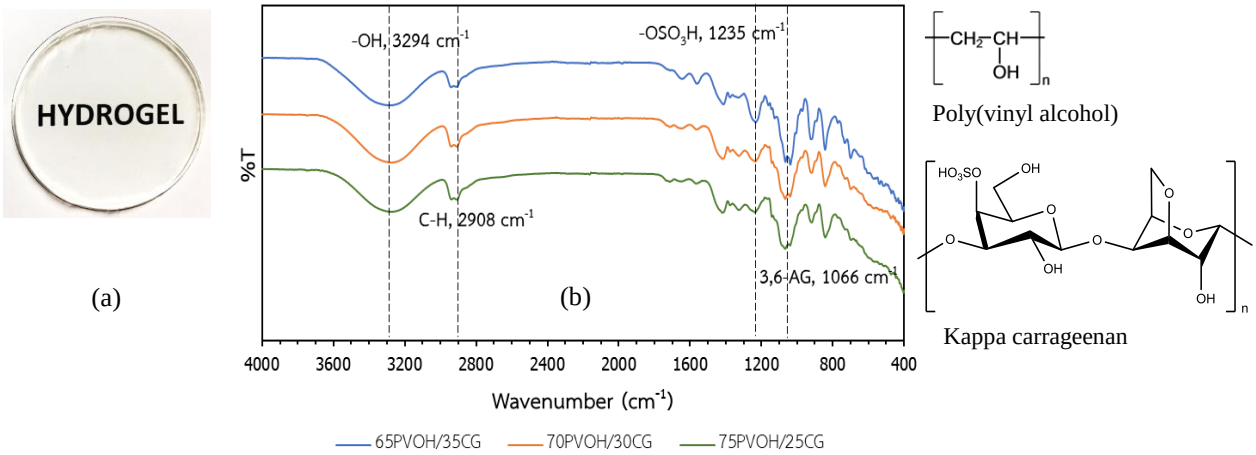

Figure 1 (a) A digital photograph and (b) ATR-FTIR spectra of the PVOH/CG hydrogels.

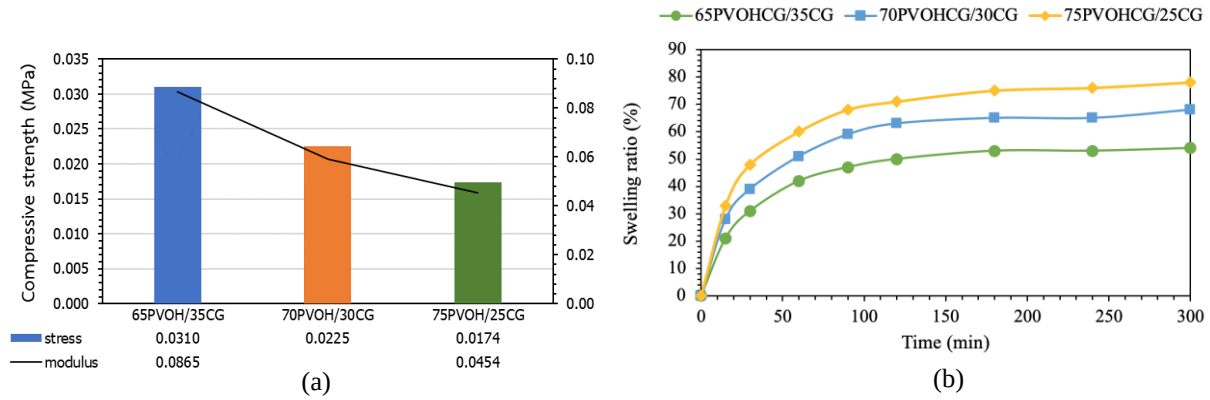

Figure 2 (a) Compressive strength and (b) Swelling behavior of the PVOH/CG hydrogels.

3.2. Physicochemical characterization of the crosslinked PVOH/CG hydrogel

In order to enhance the strength and stability of the PVOH/CG hydrogel, a solution of calcium ion was homogeneously mixed with the polymer solution prior to the forming step by a casting method. Figure 3 demonstrated an ionic crosslinking between the sulfate functional groups of kappa-carrageenan and the divalent calcium ions. The obtained hydrogel was semi-interpenetrating polymer networks of linear poly(vinyl alcohol) entangled with the ionically crosslinked kappa-carrageenan network. The prepared 65PVOH/35CG-8Ca hydrogel was characterized by ATR-FTIR technique. Its spectrum was compared with the non-crosslinked hydrogel and shown in Figure 4 where the lower intensity of the characteristic peaks at 1235 cm^{-1} of carrageenan-sulfate ester and the slight shift at 1066 $cm^{-1}$of the 3,6-anhydride-galactose were observed as a result of crosslinking.

Swelling profiles of the 65PVOH/35CG-Ca crosslinked with different content of calcium ions were studied in pH 7.4 buffer solution and the results are displayed in Figure 5(a). As expected, incorporation higher content of calcium hydroxide led to a denser network structure and a decrease in swelling capacity. The fabricated hydrogels were also tested for their %loss of moisture at room temperature and it was revealed that the difference in crosslinking content had no significant effect on the moisture holding property, Figure 5(b).

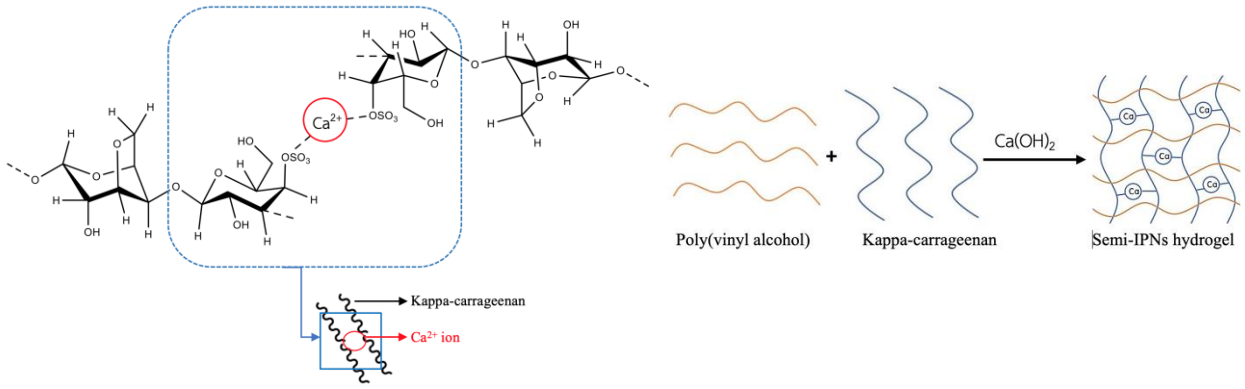

Figure 3 The ionic crosslinking of kappa-carrageenan by calcium ion and the formation of semi-IPNs hydrogel.

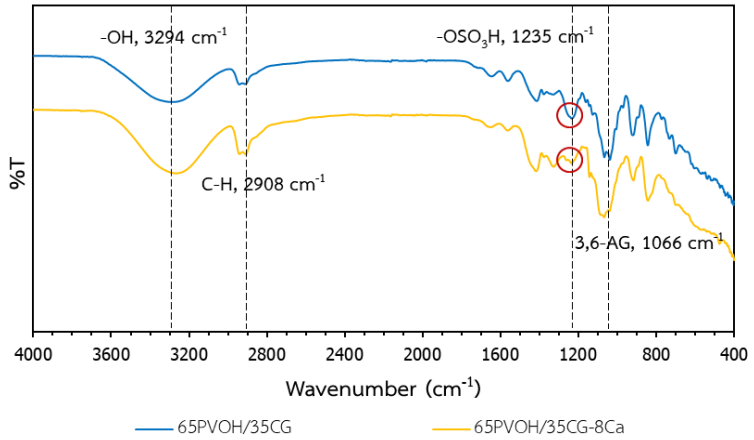

Figure 4 ATR-FTIR spectra of the 65PVOH/35CG and the ionic crosslinked-65PVOH/35CG-8Ca hydrogels.

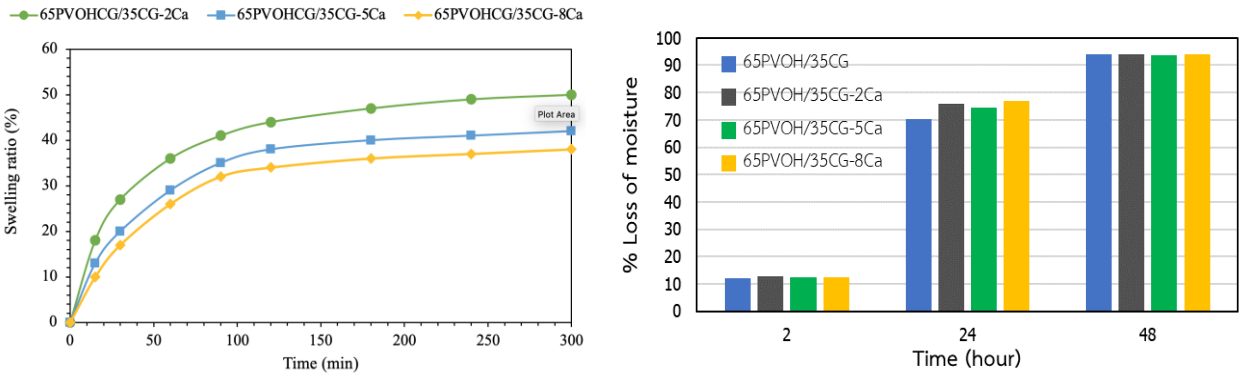

Figure 5 (a) Swelling behavior and (b) Loss of moisture of the crosslinked PVOH/CG hydrogels.

Surface morphology of the 65PVOH/35CG and 65PVOH/35CG-8Ca samples was analysed by SEM at 250 magnification and displayed in Figure 6. Neither phase separation nor heterogeneity was observed in the non-crosslinked and the ionic-crosslinked sample. SEM-EDX technique was used to evaluated to elemental composition (C, O and Ca) of the hydrogel samples. The results confirmed that calcium crosslinked semi-IPNs was successfully prepared, see Figure 7.

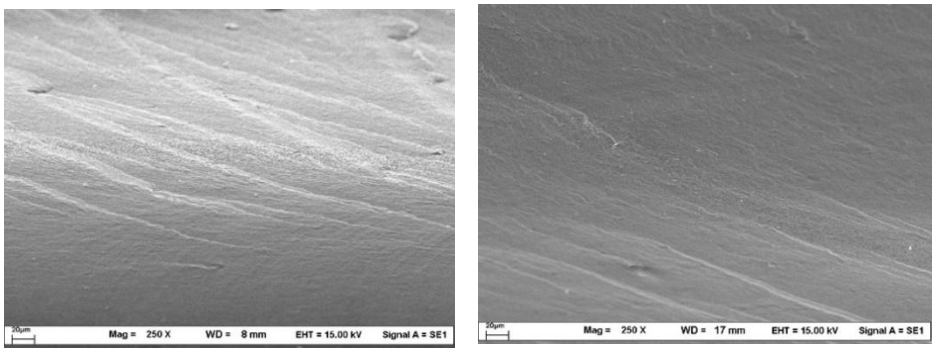

(a) (b)

Figure 6 SEM micrographs of the hydrogels: (a) 65PVOH/35CG and (b) 65PVOH/35CG-8Ca.

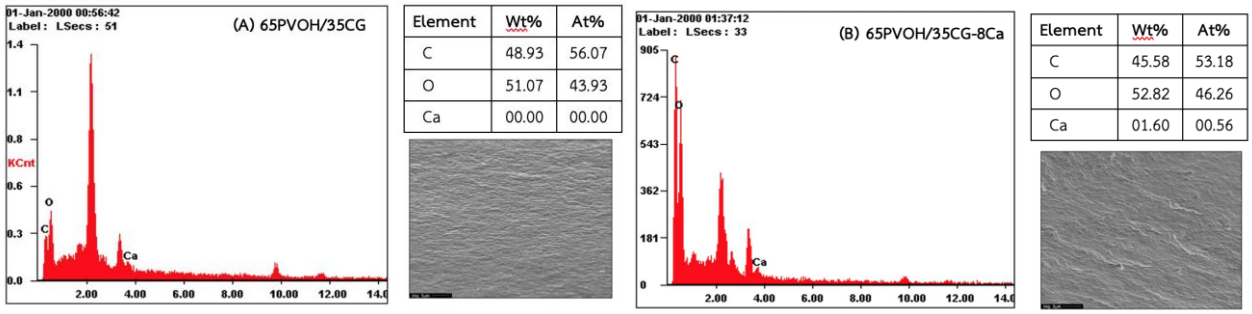

Figure 7 SEM-EDX micrographs and elemental composition of the hydrogels: (a) 65PVOH/35CG and (b) 65PVOH/35CG-8Ca.

3.3. Physicochemical characterization of the mangosteen extract loaded crosslinked PVOH/CG hydrogel

In this study the xanthone extract obtained from mangosteen peel waste was used as a model bioactive agent and loaded into the hydrogel. The extract has been known to contain compounds that act as antioxidants, antibacterial and fight infections (Chiaoprakobkij, *et al*., 2022). The fabricated samples containing different contents of the extract with brown shade color were 65PVOH/35CG-8Ca-4M, 65PVOH/35CG-8Ca-6M and 65PVOH/35CG-8Ca-8M. Their appearance can be seen in Figure 8. The hydrogels were brownish and translucent because of the mangosteen extract component.

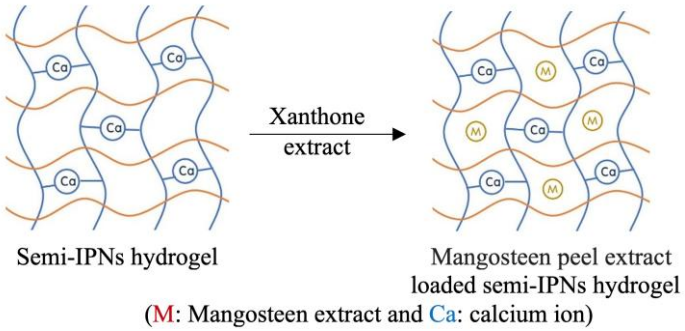

Figure 8 Digital photographs of the hydrogels containing mangosteen peel extract: (a) 65PVOH/35CG-8Ca-4M, (b) 65PVOH/35CG-8Ca-6Ca and (c) 65PVOH/35CG-8Ca-8M.

The effects of mangosteen peel extract on the loss of moisture and compressive strength of the hydrogels were investigated. Figure 9(a) shows that the hydrogels can hold moisture in their matrix up to 48 h which is useful for the applications of facial mask, wound dressing material and other biomedical devices. Addition of the extract did not significantly affect the moisture holding ability. Investigation on compressive strength of the specimens revealed that the incorporation of mangosteen extract slightly decreased the strength of the specimen but had no effect on the modulus, see Figure 9.

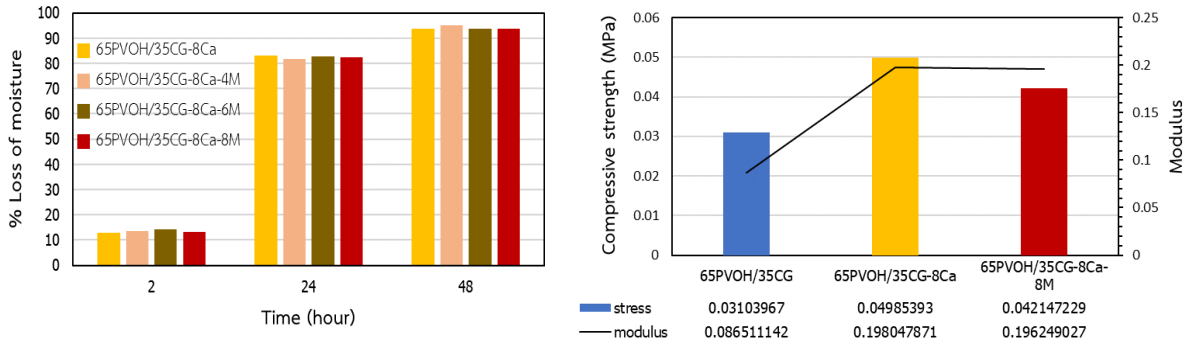

(a) (b)

Figure 9 (a) Swelling behavior and (b) %Loss of moisture of the crosslinked PVOH/CG and the hydrogels loaded with mangosteen peel extract.

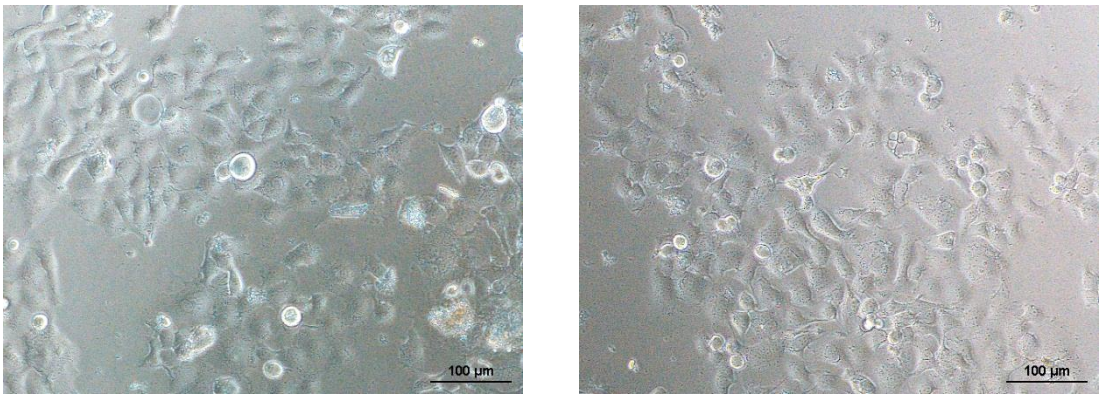

(a) (b)

Figure 10 Morphology of the cells after cell culture using (a) Control and (b) 65PVOH/35CG-8Ca-8M hydrogels.

In vitro cytotoxicity tests using cell cultures have been widely used as a preliminary step for biosafety investigation (Rodríguez, *et al*., 2020). In this study, the immortal keratinocyte cell line from adult human skin (HaCat) was used to examine the cytotoxicity of 65PVOH/35CG-8Ca-8M and compared with the control system without hydrogel sample. The results in Figure 10 indicate cell viability after culturing for 24 h. Comparing to the control, the presence of hydrogel loaded with mangosteen extract did not affect the morphology and cell growth.

4. Conclusions

In this work, a series of poly(vinyl alcohol)/kappa-carrageenan hydrogels (PVOH/CG) was prepared by an aqueous solution casting method. Regarding the results from physicochemical tests, the 65PVOH/35CG hydrogel was selected for optimization *via* ionic crosslinking of the kappa-carrageenan component using calcium ions. After crosslinking, the semi-interpenetrating polymer network hydrogels were obtained comprising the linear poly(vinyl alcohol) chains entangled with the ionically crosslinked kappa-carrageenan networks. Surface morphology analysed by SEM micrograph revealed good compatibility of the homopolymers with no evidence of phase separation. Potential use of the crosslink 65PVOH/35CG-Ca hydrogel was evaluated in terms of moisture holding ability and mechanical strength. Mangosteen peel extract, a natural compound with several bioactivity, was loaded at different contents into the crosslinked hydrogel. The cytotoxicity test showed that the 65PVOH/35CG-Ca-M, the hydrogel loaded with mangosteen peel extract, had no apparent cytotoxicity. The tunable physicochemical properties of the hydrogel could be achieved by alteration of their homopolymer composition, crosslink density and incorporation of the bioactive compound. The developed semi-interpenetrating polymer network hydrogels possess strong potential for the application of biomedical devices.

5.Acknowledgements

The authors acknowledge the technical support provided by Department of Chemistry, Faculty of Science, Burapha University, Thailand.

6. References

Ansori, A. N. M., Fadholly, A., Hayaza, S., Susilo, R. J. K., Inayatillah, B., Winarni, D., & Husen, S. A. (2020). A review on medicinal properties of mangosteen (Garcinia mangostana L.). Research Journal of Pharmacy and Technology, Vol.13(2), p. 974-982.

Catoira, M. C., Fusaro, L., Di Francesco, D., Ramella, M., & Boccafoschi, F. (2019). Overview of natural hydrogels for regenerative medicine applications. Journal of Materials Science: Materials in Medicine, Vol.30, p. 1-10.

Chiaoprakobkij, N., Seetabhawang, S., Okhawilai, M., Uyama, H., & Phisalaphong, M. (2022). Multifunctional bacterial cellulose-gelatin containing mangosteen extract films with improved antibacterial and anticancer properties. Cellulose, Vol.29(12), p. 6811-6830.

Croitoru, C., Roata, I. C., Pascu, A., & Stanciu, E. M. (2020). Diffusion and controlled release in physically crosslinked poly (vinyl alcohol)/iota-carrageenan hydrogel blends. Polymers, Vol.12(7), p. 1544.

Ma, L., Liu, M., Liu, H., Chen, J., & Cui, D. (2010). In vitro cytotoxicity and drug release properties of pH-and temperature-sensitive core–shell hydrogel microspheres. International journal of pharmaceutics, Vol.385(1-2), p. 86-91.

Milan, E. P., Martins, V. C., Horn, M. M., & Plepis, A. M. (2022). Influence of blend ratio and mangosteen extract in chitosan/collagen gels and scaffolds: Rheological and release studies. Carbohydrate Polymers, Vol.292, p. 119647.

Mokhtari, H., Tavakoli, S., Safarpour, F., Kharaziha, M., Bakhsheshi-Rad, H. R., Ramakrishna, S., & Berto, F. (2021). Recent advances in chemically-modified and hybrid carrageenan-based platforms for drug delivery, wound healing, and tissue engineering. Polymers, Vol.13(11), p. 1744.

Rodríguez- Rodríguez, R., Velasquillo- Martínez, C., Knauth, P., López, Z., Moreno- Valtierra, M., Bravo- Madrigal, J., ... & García- Carvajal, Z. Y. (2020). Sterilized chitosan- based composite hydrogels: Physicochemical characterization and in vitro cytotoxicity. Journal of Biomedical Materials Research Part A, 108(1), 81-93.

Simona, J., Dani, D., Petr, S., Marcela, N., Jakub, T., & Bohuslava, T. (2021). Edible films from carrageenan/orange essential oil/trehalose-structure, optical properties, and antimicrobial activity. Polymers, Vol.13(3), p. 332.

Thomas, N., Rusdin, A., Tulsyahra, M., Wathoni, N., & Kuswandi, A. (2020). Accelerated wound healing ability of Jatropha sap by iota carrageenan-poly (vinyl alcohol) hydrogel film. Journal of Advanced Pharmaceutical Technology & Research, Vol.11(4), p. 226.

Super Hydrophobic Peptides for Drug Development : Synthesis and Purification

Nattamon Trirattanaporn[a] and Panumart Thongyoo[a,*]

[a]*Medicinal Chemistry Research Unit, Department of Chemistry, Faculty of Science and Technology, Thammasat University, Pathumthani, 12120, Thailand*

*Corresponding author. Tel. 0870711240; *E-mail address:* tpanumas@tu.ac.th

Abstract

The syntheses and purification of highly hydrophobic peptides can possibly be of great difficulty, especially when these peptides exhibit poor solubility in all solvents (both aqueous and organic solvents). In this research, we presented the syntheses and purification of a mutant mortiamide derived from mortiamide A, comprising of seven hydrophobic residues. Unfortunately, the HPLC purification of super hydrophobic peptides could be a problem, particularly its exceptionally poor solubility properties. To address this challenge, a modified extraction has been utilized for the purification process. This effectively eliminated the need for HPLC purification, resulting in yields of 59% and 70% for linear and cyclic mutant mortiamide, respectively.

Keywords: Cyclic peptide, Hydrophobic, Malaria, Solid phase peptide synthesis (SPPS)

1. Introduction

Synthetic peptides play an important role in drug development, biomaterials, and diagnostics mainly due to its efficacy and high biocompatibility. To date, there is of great interest for peptides in pharmaceutical research and development (R&D)[1]. Mortiamide is an example peptide with promising biological activities, showing the great potential in drug development, and its structure is shown in **Figure 1**.

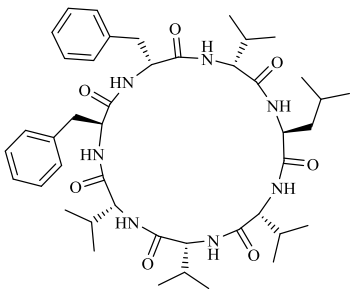

Figure1. The structure of mortiamide A

In 2017, Alyssa L. Grunwald and team discovered the cyclic heptapeptides named mortiamide A-D which were isolated from *Mortierella sp*. found in marine sediment. The structure of mortiamide is a cyclic peptide containing seven hydrophobic amino acids, five of which are D-configuration. Mortiamide A-D did not exhibit any significant activity against methicillin-resistance *Staphylococcus aureus*, vancomycin-resistance *Enterococcus faecium*, *Staphylococcus warneri*, *Pseudomonas aeruginosa* and *Candida albicans* or cytotoxicity against keratinocyte fibroblast, HTB-26 and MCF-7 breast cancer cell line.[2]

In 2019, Christopher Berube and his research group reported the syntheses of mortiamide A-D which were a cyclic heptapeptide. The synthesis was mainly carried out by using solid support and cyclization was performed without an oligomerization side reaction. Additionally, it exhibited an inhibitory effect against *Plasmodium falciparum* proliferation strain 3D7 and Dd2. Mortiamide A, B and D showed an IC_{50} value against 3D7 and Dd2 strains of 1.31-7.85 µM and 0.94-5.31 µM respectively.[3]

Solid phase peptide synthesis (SPPS) has made significant progress in terms of speed, enabling the production of peptide precursors with high yield and great purity.[4] Despite the advancement in synthetic protocols, SPPS still encounters the great challenges; namely incomplete reactions during the iterative amino acid assembly and a difficult coupling of high hydrophobicity in particular peptide sequences. The purification remains a significantly crucial step for the syntheses of peptides. Preparative reverse-phase high-performance liquid chromatography (RP-HPLC) is commonly chosen for the peptide purification due to its wide applicability and effective separation capabilities. Nevertheless, RP-HPLC has a number of limitations also when it comes to the purification of super hydrophobic peptides with low solubility in all solvents and a strong tendency to aggregate. These types of peptides can pose challenges during the purification process by using RP-HPLC.[5] Modified extraction strategies are required to address these difficulties to achieve the purification of super hydrophobic peptides.

In this work, we investigated the efficacy of super hydrophobic peptide purification by utilizing an aqueous extraction-based purification technique, which eliminated the requirement for the use of preparative HPLC.

2. Methodology

Chemical and Instrument

L-amino acids were purchased from Chinapeptide (Shanghai, China). Fmoc-L-Phe-OH, DCC, HOBt, and HATU were obtained from AAPPTec LLC (Louisville, KY, USA). 2-CTC resin was purchased from BIOSYNTH (Berkshire, UK). DIPEA and piperidine were purchased from Merck (Billerica, USA). DMAP was obtained from TCI (Tokyo, Japan). Monitoring of reaction progress was determined by analytical HPLC (PU-4180, Jasco UV-4070 UV/Vis detector) using a Finepak SIL C18T-5, 5 µm, C18, 300°A column (4.6 × 250 mm, Jasco) and flow rate of 1 mL/min. The used gradient conditions were solvent A (0.01% formic acid in water) and solvent B (0.01% formic acid in ACN): 10%-100% in 35 min, with UV detection at 220 and 280 nm. Lyophilization was performed with Flex-DryTM-MP. ^{1}H and ^{13}C NMR spectra were recorded in DMSO-d_6 using a Bruker ADVANCE 400 NMR spectrometer with TopSpin 4.0.7 software.

The first amino acid loading on 2-chlorotrityl chloride resin

2-Chlorotrityl chloride resin (2.0 g, 0.84 mmol) was added to 250 ml round bottom flask and then added Fmoc-L-Val-OH (0.8553g, 2.52 mmol), DMF (15 ml), and DIPEA (428.6 µL, 2.52 mmol). This reaction mixture was carried out under nitrogen atmosphere and stirred at ambient temperature for overnight. The reaction was filtered and washed by DMF (3×2 mL), DCM (3×2 mL), and diethyl ether (1×2 mL), respectively. The resin was dried by vacuum desiccator overnight. The first amino acid loading was calculated by using Fmoc test.

Calculated amino acid loading by using Fmoc test

Fmoc-L-Val-2-chlorotrityl chloride resin (2 mg) was added into vial then added 3 mL of 20% piperidine in DMFF. The reaction mixture was allowed to shake at ambient temperature for 30 minutes for the deprotection of a Fmoc group. The reaction mixture was filtered and measured the absorption at 301 nm by UV-vis spectroscopy. Then, % amino acid loading was calculated by using the following equation.

$$\text{mmol amino acid/gram of resin} = (\text{Abs.})/(1.65\times\text{mg})$$

$$\%\ \text{amino acid loading} = [(\text{mmol of amino acid/gram of resin})/(\text{mmol/gram of loading resin})]\times 100$$

Amino acids assembly via solid phase peptide synthesis (SPPS)

The preloaded Fmoc-L-Val-resin (1 eq, 0.3 g, 0.1512 mmol) was allowed to shake at ambient temperature by DMF (3 mL) for 30 minutes and then treated with 20% piperidine in DMF (3 mL) for 30 minutes at ambient temperature to remove Fmoc protecting groups to give a free amino moiety. Then, resin was drained off and washed with DMF (3×3 mL). Fmoc-Leu-OH was activated in an active form by reacting Fmoc-Leu-OH (2 eq, 0.1069 g, 0.3025 mmol) in DMF (1 mL) with the mixing of DCC (2 eq, 0.0767 g, 0.37 mmol) in DMF (0.5 mL), DMAP (2 eq, 0.0450 g, 0.37 mmol) in DMF (0.5 mL) and HOBt (2 eq, 0.0767 g, 0.37 mmol) in DMF (0.5 mL) as coupling reagents. The reaction mixture was allowed to shake for 60 minutes at ambient temperature for coupling an amino group. Then, the reaction mixture was filtered off and washed with DMF (3×3 mL). The synthesis was repeatedly performed by replacing Fmoc-Leu-OH (2 eq, 0.1069 g, 0.3025 mmol) with Fmoc-Phe-OH (2 eq, 0.1172 g, 0.3025 mmol), Fmoc-Phe-OH (2 eq, 0.1172 g, 0.3025 mmol), Fmoc-Val-OH (2 eq, 0.1027 g, 0.3025 mmol), Fmoc-Val-OH (2 eq, 0.1027 g, 0.3025 mmol) and Fmoc-Val-OH (2 eq, 0.1027 g, 0.3025 mmol), respectively as shown in **Figure 2**. After the synthesis was completed, the resin was drained off and washed with DMF (3×3 mL), DCM (3×3 mL) and diethyl ether (3×3 mL), respectively. Then the resin was dried *in vacuo* for 24 hours.

The synthesis of H_2N-L-Val-L-Val-L-Val-L- Phe-L-Phe-L-Leu-L-Val-COOH

The linear peptide anchored on 2-chlorotrityl chloride was further cleaved with 1% TFA in DCM (5 mL) and allowed to shake for 5 minutes, affording a linear mutant mortiamide, which was used without further purification of HPLC chromatography. ^{1}H-NMR (400 MHz, DMSO-d_6): δ (ppm) 8.58 (s, 1H), 8.38 (d, 1H, *J* = 6.2 Hz), 8.23-8.15 (m, 2H), 7.97 (d, 2H, *J* = 9.7 Hz), 7.83 (d, 1H, *J* = 9.1 Hz), 7.52 (d, 1H, *J* = 5.5 Hz), 7.31-7.23 (m, 4H), 7.24-7.19 (m, 2H), 7.19-7.14 (m, 4H), 4.61 (dd, 2H, *J* = 16.7, 8.1 Hz), 4.23 (dt, 2H, *J* = 19.5, 8.0 Hz), 4.12 (dd, 1H, *J* = 8.9, 4.2 Hz), 3.98-3.86 (m , 2H), 3.56-3.48 (m, 1H), 2.84-2.62 (m, 4H), 2.41-2.31 (m, 2H), 1.87 (qd, 2H, *J* = 13.6, 6.5 Hz), 1.65 (dq, 1H, *J* = 13.4, 6.6 Hz), 1.37-1.18 (m, 1H), 0.96 (d, 6H, *J* = 16.5 Hz), 0.92 (t, 6H, *J* = 6.2 Hz), 0.89-0.83 (m, 6H), 0.80 (d, 3H, *J* = 4.1 Hz), 0.74 (d, 3H, *J* = 6.1 Hz), 0.69 (d, 3H, *J* = 6.1 Hz), 0.55 (d, 3H, *J* = 6.7 Hz). ^{13}C-NMR (100 MHz, DMSO-d_6): δ (ppm) 172.89, 172.73, 172.66, 171.38, 171.08, 170.51, 168.83, 139.46, 137.66, 129.34, 129.31, 128.71, 128.57, 126.90, 126.56, 61.07, 60.82, 59.00, 58.42, 57.07, 56.24, 52.09, 38.22, 29.24, 28.99, 28.84, 28.59, 24.45, 23.72, 22.32, 19.83, 19.79, 19.73, 19.65, 19.37, 19.23, 18.85, 18.84. HR-TOF-MS (ESI) m/z found 908 $[M+2MeOH+Na]^+$; Calculated 821.51 $[M]^+$. HPLC t_r = 20.137/45.00 min.

The synthesis of cyclo- (L-Val-L-Val-L-Val-L- Phe-L-Phe-L-Leu-L-Val)

The linear hybrid peptide (0.02 g, 0.0243 mmol) was dissolved in DMF (20 mL) and subsequently cyclized using DIPEA (2.0 eq, 8.28 µL, 0.0487 mmol) and HATU (2.0 eq, 0.0185 g, 0.0487 mmol) as a coupling agent under dilution condition (1.0 mg/mL). The reaction mixture was allowed to stir at ambient temperature for two days. ^{1}H-NMR (400 MHz, DMSO-d_6): δ (ppm) 8.39 (d, 2H, *J* = 8.5 Hz), 8.31 (d, 1H, *J* = 4.5 Hz), 8.22 (d, 1H, *J* = 8.3 Hz), 7.83 (d, 1H, *J* = 9.2 Hz), 7.77 (d, 1H, *J* = 10.4 Hz), 7.58 (d, 1H, *J* = 4.5 Hz), 7.34-7.27 (m, 4H), 7.24 (dd, 2H, *J* = 13.7, 6.3 Hz), 7.21-7.14 (m, 4H), 7.14-7.07 (m, 2H), 4.30-4.21 (m, 1H), 4.11-4.01 (m, 3H), 3.97-3.89 (m, 2H), 3.85-3.78 (m, 1H), 2.71-2.63 (m, 2H), 2.44-2.32 (m, 1H), 2.25 (dd, 2H, *J* = 12.9, 5.3 Hz), 2.14 (dt, 1H, *J* = 11.0, 5.9 Hz), 1.80 (dd, 1H, *J* = 15.7, 6.6 Hz), 1.71-1.61 (m, 1H), 1.52-1.40 (m, 1H), 1.31-1.20 (m, 2H), 0.94 (d, 3H, *J* = 6.5 Hz), 0.89 (d, 9H, *J* = 6.5 Hz), 0.87-0.77 (m, 15H), 0.69 (dd, 3H, *J* = 6.5, 12.7 Hz). ^{13}C-NMR (100 MHz, DMSO-d_6): δ (ppm) 172.38, 172.10, 171.36, 170.42, 170.36, 169.58, 136.61, 136.09, 129.27, 128.85, 128.08, 127.97, 126.44, 126.35, 60.74, 60.43, 58.23, 57.64, 56.06, 54.86, 50.73, 36.59, 35.77, 31.42, 28.79, 28.58, 27.72, 24.46, 23.19,

21.97, 20.35, 19.84, 19.38, 19.01, 18.93, 18.69, 18.63, 16.30, 13.84. HRMS (LCMS-IT-TOF) m/z found 804 $[M+H]^+$; Calculated 803.21 $[M]^+$. HPLC t_r = 19.620/45.00 min.

The purification of mutant mortiamide

The synthetic linear and cyclic mutant lugdunin (20 mg) were added dichloromethane (20 mL), n-butanol (5 mL), water (50 mL) and sat. NaCl (5 mL). After phase separation, the aqueous phase was extracted with dichloromethane (2×20 mL). The combined organic extracts were washed with $KHSO_4$ (10% v/v, 4×35 mL), sat. $NaHCO_3$ (3×35 mL), ACN/H_2O (10% V/V, 2×35 mL), and sat. NaCl (3×35 mL). The solvent was removed and lyophilized by using Flexi-Dry™ MP freeze dryer. Linear and cyclic mutant mortiamide were afforded without further purification of HPLC chromatography with yields of 59% and 70%, respectively.

3. Results and Discussion

The synthetic strategy of mutant mortiamide has encountered several challenges, ranging from difficult coupling in particular amino residues to the limited solubility of super hydrophobic peptide property. In this modification, all unusual D-amino acids were replaced by L-amino acid in order to simplify the synthetic strategy, and the purification protocol was carried out by using an aqueous extraction-based purification technique without the need of using HPLC. In this research, the synthetic strategy of mutant mortiamide was classified into three main steps. (1) An amino acid assembly of linear peptide precursors by using solid phase peptide synthesis (SPPS). (2) The peptide cyclization under high dilution condition. (3) The purification of mutant mortiamide by an aqueous extraction-based purification.

The synthesis of H_2N-L-Val-L-Val-L-Val-L- Phe-L-Phe-L-Leu-L-Val-COOH

The linear precursor was assembled by using solid phase peptide synthesis (SPPS) strategy. Fmoc-Val-OH was firstly loaded onto 2-chlorotrityl chloride resin with 78 % loading calculated based on Fmoc test. Then, an amino acid assembly was carried out *via* standard Fmoc strategy. Fmoc-Leu-OH, Fmoc-Phe-OH, Fmoc-Phe-OH, Fmoc-Val-OH, Fmoc-Val-OH and Fmoc-Val-OH were consecutively coupled to the corresponding Fmoc-Val-2-chlorotrityl chloride resin. Finally, the linear precursor could be selectivity cleaved under mild acid condition (1% TFA/CH_2Cl_2) to liberate a free carboxyl linear precursor. The purity of a linear precursor was verified by using HPLC, showing the distinct peak at 20.1 min as depicted in **Figure 3**.

The synthesis of cyclo- (L-Val-L-Val-L-Val-L- Phe-L-Phe-L-Leu-L-Val)

To maximize the cyclization efficacy of linear mortiamide precursor, the increase of cyclization time was further investigated, and it was found that an extended reaction time (approximately 2 days) at room temperature allowed the cyclization of linear mortiamide precursor reaching to completion with the highest yield (53 %). The progress of cyclization was monitored by using analytical HPLC, showing the distinct peak at a retention time at 19.6 min as shown in **Figure 3**.

The purification of mutant mortiamide

Resulting cyclization products of mutant mortiamides were purified through an aqueous extraction-based purification, which could be described in details as follows: (1) an initial extraction: resulting cyclization products were consecutively extracted by using dichloromethane, n-butanol, water, and sat. NaCl, respectively. This step aimed to separate non-reacted HATU, a coupling agent used in the cyclization process. (2) an aqueous phase extraction: The aqueous phase obtained from the initial extraction was further extracted with dichloromethane. This step helped to extract an organic component that suspended in water layer. (3) wash step: an organic extract

obtained from the previous steps is consecutively washed by using different solvents: (3.1) Using $KHSO_4$: it is used as an amine protonating agent, resulting in the formation of an ammonium salt that is well-dissolved in water. This has greatly increased the extraction efficacy. (3.2) Using sat. $NaHCO_3$: It is used to convert a carboxylic acid into its more water-soluble ionic carboxylate form, assisting for the extraction of cyclization precursor. (3.3) using ACN/H_2O: This condition selectively extracted the mutant mortiamide based on its solubility property and also helped to separate a mutant mortiamide from an aqueous phase. (3.4) Using sat. NaCl: this final step is used to remove all residual water from an organic phase. Resulting extracted peptides were obtained as white solids after lyophilization. The overall yield of the linear mutant mortiamide and cyclic mutant mortiamide were moderate with the yield of 75% and 53%, respectively. The purity of the linear mutant mortiamide was further confirmed using analytical RP-HPLC, which clearly showed a retention time of 20.1 min as shown in **Figure 3**. In the comparison, the HPLC chromatogram of linear and cyclic mortiamide showed distinct peaks with different retention time at 20.1 and 19.6 min, respectively. This clearly confirmed the hydrophobic property of cyclic mortiamide A, possessing lower hydrophobicity (lower t_r) relative to that of linear mortiamide A. HPLC chromatogram comparison between the resulting cyclization product and a purified product after an aqueous extraction clearly demonstrated the effectiveness of superhydrophobic purification platform without the need of preparative HPLC as shown in **Figure 3**.

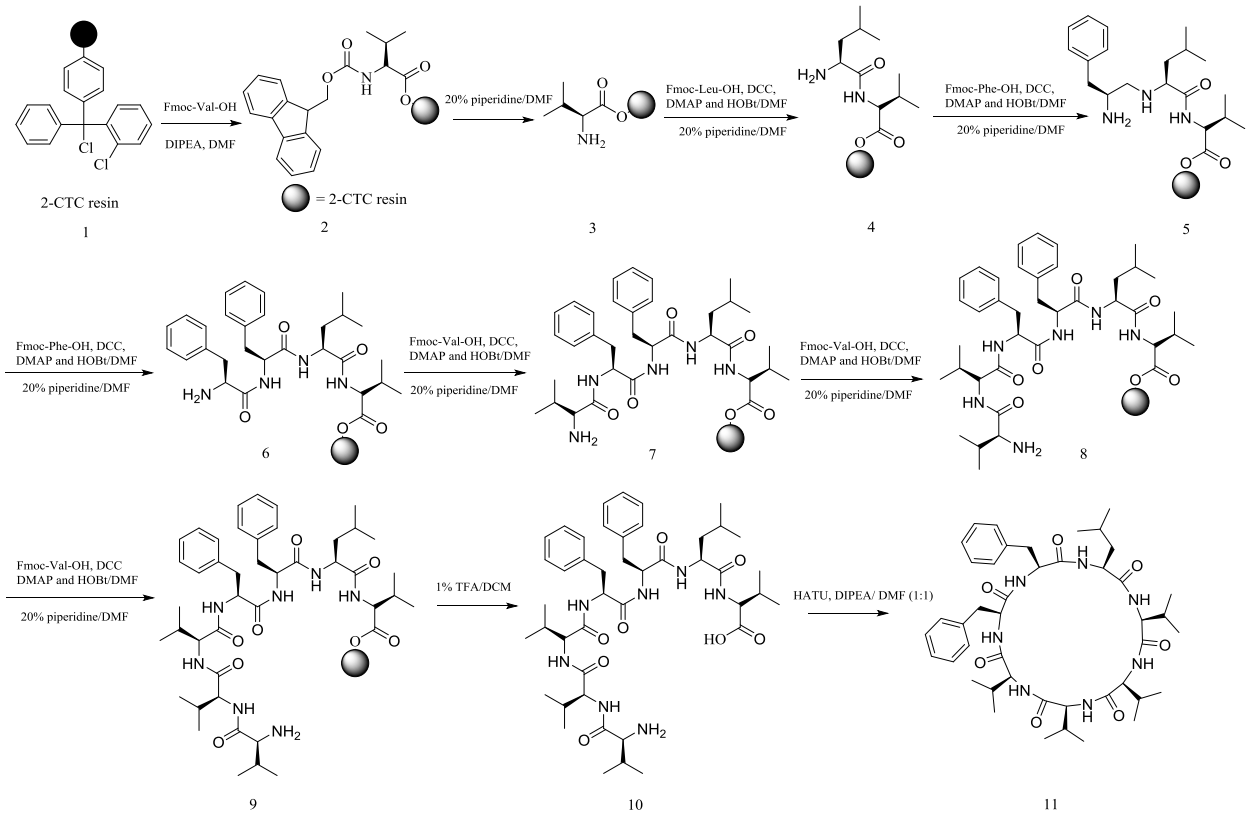

Figure 2. The syntheses of linear (**10**) and cyclic (**11**) mutant mortiamide

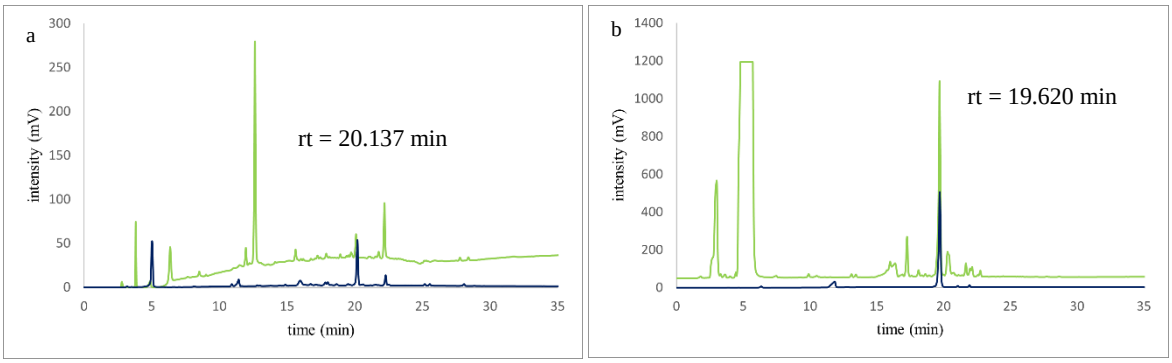

Figure 3. Comparison of HPLC chromatograms between crude product (green) and after purification by using aqueous extraction (blue). Linear mutant lugdunin (a) and cyclic mutant mortiamide (b).

4. Conclusions

The mutant mortiamide was chemically synthesized using solid-phase peptide synthesis (SPPS). The synthetic strategy was successfully classified into three main steps. Firstly, an amino acid assembly of H_2N-L-Val-L-Val-L-Val-L-Phe-L-Phe-L-Leu-L-Val-COOH was performed by using the standard Fmoc strategy. This involved a sequential amino acid coupling on the solid support. Secondly, the cyclization of H_2N-L-Val-L-Val-L-Val-L-Phe-L-Phe-L-Leu-L-Val-COOH was carried out by using HATU as an effective coupling agent. This step facilitated the formation of the desired cyclic mutant mortiamide. Finally, the resulting reaction mixture without purification through aqueous extraction, eliminating the need for preparative HPLC. The purpose of this method is to prevent the precipitation of hydrophobic peptides in the HPLC column, thereby increasing the overall yield. This purification technique involved the separation and isolation of the desired linear and cyclic mutant mortiamides with yields of 59% and 70%, respectively.

5. Acknowledgements

This work has been supported by scholarship for talent student to study graduate program in Faculty of Science and Technology Thammasat University, Contract No. TB 21/2019, and department of chemistry, Faculty of Science and Technology Thammasat University.

6. References

Bérubé, C.; Gagnon, D.; Borgia, A.; Richard, D.; Voyer, N., Total synthesis and antimalarial activity of mortiamides A–D. *Chemical Communications* **2019,** *55* (52), 7434-7437.

Fosgerau, K.; Hoffmann, T., Peptide therapeutics: current status and future directions. *Drug discovery today* **2015,** *20* (1), 122-128.

Grunwald, A. L.; Berrue, F.; Robertson, A. W.; Overy, D. P.; Kerr, R. G., Mortiamides A–D, cyclic heptapeptides from a novel Mortierella sp. obtained from Frobisher Bay. *Journal of natural products* **2017,** *80* (10), 2677-2683.

Kim, S. J.; McAlpine, S. R., Solid phase versus solution phase synthesis of heterocyclic macrocycles. *Molecules* **2013,** *18* (1), 1111-1121.

Reimann, O.; Seitz, O.; Sarma, D.; Zitterbart, R., A traceless catch- and- release method for rapid peptide purification. *Journal of Peptide Science* **2019,** *25* (1), e3136.

Ultrafast Production of Reduced Graphene Oxide *via* Laser-Based Reduction Under Ambient Air Conditions

Komsak Aranmala[a], Natthapong Kamma[a], Supawee Inlumphan[c], Jeffrey Nash[b], Annop Klamchuen[d] and Nonglak Meethong[a,b*]

[a]*Materials Science and Nanotechnology Program, Department of Physics, Faculty of Science, Khon Kaen University, Muang District 40002, Khon Kaen, Thailand*

[b]*Institute of Nanomaterials Research and Innovation for Energy (IN-RIE), Khon Kaen University, Muang District 40002, Khon Kaen, Thailand*

[c]*College of Materials Innovation and Technology (CMIT), King Mongkut's Institute of Technology Ladkrabang (KMITL), Ladkrabang, Bangkok 10520, Thailand*

[d]*National Nanotechnology Center, National Science and Technology Development Agency (NSTDA), Khlong Luang, Pathum Thani 12120, Thailand*

*Corresponding author. Tel.: +66 43 203 166; *E-mail address: nonmee@kku.ac.id*

Abstract

Reduced graphene oxide (RGO) is a promising material with many applications, such as energy storage, drug delivery, environmental treatment, and sensors, owing to its numerous advantages. The techniques used to reduce oxygen functional groups to form RGO are high-temperature processes that are energy-intensive and environmentally unfriendly. In this work, we focused on improving RGO using laser-based methods to convert graphene oxide (GO) into RGO. This inexpensive process was performed efficiently under ambient conditions. RGO was reduced using direct laser writing (DLW) with a CO_2 source, which involved a one-step ultrafast laser treatment with different laser powers, 6, 8, 10, and 12 W. This technique improves the removal of oxygen functional groups on graphene surfaces and decreases sheet resistance from 205 MΩ/sq to 0.22 MΩ/sq without affecting the graphene structure. This method achieves results within seconds and prevents reformation of oxygen chemical functional groups of under ambient air conditions. The results of this study may have significant implications for the development of advanced materials and the design of new laser-based processes for the production of RGO.

Keywords: Reduced graphene oxid, graphene oxide, direct writing laser

1. Introduction

Graphene, a 2D lattice of carbon atoms arranged in a honeycomb structure, was initially regarded as a fundamental constituent of other carbon-based materials, such as fullerenes, carbon nanotubes, and graphite. The scientific community viewed graphene as an "academic material," with no expectation of its stand-alone utility until 2004. At this time, Andre Geim and Konstantin Novoselov at the University of Manchester were able to isolate a single-atom-thick layer of carbon, which sparked a surge in research interest in graphene. This led to the emergence of what is commonly known as the "graphene gold rush," with scientists exploring its unique mechanical, electrical, and thermal properties. [1, 2] The number of publications related to graphene research has been steadily increasing as shown in **Figure. 1**. This suggests a growing interest and focus on this field of study.

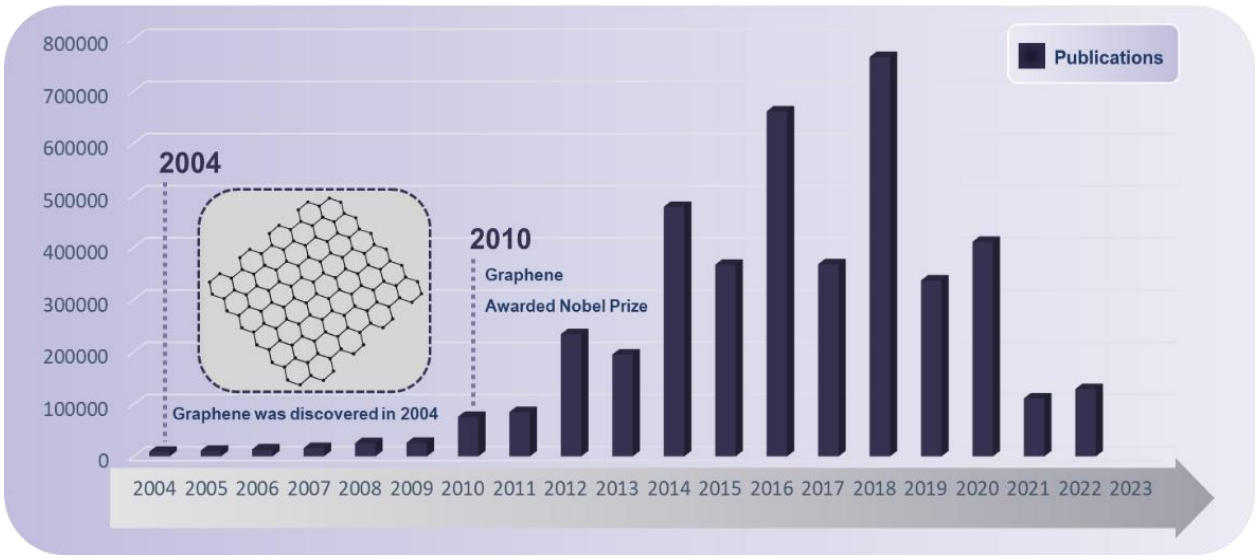

Figure 1. Graphene research and the growing number of publications per year from Google Scholar using "Graphene" as a keyword.

Research into graphene has since expanded. Scientists have discovered various forms of graphene, including reduced graphene oxide (RGO). RGO is produced by reducing graphene oxide, which is graphene that has been treated with various chemicals. RGO retains many of the properties of graphene, such as high hardness, electrical conductivity, and thermal conductivity, making it an attractive material for applications such as batteries, sensors, and composites. It is also relatively easy to produce and can be made in large quantities, leading to its higher commercially viability than pure graphene. [1]

There are various methods available for synthesizing RGO that involve specific size and quality considerations. Some of the commonly used approaches for RGO synthesis include chemical synthesis, thermal reduction, microwave-assisted reduction, photochemical reduction, and the direct laser writing (DLW), as shown in Fig. 2. These methods have been extensively studied and each has advantages and disadvantages. [3–5]

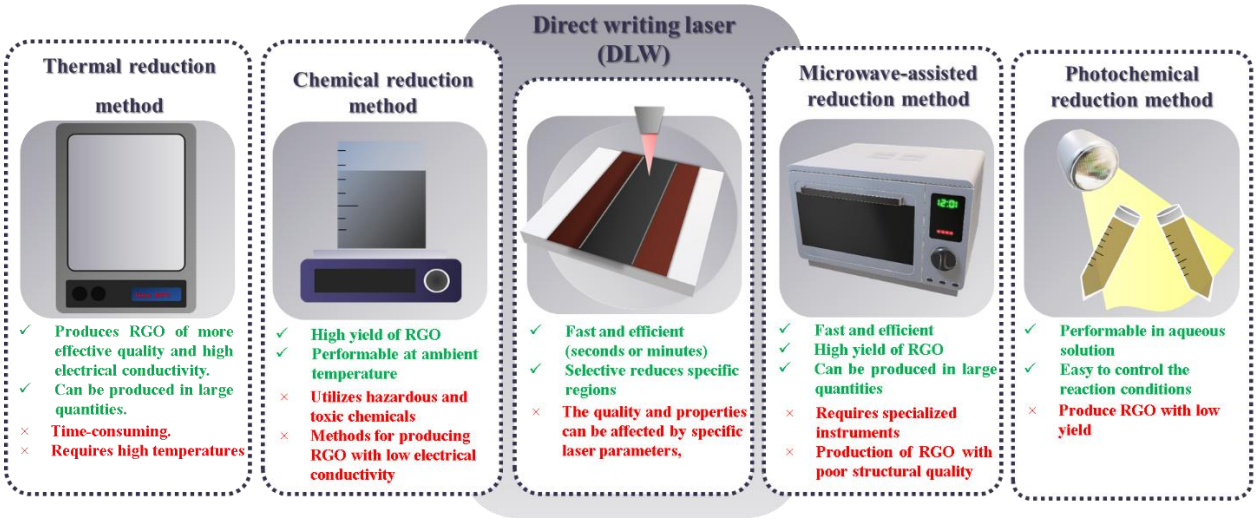

Figure 2 Advantages and disadvantages of the RGO synthesis methods.

The current study focuses on the direct laser writing (DLW) method, a relatively new approach for synthesizing RGO that utilizes laser radiation to induce the reduction of graphene oxide (GO). Other methods control the atmospheric conditions during the reduction of GO, typically under an argon or nitrogen atmosphere, in order to avoid reformation of oxygen functional groups. The DLW method requires only seconds and removes oxygen under ambient air by breaking oxygen bonds and allowing insufficient time for oxygen to reform its chemical functional groups. Laser radiation provides a high degree of control over the reduction process, allowing for precise control over the extent of reduction, the resulting structural features and properties of the RGO. The process typically involves exposing a thin film of GO to laser radiation, which induces localized heating and reduction of the GO. DLW is defined by its ability to produce patterned RGO structures. By selectively irradiating specific regions of a GO sheet with laser radiation, it is possible to induce reduction only in those regions, resulting in the formation of patterned RGO structures. RGO synthesis can be achieved in a matter of seconds or minutes, resulting in high-quality RGO. This method can have various practical applications.

2. Methodology

2.1. Method

To prepare GO using a modified Hummer's method, in step 1: graphite (4 g), $NaNO_3$ (2 g), and H_2SO_4 (100 ml) were combined and stirred at 0 °C for 30 minutes. This results in formation of HNO_3 and O_2, which react with the surfaces of interlayer graphite as a pretreatment for oxidation, as depicted in Fig. 3(b). Steps 2-3: 14 g of $KMnO_4$ were added and the mixture was stirred for 10 minutes at 20 °C. $KMnO_4$ and H_2SO_4 reacted to form Mn_2O_7, which then diffused and intercalated into the graphite layer to break the Van der Waal forces within the intercalation layer. The solution was then stirred for 12 hours at 35 °C or until the color changed from dark green to dark. Afterwards, 150 mL of deionized water was added, and the mixture was agitated for an hour. H_2O_2 was added to stop the oxidation process, and the solution was centrifuged with HCl to remove contaminants. DI was added until the pH was neutral. Finally, the solution was freeze-dried overnight. [6–9]

To obtain GO film, 0.1 g of GO was added to 5 ml of DI and cast on an acrylic sheet, and then dried at room temperature. The reduction of GO powder was done using a laser-based method with a Trotec Speedy 300 CO_2 source. The pulse frequency had a range of 500–1000 Hz, and the speed limit was 22.4 cm s^{-1}. Laser power was controlled at 6, 8, 10, and 12 W, and laser processing was conducted under ambient conditions. The transmittance at 10.6 µm was also determined during the process. [10]

2.2. Characterization

The form of oxygen in the synthesis of GO by a modified Hummer's method and its reduction *via* laser-based methods were characterized using a variety of analytical techniques. These included X-ray diffractometry (XRD Model: EMPYREAN), Fourier transform infrared spectroscopy (FT-IR Model: TENSOR27), scanning electron microscopy (SEM Model: LEO-1450VP), transmission electron microscopy (TEM Model: TECNAI G2 20), and Keithley (Model: 2450 SourceMeter).

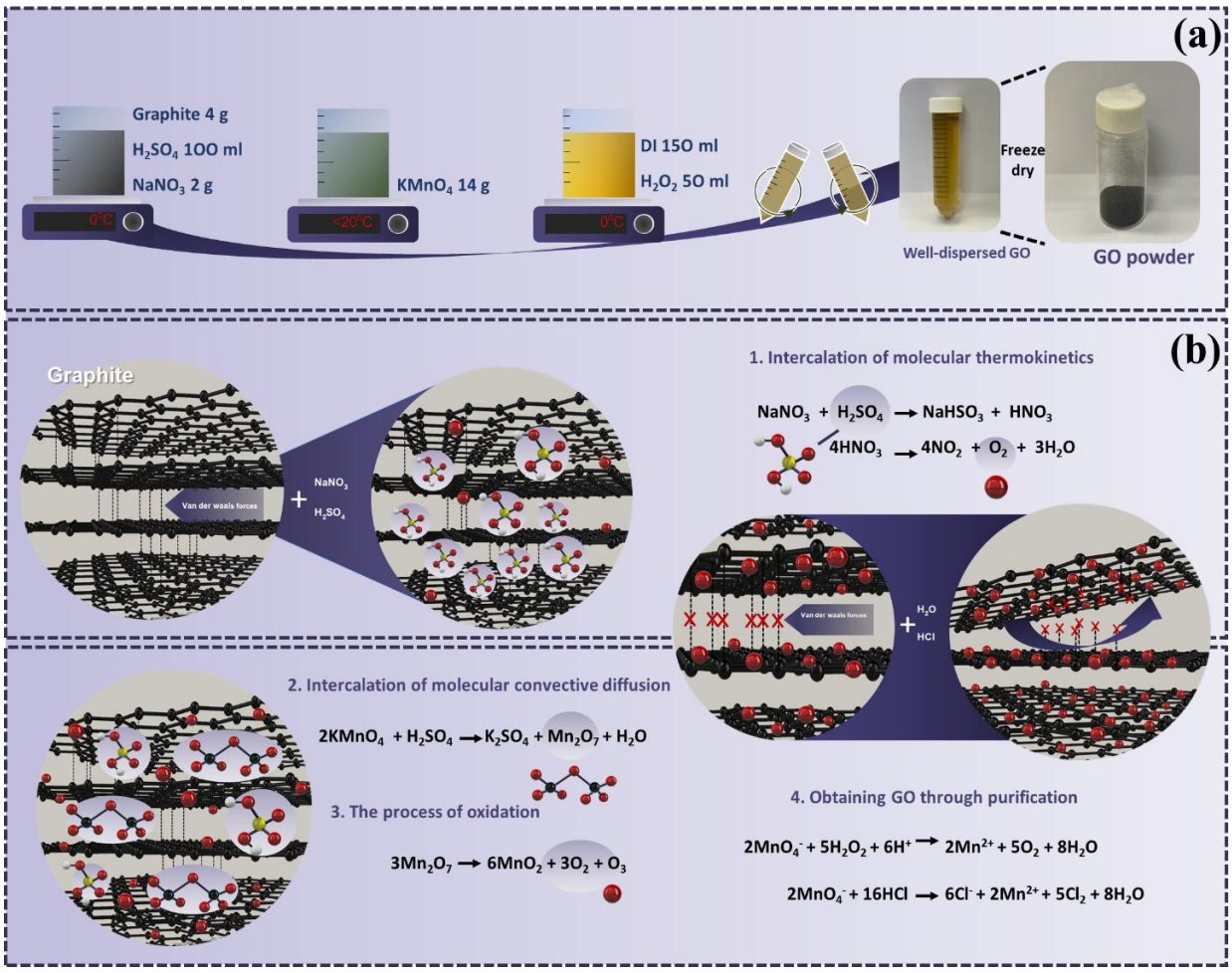

Figure 3 (a) Synthesis of GO using a modified Hummer's method, (b) chemical reactions that occur during the process.

3. Results and Discussion

3.1. GO powder analysis

Figure 4 (a) shows the XRD patterns of graphite and GO. The XRD pattern of graphite exhibits a single, sharp peak at 26.51°, which corresponds to the (002) crystal plane that is typical of the hexagonal, close-packed structure of graphite. The calculated interlayer spacing of graphite is 0.33 nm. GO displays a peak at 9.89°, which corresponds to the (001) crystal plane, and the calculated interlayer spacing is 0.89 nm. These results suggest that graphite was successfully oxidised to GO using the modified Hummer method, as evidenced by the formation of oxygen functional groups within the graphite structure and disruption of the regular hexagonal lattice structure of graphite, leading to a wider interlayer spacing in GO. [11] The FT-IR spectra shown in Fig. 4 (b) provide information about the form of oxygen in GO. Specifically, the spectrum of GO exhibits peaks at wavenumbers of 3224, 1722, 1622, and 1043 cm^{-1}, which correspond to the O–H vibration, C=O carbonyl stretching, stretching of the C=C alkene group, and C–O, respectively. [12]

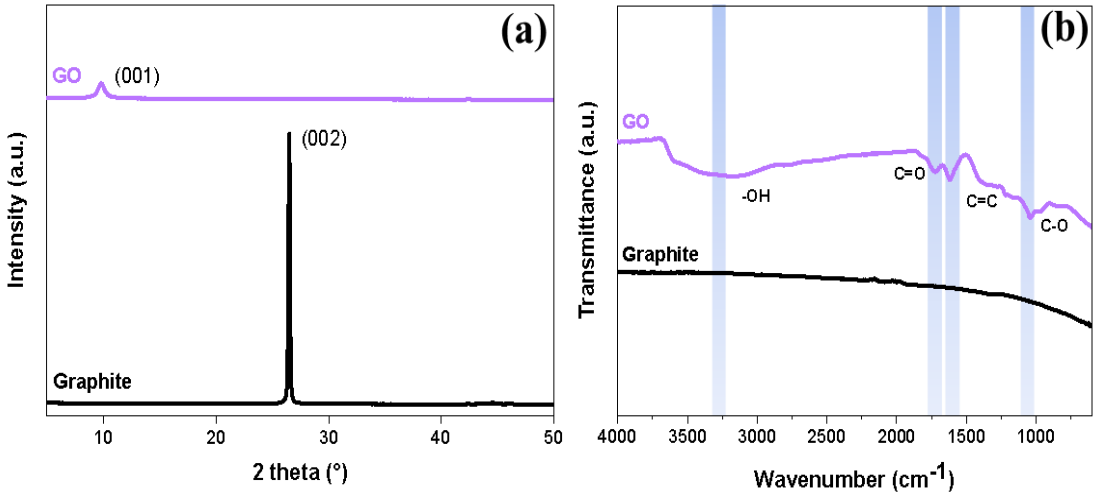

Figure 4 Graphite and GO characterization (a). XRD patterns (b). FT-IR spectrum.

3.2. Morphology of LRGO

The morphology of GO powder was found to have a smooth surface, as observed in Fig. 5 (b). However, after the laser-based reduction of the oxygen functional group, the surface of the laser-reduced graphene oxide (LRGO) became rough. SEM images clearly depict that the surface area of the LRGO increased significantly due to expansion of the graphene layers, as shown in Figs. 5 (c–f). This expansion of graphene layers also resulted in a more porous LRGO structure, which could provide more active sites that are beneficial for its potential use in various applications such as energy storage and catalysis. [13]

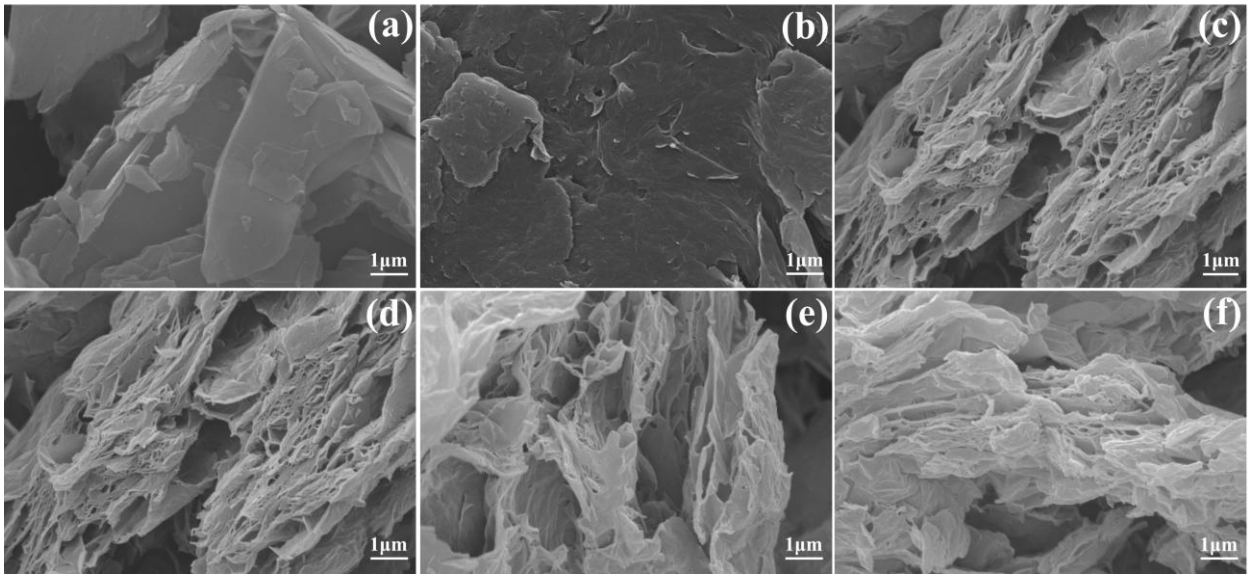

Figure 5 SEM images of (a) graphite powder, (b) GO, and (c-f) LRGO of 6 W, 8 W, 10 W, and 12 W, respectively.

TEM images of GO and LRGO after exposure to various laser powers, 6 W, 8 W, 10 W, and 12 W, are shown in Fig. 6. The diffraction patterns in the images demonstrate the interplanar distances for the (110) and (100) planes that are typical for the graphene lattice. The results show that even with different laser powers, the characteristic interplanar distances of graphene are still active, indicating that the power of the laser had no effect on the structure of graphene. This suggests that the graphene lattice structure remains intact and stable under the experimental conditions, regardless of the laser power applied. [10]

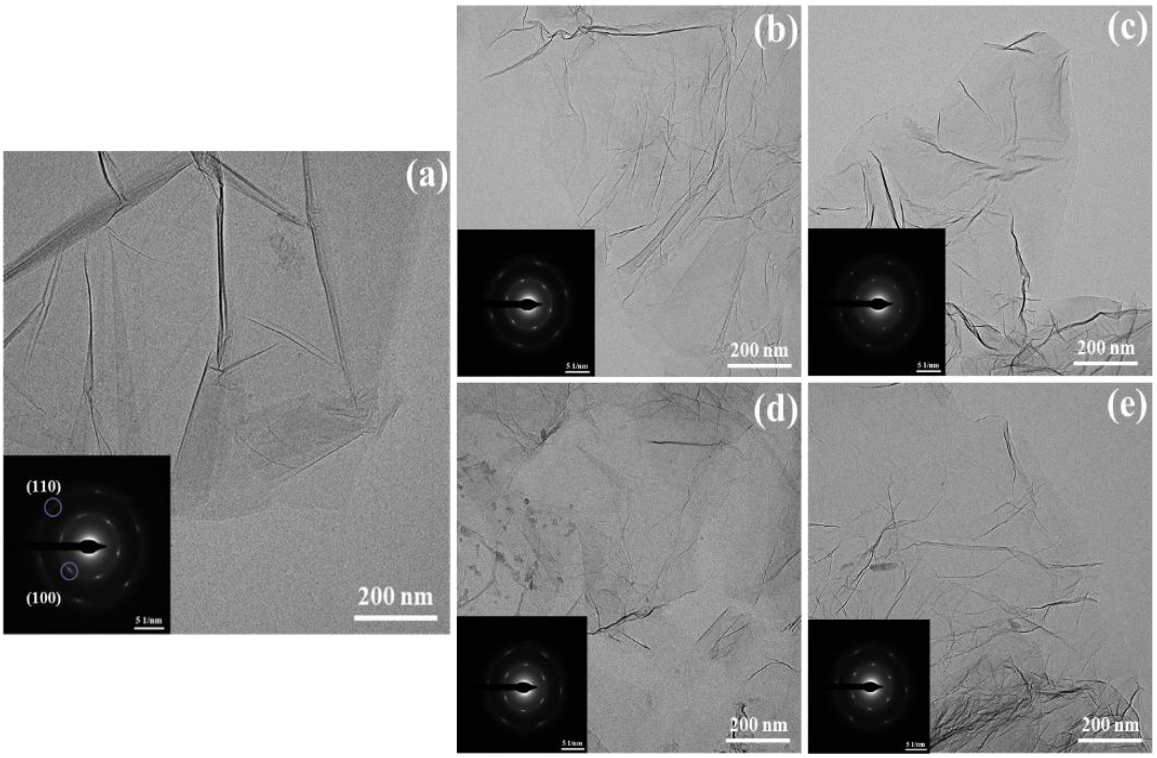

Figure 6 TEM images of (a) GO, (b-e) LRGO, 6 W, 8 W, 10 W, and 12 W, respectively.

3.3. Removal of oxygen using a laser-based method

The FT-IR spectra obtained for GO and LRGO samples treated with different laser powers (6, 8, 10, and 12 W) are shown in Fig. 7. GO contains functional groups such as hydroxyl, carbonyl, alkene, and C-O in its structure, which are evident from the FT-IR spectra. By comparing the spectra of GO and LRGO, it is clear that even at a low laser power of 6 W, the functional groups of hydroxyl, carbonyl, and C-O have been removed from the LRGO sample, as confirmed by the absence of their corresponding peaks in the FT-IR spectrum. This demonstrates that laser-based methods can be used to effectively remove oxygen functional groups from graphene oxide, even at low laser power, resulting in the formation of LRGO.

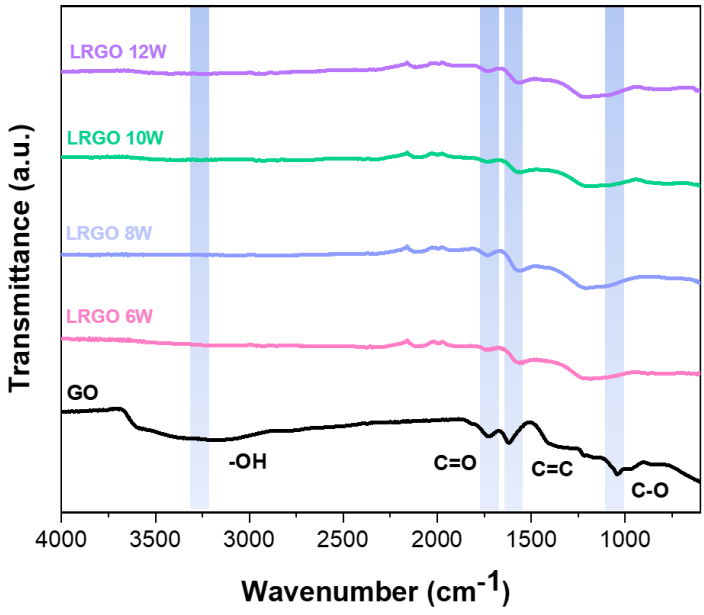

Figure 7 FT-IR spectra of GO and LRGO with different laser powers.

3.4. Sheet resistance of LRGO

The sheet resistance of GO and LRGO samples with different laser powers was measured to determine the removal of oxygen functional groups relative to FT-IR spectra as shown in Fig. 8. The initial resistance of GO powder was found to be 205 MΩ/sq. After laser reduction, the sheet resistance of LRGO decreased significantly to 1.39 MΩ/sq at a laser power of 6 W, a decrease of 67.80%. As the laser power was increased to 8, 10, and 12 W, the sheet resistance continued to decrease, reaching 0.30, 0.22, and 0.22 MΩ/sq, respectively. These results suggest that the removal of oxygen functional groups from the GO structure by laser treatment improves the electrical conductivity of the resulting LRGO. The removal of oxygen defects and disruptions in the lattice results in a more structurally pure and orderly graphene lattice. This allows electrons to move through RGO, which leads to improved electrical conductivity and a decrease in sheet resistance. The decreased sheet resistance observed with increasing laser power can be attributed to removal of oxygen functional groups from the GO structure, resulting in improved electrical conductivity of the LRGO sample. [14]

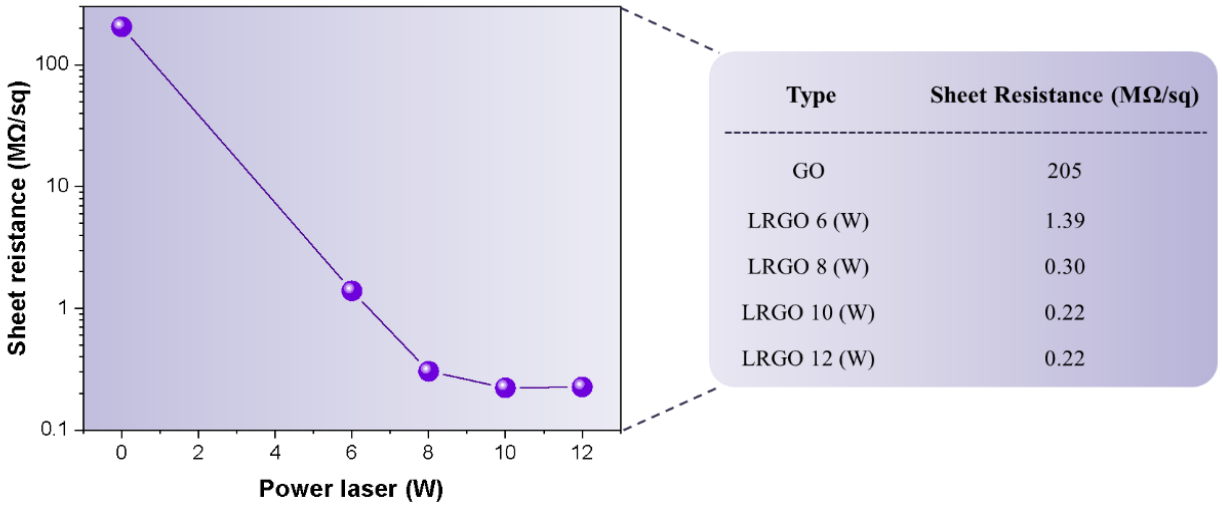

Type	Sheet Resistance (MΩ/sq)
GO	205
LRGO 6 (W)	1.39
LRGO 8 (W)	0.30
LRGO 10 (W)	0.22
LRGO 12 (W)	0.22

Figure 8 Sheet resistance of LRGO with different power lasers.

4. Conclusions

The purpose of this study was to investigate the formation and removal of oxygen functional groups in graphene oxide (GO) using a modified Hummer's method and a laser-based reduction method at various power levels (6, 8, 10, and 12 W). The results revealed that during the synthesis of GO from graphite powder, oxygen functional groups such as hydroxyl, carbonyl, and C-O were formed. Following reduction using the laser-based method, the surfaces of the GO became rough, and there was an expansion of the graphene layers and characteristic interplanar distances for the (110) and (100) planes, typical for the graphene lattice. The FT-IR spectra also showed a clear decrease in the peaks associated with oxygen functional groups at wavenumbers of 3224, 1722, and 1043 cm^{-1}, even at low laser power. Moreover, the sheet resistance of GO decreased significantly from 205 MΩ/sq to 1.39 MΩ/sq at 6 W, and continued to decrease to 0.30, 0.22, and 0.22 MΩ/sq at 8, 10, and 12 W, respectively. Removal of oxygen within seconds under ambient air conditions demonstrates that the structure is unable to form chemical functional groups such as hydroxyl, carbonyl, alkene, and C-O with oxygen in the surrounding air. Instead, it breaks the bonding of oxygen using a fast laser, so that oxygen in ambient air lacks sufficient time to form such chemical functional groups. These results suggest that the laser-based method is an efficient and cost-effective technique for removing oxygen functional groups from GO, resulting in the formation of laser-reduced graphene oxide (LRGO) with improved electrical conductivity

5.Acknowledgements

This work was supported by the Institute of Nanomaterials Research and Innovation for Energy (IN-RIE), Khon Kaen University, Thailand. KA acknowledges the support of the Thailand Graduate Institute of Science and Technology (TGIST) (Grant No. SCA–CO–2565-17194-TH).

6. References

A. Adetayo and D. Runsewe, "Synthesis and Fabrication of Graphene and Graphene Oxide: A Review," *Open J. Compos. Mater.*, vol. 09, no. 02, Art. no. 02, Apr. 2019, doi: 10.4236/ojcm.2019.92012.

A. K. Geim and K. S. Novoselov, "The rise of graphene." arXiv, Feb. 26, 2007. doi: 10.48550/arXiv.cond-mat/0702595.

R. K. Singh, R. Kumar, and D. P. Singh, "Graphene oxide: strategies for synthesis, reduction and frontier applications," *RSC Adv.*, vol. 6, no. 69, pp. 64993–65011, Jul. 2016, doi: 10.1039/C6RA07626B.

Y. Wu, S. Wang, and K. Komvopoulos, "A review of graphene synthesis by indirect and direct deposition methods," *J. Mater. Res.*, vol. 35, pp. 76–89, Jan. 2020, doi: 10.1557/jmr.2019.377.

Y. L. Zhong, Z. Tian, G. Simon, and D. Li, "Scalable production of graphene via wet chemistry: Progress and challenges," *Mater. Today*, vol. 18, Sep. 2014, doi: 10.1016/j.mattod.2014.08.019.

A. Pareek, J. Shanthi Sravan, and S. Venkata Mohan, "Graphene modified electrodes for bioelectricity generation in mediator-less microbial fuel cell," *J. Mater. Sci.*, vol. 54, no. 17, pp. 11604–11617, Sep. 2019, doi: 10.1007/s10853-019-03718-y.

C. Li, X. Chen, L. Shen, and N. Bao, "Revisiting the Oxidation of Graphite: Reaction Mechanism, Chemical Stability, and Structure Self-Regulation," *ACS Omega*, vol. 5, no. 7, pp. 3397–3404, Feb. 2020, doi: 10.1021/acsomega.9b03633.

A. M. Dimiev and J. M. Tour, "Mechanism of Graphene Oxide Formation," *ACS Nano*, vol. 8, no. 3, pp. 3060–3068, Mar. 2014, doi: 10.1021/nn500606a.

X. Chen, Z. Qu, Z. Liu, and G. Ren, "Mechanism of Oxidization of Graphite to Graphene Oxide by the Hummers Method," *ACS Omega*, vol. 7, no. 27, pp. 23503–23510, Jul. 2022, doi: 10.1021/acsomega.2c01963.

N. D. Orekhov *et al.*, "Mechanism of graphene oxide laser reduction at ambient conditions: Experimental and ReaxFF study," *Carbon*, vol. 191, pp. 546–554, May 2022, doi: 10.1016/j.carbon.2022.02.018.

I. Sandhu, M. Chitkara, S. Rana, G. Dhillon, A. Taneja, and S. Kumar, "Photocatalytic performances of stand-alone graphene oxide (GO) and reduced graphene oxide (rGO) nanostructures," *Opt. Quantum Electron.*, vol. 52, Jul. 2020, doi: 10.1007/s11082-020-02473-8.

M. Cheng *et al.*, "Synthesis of graphene oxide/polyacrylamide composite membranes for organic dyes/water separation in water purification," *J. Mater. Sci.*, vol. 54, no. 1, pp. 252–264, Jan. 2019, doi: 10.1007/s10853-018-2828-9.

D. A. Sokolov, C. M. Rouleau, D. B. Geohegan, and T. M. Orlando, "Excimer laser reduction and patterning of graphite oxide," *Carbon*, vol. 53, pp. 81–89, Mar. 2013, doi: 10.1016/j.carbon.2012.10.034.

C.-R. Yang, S.-F. Tseng, and Y.-T. Chen, "Laser-induced reduction of graphene oxide powders by high pulsed ultraviolet laser irradiations," *Appl. Surf. Sci.*, vol. 444, pp. 578–583, Jun. 2018, doi: 10.1016/j.apsusc.2018.03.090.

The Study of Sample Preparation for Spectrophotometric Determination of Formaldehyde in Food Samples

Nutnicha Sakornkhum[a] and Netnapit Kaewchuay*[a]
[a]*Department of chemistry, Faculty of Science and Technology, Rajamangala University of Technology Thanyaburi Pathum Thani, 12110 Thailand*
*Corresponding author. Tel.: 091-5188914; fax: 02-549 4119; *E-mail address:* netnapit_k@rmutt.ac.th

Abstract
Formaldehyde is a highly toxic substance commonly used in the food industry to prevent food from perishing and keep food fresh. Studies have demonstrated that formaldehyde is sensitive to biomolecules in living organisms, leading to both acute and chronic toxicity. This study is focused on investigating sample preparation techniques for extraction formaldehyde in food samples. Various techniques such as solvent extraction, ultrasonic, microwave, and vortex were employed for sample extraction. Among these techniques, ultrasonic-assisted extraction was chosen as the optimal technique for extracting formaldehyde from shiitake mushrooms. Under optimum conditions, which included a power rate of 60% for 10 minutes and the use of acetic acid as a solvent, formaldehyde extraction was performed successfully. A simple and very sensitive method for the determination of formaldehyde level was developed using the UV-visible spectrophotometer after derivatization with Nash reagent. The calibration curve in the concentration range of 0.1-10 mg/L was obtained liner range is Y=0.103x + 0.06 with correlation coefficients (R^2) of 0.9996.

Keywords: Formaldehyde, Ultrasonic Assisted Extraction, Food samples, Sample preparation

1. Introduction
Formaldehyde toxicity has been raised as an important issue in many industries, especially the food industry. due to the use of formaldehyde in food to help food stay fresh for a long time, and not easily perishable this is very dangerous if consumers consume food that has been soaked with formaldehyde in excess or continuously receive it, it will affect health and cause cancer. including irritation of the conjunctiva, nasal mucosa, and respiratory tract. The International Research Organization on Cancer has classified formaldehyde as a group 1 human carcinogen as highly dangerous and is regulated by the Department of industrial works and the Department of Fisheries according to the substances act. 2535 and has a hazardous chemical concentration limit B.E. 2560 indicating the average hazardous chemical concentration limit over a normal working period not exceeding 0.75 mg/L. the hazardous chemical concentration limit for exposure in a short duration is no more than 2 mg/L for 15 minutes.

Formaldehyde exists as a gas at normal temperature it has a pungent smell, is colourless, and is easily flammable at room temperature. better known as formalin, which is chemically the same substance. only in the form of a solution that consists of about 37 percent by weight of formaldehyde gas in water. 10–15% of methanol was added to prevent polymerization. (This solution is usually unstable when stored for a long time, especially at high temperatures. will become formic acid therefore, 5-15% of methanol is added to stabilize the substance). formaldehyde is used in various industries such as the use in the plastics chemical industry as a precursor to the production of various plastic resins, used in the fabric and textile industries. it is used as a fabric softener in the production of finished fabrics so that the fabric remains stable and does not wrinkle or wrinkle. or used to make fabric dyes, use tanning in medicine. used in different concentrations from 10 percent or more as a mixture. depending on the purpose of use, for example, it is mainly used to kill germs and fungi. As a deodorant and an embalming solution in agriculture, it is used to kill germs and insects in the soil. and used to prevent insects in the grain after harvest. used in other industries such as the production of rubber, resin, paper products, fiberglass, film, explosives, skin care products, paints, etc., but formaldehyde is not allowed to be used in the food industry. the amount of formaldehyde present in nature most of them have a very small amount, not more than 1 ppm, which does not cause harm to the body. while formaldehyde is used in excessive amounts and is used in conjunction with the food industry to soak marine animal foods. to maintain freshness or to make crispy squid.

Normally, formaldehyde measurement can be detected in 2 ways: free formaldehyde and total formaldehyde measurement are measured differently. For free formaldehyde analysis, samples are extracted with solvents such as water or acidic solutions by using high-frequency waves or vortex to separate formaldehyde from the sample and then measure it with appropriate techniques. The disadvantage is that the interference cannot be eliminated, causing problems in the measurement range. And for total formaldehyde analysis, samples were prepared by steam distillation under acidic conditions to separate formaldehyde, both free formaldehyde and total formaldehyde from the sample solution into the solvent. and then measure with appropriate techniques. Distillation is a good method for removing interference, but it has the disadvantage of taking a long time to separate formaldehyde from the sample. There are several ways to measure formaldehyde in food, divided according to the technique and methods used in

the analysis as follows: Spectrophotometry is a reaction between formaldehyde and a specific chemical to form a colored or colorless solution and measure the solution at a wavelength suitable for that substance. such as Nash method is a reaction between acetylacetone, ammonium acetate, and formaldehyde incubation to catalyze the reaction. This method has specificity and sensitivity, the disadvantage is that takes time and heat for the reaction and limits its potential to be developed into automated analysis or field applications. The 2,4-Amino-3-hydrazino-5-mercapto-1,2,4-triazole (AHMT) method is the reaction of formaldehyde in a strong alkaline. This method is sensitive to measurements and the disadvantage is that it must be in strong alkaline conditions and carbonates are formed. The Kinetic Method is a measure of the catalytic effect in the reaction of a substance, increasing the sensitivity and specificity of the analysis. Chromatography is the separation of formaldehyde or derivatives from other mixtures to be purified by carriers moving on stationary phases and measured with a suitable detector for the isolated substance. Popular techniques are High-performance liquid chromatography (HPLC), Gas chromatography (GC), and Solid Phase Microextraction (SPME). Fluorometry is an Analytical instrument that is more expensive compared to spectrophotometers but has better analytical sensitivity. An electronic nose is a working principle that uses a sensor whose electrical resistance change when absorbing volatile substances as a measure of formaldehyde gas. This technique is a fast analysis and easy to use when welding with chemometric techniques. Biosensor uses biomass to capture formaldehyde and cause biological processes to cause chemical changes. Screening test using an analytical technique that can quickly see results by comparing colors, there is a limitation in measurement sensitivity.

In this research, we are interested in the development of sample preparation and measurement methods for formaldehyde contaminants in food. Extraction of food samples with high-frequency waves using Ultrasonic Assisted Extraction (UAE) technique. The formaldehyde extracted was measured by the Nash method with Nash's reagent reaction and then analyzed by a UV-visible spectrophotometer.

2. Methodology

2.1. Materials

All chemicals in this work were of analytical grade. Formaldehyde, acetylacetone, ammonium acetate, and acetic acid, as reagents were purchased from Merck KGaA (Darmstadt, Germany) or Fluka (Buchs, Switzerland). Standard formaldehyde (1000 mg/L) was prepared by diluting a 37% (v/v) formaldehyde solution in distilled water as stock solution. The working standard solutions were prepared daily by successive dilution of stock solution with distilled water to get the required concentrations in the range of 0.1 - 10 mg/L. Nash's reagent was prepared with ammonium acetate 150 g dissolved with 300 ml distilled water, add 3 mL acetic acid and 2 mL acetylacetone, and then adjusted the volume to 1000 ml with distilled water. The reagent was stored in a dark bottle at 0^{o} C. 0.1 % Acetic acid prepared by pipet 1 mL acetic acid adjust the volume 1000 mL. Instrumentals spectrophotometry was carried out on a Jasco V-570 UV-Vis spectrophotometer (Tokyo) equipped with 1 mL quartz (Starna Company, UK), Ultrasonic cell crusher noise isolating chamber (model JY88-IIN, Fujian, China), Vortex (model VTL 107, LSM), Centrifuge PRP (model CTF-TL4S), Water bath (model WNB7, Germany).

2.2. Study of optimum wavelength

From studying the absorbance of the formaldehyde standard solution, the formaldehyde standard solution was prepared at a concentration of 10 mg/L. The formaldehyde was derivatized with Nash's reagent reaction. The reaction between acetylacetone, formaldehyde, and ammonia acetate was reacted as in Figure 1. In the catalytic heat condition, it is 3,5-diaacetyl-1,4-dihydrolutidine (DDL), derivatization of formaldehyde, and the amount of light wave absorption was measured with a UV visible spectrophotometer at wavelengths ranging from 300-800 nm.

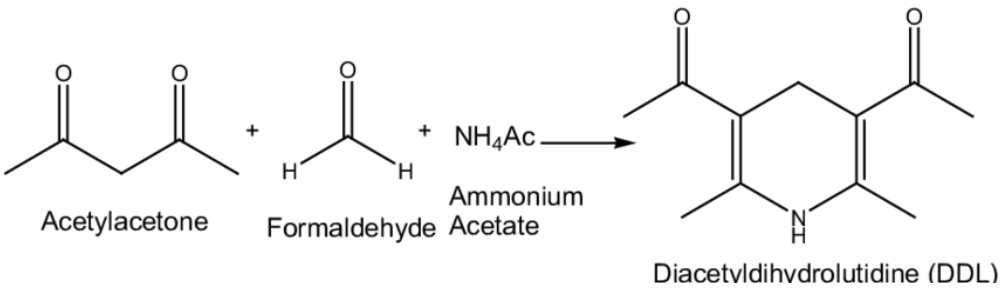

Figure 1 The reaction between Nash's reagent and Formaldehyde.

2.3. Study of the linearity of the calibration curve

The calibration curve analyzed formaldehyde standard solution in the concentration range from 0.1 to 10 mg/L absorbance at wavelength 413 nm. The linearity was evaluated by determining the correlation coefficient (R^2) of linear regression analysis (y=bx+a) of the calibration curve constructed between the absorbance signal and concentration range of the formaldehyde standard solution.

2.4. Study of suitable solvents for extraction

For the preparation of the samples, shiitake mushroom samples were weighed 1 g and extracted with 30 ml of 0.1% acetic acid solution and were compared with distilled water as solvents for extraction. Then, added 15 mL acetonitrile, centrifuge, and filter. The solution reacted with Nash's reagent, measuring the absorbance at 413 nm.

2.5. Study of extraction techniques for formaldehyde extraction from food products

Extraction techniques such as solvent extraction, ultrasonic, microwave, and vortex were studied in shiitake mushroom samples. In each technique, prepared 1 g of shiitake mushroom was added to 30 ml of 0.1% acetic acid solution. The solvent extraction was performed by soaked the solution at room temperature for 1 h. The ultrasonic technique uses a power rate of 40% for 5 minutes. The microwave technique uses power at 150 watts for 5 minutes. The vortex technique uses the lowest power for 5 minutes. The resulting solution was a reaction with Nash's regent, incubated at 37 °C, and the absorbance was measured at 413 nm.

2.6. Study on Optimum Conditions of Ultrasonic Machine for Formaldehyde Extraction

Ultrasonic extraction was studied by studying the appropriate extraction power rate and time. Samples were prepared and weighed 1 g of shiitake mushroom, added with 30 ml of 0.1% acetic acid solution, and extracted at different conditions.

2.6.1. Power rate of ultrasonic method

The study of optimum power rate was extracted using a power rate range of 20-80%, process time of 5 min. Added 15 mL acetonitrile, centrifuge, and filter. The resulting solution was reacted by Nash's regent, incubated at 37 °C, and the absorbance was measured at 413 nm.

2.6.2. Power rate of extracting ultrasonic time

The Study of extraction time by ultrasonic using process time range from 5-30 min, power rate of 60 %. Added 15 mL acetonitrile, centrifuge, and filter. The resulting solution was reacted by Nash's regent, incubated at 37 °C, and the absorbance was measured at 413 nm.

3.Results and Discussion

3.1. Study of optimum wavelength (λ max)

The absorbance of the formaldehyde standard solution was examined and prepared a solution with a concentration of 10 mg/L. The solution was then reacted with Nash's reagent and incubated at 37 °C. The measurement of 3,5-diacetyl-1,4-dihydrolutidine (DDL) was conducted using a UV-visible spectrophotometer across a wavelength range of 300-800 nm. The results, as shown in Figure 2, indicated that the maximum signal for DDL was observed at a wavelength of 413 nm.

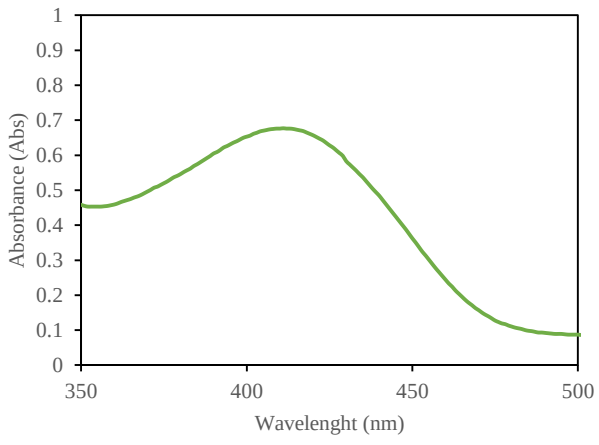

Figure 2 Absorbance spectra for standard of formaldehyde, 10 ppm, reaction with Nash's reagent

3.2. Study of the calibration curve

The calibration curve analyses formaldehyde standard solution in the concentration range from 0.1 to 10 mg/L. The absorbance of UV-visible detection at wavelength 413 nm. Under the selected optimum experimental condition, this method was applied to a series of standard solutions containing various concentrations of analyte, in order to evaluate the efficiency of it. The calibration curve was obtained liner in the concentration range 0.1-10 mg/L with correlation coefficients (R^2) of 0.9996. The least-square equation over the dynamic linear range is Y= 0.103X + 0.06, in which Y and X are absorbance and concentration of formaldehyde in the sample, respectively.

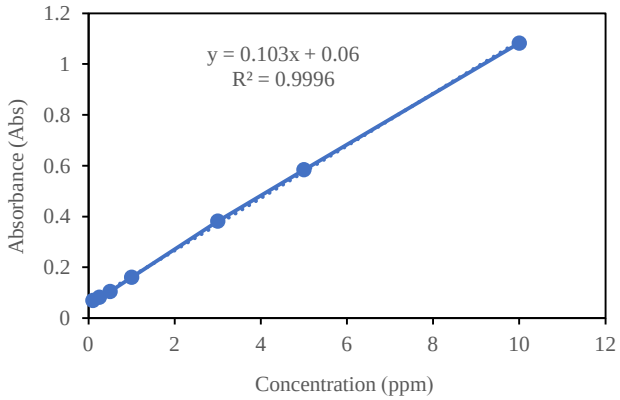

Figure 3 Calibration curve of analyses formaldehyde standard solution.

3.3. Study of suitable solvents for extraction

In order to determine the suitable solvent for extraction, both acetic acid and deionized water (DI) were considered for solvent extraction. Shiitake mushroom samples weighing 1 g were extracted using 30 ml of a 0.1% acetic acid solution, and this was compared to the use of an equal amount of deionized water. Subsequently, 15 mL of acetonitrile was added, followed by centrifugation and filtration. The resulting solution was then reacted with Nash's reagent and incubated at 37 °C. The DDL, formaldehyde derivatized, was measured at 413 nm. It was determined that the 0.1% acetic acid solution was the optimal solvent for extracting formaldehyde from shiitake mushrooms.

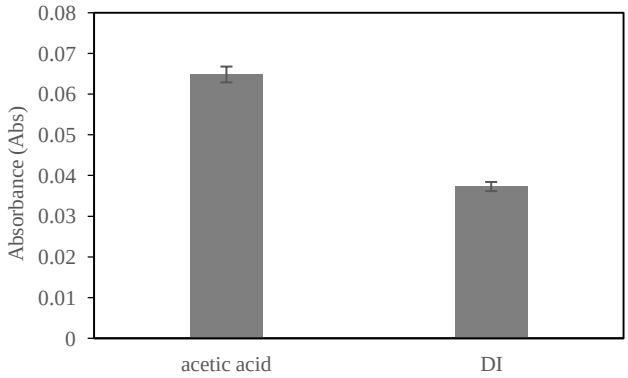

Figure 4 Effects of solvent on the formaldehyde extraction.

3.4. Study of extraction techniques for formaldehyde extraction from food products

Various extraction techniques, including solvent extraction, ultrasonic, microwave, and vortex, were studied extracting formaldehyde from shiitake mushroom samples. In each technique, 1 g of the sample was added 30 ml of 0.1% acetic acid solution and centrifuged. For solvent extraction techniques, the solution was left at room temperature for 1 hour. The ultrasonic technique utilized a power rate of 40% for 5 minutes. The microwave technique operated at 150 watts for 5 minutes. As for the vortex technique, the lowest power setting was used for 5 minutes. The resulting solution was then subjected to a reaction with Nash's reagent, followed by incubation at 37 °C, and the absorbance was measured at 413 nm. A comparison of these techniques is presented in Figure 5. According to the results, the Ultrasonic technique was the optimal method for formaldehyde sample extraction.

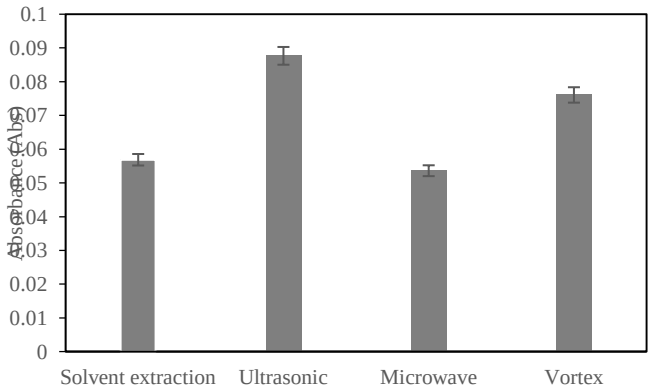

Figure 5 Effects of sample extraction method on the formaldehyde extraction.

3.5. Study on Optimum Conditions of Ultrasonic method for Formaldehyde Extraction

Ultrasonic extraction was studied, focusing on determining the optimal extraction time and power rate. To prepare the samples, 1 g of shiitake mushroom was weighed and combined with 30 ml of a 0.1% acetic acid solution. The extraction process was carried out under various conditions, and the resulting solution was subjected to a reaction with Nash's reagent. Following that, the solution was incubated at 37 °C, and the absorbance was measured at 413 nm.

3.5.1. Effects of power rate of ultrasonic technique

The power rate of the ultrasonic technique plays an important in the extraction of the samples. In this work, the effect of power rate of ultrasonic technique on the extraction process within the range of 20% to 80% was investigated. The results indicate that increasing the power rate of the ultrasonic method led to an increase in the extraction efficiency. The highest intensity was achieved at a power rate of 60%, after that, decreased. Therefore, a power rate of 60% was selected for extracting the samples in this study.

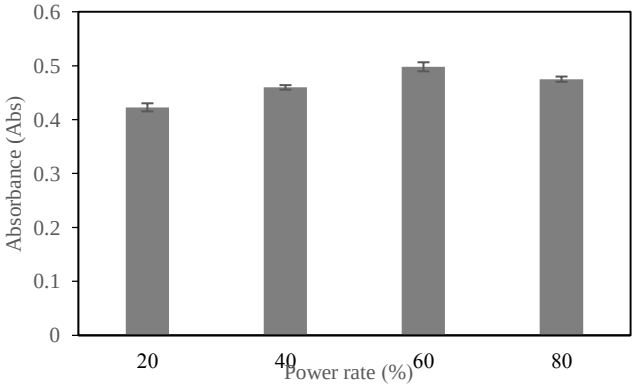

Figure 6 Effects of power rate of ultrasonic method on the formaldehyde extraction

3.5.2. Effects of extracting ultrasonic time

The Effects of extracting ultrasonic time on the absorbance intensity was studied. The results, as shown in Fig.7, revealed variations in absorbance within the time range of 5-30 minutes. Accordingly, the optimum extraction time for formaldehyde samples was determined to be 10 minutes.

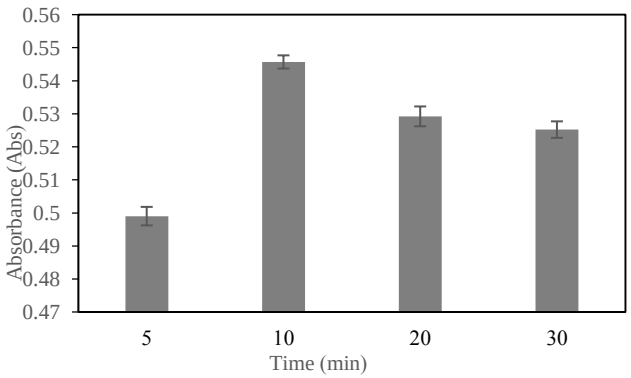

Figure 7 Effects of extracting ultrasonic time on the formaldehyde extraction.

3. Conclusions

In this study, we examined the sample extraction method for determining formaldehyde in food samples, specifically shiitake mushrooms. We investigated various sample extraction techniques, including solvent extraction, ultrasonic, microwave, and vortex methods. We found that the highest amount of formaldehyde was extracted from shiitake mushroom samples using 0.1% acetic acid as a solvent and employing the ultrasonic technique, compared to the other methods. We emphasized the potential of ultrasonic techniques for extracting formaldehyde from shiitake mushrooms, focusing on extraction parameters such as extraction time and power rate of the Ultrasonic Machine. The optimal conditions for formaldehyde extraction were a power rate of 60% for 10 minutes. To measure formaldehyde content, we reacted it with Nash's reagent solution, which produced a yellow dye. We quantified formaldehyde using a UV-visible spectrophotometer with a λmax of 413 nm. The formaldehyde content in food samples was determined using a calibration curve, which showed a linear range of Y=0.103x + 0.06 in the concentration range of 0.1-10 mg/L, with a correlation coefficient (R2) of 0.9996. This method is sensitive, inexpensive, simple, fast, and requires only a small volume of organic solvents. Further research is needed to explore the solid-phase extraction technique, which can help overcome interference from the matrix and improve preconcentration before detection. This proposed method is suitable for analyzing trace amounts of formaldehyde in food samples.

4. Acknowledgements

The authors thank for Thailand Science Research and Innovation (FRB66E0638) for financial support in this research.

5. References

Ahmed Salem Sebaei , Ahmed M. Gomaa, A. A. El-Zwahry, and E. A. Emara, 2018, Determination of Formaldehyde by HPLC with Stable Precolumn Derivatization in Egyptian Dairy Products, Vol. 2018.

B. N. Aini, S. Siddiquee, and K. Ampon, 2016, Development of formaldehyde biosensor for determination of formalin in fish samples; Malabar red snapper and longtail tuna, Biosensors, Vol. 6, p. 1–15.

Claeys W, Vleminckx C, Dubois A, Huyghebaert A, Hofte M, Daenens P, 2009, Formaldehyde in cultivated mushroom: a negligible risk for the consumer, Food Addit Contam, Vol.9, p. 1265-1272.

Compton BJ, and Purdy WC, 1980, The mechanism of the reaction of the Nash and the Sawicki aldehyde reagent, CAN.J. CHEM, Vol. 58, p. 2207-2211.

Farrhin Nowshad, Md N. Islam, and Mohidus S. Khan, 2018, Analysis of the Concentration and Formation Behavior of Naturally Occurring Formaldehyde Content in Food, International Journal of Food Engineering, Vol. 4, p. 71-75.

International Agency for Research on Cancer Formaldehyde, 2006, 2- butoxyethanol and 1- tert-Butoxypropan-2-ol, IARC Monogr Eval Carcinog Risks Hum, Vol. 88, P 39-325.

Kaminski, A. S. Atwal, and S. Mahadevan, 1993, Determination of formaldehyde in fresh and retail milk by liquid column chromatography, Journal of AOAC International, Vol. 76, p. 1010–1013.

Kobun Rovina, Joseph Merillyn Vonnie, Sulaiman Nurul Shaeera, Su Xin Yi, Nur Fatihah Abd Halid, 2020, Development of biodegradable hybrid polymer film for detection of formaldehyde in seafood products, Sensing and Bio-Sensing Research, Vol. 27, p.100310.

Mason DJ, Sykes MD, Panton SW, Rippon EH, 2004, Determination of naturally occurring formaldehyde in raw and cooked Shiitake mushrooms by spectrophotometry and liquid chromatography-mass spectrometry, Food Addit Contam, Vol. 21(11), p.1071- 1082.

Nash T, 1953, The colorimetric estimation of formaldehyde by means of the Hantzsch reaction, G.H. Wiltshire, Vol. 55, p. 416-421.

Nur Indang M, Abdulamir AS, Abu Bakar A, Salleh AB, Lee YH, and Nor Azah Y, 2009, A review: method of determination of health-endangering formaldehyde in diet, Research Journal of Pharmacology, Vol.3(2), p.31-47.

Qiong LI, Piyanete SRITHARATHIKHUN, and Shoji MOTOMIZU, 2007, Development of Novel Reagent for Hantzsch Reaction for the Determination of Formaldehyde by Spectrophotometry and Fluorometry, ANALYTICAL SCIENCES, Vol. 23, p.413-417.

Taina Ohra-aho*, Léon Rohrbach, Jozef G. M. Winkelman, Hero J. Heeres, Atte Mikkelson, Anja Oasmaa, Bert van de Beld, Evert. J. Leijenhorst, and Hans Heeres, 2021, Evaluation of Analysis Methods for Formaldehyde, Acetaldehyde, and Furfural from Fast Pyrolysis Bio-oil, p. 18583–18591.

Tai-Sheng Yeh, Tzu-Chun Lin, Ching-Chuan Chen, Hwui-Mei Wen, 2013, Analysis of free and bound formaldehyde in squid and squid products by gas chromatography-mass spectrometry, Journal of Food and Drug Analysis, p.190-197.

U. Kleeberg; W. Klinger, 1982, Sensitive formaldehyde determination with NASH's reagent and a 'tryptophan reaction', Vol. 8(1), p. 19–31.

Yi Zhu, Zengqi Peng, Min Wang, Rongrong Wang, Luming Rui, 2012, Optimization of extraction procedure for formaldehyde assay in smoked meat products, Journal of Food Composition and Analysis, Vol. 28, p. 1-7.

Zelalai Simayi, Wusimanjiang Aierken, Parhat Rozi, Gulimire Ababaikeri, Cao Bo, Zhou Chenglin, Guzalnur Askar, Yang Xiaojun, 2023, Optimization of ultrasound-assisted extraction, structural, functional, and antioxidant properties of Glycyrrhiza uralensis seed protein, Process Biochemistry, Vol.124, p. 1-12.

Characterization of Attenuated Precocious Line of *Eimeria Tenella*

Wipaporn Jarujareet[a*], Paphatsara Jamnongjit[a], Phanrapi Noochuay[a], and Khompakorn Thanasut[a]

[a]*Faculty of Veterinary Science, Rajamangala University of Technology Srivijaya, Nakhon Si Thammarat, 80240, Thailand*
*Corresponding author. Tel +66874940005, *E-mail address:* wipaporn.j@rmutsv.ac.th

Abstract
The changes of biological characteristics of an attenuated precocious line of *E. tenella* were studied. After 34 passages, the prepatent period of the precocious line was reduced from 180 to 132 hours. The peak of oocysts output of this precocious line was 3 days earlier than that of the parental strain. The pathogenicity of the precocious line by means of lesion score, maximum of oocysts per gram of feces and oocyst output was significantly reduced when compared to the parent strain. However, traces of bloody feces could still be seen in chickens infected with the precocious line, which is almost the same as the parental strain. Deletion of any stage of the life cycle was not confirmed but accelerated growth in second-generation shizogony was found in the precocious line. The attempt of introducing fluorescent protein into the precocious line of *E. tenella* by cationic lipid-mediated transfection method was successful as the fluorescence was detected in unsporulated oocysts. However, as the oocyst continue to sporulate, the fluorescent protein could not be detected in the fully sporulated.

Keywords: Chicken, Coccidiosis, *Eimeria tenella*, Precocious line

1. Introduction
Chicken coccidiosis is a protozoan disease caused by *Eimeria* species considered of worldwide economic importance for poultry farms (Aziz et al., 2016). The clinical signs are characterized by diarrhea ranging from mucoid and watery to hemorrhagic, reduction in weight or weight gain, high morbidity, and sudden death. The five highly pathogenic species are *E. tenella, E. necatrix, E. maxima, E. brunetti, and E. acervulina* (Allen and Fetterer, 2002; Kawahara et al., 2014). Immunization with live attenuated vaccines is increasingly playing and important role in the control of coccidiosis in the poultry industry because of the increasing of drug resistance to the available coccidiostats and customer concern about drug residues in poultry products (Dong et al., 2006; Jorgensen et al., 2006; Constantinoiu et al., 2011). The attenuated live anticoccidial vaccines, like Paracox® and Livacox®, are widely used. The former was obtained from precocious line, while the latter was acquired from precocious and egg-passaged lined (Dong et al., 2006). Previous study stated that the low-virulence attenuated precocious line of *E. tenella* could be obtained by successive passages of oocysts first collected from feces of previously infected chickens, which can then be used as vaccine (Jeffers, 1975). Compared with the parental strain, the low-virulence attenuated precocious lines should have reduced prepatent period, reduced pathogenicity, and much lower reproductive potential, but maintained at the level that allows economically commercial production (Dong et al., 2006; Jorgensen et al., 2006). In this study, the biological characteristics of an attenuated precocious line of *E. tenella* were studied and compared with its parental strain. In addition, transfection of the precocious line was tried out to investigate whether the transfected precocious line could express fluorescent protein throughout the life cycle for their potential use as a vaccine marker.

2. Materials and Methods
2.1. Parasite
E. tenella oocysts were purified from filed sample by a single oocyst isolation and have been maintained by propagation in the chickens.

2.2. Animals
Seven-day-old Boris brown chicken were used in this study. The chickens, with ad libitum access to water and feed (Pet's One Bird food, Cainz Co., Ltd., Saitama, Japan), were kept and handled according to the rules and regulations laid down by the Institutional Animal Care and Use Committee (IACUC) of Azabu University. Feces were test by sugar centrifugal flotation technique prior to experimentation to confirm that the chickens were free from coccidia.

2.3 Selection for the precocious line of E. tenella
The precocious line was obtained by serial passaging through chickens. Only earliest shed oocysts were used as the inoculum for the next passage. For each passage, five chickens were inoculated with 1×10^3 sporulated oocysts. Feces collection were made at 4 h intervals starting to 12 h before the time of patency, calculated from the previous passage. Pooled feces sample were examined for presences of oocysts using the sugar centrifugal flotation technique.

2.4 Biological characterization of precocious line of E. tenella

The changes in biological characteristics were monitored during production of precocious line of *E. tenella*. The chickens in each passage were observed for 15 consecutive days, and clinical signs, mainly bloody diarrhea and mortality were recorded. Oocysts excreted in feces were also checked and count daily from 4 to 15 day post-inoculation (PI) using McMaster chamber. All chickens were sacrificed on the 15-day PI. The oocysts count was determined in cecal content sample from each chicken and lesion score were graded according to Johnson and Reid (1970). The scoring scales ranged from 0 to +4, where 0 = no gross lesion, +1= mild lesion with few scattered petechial on the cecal wall, no thickening of the cecal wall, normal cecal contents present, +2= moderate lesion with numerous petechial, bleeding and slight thickening of cecal wall, +3= severe lesion with severe bleeding or cecal core present, cecal wall greatly thickened and +4= extremely severe lesion with severe bleeding or large caseous core, a much thickened or ruptured cecal wall, gangrene or death.

2.5 Observations on the endogenous development of the precocious line and the parent strain

Differences in the rate of development of precocious line and parental strain were assessed by microscopic examination of the endogenous stages. Fourteen, seven-day-old chickens were inoculated with 1×10^4 sporulated oocysts for the parental strain and precocious line. One chicken infected with parental strain and one with precocious line were sacrificed at 24 h intervals, from 24 h until 168 h. The infected caeca were removed, fixed in 10% buffered formalin at room temperature, and cut into 5 part at a length of 3-5 mm, embedded in paraffin, cut as cross-sections at a thickness of 4 μm and stained with hematoxylin and eosin.

2.6 Transfection of E. tenella precocious line

The plasmid pH4-DHFR-eYFP-P2A-RFP-3'Act (kindly provided by Dr. Xianyong Liu from China Agricultural University), containing a dihydrofolate reductase thymidylate synthase (DHFR-TS) derived from *Toxoplasma gondii*, enhanced yellow fluorescent protein (eYFP) and red fluorescent protein (RFP) as the reporter genes flanked by histone 4 promoter and 3′ region of actin of *E. tenella* and porcine teschovirus-1 2A peptide (P2A), was introduced into sporozoites of *E. tenella* precocious line as describe below. For transfection, sporocysts were released from oocysts by grinding with 0.5 mm glass-beads, followed by excystation with trypsin-bile solution (0.75% w/v trypsin and 10% v/v chicken bile in PBS) (Shi et al., 2008). Sporozoites were separated from oocysts walls and sporocyst debris by filtration using an Advantec® qualitative filter paper, grade No. 2 (Toyo Roshi Kaisha, Ltd., Tokyo, Japan). The purified sporozoites were wash once with PBS and suspended in DMEM. The cationic lipid-mediated transfection was conducted by using Lipofectamine® LTX DNA transfection reagents (Thermo Fisher Scientific Inc., Massachusetts), which comprising of Lipofectamine® LTX reagent, Opti-MEM® medium and PLUSTM reagent. Transfection was performed according to manufacturer's protocol. Briefly, the Lipofectamine® LTX reagent was diluted in Opti-MEM® medium. The plasmid DNA was also diluted in Opti-MEM® medium, then add PLUSTM reagent. Diluted plasmid DNA was added to diluted Lipofectamine® LTX reagent (1:1 ratio) and incubated for 5 min at room temperature. The plasmid DNA-lipid complex was then added to 500 µl of sporozoites suspension (1×10^6 sporozoites/ 1 ml) and incubate at 37 °C for 24 h. Sporozoites were wash with PBS, re-suspended in DMEM and inoculated into seven-day-old chicken via the cloacal route for the in vivo stable transfection. Chickens were sacrificed at 8 day PI and oocysts from cecal content were collected and checked by fluorescence microscope.

3. Results

3.1. Selection of precocious line

Reduction in prepatent period is shown in Figure 1. The prepatent period was progressively reduced from 180 h for the parent strain to132 h by passage number 34 (48 h reduction).

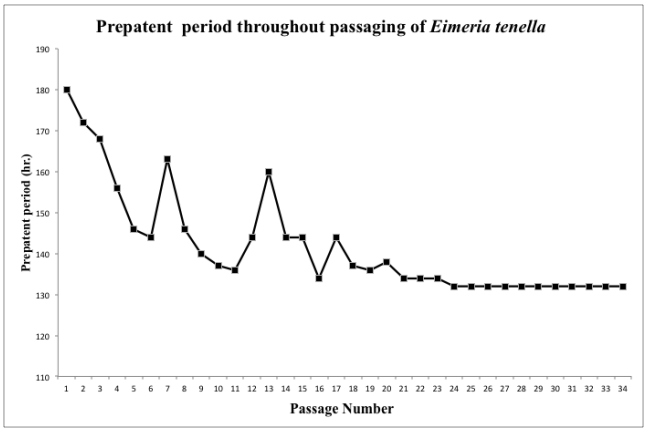

Figure 1. Prepatent period throughout passaging of *Eimeria tenella*

3.2. Biological characterization of precocious line of E. tenella

The fecal oocysts shedding of precocious line (P34) reached a peak on day 7 PI, but the parent strain reached a peak on day 10 PI. The number of shed oocysts decreased after reach the peak point in both P34 and parent strain (Figure 2). The maximum of oocysts per gram of feces (OPG) was reduced from 1.57 × 106 to 0.88 × 106. The average number of oocysts in cecum was reduced relative to the parent strain. The pathogenicity of the precocious line by mean of lesion score was also reduced compared to the parent strain (Table 1).

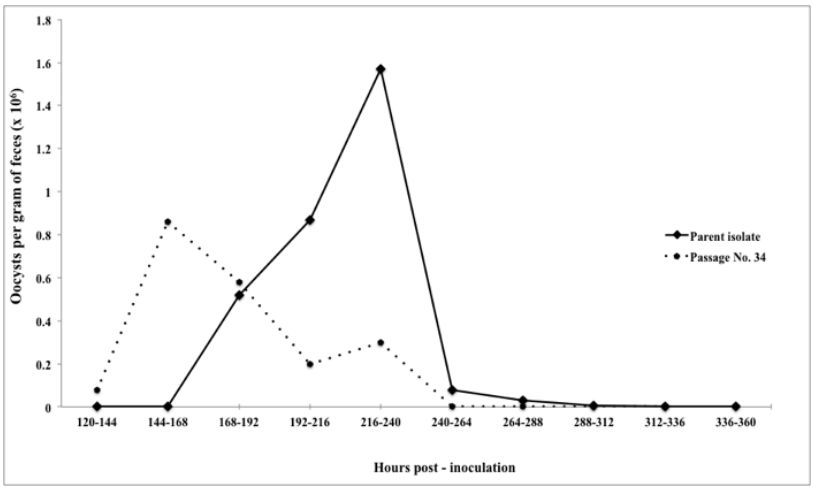

Figure 2. Oocysts shedding patterns of *Eimeria tenella* precocious line and parent strain

Table 1. Biological characteristics of *Eimeria tenella* precocious line (P34) compared with parent strain (P1)

Biological characteristics	P1	P34
Time bloody feces occurred (DPI)	5,6,7	5,6
Mortality	0	0
Lesion score (mean ± SD)	2.4 ± 1.3	1.3 ± 0.6
Average number of oocysts in cecum at 15 DPI ($\times 10^3$)	13.8	2.67
Maximum OPG ($\times 10^6$)	1.57	0.88

DPI = Day post-inoculation
OPG = Oocysts per gram of feces

3.3. Observations on the endogenous development of the precocious line and the parent strain

Histological observation was conducted on the cecal samples of chickens inoculated with oocysts of the parent strain or precocious line. The results are summarized in Table 2. In the parent strain infected chickens, immature second-generation of schizonts (Figure 3A) were observed at 96 h PI and mature second-generation of schizonts (Figure 3B) were found at 120 h PI. Gametes and oocysts appeared at 144 h PI. Second-generation schizogony proceeds at a much faster rate in the precocious line, resulting in a predominance of mature second-generation of schizonts (Figure 3C) by 96 h and oocysts (Figure 3D, E) by 120 h after inoculation.

Table 2. Summary of observations on the endogenous development of the precocious line and the parent strain

	Endogenous stages observed	
H	Parent strain (P1)	Precocious line (P 34)
96	Immature second generation schizonts	Immature and mature second generation schizonts
120	Immature and mature second generation schizonts	Mature second generation schizonts, gametes and a few oocysts oocysts
144	Gametes and a few oocysts	Gametes and oocysts
168	Gametes and mature oocysts	Gametes and mature oocysts

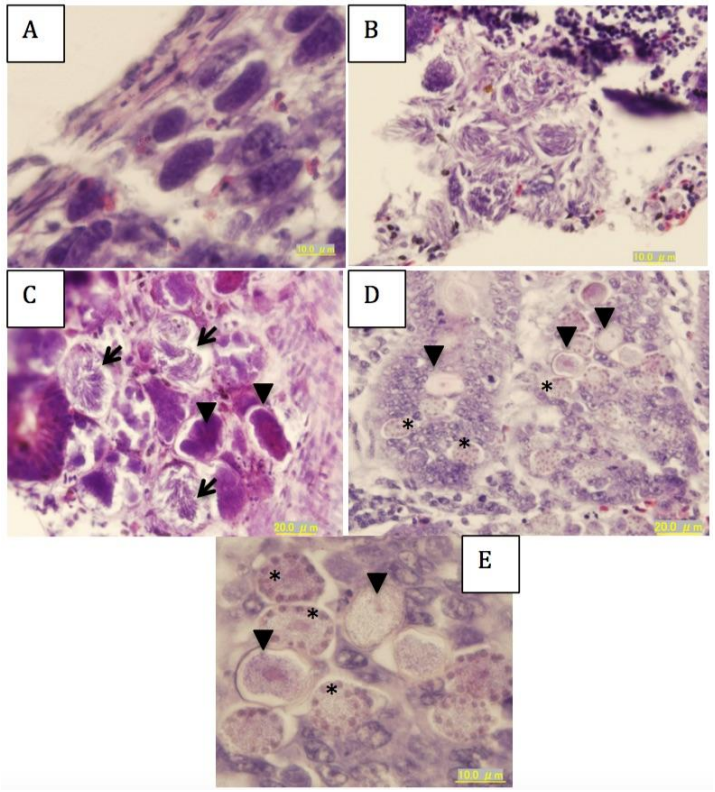

Figure 3. Photomicrographs of endogenous stages of *Eimeria tenella* precocious line and parent strain in cecal tissue. Haematoxylin and eosin staining. A: immature second-generation schizonts of parent strain at 96 h after inoculation. B: mature second-generation schizonts of precocious line at 96 h after inoculation. C: immature (arrowheads) and mature (arrows) second-generation schizonts of parent strain at 120 h after inoculation. D: shows macrogametocytes (asterisks) and zygotes or early oocysts (arrowheads) of precocious line at 120 h after inoculation. E: high magnification of macrogametocyes (asterisks) and early oocysts (arrowheads).

3.4. Transfection of E. tenella precocious strain

Only a few fluorescence unsporulated oocysts were detected from inoculated chickens (Figure 4A). No fluorescence was detected from sporulated oocysts (Figure 4B). In control experiments, no fluorescence was detected when the same numbers of sporozoites were incubated in the presence or absence of plasmid DNA with or without incubation with Lipofectamine® LTX DNA transfection reagents (Figure 4C).

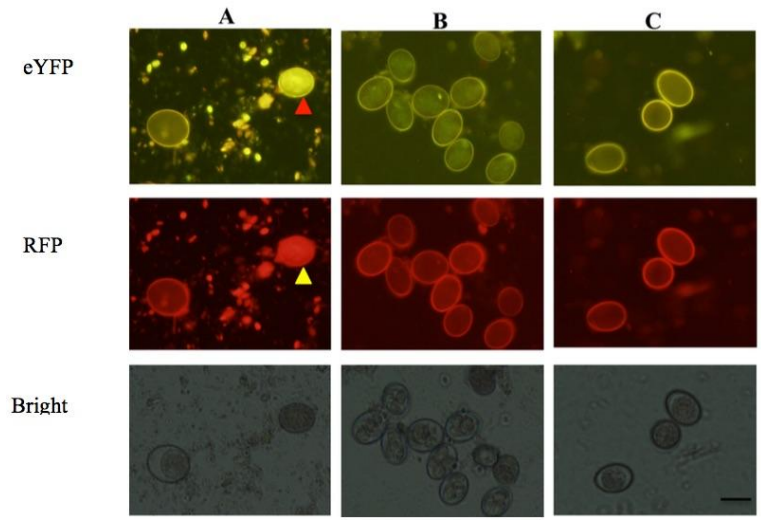

Figure 4. Transfection of *Eimeria tenella* precocious strain. A: unsporulated oocysts, B: sporulated oocysts, C: control experiment, Bar = 20 µm

4. Discussion

The prepatent period has been considered as a species-specific trait among the coccidia (Jeffers, 1975). The prepatent periods of parent strain of *E. tenella* used for attenuation have been recorded as 120 h, 121 h, 136 h, 139 h and 144 h (Jeffers, 1975; Kawaguchi et al., 1988; Long and Johnson 1988; Jorgensen et al., 2006). In comparison, the parent stain used in this study had prepatent period of 180 h. This variability in prepatent periods among different strains casts substantial doubt on the reliability of using prepatent period as a diagnostic tool for differentiating species of *Eimeria* (Jorgensen et al., 2006). In this study, after 34 passages of selection for the precocious strain, the prepatent periods was reduced from 180 to 132 hours. This finding is quite different from the results obtained by Jeffers (1975) for the precocious line of the Wisconsin strain of *E. tenella*. The shorter period of 168 h for the parent strain was obtained compared to 120 for the precocious line. Kawaguchi et al. (1988) reported a shortening from 136 to 112 h for the Japanese NIAH strain whereas Jorgensen et al. (2006) obtained a reduction from 144 h to 120 h for the Redlands strain and from 139 h to 116 h for the Darryl strain. It seems that different strains from the same species possess character variation for precociousness (Kawazoe et al., 2005).

The reproduction and pattern of oocyst output are two important characters for *Eimeria* parasites when comparing a precocious line or a newly isolated population with a parental strain or a reference strain (Yan et al., 2009). The oocyst production of the parent strain of *E. tenella* peaked on the 10-day PI in seven-day-old Boris brown chicken in this study. This result was different from that in the study by Jeffers (1975), which the peak time occurred on the 7.5-day PI, probably due to the host genotype differences, or oocyst genetic variations, or both (Dong et al., 2006). Differences in oocyst output and the pattern of oocyst shedding between host genotypes have been reported for *Eimeria* species (Bumstead and Millard, 1992; Cha et al., 2018). The early in peak time of oocysts production of P34 compared to the parent isolated (7 days PI vs. 10 days PI) in this study was probably related to genetic changes in the parasite by the selection of the precocious development (Dong et al., 2006). Further studies are necessary to confirm whether the precocious line has genetic difference from the parent isolate.

Selection for precocious development can lead to the loss or modification of various reproductive stages with a concomitant reduction in reproductive potential and pathogenicity (Jeffers, 1975; Long and Johnson 1988; Jorgensen et al., 2006). In this study, the maximum of oocysts per gram of feces (OPG) and the average number of oocysts in cecum was reduced relative to the parent isolate indicates that, the precocious strain developed in this work had reduced reproductive potentials. The pathogenicity of the precocious strain by mean of lesion score was also reduced compared to the parent isolate. However, traces of bloody feces could still be seen in the P34, which is almost the same as the parent isolate, suggesting that further selection of P34 might produce an effective and safe vaccine line.

Previous studies had shown that deletion or acceleration of the early stages of the life cycle results in shortening of the prepatent period of *E. tenella* precocious line (Jeffers, 1975; Kawaguchi et al., 1988). In this study deletion of any stage of the life cycle was not confirmed but accelerated growth in second generation shizogony was found in the precocious line of *E. tenella*.

Stable transfection of *Eimeria* species has been difficult to achieve because of the obligate requirement for in vivo amplification and selection of the parasites (Clark et al., 2008). Previous studies reported that electroporation along with the restricted enzyme-mediated integration is the optimal method for stable transfection of *Eimeria* species (Clark et al., 2008; Yan et al., 2009; Tao et al., 2017). In this study, the attempt of introducing fluorescent protein into the precocious line of *E. tenella* by cationic lipid-mediated transfection method was successful as the fluorescence was detected in unsporulated oocysts. However, as the oocyst continue to sporulate, the fluorescent protein could not be detected in the fully sporulated oocyst.

5. Conclusion

After 34 passages of selection for the precocious strain, the prepatent periods was reduced from 180 to 132 hours. The maximum of OPG, oocyst output and lesion score were reduced but there were still traces of bloody feces like those seen in the parent isolate. Deletion of any stage of the life cycle was not confirmed but accelerated growth in second generation shizogony was found in the precocious line. The attempt of introducing fluorescent protein into the precocious line of *E. tenella* was successful as the fluorescence was detected in unsporulated oocysts. However, no fluorescent protein was detected in the fully sporulated oocyst.

6. References

Allen, P. C. and Fetterer, R. H., 2002, Recent advances in biology and immunobiology of *Eimeria* species and in diagnosis and control of infection with these coccidian parasites of poultry, Clinical Microbiology, Vol. 15(1), p. 58–65.

Aziz, A. E., Orma, O. A., Awadin, W. F. and Seady, Y. E. L., 2016, Effects of supplementation of broiler diets with fish oil and linseed oil on growth performance, cytokine, and cecal histopathological changes in broiler chicken infected by *Eimeria tenella*, International Journal of Agricultural Sciences and Veterinary Medicine, Vol. 4(4), p. 12–27.

Bumstead, N. and Millard, B. J., 1992, Variation in susceptibility of inbred lines of chickens to seven species of *Eimeria*, Parasitology, Vol. 104(3), p. 407–413.

Cha, J. O., Zhao, J., Yang, M. S., Kim, W. I., Cho, H. S., Lim, C. W. and Kim, B., 2018, Oocyst-shedding patterns of three *Eimeria* species in chickens and shedding pattern variation depending on the storage period of *Eimeria tenella* oocysts, Journal of Parasitology, Vol. 104(1), p. 18–22.

Clark, J. D., Billington, K., Bumstead, J. M., Oakes, R. D., Soon, P. E., Sopp, P., Tomley, F. M. and Blake, D. P., 2008, A toolbox facilitating stable transfection of *Eimeria* species, Molecular and Biochemical Parasitology, Vol. 162 (2008), p. 77–86.

Constantinoiu, C. C., Molloy, J. B., Jorgensen, W. K. and Coleman, G. T., 2011, Characterization of the antibody response in birds following infection with wild-type and attenuated strain of *Eimeria tenella* and *Eimeria necatrix*, Veterinary Parasitology, Vol. 175(2011), p. 47–51.

Dong, H. Suo, X., Wang, M. and Teng, K., 2006, Characteristics of a line of *Eimeria necatrix* after 16 successive passages of oocysts collected after peak oocyst production, Journal of Parasitology, Vol. 92(6), p. 1229–1234.

Jeffers, T. K., 1975, Attenuation of *Eimeria tenella* through selection for precociousness, The Journal of Parasitology, Vol. 61(6), p. 1083–1090.

Johnson, J. and Reid, W.M., 1970, Anticoccidial drugs: lesion scoring techniques in battery and floor-pen experiments with chickens, Experimental Parasitology, Vol. 28, p. 30–36.

Jorgensen, W. K., Anderson, G.R., Jeston, P.J., Blight, G.W. and Molloy, J.B., 2006, Selection and characterization of two attenuated vaccine line of *Eimeria tenella* in Australia, Australian Veterinary Journal, Vol. 84(3), p. 89–94.

Kawaguchi, H., Konishi, T. and Nakamura, T., 1988, Characteristics of a precocious line of *Eimeria tenella*: pathogenicity and endogenous development, Japanese Journal of Veterinary Science, Vol. 50(2), p. 445–452.

Kawahara, F., Zhang, G., Suzuki, T., Iwata, A. and Nagamune, K., 2014, Characterization of *Eimeria brunetti* isolated from a poultry farm in japan, The Journal of Veterinary Medical Science, Vol. 76(1), p. 25–29.

Kawazoe, U., Bordin, E. L., Lima, C. V. and Dias, L. A. V., 2005, Characterisation and histopathological observation of a selected Brazilian precocious line of *Eimeria acervulina*, Veterinary Parasitology, Vol. 131(1-2), p. 5–14.

Long, P. L. and Johnson, K., 1988, *Eimeria* of American chicken: characteristics of six attenuated strains produced by selection for precocious development, Avian Pathology, Vol. 17, p. 305–314.

Shi, T., Liu, X., Hao, L., Li, J., Gh, A. N., Abdille, M. H. and Suo, X., 2008, Transfected *Eimeria tenella* could complete its endogenous development In vitro, Journal of Parasitology, Vol. 94(4), p. 978–980.

Tao, G., Shi, T., Tang, X., Duszynski, D. W., Wang, Y., Li, C., Suo, J., Tian, X., Liu, X. and Suo, X., 2017, Transgenic *Eimeria magma* Perard, 1925 displays similar parasitological properties to the wild-type strain and induces an exogenous protein specific immune response in rabbits (*Oryctolagus cuniculus* L.), Frontiers in Imunology, Vol. 8(2), http://doi: 10.3389/fimmu.2017.002.

Yan, W., Liu, X., Shi, T., Hao, L., Tomley, F. M. and Suo, X., 2009, Stable transfection of *Eimeria tenella*: constitutive expression of the YFP-YFP molecule through the life cycle, International Journal for Parasitology, Vol. 39(1), p. 109–117.

Editorial Board

Co-organized by

Thank You for Supporters:

THE 12TH RAJAMANGALA UNIVERSITY OF TECHNOLOGY INTERNATIONAL CONFERENCE (12TH RMUTIC)

RMUTCON

30 August – 1 September, 2023

Nongnooch Tradition Center Hall,
NongnoochPattaya Garden, Chonburi, Thailand

ADVISORY BOARD

1. President of the University Council, Rajamangala University of Technology Tawan-ok (Professor Dr. Soontorn Boonyatikarn)
2. President of 9 Rajamangala University of Technology
3. Department of Livestock Development
4. Managing Director of Nongnooch Garden Pattaya
5. Governor of Chonburi Province
6. President of National Research Council of Thailand
7. Director General of The Zoological Park Organization of Thailand
8. Eastern Research Administration Network
9. President of Agricultural Research Development Agency (Public Organization)
10. Director of Institute of Research and Development, 9 Rajamangala University of Technology
11. Professor Dr. Wisanu Pecharapa
12. Professor Dr.Alongklod Tanomtong
13. Associate Professor Vikorn Tanthawuttho

BY:
Institute of Research and Development of Rajamangala University of Technology Tawan-ok

FOR MORE INFORMATION:

033 - 136099 ext. 1181-1185 irdi@rmutto.ac.th https://rmutcon2023.rmutto.ac.th

The 13th Rajamangala University of Technology National Conference (13th RMUTNC)
The 12th Rajamangala University of Technology International Conference (12th RMUTIC)
and 5th RMUT Innovation Awards 2023

"9 RMUT Empowering and Promoting of Sustainable Innovation and BCG Model for the Next Normal"

Institute for Research and development,
Rajamangala University of Technology Tawan-ok,
Bangpra, Sriracha, Chonburi, Thailand, 20110

(+66) 033 - 136099 ext. 1181-1185
https://rmutcon2023.rmutto.ac.th
irdi@rmutto.ac.th